

Computational Studies of Chemical Interactions: Molecules, Surfaces and Copper Corrosion

Joakim Halldin Stenlid

KTH Royal Institute of Technology
School of Chemical Science and Engineering
Department of Chemistry
Applied Physical Chemistry
SE-100 44 Stockholm, Sweden

Copyright © Joakim Halldin Stenlid, 2017. All rights reserved. No parts of this thesis can be reproduced without permission from the author.

Paper II © 2016 American Chemical Society

Paper III © 2016 American Chemical Society

Paper IV © 2016 the PCCP Owner Societies

Paper VI © 2017 AIP Publishing

Paper VIII © 2017 American Chemical Society

Paper IX © 2017 American Chemical Society

TRITA CHE Report 2017:35

ISSN 1654-1081

ISBN 978-91-7729-506-8

Akademisk avhandling som med tillstånd av Kungliga Tekniska Högskolan i Stockholm framlägges till offentlig granskning för avläggande av teknologie doktorsexamen i kemivetenskap fredagen den 29:e september kl 10:00 i sal F3, KTH, Lindstedtsvägen 26, Stockholm. Avhandlingen försvaras på engelska.

Fakultetsopponent: Dr. Thomas Bligaard, Department of Chemical Engineering, Stanford University, Stanford, USA och SUNCAT Center for Interface Science and Catalysis, SLAC National Accelerator Laboratory, Menlo Park, USA.

Till Mormor och Morfar,
Farmor och Farfar

*"My dear, here we must run as fast as we can, just to stay in place.
And if you wish to go anywhere you must run twice as fast as that."*

The Red Queen in Lewis Carroll's Alice in Wonderland

Abstract

The chemical bond – a corner stone in science and a prerequisite for life – is the focus of this thesis. Fundamental and applied aspects of chemical bonding are covered including the development of new computational methods for the characterization and rationalization of chemical interactions. The thesis also covers the study of corrosion of copper-based materials. The latter is motivated by the proposed use of copper as encapsulating material for spent nuclear fuel in Sweden.

In close collaboration with experimental groups, state-of-the-art computational methods were employed for the study of chemistry at the atomic scale. First, oxidation of nanoparticulate copper was examined in anoxic aqueous media in order to better understand the copper-water thermodynamics in relation to the corrosion of copper material under oxygen free conditions. With a similar ambition, the water-cuprite interface was investigated with regards to its chemical composition and reactivity. This was compared to the behavior of methanol and hydrogen sulfide at the cuprite surface.

An overall ambition during the development of computational methods for the analysis of chemical bonding was to bridge the gap between molecular and materials chemistry. Theory and results are thus presented and applied in both a molecular and a solid-state framework. A new property, the *local electron attachment energy*, for the characterization of a compound's local electrophilicity was introduced. Together with the *surface electrostatic potential*, the new property predicts and rationalizes regioselectivity and trends of molecular reactions, and interactions on metal and oxide nanoparticles and extended surfaces.

Detailed atomistic understanding of chemical processes is a prerequisite for the efficient development of chemistry. We therefore envisage that the results of this thesis will find widespread use in areas such as heterogeneous catalysis, drug discovery, and nanotechnology.

Keywords: computational chemistry, density functional theory, chemical interactions, reactivity descriptors, copper corrosion, surface and materials science, nucleophilic substitution reactions, heterogeneous catalysis, transition metal oxides, nanotechnology

Sammanfattning på svenska

Den kemiska bindningen – en hörnsten inom naturvetenskapen och oumbärlig för allt liv – är det centrala temat i den här avhandlingen. Både grundläggande och tillämpade aspekter behandlas. Detta inkluderar utvecklingen av nya beräkningsmetoder för förståelse och karaktärisering av kemiska interaktioner. Dessutom behandlas korrosion av kopparbaserade material. Det sistnämnda är motiverat av förslaget att använda koppar som inkapslingsmaterial för hanteringen av kärnavfall i Sverige.

Kvantkemiska beräkningsmetoder enligt *state-of-the-art* har använts för att studera kemi på atomnivå, detta i nära samarbete med experimentella grupper. Initialt studerades oxidation av kopparnanopartiklar under syrgasfria och vattenrika förhållanden. Detta för att bättre kartlägga koppar-vattensystemets termodynamik. Av samma orsak detaljstuderades även gränsskiktet mellan vatten och kuprit med fokus på dess kemiska sammansättning och reaktivitet. Resultaten har jämförts med metanols och vätesulfids kemiska beteende på ytan av kuprit.

En övergripande målsättningen under arbetet med att utveckla nya beräkningsbaserade analysverktyg för kemiska bindningar har varit att överbrygga gapet mellan molekylär- och materialkemi. Därför presenteras teoretiska aspekter samt tillämpningar från både ett molekylärt samt ett fast-fas perspektiv. En ny deskriptor för karaktärisering av föreningars lokala elektrofilicitet har introducerats – den *lokala elektronadditionsenergin*. Tillsammans med den *elektrostatiska potentialen* uppvisar den nya deskriptorn förmåga att förutsäga samt förklara regioselektivitet och trender för molekylära reaktioner, och för interaktioner på metal- och oxidbaserade nanopartiklar och ytor.

En detaljerad förståelse av kemiska processer på atomnivå är en nödvändighet för ett effektivt utvecklande av kemivetenskapen. Vi förutspår därför att resultaten från den här avhandlingen kommer att få omfattande användning inom områden som heterogen katalys, läkemedelsdesign och nanoteknologi.

Nyckelord: beräkningskemi, täthetsfunktionalteori, kemiska interaktioner, reaktivitetsdeskriptorer, kopparkorrosion, yt- och materialvetenskap, nukleofila substitutionsreaktioner, heterogen katalys, överångsmetalloxider, nanoteknologi

List of papers

I. Searching for the Thermodynamic Limit – a DFT Study of the Step-Wise Water Oxidation of the Bipyramidal Cu₇ Cluster

Joakim Halldin Stenlid, Adam Johannes Johansson, and Tore Brinck

Phys. Chem. Chem. Phys., **2014**, 16, 2452–2464

II. Aqueous Solvation and Surface Oxidation of the Cu₇ Nanoparticle: Insights from Theoretical Modeling

Joakim Halldin Stenlid, Adam Johannes Johansson, Lars Kloo, and Tore Brinck

J. Phys. Chem. C, **2016**, 120, 1977–1988

III. The Surface Structure of Cu₂O(100)

Markus Soldemo, Joakim Halldin Stenlid, Zahra Besharat, Milad Ghadami Yazdi, Anneli Önsten, Christofer Leygraf, Mats Göthelid, Tore Brinck, and Jonas Weissenrieder

J. Phys. Chem. C, **2016**, 120, 4373–4381

IV. Reactivity at the Cu₂O(100):Cu–H₂O Interface: a Combined DFT and PES Study

Joakim Halldin Stenlid, Markus Soldemo, Adam Johannes Johansson, Christofer Leygraf, Mats Göthelid, Jonas Weissenrieder, and Tore Brinck

Phys. Chem. Chem. Phys., **2016**, 18, 30570–30584

V. Computational Analysis of the Early Stage of Cuprous Oxide Sulphidation: A Top-Down Process

Joakim Halldin Stenlid, Adam Johannes Johansson, Christofer Leygraf, and Tore Brinck

Corros. Eng. Sci. Techn., **2017**, 52, 50–53

VI. Dehydrogenation of Methanol on Cu₂O(100) and (111)

Zahra Besharat, Joakim Halldin Stenlid, Markus Soldemo, Kess Marks, Anneli Önsten, Magnus Johnson, Henrik Öström, Jonas Weissenrieder, Tore Brinck, and Mats Göthelid

J. Chem. Phys., **2017**, 146, 244702

VII. Local Electron Attachment Energy and Its Use for Predicting Nucleophilic Reactions and Halogen Bonding

Tore Brinck, Peter Carlqvist, and Joakim Halldin Stenlid

J. Phys. Chem. A, **2016**, 120, 10023–10032

VIII. Nucleophilic Aromatic Substitution Reactions Described by the Local Electron Attachment Energy

Joakim Halldin Stenlid, and Tore Brinck

J. Org. Chem., **2017**, 82, 3072-3083

IX. Extending the σ -Hole Concept to Metals: An Electrostatic Interpretation of the Effects of Nanostructure in Gold and Platinum Catalysis

Joakim Halldin Stenlid, and Tore Brinck

J. Am. Chem. Soc., **2017**, 139, 11012–11015

X. σ -Holes on Transition Metal Nanoclusters and Their Influence on the Local Lewis Acidity

Joakim Halldin Stenlid, Adam Johannes Johansson, and Tore Brinck

Crystals, **2017**, 7, 222

XI. σ -Holes and σ -Lumps Direct the Lewis Basic and Acidic Interactions of Noble Metal Nanoparticles: Introducing Regium Bonds

Joakim Halldin Stenlid, Adam Johannes Johansson, and Tore Brinck

Manuscript

XII. Local Lewis Acidity of $(\text{TiO}_2)_n$ $n=7-10$ Nanoparticles Characterized by DFT-Based Descriptors

Joakim Halldin Stenlid, Adam Johannes Johansson, and Tore Brinck

Manuscript

XIII. The Local Electron Attachment Energy and the Electrostatic Potential as Descriptors of Surface-Adsorbate Interactions

Joakim Halldin Stenlid, Adam Johannes Johansson, and Tore Brinck

Manuscript

The author contribution to the appended papers

Paper I-II, IV-V, VIII. Principal author. I formulated the research problem together with my coauthors, performed all calculations and wrote most of the paper.

Paper III, VI. I performed all DFT calculations, and wrote parts of the paper.

Paper VII. I performed parts of the DFT calculations, analyzed the results and assisted in the writing of the paper.

Paper IX. I co-developed the conceptual framework of the research, I performed all calculations and assisted in the writing of the paper.

Paper X-XIII. Principal author. I formulated the research project, defined the research problem together with my coauthors, performed all calculations and wrote most of the paper.

Other papers of the author not included in this thesis

Cuprous Oxide Surfaces Exposed to Sulfur Dioxide and Near-Ambient Pressures of Water

Markus Soldemo, Joakim Halldin Stenlid, Zahra Besharat, Niclas Johansson, Anneli Önsten, Jan Knudsen, Joachim Schnadt, Mats Göthelid, Tore Brinck and Jonas Weissenrieder

Submitted to J. Phys. Chem. C, 2017

On the Kinetic and Thermodynamic Properties of Aryl Radicals Using Electrochemical and Theoretical Approaches

Line Koefoed, Karina H. Vase, Joakim Halldin Stenlid, Tore Brinck, Yuichi Yoshimura, Henning Lund, Steen U. Pedersen and Kim Daasbjerg

Submitted Manuscript

Poly(styrene) Resin-Supported Cobalt(III) Salen Cyclic Oligomers as Active Heterogeneous HKR Catalysts

Michael G. C. Kahn, Joakim Halldin Stenlid and Marcus Weck

Adv. Synth. Catal. **2012**, 354, 3016-3024.

Table of Contents

1. INTRODUCTION	1
1.1. CHEMICAL INTERACTIONS.....	1
1.2. THE SAFE DISPOSAL OF SPENT NUCLEAR FUEL.....	2
1.3. AIMS AND SCOPE OF THE THESIS	4
2. SCIENTIFIC BACKGROUND	6
2.1. INTERACTIONS AND REACTIONS – GENERAL CONSIDERATIONS	6
2.1.1. <i>Basic thermodynamics and equilibrium theory</i>	6
2.1.2. <i>Reaction kinetics and transition state theory</i>	8
2.1.3. <i>Energy decomposition analysis</i>	10
2.1.4. <i>Examples of molecular reactivity and intermolecular bonding</i>	13
2.1.5. <i>Interactions at particles and surfaces</i>	15
2.2. COPPER AND ITS OXIDIZED STATES	18
2.2.1. <i>Metallic copper</i>	18
2.2.2. <i>Cuprous and cupric compounds</i>	19
2.2.3. <i>Corrosion</i>	21
2.2.4. <i>The Forsmark repository conditions</i>	22
2.2.5. <i>Copper corrosion in pure anoxic water</i>	24
2.2.6. <i>Behavior of copper under initial, transient and long-term repository conditions</i>	30
3. OVERVIEW OF COMPUTATIONAL METHODS	32
3.1. COMPUTATIONAL CHEMISTRY	32
3.1.1. <i>Introduction to quantum chemistry and wave function theory</i>	32
3.1.2. <i>Hartree-Fock theory</i>	39
3.1.3. <i>Post Hartree-Fock methods and correlation energy</i>	41
3.1.4. <i>Density functional theory</i>	43
3.1.5. <i>Band structure theory</i>	47
3.1.6. <i>Molecular mechanics and other (semi)-empirical methods</i>	48
3.1.7. <i>Solvation models</i>	50
3.1.8. <i>Molecular dynamics</i>	51
3.1.9. <i>Optimization procedures</i>	52
3.2. <i>AB INITIO</i> ATOMISTIC THERMODYNAMICS.....	53
3.3. ESTIMATIONS OF SURFACE PROPERTIES	56
3.3.1. <i>Surface related properties and phenomena</i>	56
3.3.2. <i>X-ray photoemission spectroscopy (XPS)</i>	57
3.3.3. <i>Scanning tunneling microscopy (STM)</i>	59
3.4. QUANTUM CHEMICAL INTERACTION AND REACTION DESCRIPTORS	60
3.4.1. <i>Frontier molecular orbital theory and Fukui functions</i>	60

3.4.2.	<i>Atomic partial charges</i>	62
3.4.3.	<i>The surface electrostatic potential</i>	63
3.4.4.	<i>The average local ionization energy</i>	66
3.4.5.	<i>Other concepts for describing bonding and interactions.....</i>	67
4.	SUMMARY OF THE RESEARCH	71
4.1.	THE BEHAVIOR OF COPPER-BASED MATERIALS.....	71
4.1.1.	<i>Aqueous solvation and oxidation of the Cu₇ nanocluster</i>	71
4.1.2.	<i>The surface structure and properties of Cu₂O</i>	80
4.1.3.	<i>Molecular interactions at the Cu₂O surface</i>	85
4.1.4.	<i>Sulphidation of Cu₂O</i>	92
4.2.	INTERACTION AND REACTIVITY ANALYSIS	95
4.2.1.	<i>The local electron attachment energy.....</i>	96
4.2.2.	<i>Nucleophilic reactions with electron deficient arenes and C=C bonds</i> <i>.....</i>	102
4.2.3.	<i>Halogen bonding.....</i>	106
4.2.4.	<i>Lewis acidity and basicity of metal and oxide nanoparticles.....</i>	107
4.2.5.	<i>Molecular adsorption on extended metal and oxide surfaces.....</i>	120
5.	OUTLOOK AND CONCLUDING REMARKS.....	124
	LIST OF ABBREVIATIONS	125
	ACKNOWLEDGEMENTS	127
	BIBLIOGRAPHY	129

1. Introduction

1.1. Chemical interactions

At the heart of the chemical science lies the formation and cleavage of chemical bonds. Every generation of chemists strive to master different classes of bonding for the sake of controlling chemical interactions and reactivity: be it with the objective to synthesize a desired compound, to prevent its decomposition or to tune the behavior of chemical systems such as living cells, batteries or catalytic processes. On a wider scale, chemical reactions and interactions are integral parts of our everyday life and in every aspect of the history, present and future of the world as we know it. The current thesis is on fundamental and applied aspects of chemical interactions.

In another perspective, and in parallel to the fast scientific progress of today, our generation has witnessed an explosive development of information technology (IT). This has revolutionized areas such as automation, data analysis, and data storage. The new technology has branched out to essentially every level of our society, and the chemical science has not been left behind. However, chemistry, like other areas of the modern society, has to keep up with the rapid changes. This thesis introduces, new conceptual tools based on computational methods that are well suited for (semi-)automated applications, in line with the current societal movements. It is the ambition to demonstrate that these tools could be useful when adapting the chemical science to modern technological trends, leading to, for instance, the accelerated identification of new materials and molecules for future applications. More specifically, it will herein be shown how local properties of molecules, particles and surfaces correlate with their chemical behavior. This can be exploited in effective screenings for identification of new drugs, economically and environmentally benign synthetic pathways or new catalytic materials, to mention but a few examples.

This thesis also encompasses detailed studies of chemical interactions of copper-based materials encouraged by the scientific concerns in connection to the safe disposal of spent nuclear fuel (SNF) in Sweden. For this purpose we have employed both the new methods mentioned above, and conventional state-of-the-art computational methods. In broad terms the thesis will here embark on two parallel journeys: one that studies the general aspects of chemical interactions and one more applied with the focus on questions regarding the behavior of copper materials under nuclear waste disposal conditions. The two areas are, however, closely intertwined as will be demonstrated in the following.

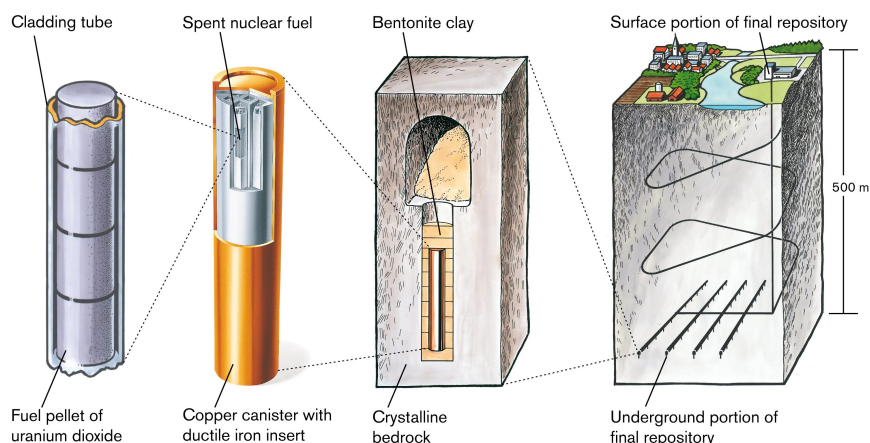


Figure 1. KBS-3 method for disposal of spent nuclear fuel (SNF) in Sweden. Illustration by Jan Rojmar. Reprinted with permission from @SKB.

1.2. The safe disposal of spent nuclear fuel

On the applied level, the safe disposal of SNF in Sweden has been a central motivation for the current thesis work. The need for a disposal originates from the forecast that, by the year of 2045, there will be approximately 12 000 tons of SNF in Sweden accumulated from nuclear power plants.¹ The waste will remain radioactive, and thus potentially harmful, for long time-periods amounting to hundreds of thousands and even millions of years. Therefore it must be kept isolated until the radioactivity has decayed to safe levels. It is estimated that the radioactivity of the waste will reach normal background levels after approximately 100 000 years.²

Scientifically, the planning of how to handle the disposal of SNF encompasses numerous different areas. This includes – but is not limited to – chemistry, microbiology and geology, as well as human behavioral and political sciences.² In addition, a vast range of scales must be covered, spanning over macro to the nanometer scale, as well as over the subfemtosecond timescale of light-matter interactions to geological timescales amounting to thousands and millions of years. From the viewpoint of chemical interactions, managing the radioactive waste embodies many appealing topics, including e.g. ion sorption, water and solute transportation, and a multitude of surface and interfacial processes. Among these, the primary focus of this thesis work has been on understanding processes related to the atomic scale corrosion behavior of the waste-encapsulating material, i.e. oxygen-free phosphorous-doped copper (Cu-OFP).

Internationally, the concept of deep geological storages (repositories) is regarded as one of the safest and most promising alternatives for the disposal of

SNF.³ In the proposed strategy for the construction of a SNF repository in Sweden – the so-called KBS-3 concept² – multiple integrated engineering barriers will operate jointly to keep the radioactive waste safely isolated from the biosphere for a minimum time-period of 100 000 years (see **Figure 1** for a schematic illustration of the KBS-3 concept). Similar disposal methods are being considered by other nations, e.g. Finland⁴ and Canada.⁵

In the KBS-3 design, the nuclear waste is to be placed in 4.835 m tall and 50 mm thick cylindrical copperⁱ canisters with outer radius of 0.5025 m. The canisters are reinforced by nodular cast iron inserts.^{6,8} Upon waste loading and sealing by friction stir welding, the copper canisters will weigh 25-28 tons depending on the type of contained waste.⁶ These canisters are to be deposited in the crystalline granite bedrocks 450-500 m underneath the Forsmark site in the northeast of Uppland, Sweden. A bentonite clay matrix (composed of primarily water and the montmorillonite mineral) will further protect the canisters. Bentonite will also be used to backfill the operational tunnels used during the transportation of the canisters to their repository sites. The role of the bentonite clay is multifold; it will hold the copper canister in place, protect it from load caused by movement of the bedrock, reduce microbial activity and retard the transportation of ground water and dissolved species to and from the copper canisters. The copper canister will act as a corrosion barrier hindering the radioactive nuclei from coming into contact with and dissolving in the ground water and thereby preventing the hazardous radio nuclei from transportation to the biosphere. It should, however, be noted that even if the copper barrier would fail, the transportation of radio nuclei is slow due to, e.g., the enclosing by the iron insert, the low solubility of the spent fuel in the ground water, the beneficial flow direction of the ground water as well as sorption to the bentonite clay and bedrock.

In order to assure an overall safe disposal, careful evaluations of a multitude of possible scenarios have been performed at numerous occasions. More detailed accounts of the complete safety analysis of the KBS-3 concept can be found elsewhere.^{2,9,10} The behavior and integrity of the copper canisters will be further discussed under the sections 2.2 and 4.1 of this thesis.

ⁱ In Sweden, copper of Cu-OFP quality is proposed as canister material based on multiple criteria, e.g. its resistivity to corrosion by water, its low susceptibility to hydrogen embrittlement, and the enhanced creep ductility of phosphorous-doped copper. The (complete) canister shall also be cost-effective, withstand considerable isostatic loads and shear, as well as being sufficiently resistant to corrosion under the ambient disposal conditions caused by species other than water.⁶ Alternative canister materials besides copper have been proposed over the years, including carbon steel and stainless steel, cast iron, titanium alloys, copper alloys, and nickel alloys.⁷

1.3. Aims and scope of the thesis

The aim of this thesis work is two-fold:

1. To improve the atomistic understanding of processes related to the behavior of copper under the prevailing conditions of the disposal of SNF as defined by the Swedish KBS-3 concept proposal. More specifically, the present study aims to extend the current knowledge of the copper-water interface and, to a limited degree, aid in the assessment of the long-term operational fitness of copper as a waste encapsulating material. A working hypothesis in this part of the thesis is that, while any corrosion process must be thermodynamically feasible, the thermodynamics of the copper-water interface differs from the bulk thermodynamics due to the nanostructure of the copper surface. We hypothesize that this may allow for a limited surface oxidation and the plausibility of this is evaluated by computational investigations. In addition, we consider the effect of the hydrogen sulfide and methanol molecules on the copper(I)oxides surfaces. Sulfides will be the leading copper corrodents during the main part of the SNF disposal, whereas the methanol studies aids in the general understanding of the behavior of the copper oxide surface.
2. To develop and apply computational tools for the description of chemical interactions and reactions of molecules, particles and surfaces. These tools should be based on physically motivated properties and allow for fast and reliable predictions of interaction characteristics while providing enhanced chemical insight. In essence, our studies in this area are based on the hypothesis that many chemical interactions, and particularly interaction trends, can be captured by variations in the ground state properties of the investigated compounds. In addition we hypothesize that, with the modern computational methods at hand, traditional ground state concepts like atomic charges or the frontier molecular orbital (FMO) theory for rationalizing chemical interactions can be extended to reflect a larger part of a compound's chemical properties and thereby offering a more powerful instrument for understanding chemical bonding. An overall ambition is to bridge the gap between molecular and materials science; we therefore aim to translate (and employ) reactivity concept from molecular theory to solid-state materials such as nanoparticles and extended metal and oxide surfaces.

The two points overlap in several of the studies included in the current thesis. Nonetheless, **Papers I-VI** will primarily cover point 1, whereas **Papers VII-XIII** cover point 2. In the two first studies of the thesis, **Papers I-II**, examines the

details of aqueous oxidation of a Cu_7 nanocluster. These studies provide insight into the mechanism and method dependency in the description of aqueous copper oxidation. **Paper III-IV** characterize the structures of the $\text{Cu}_2\text{O}(100)$ surface and the $\text{Cu}_2\text{O}(100)$ -water interface. **Paper V** elaborates on the initial mechanism and thermodynamics of the sulphidation of the $\text{Cu}_2\text{O}(100)$ and $\text{Cu}_2\text{O}(111)$ surfaces by H_2S , whereas **Paper VI** examines the behavior of the methanol molecule on the same surfaces. This thesis also introduces the new *local electron attachment energy* property for use in estimation and prediction of site resolved electrophilicity and Lewis acidity (**Paper VII**). The new property is compared to, and used complementary to, the surface electrostatic potential and the local average ionization energy quantities for characterization of surface, particle and molecular interactions and reactions in **Papers VII-XIII**. This includes the study of nucleophilic reactions with electron deficient arenes and activated C=C bonds, and the study of halogen bonding (**Papers VII-VIII**). Included are also characterizations of interactions at transition metals (**Papers IX-XI**) and oxide nanoparticles (**Paper XII**), as well as interactions with metal and oxide surfaces (**Paper XIII**).

2. Scientific Background

This chapter is intended to give a scientific context to the work performed in this thesis. It will introduce the basic theoretical aspects for the study of chemical interactions and reactions. It will also present the central aspects of importance to the safe disposal of SNF in Sweden, and briefly summarize the scientific work in the area leading up to this thesis.

2.1. Interactions and reactions – general considerations

The most central theories for describing chemistry are arguably thermodynamics and quantum mechanics (QM, see section 3.1). Whereas chemical thermodynamics provides the physical relation between the states of matter and relates heat and work to chemical reactions, quantum mechanics gives the physical description to chemical behavior on an atomic level. The link between the two is obvious and quantum mechanics can be used to estimate thermodynamic properties as will be outlined in section 3.2. While the proper introduction to QM is given in chapter 3, this part of the thesis will discuss the essential thermodynamic properties necessary for the study of chemical interactions and reactions. The thermodynamic laws will be put in relation to equilibrium theory, and to reaction kinetics as described by the conventional transition state (TST) theory. In addition, various theoretical approaches of decomposing interactions and reaction into its fundamental parts are discussed under section 2.1.3. Some specific molecular, particle and surface interaction and reactions are reviewed in sections 2.1.4-2.1.5. Included in section 2.1.5 are also some central crystallographic and condensed phase physics concepts for describing extended materials.

2.1.1. Basic thermodynamics and equilibrium theory

From a theoretical point of view, one of the most fundamental properties of a chemical system is its free energy. The free energy is by definition the energy of a thermodynamic system that can be converted into reversible work. Chemical processes are thoroughly represented by the free energy and it describes e.g. reactions and chemical equilibria. Furthermore, the laws of thermodynamics state that any spontaneous process will result in a reduction of the free energy and the release of heat (work). *Vice versa*, work must be provided for a non-spontaneous process to occur. Different definitions of the free energy exist depending on the type of system considered. The Gibbs free energy, G , and the Helmholtz free energy, A , are arguable the most commonly used for chemical purposes where G is valid under constant temperature and pressure and A is valid under constant temperature and volume. By definition:

$$G(p, T) \equiv \underbrace{U + pV}_H - TS = H - TS \quad (2.1)$$

$$A(V, T) \equiv U - TS \quad (2.2)$$

In the above U is the internal energy of the system including its kinetic and potential energies, H is the enthalpy, S is the entropy, and p , T , and V are the pressure, absolute temperature and volume of the system. S is here defined based on the number of accessible microscopical configurations Ω of the system as

$$S = k_B \ln \Omega \quad (2.3)$$

where k_B is the Boltzmann constant. G , U , H , and S are related to statistical ensembles of the system that may be represented by so-called *partition functions*, further discussed under section 3.2. G , U , H , and S are, moreover, extensive state functions that can be expressed as a sum of the properties of the subsystems. The change in U (i.e. dU) can e.g. be obtained by:

$$dU = TdS - pdV + \sum_{i=1}^n \mu_i dN_i \quad (2.4)$$

In the above, the μ_i is the chemical potential of the i^{th} species of the system. The chemical potential is an useful thermochemical property that is defined as the rate of change in free energy as the number of entities (N_i) of species i is changed under constant concentrations of other compounds. For constant pressure and temperature:

$$\mu_i = \left(\frac{\partial G}{\partial N_i} \right)_{T, p, N_{j \neq i}} \rightarrow dG = \sum_{i=1}^n \mu_i dN_i \quad (2.5)$$

Moreover:

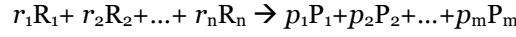
$$\mu_i = \mu_i^\circ + RT \{i\} \quad (2.6)$$

where μ_i° is the chemical potential at the standard state of $T=298.15$ K, $p=1$ bar and a concentration of 1 M. For a dissolved or liquid phase species, $\{i\}$ is the activity a_i of species i with $\{i\}=a_i=\gamma_i[A_i]$. γ_i is the activity coefficient that equals unity for an ideal solute. For a gas phase species, $\{i\}$ is the fugacity $f_i = p_i \varphi_i$ where p_i is the partial pressure of species i and φ_i is the fugacity coefficient. $\varphi_i=1$ for an ideal gas.

Equipped with the above relations we can study chemical systems, e.g. their equilibrium states. At equilibrium the free energy is at its minimum, thus:

$$dG = \sum_{i=1}^n \mu_i dN_i = 0 \quad (2.7)$$

We can furthermore relate the equilibrium constant K of an arbitrary reaction



to its standard Gibbs reaction free energy $\Delta_r G^\circ$ as

$$\Delta_r G^\circ = -RT \ln K \quad (2.8)$$

with

$$\Delta_r G^\circ = \sum_{j=1}^m p_j G_j^\circ - \sum_{i=1}^n r_i G_i^\circ \quad (2.9)$$

and

$$K = \frac{\prod_{j=1}^m \{P_j\}^{p_j}}{\prod_{i=1}^n \{R_i\}^{r_i}} \quad (2.10)$$

In the above R_i and P_j are reactants and products, respectively, with stoichiometry coefficients r_i and p_j . For an electrochemical reaction the Gibbs free energy is related the cell potential E_{cell} via Faradays constant, F , and the number of electrons transferred in the cell reaction (n):

$$\Delta G = -nFE_{\text{cell}} \quad (2.11)$$

2.1.2. Reaction kinetics and transition state theory

According to the conventional transition state theory (TST) for describing chemical reaction kinetics, the temperature (T) dependent rate constant $k(T)$ of an elementary reaction step can be written as:

$$k(T) = \kappa \frac{k_B T}{h} e^{-\frac{\Delta G^\ddagger}{RT}} \quad (2.12)$$

This is known as the Eyring equation¹¹ and has a similar form as the empirical Arrhenius equation. It is based on the assumption that the reactants are in quasi-equilibrium with the transition state (TS).

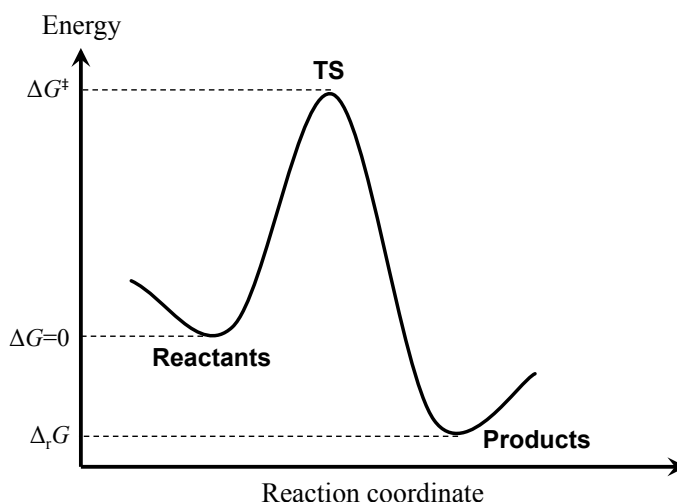


Figure 2. Potential energy surface (PES) describing an arbitrary chemical reaction. The transition state (TS) represents the highest energy point on a minimum energy path connecting the reactants with the products.



In the Eyring equation, ΔG^{\ddagger} is the Gibbs free energy difference between the reactants and the TS, $R(=N_A k_B)$ is the ideal gas constant, whereas k_B and h are the Boltzmann and Planck constants, respectively. The transmission coefficient, κ , corrects for the statistical possibility that some reaction paths leading to the TS falls back to the reactants instead of the product (often neglected and thereby assuming $\kappa=1$). From the above, the reaction rate, r , for an irreversible elementary reaction $A \rightarrow B$ is given by:

$$r = -\frac{d[A]}{dt} = k(T)[A] \quad (2.14)$$

with $[A]$ being the molar concentration of A. This can be formulated for an arbitrary reversible elementary reaction with the forwards and backwards reaction constants k_1 and k_{-1} :

$$r_{tot} = r_1 - r_{-1} = k_1 \prod [R_i]^{r_i} - k_{-1} \prod [P_j]^{p_j} \quad (2.15)$$

TST can, by and large, be applied to reaction systems of any given complexity. Nevertheless, TST breaks down under certain circumstances. A basic assumption in TST is for instance that the atom nucleus can be treated as classical particles and thus need a sufficiently large thermal energy to overcome the reaction barrier

(ΔG^\ddagger). However, the laws of quantum mechanics allow for the particles to tunnel through any finite barrier. In cases of large reaction barriers the tunneling probability is infinitesimally small, but the probability increases with decreasing barrier heights. Similarly the tunneling probability increases for light elements such as hydrogen. Thus TST often gives bad estimations for very fast reactions, and more often so for light elements. TST also assumes that all reactions proceed over the lowest saddle point on the potential energy surface (PES, see **Figure 2**), why TST tends to fail for high temperature reaction or reactions with very flat TS regions. In addition, TST resides on the assumption that the reactants have adopted Boltzmann distribution. For short-lived species, such as reaction intermediates, this may not be true leading to the break down of TST. In the general case, however, TST is valid and a useful tool for describing chemical reaction kinetics. Improvements of TST can be obtained by for instance adding dynamic corrections to the TST reaction rates.

2.1.3. Energy decomposition analysis

Ultimately, chemistry originates in the pair-wise interaction of chemical entities (three body effects can, in most cases, be neglected). Over the years, numerous methods have been developed that aim to elucidate the origin of molecular interactions by the partitioning into their (ideally) fundamental components. This procedure is often referred to as energy decomposition analysis (EDA).^{12–14} Although there is no unique partitioning scheme for chemical interactions, any physically motivated decomposition should be based on the laws of quantum mechanics; hence essentially being a function of the mutual electronic and nuclear electrostatics, the kinetic energy of the electrons and nuclei, and the necessity of the fermionic electrons to obey the Pauli exclusion principle. Therefore, most decomposition schemes include similar components, often sorted under contributions from “quasi-classical” electrostatics (E_{EL}), Pauli repulsion (exchange, E_{EX}), as well as orbital mixing and relaxation (charge-transfer, E_{CT} , and polarization, E_{POL}). Some schemes also implicitly or explicitly include dispersion effects (E_{DISP}) and deformation energy (E_{DEF}), the latter resulting from the geometrical distortion of two compounds upon interaction, which in certain cases can be related to sterical hindrance. In summary the pair-wise molecular interaction energy (ΔE_{int}) may be decomposed into some or all of the above components as (E_{REST} is a rest term):

$$\Delta E_{\text{int}} = E_{\text{EL}} + E_{\text{EX}} + E_{\text{POL}} + E_{\text{CT}} + E_{\text{DISP}} + E_{\text{DEF}} + E_{\text{REST}} \quad (2.16)$$

In the case of interactions in condensed phase, a term accounting for the solute-solvent interactions may also be added. The various contributions to ΔE_{int} can be sorted under frozen interactions (E_{EL} , E_{EX} , and E_{DISP}) and relaxation effects (E_{CT}

and E_{POL}). In an computational framework, it should also be noted that, in the limit of an infinite basis set, the distinction between charge-transfer and polarization becomes ill-defined,^{12,15} why these are sometimes grouped into $E_{\text{CT/POL}}=E_{\text{CT}}+E_{\text{POL}}$.ⁱⁱ Furthermore, most EDA schemes amount to estimations of interaction enthalpies at zero K, usually neglecting thermal effects and entropic contributions all together.

The majority of the established EDA methods estimate the energy contributions by comparison of monomer and dimer energies of the interacting compounds via well-defined schemes of calculations of constrained and relaxed wave functions (or DFT densities). Such methods include the original KM-EDA^{17–19} by Kitaura and Morokuma as well as its later revisions: the absolute localized molecular orbital (ALMO) EDA²⁰ and pair-interaction PIEDA²¹ methods. Other EDA schemes are the extended transition state EDA (ETS EDA) method by Ziegler and Rauk,^{22–24} and the natural EDA method based on the natural bond orbital analysis.^{25–28} In another family of methods, the interaction energy is decomposed on the basis of (especially Møller-Plesset) perturbation theory. The most well known of these is, arguably, the symmetry adapted perturbation theory SAPT^{29–31}

The methods discussed above reside on the study of both the adduct and the separated monomers. However, in estimations of a chemical compound's reactivity or interaction affinity, it can often be advantageous to make use of the ground state properties of the individual compounds. Such properties for instance encompass electronegativity, dipole moment, electron affinity (EA),ⁱⁱⁱ ionization energy (I)ⁱⁱⁱ and polarizability. On the basis of ground state properties, and/or the knowledge of a compounds mode of interaction, it is possible to characterize its interaction behavior. For instance, in the Hard-Soft Acid-Base theory (HSAB)³² of Pearson a species is categorized as either hard with primarily electrostatically controlled interactions, or soft with interactions controlled by charge-transfer.

This thesis will primarily consider a framework developed by Brinck, Politzer and coworkers,^{33–36} for estimations of molecular properties for predictions and rationalization of both covalent and non-covalent molecular interactions. Here, the Coulombic part of the interaction is derived from the interaction of a molecule and a point charge q at position \mathbf{r} in space. From perturbation theory,

ⁱⁱ In addition, if small basis sets are used, counterpoise corrections according to the suggestions by e.g. Boys and Berardi¹⁶ should be employed to minimize the basis set superposition error.

ⁱⁱⁱ Although the EA and the I are not commonly defined solely in terms of a compound's ground state, the two properties can be derived from the ground state as demonstrated further on in this thesis.

the Coulombic contribution to the interaction energy, $\Delta E_{\text{EL}}(q, \mathbf{r})$, may be defined by a power series:

$$\Delta E_{\text{EL}}(q, \mathbf{r}) = qE_{\text{EL}}^{(1)}(\mathbf{r}) + q^2E_{\text{EL}}^{(2)}(\mathbf{r}) + q^3E_{\text{EL}}^{(3)}(\mathbf{r}) \dots \quad (2.17)$$

For most chemical applications, terms greater than second order in eq. 2.17 can be omitted without the loss of important information. $E_{\text{EL}}^{(1)}(\mathbf{r})=V(\mathbf{r})$ corresponds to the molecular electrostatic potential, whereas $E_{\text{EL}}^{(2)}(\mathbf{r})=P(\mathbf{r})$ is a polarization correction to $V(\mathbf{r})$.³⁴ Both quantities are further discussed and defined under section 3.4.3. Brinck, Politzer and coworkers have shown that these quantities, when evaluated on a molecular isodensity surface (*vide supra*), can be used to understand molecular interactions. Better descriptions of chemical interactions can be obtained if the Coulombic contributions are evaluated alongside other quantities describing e.g. the molecular charge-transfer capacities. The latter have traditionally been characterized by the average local ionization energy property, $\bar{I}(\mathbf{r})$, defined by Sjöberg et al.³⁷ for Lewis basic (nucleophilic) compounds, as described in section 3.4.4. A corresponding property for Lewis acidic (electrophilic) compounds, referred to as the electron attachment energy, $E(\mathbf{r})$, is introduced in **Paper VII** and section 4.2.1 of this thesis. Inspired by Brinck's^{34,38} modified interaction properties function, the interaction energy contribution, ΔE_{int} , of a Lewis base ($b=1$, $a=0$) or Lewis acid ($b=0$, $a=1$) can be captured by a multi-linear relationship of the above properties:

$$\Delta E_{\text{int}} \approx \alpha V(\mathbf{r}) + \beta P(\mathbf{r}) + \gamma [b\bar{I}(\mathbf{r}) + aE(\mathbf{r})] + \delta \quad (2.18)$$

In the eq. 2.18 the δ rest term includes e.g. dispersive, entropic, thermal as well as sterical effects. In line with the ambiguous distinction between charge-transfer and polarization effects (*vide supra*), charge-transfer/polarization effects are often grouped together. Hence eq. 2.18 resembles the EDA decomposition of eq. 2.16, but from a monomer perspective.

Making use of Coulombs law and a thermodynamic cycle for charge-transfer, the total interaction of a Lewis base (B) interacting with a Lewis acid (A) may be described by the product of the electrostatic contributions (*cf.* Coulomb's law), and the difference between the electron affinity of the Lewis acid [here taken as $E(\mathbf{r})$] and the ionization energy [$\bar{I}(\mathbf{r})$] of the Lewis base as:

$$\Delta E_{\text{int}}^{\text{tot}} \approx C_1 E_{\text{EL,A}}(\mathbf{r}) E_{\text{EL,B}}(\mathbf{r}) + C_2 [\bar{I}(\mathbf{r}) - E(\mathbf{r})] + C_3 (\delta_A + \delta_B) \quad (2.19)$$

where

$$E_{\text{EL}}(\mathbf{r}) = [\alpha V(\mathbf{r}) + \beta P(\mathbf{r})] \quad (2.20)$$

and C_1 , C_2 and C_3 are coefficients. Linear relations of ground state properties to describe chemical interaction energies will be further exploited under section 4.2.

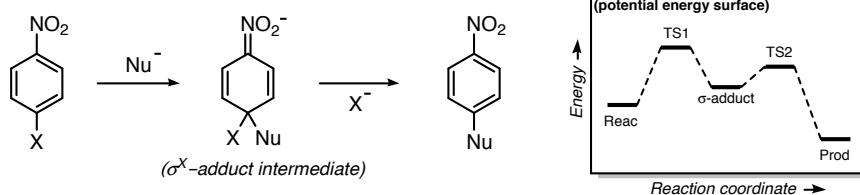
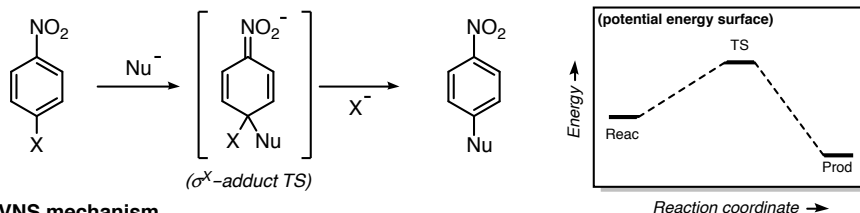
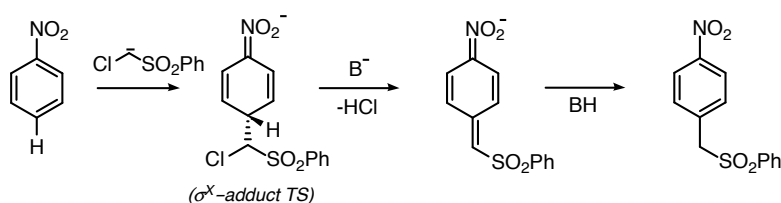
2.1.4. Examples of molecular reactivity and intermolecular bonding

An overwhelming number of molecular reactions and intermolecular interactions have been described in the chemical literature. This includes weak, non-covalent interactions such as hydrogen bonding and van der Waals interactions. It also includes formation and breakage of stronger bonds via e.g. addition, decomposition, replacement and redox reactions. In the following, some of the molecular reactions and interactions considered in this thesis will be introduced.

Nucleophilic aromatic substitutions

The nucleophilic aromatic substitution (NAS) reactions studied in **Papers VII-VIII** are useful and common tools in synthetic chemistry with wide-spread applications in both academia and in the chemical industry.³⁹⁻⁴³ Aromatic subgroups are, for instance, present in a majority of our medical drugs and nucleophilic aromatic reactions are regularly employed in their manufacturing. The most well-known and versatile kind of NAS reaction is arguable the S_NAr reaction. Overall, this reaction leads to the substitution of a suitable leaving group (nucleofug, often an halide $X=F, Cl, Br$ or I) directly attached to an aromatic group of the starting material with a nucleophilic reactant (Nu^- or NuH). In its putative mechanism, the reaction proceeds over a σ -adduct intermediate at which the aromaticity of the reacting arene is lost. The aromaticity is regained upon expulsion of the leaving group in a subsequent step (see **Scheme 1.a**).^{40,41,43} Altogether, this is known as the step-wise mechanism. Some alterations to the putative mechanism persist, however. It has, for instance, been found that the reaction is likely to proceed without the formation of an intermediate σ -adduct for the cases of favorable nucleofugs such as Cl^- , Br^- or I^- and/or deactivated to intermediately activated reactants. These cases instead lead to a concerted mechanism (**Scheme 1.b**).⁴⁴⁻⁴⁷ Further variations to the reaction mechanism are introduced if the nucleophile is protonated resulting in an additional deprotonation step that can take place at either stage of the reaction. Electron-withdrawing groups such as nitro groups activate NAS reactions, where the nitro group primarily activates the ortho and para positions.

The vicarious nucleophilic substitution (VNS) reaction class is closely related to S_NAr , but less well-recognized.^{42,48-52} In VNS an H of the aromatic reactant is replaced by a nucleophile. Using the standard S_NAr mechanism, such an operation would result in the expulsion of a hydride ion (H^-), a very reluctant leaving group. Hence, this is not a beneficial reaction route. A more favorable situation can be achieved by the use of e.g. the chloromethyl phenyl sulfone carbanion nucleophile. Upon addition of this nucleophile to the arene, HCl leaves

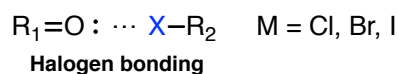
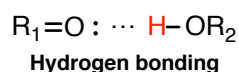
a) Step-wise S_NAr mechanism

b) Concerted S_NAr mechanism

c) VNS mechanism


Scheme 1. Showing the putative step-wise S_NAr mechanism in a) e.g. applicable if $X=F$, the concerted S_NAr mechanism in b) e.g. with $X=Cl, Br$ or I , and the VNS mechanism in c).

via a β -elimination. HCl is a much better leaving group than H^- and the substitution reaction is made feasible. The above corresponds to the VNS mechanism as outlined in **Scheme 1.c**.

Hydrogen and halogen bonding

Hydrogen bonding (H-bonding) is an important class of non-covalent interactions taking place between a compound with a H bonded to a strongly electronegative atom, an H-donor, and another strongly electronegative atom, an H-acceptor. The electronegative atoms are usually O, N or F. Examples of H-bonds are the hydrogen-bonding network in water ($HO-H \cdots OH_2$) and the base pairing in DNA.



Scheme 2. Comparison of halogen and hydrogen bonding, $X=Cl, Br$ or I .

Another very similar intermolecular interaction type is known as halogen bonding (see **Scheme 2** for a comparison to hydrogen bonding). The halogen bond takes place between a singly coordinated third to fifth row halogen atom ($X=\text{Cl}$, Br or I , $X\neq\text{F}$) and the lone pair of another electronegative atom. At first glance this type of bonding may appear counterintuitive since an interaction between two electronegative atoms usually results in a net repulsion, as is e.g. the case between O and F . Brinck et al.⁵³ were the first to show that, although the lone pair regions perpendicular to the X-R bond are indeed negative for $X=\text{Cl}$, Br and I , the region along the X -extension of the X-R bond has a positive electrostatic potential (see section 3.4.3). This explains the propensity for the heavier halogen atoms to interact with electron donating molecules. For F the corresponding region along the bond extension usually has a negative electrostatic potential. The abovementioned interaction was later denoted halogen bonding⁵⁴ and has, together with e.g. hydrogen bonding, found wide applications the field of supra molecular chemistry. Halogen bonds are, for instance, considered in areas such as enzyme design and crystal engineering. Halogen bonds are discussed further in **Paper VII** and section 4.2 of this thesis.

2.1.5. Interactions at particles and surfaces

Many properties of particles and materials are dictated by the chemical interactions of the material surfaces and interfaces with its ambient environment. The chemical behavior at surfaces controls properties such as biocompatibility and toxicity, corrosion resistance and degradation, catalytic activity, wettability and hydrophobicity, sorption properties, solubility and nucleation, and to a certain degree electronic and thermal conductivity. Thus the understanding of interactions on materials and particle surfaces is of uttermost importance. Proper characterization is essential for an effective design and utilization of new and established materials in various applications spanning over electronics, medical therapy, heterogeneous catalysis, drug delivery, solar cells, and sensors, to mention but a few examples. Interactions and reactions of particles and surfaces are discussed further in **Papers I-VI** and **IX-XIII**, and in chapter 4 of this thesis. Below follow a short background.

Nanoparticles

Transition metal (TM) and oxide nanoparticles (NPs) and nanoclusters (subnanosized particles) have been studied in **Papers I-II** and **IX-XII**. This includes the characterization of the anoxic oxidation behavior of copper NPs in aqueous environments, but also fundamental investigations of the properties that govern interactions of these particles.

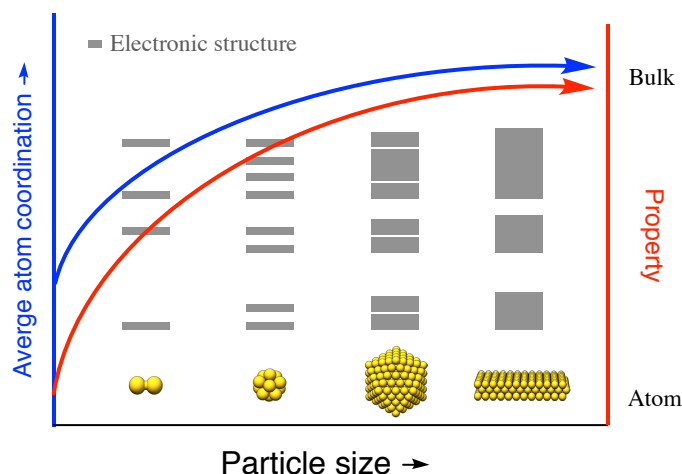


Figure 3. Illustration of the difference and connection between metal atoms (left), clusters (middle) and crystalline metallic material (right).

Nanosized materials are attractive owing to their unique properties that often differ considerably from the properties of the bulk materials, e.g. with regards to their chemical reactivity. The properties of nanosized material can largely be explained by atomic undercoordination and quantum size effects.⁵⁵ As illustrated by **Figure 3**, the electronic structure of a metal NP goes from having discrete one-electron states (orbitals) to the continuum band structure of bulk material as the particle size increases. Simultaneously the average atomic coordination is increased. This closely follows the size-dependent convergence of the properties of the particles towards that of the crystalline solid. At some point the NP can be considered to behave identically to the bulk material. As an example, Kleis et al.⁵⁶ argue that the bulk limit is reached around the size of an Au_{561} particle ($\phi \leq 3$ nm) based on adsorption properties of Au NPs.

Owing to the finite size of the NP, the same computational toolbox as is employed for molecular interactions can, by and large, be applied to NP. Therefore the study of NP is a natural step from the molecular towards the materials perspective. This is particularly useful for the work conducted in this thesis where an ambition is to employ quantum chemical concepts (descriptors) from molecular theory for the understanding of the chemical properties of materials.

The interactions of NPs with molecular compounds in their near field is an important aspect of their applicability. Supported NPs are e.g. used as exhaust gas catalysts in automobiles.^{57,58} In addition NPs' potential application in drug delivery and cancer therapy are investigated.^{59–61} In their applications, the NPs will experience conditions that are challenging from an engineering point of view where the NPs are in constant contact with harsh chemical environments. Thus, a

detailed knowledge of the NPs interaction behavior is necessary in order to optimize their performances.

In the work covered by this thesis, interactions and reaction properties of NPs have been considered primarily for particles of the smaller nanorealm, with some exceptions. In order to probe Lewis acidity and basicity of the NPs, probe molecules comprising the H₂O, H₂S, NH₃ and CO nucleophiles, and the BH₃, BF₃, Na⁺ and HCl (H-down) electrophiles have been employed. These results are compared to predictions based on the various quantum chemical descriptors. The studies encompass e.g. Au nanoparticles of sizes from subnanometer (Au₉) to ~3nm (Au₅₆₁), with low C_s symmetry to highly symmetric I_h clusters in **Papers IX-XI**. The behavior of Au is also compared to the other group 11 metals, Ag and Cu. In addition are TM₁₃ NP of Pt, Pd, Cu, Au, Rh, Ru, Co, Ir studied in **Paper X** and (TiO₂)_n, n=7-10, NP in **Paper XII**, see section 4.2.4.

Metal and oxide surfaces and interfaces

Interactions with extended surfaces and interfaces are central in many areas of the chemical and materials sciences. For instance, electrode reactions in batteries and fuel cells take place at the electrode surface, as do catalytic reactions. Not only reactions are important but also weaker interactions, which controls e.g. wetting properties and agglomeration. Although surface interactions may entail processes on many kinds of materials such as biomaterials, composites, plastics, all sorts of metals and alloys, ceramics and glasses, and various semiconductors, this thesis focuses on the surface interaction characteristics of non-alloyed transition metals and semiconducting transition metal oxides.

In the study of extended metal and oxide surfaces, it is important to consider the unique characteristics of crystalline solids. Crystalline structures are usually close-packed and constructed by repeating units, motifs. These are sorted under the 230 unique space groups that describe the symmetry of a crystal lattice. The formation of surfaces may be achieved by cutting the crystal in two halves. The surface energy γ is a measure of the cost of creating a particular surfaces and correlates with its reactivity. γ can be defined as the energy difference between two surfaces of area A created from the native crystal as:

$$\gamma = \frac{1}{2A} (E_{crystal} - 2E_{surf}) \quad (2.21)$$

There are a large number of possible ways to cut the crystal into two. Well-order surfaces are obtained when cut along low index crystallographic plans with Miller index (hkl). Examples are the low index *fcc* (111), (110), and (100) surfaces that will be discussed to some extent in this thesis. In order to lower the surface energy or to

adapt to adsorbate interactions, the surface can reconstruct forming new structural patterns. These may have the same or a dissimilar symmetry compared to the ideal crystalline surface. Surface reconstruction is superficially related to surface roughness, but the latter is associated to the macroscopic scale and reflects the ratio between the real area of a surface to the geometrical area.

The atomic coordination is of importance to the interaction properties of the surface, where the surface atoms are undercoordinated compared to the bulk. Lower coordination leads, in the normal case, to a larger tendency to interact. Reactivity and interactions characteristics of a surface may further be evaluated by the use of probe molecules. The molecular concepts of Brønsted and Lewis acidity and basicity are e.g. often extended to oxide surfaces. Suitable probe molecules for evaluating Lewis acidic sites are e.g. NH_3 or CO , whereas Lewis basic sites may be probed by e.g. CO_2 or BF_3 .^{62–64} There are numerous experimental techniques for the study of surface related properties and adsorbate interactions. This includes X-ray photoelectron spectroscopy (XPS), X-ray adsorption and emission spectroscopy (XAS and XES), scanning tunneling microscopy (STM), low-energy electron diffraction (LEED), atom force microscopy (AFM), scanning electron microscopy (SEM) and thermal desorption spectroscopy (TDS). Further considerations regarding surface properties and interactions will be discussed under section 3.3-3.4, and in chapter 4. General considerations may also be found elsewhere.^{65,66}

2.2. Copper and its oxidized states

Copper is one of our oldest materials and it remains essential also in modern days with an annual world production of approximately 19.4 million tons (2016).⁶⁷ It is used in its pure metallic form, as part of alloyed material as well as in its oxidized states, primarily as Cu(I), cuprous copper, and Cu(II), cupric copper. Compounds in the oxidation states +III and +IV are known but rare.^{68–70}

2.2.1. Metallic copper

Copper in its metallic form displays excellent thermal and electronic conductivity. The latter in combination with a relatively low price, have led to its dominant role in electronic applications and power transmission. Copper is not as durable and strong as e.g. steel, but its high ductility and chemical stability (among other properties) makes it a popular construction material with applications in e.g. plumbing, roofing and industrial machinery.⁷¹ The properties of copper can largely be traced to its electronic configuration with a $3d^{10}4s^1$ valence occupation. Consequently the interatomic metal bonds in the copper material (with a face center cubic crystalline arrangement, **Figure 4**) primarily originate in the overlap

of the partly occupied electronic s -states. These bonds are comparably weak among the transition metals, and non-directional giving rise to e.g. the high ductility of copper. It also explains the high conductivity of copper since the weak bonding is related to the weak electron-phonon coupling in the material that otherwise would prohibit electron conduction. Copper belongs to the same group as silver and gold in the periodic table, but in contrast to its noble neighbors, copper is only chemically inert under oxygen free conditions as it slowly reacts with oxygen.^{68–70}

2.2.2. Cuprous and cupric compounds

The most common oxides of copper are cuprite (Cu_2O) and tenorite (CuO). Their crystal structures are shown in **Figure 4**. These are formed under oxygen rich conditions, both in (humid) air and in aqueous environments.^{72,73} A mixed Cu(I) and Cu(II) oxide, paramelaconite Cu_4O_3 , is also known but rare.⁷³ Copper, and its oxides, are common heterogeneous catalysts for production of methanol,⁷⁴ for photocatalytic water splitting,⁷⁵ as well as in CO reduction and the water-gas shift-reaction.^{57,76} Copper oxides are also used in photovoltaic applications.^{77–79} In addition are Cu-ions catalytic centers in many enzymatic reactions, e.g. in the laccase enzyme for oxidation of phenolic compounds.⁸⁰ Under oxidizing conditions, copper dissolves in water forming Cu^+ and Cu^{2+} complexes. In the following are, however, primarily solid compounds discussed.

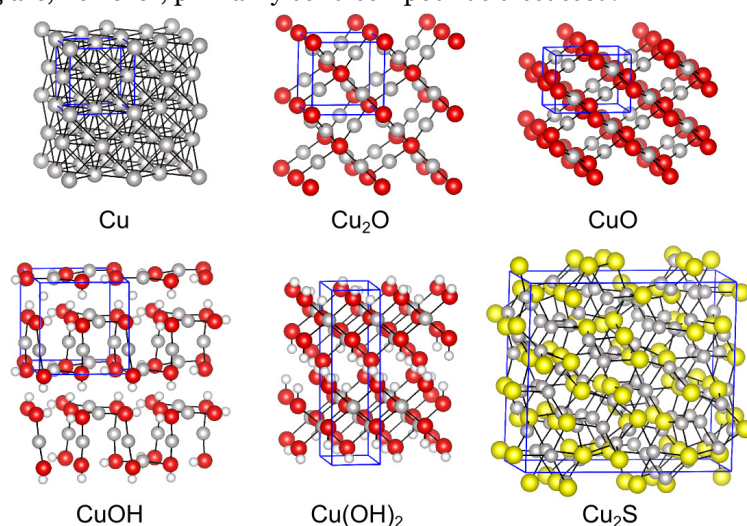


Figure 4. Crystal structures of copper (Cu), cuprite (Cu_2O) and tenorite (CuO) in the upper panel, and cuprice⁸² (CuOH), spertiniite ($\text{Cu}(\text{OH})_2$) and low chalcocite (Cu_2S) in the bottom panels. Copper in grey, oxygen in red, sulphur in yellow and hydrogen in white. Unit cells are marked in blue.

Cu₂O is studied in wealth in **papers III-VI** in this thesis motivating a more detailed description of its characteristics. Cuprite is a diamagnetic p-type semiconductor with a direct band gap of 2.17 eV and an optical band gap of 2.67 eV.^{72,81} The crystal structure can be seen as two intertwined Cu₂O networks with an overall simple cubic arrangement (space group $Pn\bar{3}m$). The cubic cell parameter of Cu₂O is 4.27 Å.^{83,84} The Cu-O bonds are largely ionic with a certain degree of covalency.⁸⁵ Alternatively, the structure can be described as built-up by a *bcc* O and an *fcc* Cu sublattice where O has tetrahedral and Cu linear coordination. The linear O-Cu-O unit is a rather unique mineralogical arrangement, and the M₂O crystal structure of cuprite is rare amongst metal oxides.⁷² The two intertwining Cu₂O networks of cuprite have traditionally been seen as bound by weak dispersive interactions.⁷² However, suggestions persist that the closely spaced (3.02 Å) Cu⁺ atoms of the two networks have a stronger (possible covalent) Cu⁺-Cu⁺ dimer bond.^{85,86} Cu₂O is used in e.g. antifouling paints, in heterogeneous catalysis, spintronics, nanoelectronics and photovoltaic applications.

Copper also forms cupric [Cu(II)] hydroxides Cu(OH)₂, spertiniite, and cuprous [Cu(I)] hydrides CuH, copper hydride. CuH₂ is only known to exist in molecular form, whereas crystalline CuOH (cuprice) is very rare but has been both synthesized and theoretically described.⁸⁷⁻⁹¹ Copper carbonates, CuCO₃ and malachite Cu(OH)₂(CO₃), are often encountered together with Cu(OH)₂. In saline environments copper can, furthermore, form Cl-containing minerals including atacamite (orthorhombic) and paratacamite (rhombooctahedral) of Cu₂(OH)₃Cl stoichiometry. In addition copper forms chlorides, primarily CuCl₂, and sulfate hydrates e.g. chalcantite, CuSO₄(H₂O)₅.

Another class of compounds of particular interest in this thesis work is copper sulphides. These exist in many forms often with non-stoichiometric compositions and crystalline structures of higher complexity than the oxides. The Cu₂S compound, chalcocite, exists in at least three phases – low and high temperature chalcocite as well as cubic chalcocite. The low temperature crystalline structure is shown in **Figure 4**. In the intermediate regions between Cu₂S and the CuS (covellite), several forms of Cu_xS exist, e.g. djurleite ($x \approx 1.94$), digenite ($x \approx 1.8$), and anilite ($x \approx 1.75$).⁹² Arguments have been raised claiming that Cu should be referred to as a Cu(I) in all sulfides with a mixture of S²⁻ and S₂²⁻ anions.^{68,93,94} The chemical properties of copper as well as its (hydr)oxides and sulphides will be further discussed below.

2.2.3. Corrosion

Degradation by corrosion is a potential threat to the integrity of the copper nuclear fuel waste canister. Corrosion is a broad concept including various kinds of processes leading to material degradation. Corrosion is, however, commonly used synonymously to electrochemical oxidation. An electrochemical corrosion process is divided into spatially separated anodic and cathodic electrode reactions on the surface of the material. The anode and cathode supplies and consumes electrons respectively, where the anodic reaction leads to oxidation and degradation of the material. These reactions are coupled by electron transport within the material and ionic transport in an electrolyte in contact with the surface forming a full electric circuit. The corrosion operates at a corrosion potential E_{corr} at which the anodic current (I_a) equals the cathodic current (I_c). The current is the product of the local current density (i) and the total electrode area (A) where $I=iA$. Since $I_a=I_c$ at the corrosion potential, $i_a A_a = i_c A_c$.

There are numerous different forms of corrosion.⁷¹ Atmospheric corrosion of the copper canister will e.g. take place under the initial phase of the nuclear waste disposal. The form that is regarded to be of most relevance to the copper canister under the long-term repository conditions is, however, aqueous corrosion, where general corrosion is the most common corrosion attack, whereas localized corrosion including pitting corrosion and related phenomena such as stress corrosion cracking (SCC) could cause the most critical damage.⁹⁵ General corrosion is distinguished by a homogenous and dynamic distribution of corrosion over the surface with $A_a \approx A_c$, whereas in the localized case anodic sites (pits) are static at fixed positions with a typical size asymmetry between the cathodic and anodic electrode areas such that $A_a < A_c$. Under highly localized corrosion, large cathodic surface areas can feed the reaction of a few small anodic pits with the consequence that even minor overall corrosion rates can lead to deep corrosion penetration (pitting).

In order for corrosion to take place, there must be a thermodynamic driving force in combination with sufficiently fast reaction kinetics. In particular, a strong enough oxidant must be present that, under the given conditions, forms a reduced state that is nobler (energetically more favorable) than the material that is to be corroded. Copper is for instance less noble than gold under standard conditions, meaning that Au^+ oxidizes copper to Cu^{2+} via $2\text{Au}^+ + \text{Cu(s)} \rightarrow 2\text{Au(s)} + \text{Cu}^{2+}$. Corrosion of copper is further discussed below.

2.2.4. The Forsmark repository conditions

In order to meet the prerequisites for a safe repository of SNF (*vide supra*), numerous aspects have to be taken under consideration for the copper material. Essential to the safety assessment is a detailed description of the prevailing conditions under different stages of the repository lifetime, and how these affect the copper material.

At the depths of 500 m, the bedrocks of Forsmark are saturated by oxygen free groundwater. The groundwater contains various dissolved species where the compounds of primary interest for the integrity of the copper canister are sulfides (≤ 0.013 mM in total), chloride (~ 150 mM), sulphates (~ 5 mM in total), and carbonates (~ 2 mM in total). The above concentrations correspond to the estimations of a series of technical reports and are associated with some uncertainties and local variations.^{2,96–100} The temperature of the bedrock at 500 m depth is around 11.2°C .^{2,101,102}

Estimations of the groundwater pH and redox potential (Eh) at the Forsmark site are also approximate. The redox potential of the ground water is generally assumed to be controlled by the balance of ferric and ferrous compounds and estimated to around -150 to -250 mV versus the standard hydrogen electrode. The more oxidizing conditions are expected if Fe(III) oxyhydroxides dominate the redox balance whereas more reducing conditions correspond to a case where the activity of sulfate-reducing microbes leading to a Fe(II) (pyrite and, primarily, amorphous iron monosulfide) controlled potential dominates.^{101–103} The pH of the groundwater is neutral to weakly alkaline ($7 < \text{pH} < 8.5$) and buffered by carbonates dissolved in the groundwater in equilibrium with calcite.^{96,97} However, the groundwater that comes into contact with the copper will most likely be slightly more alkaline than the bedrock groundwater due to the use of grout and cementitious material in the construction of the repository. Under short timeframes, pulses of pH up to 11 are possible. However, the pH will, to some extent, be buffered by the groundwater carbonates and by exchange reactions with the bentonite clay, and is not expected to be higher than $\text{pH}=9$ over longer periods. The bentonite is composed of 75–90% (dry weight) montmorillonite.^{2,104}

Although in the long-term perspective the repository will, by and large, adapt to the ambient conditions of the bedrock, the initial state differs notably from this and steady-state conditions (*vide infra*) will only gradually be reached over time periods of 10–10'000 years.² Accordingly, the safety analysis must, besides the long-term perspective, also consider processes taking place during the initial and transient stages of the repository. In the initial stage, residual oxygen trapped in the drill holes will control the redox properties of the regions close to the copper canister. The copper surface will, moreover, be covered by a (hydr)oxide film from the manufacturing process, the pre-storage and

transportation to the repository site.⁶ The residual oxygen in the drill holes (amounting to ~475 moles of O₂¹⁰⁵) is expected to be consumed to below 1% of the initial levels within 7-290 years by microbial activity, chemical processes and to some degree by corrosion of the copper surface (estimated to a maximum corrosion depth of 500 µm).^{2,99} Note that some models suggest that O₂ will be consumed already within a month after repository sealing.¹⁰⁶

During the initial period of the storage, the copper canister will, in addition, be exposed to γ -radiation from the radioactive waste amounting to a maximum dose of 1 gray s⁻¹.⁹⁹ The irradiation will be most prominent during the first centuries of the disposal and will decline gradually over time. Due to the irradiation, the copper surface will be heated yielding a temperature of 80-100°C at the copper surface.¹⁰⁷ The temperature decreases as the radioactivity of the waste decays and will be further reduced as the repository becomes water filled. Nonetheless, elevated temperatures are expected for up to several thousands of years. As concerning water saturation, mixed timescales are predicted in the near field of the copper canisters. The time period is expected to vary depending on the drill hole position and the location of fractures in the bedrock leading to saturation times spanning from <10 to 1000 years.² Wet conditions will, however, prevail on a faster timescale. In addition to the above, the slow diffusion through the bentonite clay means that reactions taking place at the copper canister surface will largely be limited by mass-transport. Consequently the near-field chemical environment of the canisters is expected to deviate from the bedrock conditions to a certain degree throughout the entire repository period.

A selection of the (potential) effects of the alternating repository conditions on the integrity of the copper canister will be discussed below, especially regarding the role of anoxic water and sulfides. The following is, however, not a fully comprehensive account, but may be regarded as a contextual overview. Radiation effects and microbial induced corrosion will not be directly considered, although they indirectly enter the discussion by their effects on the water chemistry. These topics are discussed further elsewhere.^{102,108-114} Note also that the interior environment of the canister not is expected to lead to any considerable degradation of the copper material.^{2,115}

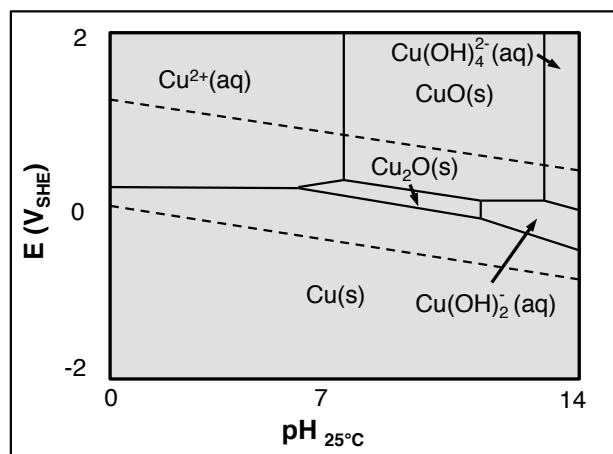


Figure 5. Pourbaix diagram of Cu-O-H system showing the prevalent species under the given pH and potential (E) for $[\text{Cu}^{2+}] = 10^{-6}$ M and 298.15 K. Copper is resistant to corrosion at low potentials for all pH, it corrodes under acidic conditions and E above 0.3 V versus SHE (standard hydrogen electrode) and is passivated for neutral to intermediately high pH and oxidizing potentials. Based on literature data.¹¹⁶

2.2.5. Copper corrosion in pure anoxic water

As outlined above, the choice of copper as encapsulating material in the planned nuclear waste repository in Sweden resides on the documented thermodynamic properties of copper. This includes its well-known resistance to corrosion in the lack of a sufficiently potent oxidant, such as oxygen, which is often visualized in an Eh-pH prevalence diagram – a Pourbaix diagram (**Figure 5**). Despite this, several reports suggesting that copper corrosion may occur under pure and anoxic water conditions have been published during the last decades.^{117–122} These results seemingly contradict the established thermodynamics^{116,123–126} and could potentially question the suitability of using copper as material in the Swedish long-term waste repository. The primary support for corrosion in the referenced studies is the build-up of large H_2 partial pressures upon immersion of copper in pure anoxic water. These pressures surpass the expected equilibrium pressure for the documented reactions between copper, its (hydr)oxides and water by many orders of magnitude (*vide infra*). Assuming that copper corrosion is indeed the source of the generated H_2 , a copper based corrosion product must also be formed – be it in solid or solvated phase. Since none of the known Cu-phases can rationalize the observed H_2 , a new and hitherto unidentified H_xCuO_y phase has been postulated that is thermodynamically more favorable than metallic copper and water. Parts of this thesis work, as well as plenty of parallel studies (*vide*

infra), have been devoted to the investigation of the possibility of the formation of such an H_xCuO_y phase (see **Papers I, II and IV** herein).

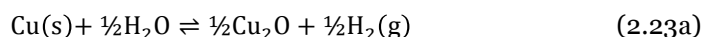
Comprehensive reports and further discussions on the behavior of copper in pure anoxic water and its potential consequences for the Swedish nuclear waste disposal can be found elsewhere.^{95,99,118,127–137} The results of the present study will be discussed under section 4.1. Below follows an overview of the research approaches conducted in the area, and a short summary of the current state of the research field.

Bulk transformation

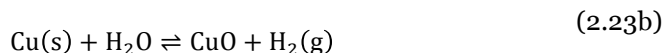
The first approach to understand the corrosion behavior of copper in pure anoxic water is to consider the complete bulk reaction of metallic copper into an oxidized state via:



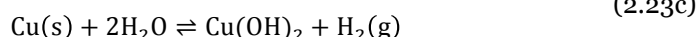
The oxidized copper state is either bound in a solid compound or dissolved as a complex. Under aqueous and anoxic conditions the electron in eq. 2.22 is most likely abstracted by water to form gaseous H_2 or H_{ad} on the solid surface. Concerning potential solid compounds, Cu_2O , CuO and $Cu(OH)_2$ are known oxidized phases of copper that are stable under certain conditions. None of these are, however, thermodynamically favorable with respect to $Cu(s)$ and $H_2O(l)$ under anoxic and aqueous conditions in the temperature range of 0–100°C, which is a prerequisite for corrosion to occur. The reaction free energies at 298.15 K for the solids mentioned above are:^{99,138,139}



$$\Delta G^\circ = 45.6 \text{ kJ mol}^{-1}$$



$$\Delta G^\circ = 107.4 \text{ kJ mol}^{-1}$$



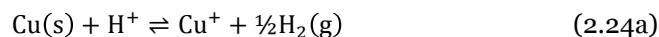
$$\Delta G^\circ = 114.3 \text{ kJ mol}^{-1}$$

In addition to the above, metastable phases of CuH , and $CuOH$ are described in the literature.^{87,88,140} A polymorph of the latter, “cuprice” was identified as a metastable state by an extensive search^{88,141} after potential H_xCuO_y candidate compounds by quantum chemical methods. It was later synthesized.^{iv,87} Neither of the considered H_xCuO_y structures – established or newly identified – have been

^{iv} Note that $CuOH$ were synthesized already in the beginning of the 20th century.^{89–91}

found thermodynamically stable with respect to copper and water and can thus not be invoked to explain the claimed anoxic corrosion of copper.^{72,82,85,88,134,141}

It is, nevertheless important to stress that the considered corrosion reactions are in equilibrium (i.e. the reactions are reversible). Hence, in accordance to le Chatelier's principle, water can indeed corrode copper given sufficiently low Cu^+ activity ($a_{\text{Cu}^+} \approx [\text{Cu}^+]$) and H_2 fugacity ($f_{\text{H}_2} \approx p_{\text{H}_2}$); for corrosion to occur the product $a_{\text{Cu}^+}(f_{\text{H}_2})^{1/2}$ should be lower than $10^{-15.6}$ at 25°C , $\text{pH}=7$ assuming the reactions:⁹⁵



One should here note that a $a_{\text{Cu}^+}(f_{\text{H}_2})^{1/2}$ product of $10^{-15.6}$ is very small and the reaction would quickly reach an equilibrium state given a sufficiently fast kinetics and a closed system. If we assume a total copper ion concentration of 10^{-12} M (similar values have been used in the literature^{134,135}) and use the equilibrium constant of $K=10^{5.8}$ for the disproportionation reaction of Cu^+ above,⁹⁹ an H_2 equilibrium pressure of 6.3×10^{-8} bar can be estimated. Similarly, by inclusion of all relevant phases of the Cu-O-H system, an H_2 pressure of 24×10^{-8} bar has been estimated.¹³⁴ For comparison, Hultquist and co-workers report H_2 partial pressure of $\sim 10^{-3}$ bar,¹²¹ the annual mean p_{H_2} in the troposphere is 5.31×10^{-7} bar,¹⁴² and the ambient H_2 pressures in the Forsmark bedrocks are estimated to 10^{-2} – 10^{-3} bar.^{98,99} In the above, Cu^+ and Cu^{2+} in aqueous solution are assumed to primarily exist in the form of hydrated ions with up to two OH^- ligand groups for Cu^+ and up to four OH^- for Cu^{2+} depending on the pH.¹¹⁶

The surface hypothesis

Since the bulk conversion of copper into an (hydr)oxide phase is found thermodynamically unfeasible, another model for aqueous reaction with copper can be proposed^{143,144} – hereafter referred to as the *surface hypothesis*.^v This model suggests that the observed H_2 originates from a surface redox reaction that is thermodynamically favorable at an initial stage but stops long before reaching a complete bulk reaction. In this way one can envisage an oxidized surface state that still obeys the established thermodynamic bulk properties. Evaluation of the surface hypothesis includes determining whether the surface structure of the copper sample affects its corrosion resistance; does for instance different

^v The expression *surface hypothesis* was coined after discussion with Dr. A. J. Johansson.

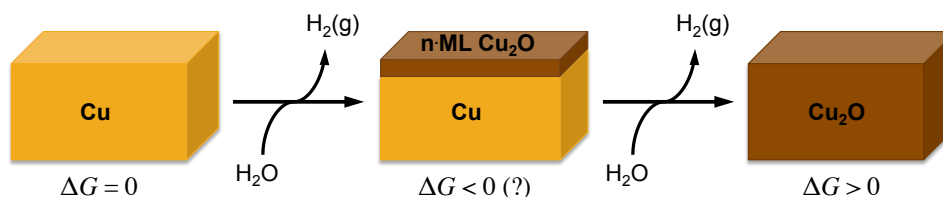
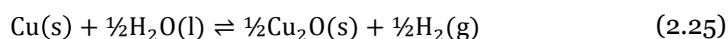


Figure 6. Schematic representation of the (homogeneous) surface hypothesis where n layers of copper are homogeneously oxidized.

crystallographic surface facets behave differently, will surface roughness and pretreatment control the behavior of the material and what are the roles of defects, nanostructures, grain boundaries, and pre-oxidation? Recent studies have e.g. shown that copper surfaces are heterogeneous and that certain nanostructures have a larger susceptibility towards corrosion than others.^{145–147} In its simplest version, the hypothesis considers a homogeneous surface reaction of n layers of copper into an oxidized state (see **Figure 6**).

The first question to be answered is: Is it reasonable to believe that the surface hypothesis could explain the observed amount of H_2 ? The soundness of the surface hypothesis can be evaluated by considering the model of **Figure 6** and the formation of the most favorable Cu_2O corrosion product via:



The evaluation is here carried out using the most reactive (based on surface H_2O dissociation, *vide supra*) low-index crystalline surface facet of copper – $Cu(110)$ ^{vi} – with a Cu surface concentration of 1.085×10^{15} Cu atoms per cm^2 . In the experiments of Hultquist et al.,¹⁴⁸ H_2 partial pressures of up to 0.7 mbar were detected at 52°C upon immersion of copper foil (total geometrical area = 140 cm^2) in water. Using the ideal gas law and the reported total volume of 180 cm^3 , such a pressure would correspond to the consumption of ~20 layers of copper from a pristine (110) surface. Due to surface roughness, the real area is estimated to be at least twice that of the geometrical area^{137,140} resulting in a decrease to ~10 layers of consumed copper. Hence, in this perspective, the (homogeneous) surface hypothesis is possible but would generate an amount of oxidized products that is well within detection limits for surface sensitive analysis techniques such as X-ray photoemission spectroscopy (XPS), Auger electron spectroscopy (AES) or electron microscopy.

^{vi} Crystallographic surface using the (hkl) Miller index notation.

The surface hypothesis is partly covered in **Papers I, II, IV and V** of this thesis work. These studies consider copper nanoparticle oxidation^{150,151} as well as water interactions with the Cu₂O(100) and (111) surfaces^{152,153} (see discussion in section 4.1.3). Research in the field prior to 2012 have been reviewed in a report by Johansson et al.¹⁴³ Later work related to the subject includes, amongst other, the computational studies by Lousada et al.^{154–156} on the ideal and defective Cu(110) surface, computational studies by Carter and coworkers,^{157,158} by Zhang et al.¹⁵⁹ and by Yu and al.¹⁶⁰ on the Cu₂O(111)-water interface, and experimental investigations by Boman and coworkers^{161,162} of copper surfaces upon exposure to oxygen free water. In short, the accumulated knowledge proposes that:

- The H₂O dissociation exothermicity on the low-index crystallographic Cu surface is (110)>(100)>(111) according to computational studies by Wang et al.¹⁶³ Dissociation could generate a small amount of H₂(g) via H₂O(g) → OH_{ad}+H_{ad}, and 2H_{ad}→H₂(g). This is in line with experimental results regarding wetting and dissociation on the (111) and (110) surfaces.¹⁶⁴
- H₂O dissociation forming ~0.5 monolayer (ML) of OH_{ad} is exergonic on the Cu(110), whereas dissociation is unfavorable on the pristine Cu(111) surface facet.^{130,139–144}
- Defective Cu(110) surfaces do not show an increased ability to dissociate H₂O.^{155,156}
- Experiments show no indication of further oxidation beyond surface hydroxylation on polycrystalline copper in pure anoxic water.^{161,162}
- Experiments and computations agree that H₂O dissociates to form ~0.4 ML of OH_{ad} on the Cu₂O(100) surface.¹⁵²
- Computational studies indicates no thermodynamic driving force for dissociation of H₂O on the Cu₂O(111) surface,^{157–160} whereas experiments suggests that ~0.2 ML are dissociated.¹⁷⁰

To conclude, the above suggests that the (homogenous) surface hypothesis of **Figure 6** is an unlikely explanation to the observed elevated H₂ pressures. However, regarding certain aspects of e.g. the effects of defects, nanostructures, and grain boundary reactivity in relation to the possibility of an enhanced oxidation compared to the bulk reaction, have not yet been fully investigated – although such effects have been partly covered in the computational studies by Lousada et al.^{161,162} and by the experimental work on polycrystalline surfaces.^{119,145–147,161,162,171–173}

Current state of the research field

Since the first reports of anoxic copper corrosion by Hultquist et al.¹¹⁷ were published many studies have been conducted that either corroborate or challenge their results. Early evidence refuting corruptions were, e.g., supplied by Simpson et al., Eriksen et al. and Möller.^{174–177} Later support in favor of the conclusions of Hultquist and co-workers includes both experimental^{118–122,178} and computational results.^{179,180}

In recent years, a series of well-controlled experiments have been conducted where the effect of different parameters have been investigated in order to better understand the behavior of copper under aqueous and anoxic conditions.^{161,162,171,172,181} These were conducted using primarily two kinds of experimental set-ups. The first set-up is very similar to the one originally designed by Hultquist and co-workers, described in detail elsewhere,^{119,161} where a copper foil is immersed in a water filled glass beaker placed in a stainless steel container that is sealed by a palladium membrane. The membrane is permeable to H₂ but no other gases, and the H₂ is collected and analyzed in an outer chamber. The second experimental series were conducted in glass vials sealed by rubber tubes.¹⁷³ Some of the conclusions from the above studies are:

- Hydrogen dissolved in the copper material can be released upon immersion in water, where hydrogen in the topmost layers is most readily accessed.
- Hydrogen gas evolution increases momentarily if the surface is scratched by SiC but not by diamond.
- The instrumental equipment used under experiments of the Hultquist design releases hydrogen gas.
- Electropolished, degased and pre-reduced copper surfaces of pure copper material (>99.95% Cu) does not give rise to H₂ pressures above background levels.
- Surface analysis (e.g. XPS, AES) could not detect any copper corrosion product.

In summary, arguments have been presented both in favor and in disfavor of anoxic copper corrosion.^{95,118,122,127–133,182,183,vii} Intriguingly, so far no clear evidence has been of a new H_xCuO_y phase that can fully support the hypothesis of copper corrosion in O₂-free water. The subject is, however, still not fully exhausted and research continues in order to resolve this long-standing scientific question.

^{vii} Two of the most important reasons to the discrepancies are, variations in surface pretreatment and in the experimental control of the hydrogen gas pressures.

2.2.6. Behavior of copper under initial, transient and long-term repository conditions

As outlined above, the copper canister will experience different phases with varying ambient conditions during the operational time of the SNF repository, as proposed in Sweden. Although deviations may persist, the phases can be summarized as: i) a short initial dry and oxygen-rich phase at elevated temperatures, ii) a temperate transient period where oxygen is consumed and the repository gradually becomes water saturated, and iii) a long-term cold, wet and anoxic phase. For the copper canister this means that corrosion will be dominated by different oxidants during the different periods. King et al.^{95,184} have simulated the corrosion behavior of copper during these phases under conditions similar to those expected at the Forsmark site, shown in **Figure 7**.

In short, the modeling predicts that O₂ corrosion will dominate initially generating Cu(I), predominantly cuprite, and Cu(II) species. At first the Cu(II) compound formed is mainly tenorite. Later, as the copper surface becomes increasingly wetted, also spertiniite, atacamite and dissolved CuCl₂⁻ are expected.^{viii} Following the initial oxidation, the model predicts that O₂ and the formed Cu(II) will continue to control the copper corrosion by oxidation to Cu(I) (cuprite) until around 300 years into the disposal period at which point HS⁻ takes over as the primary oxidant. Thereafter sulphide-induced corrosion will continue to dominate for the remainder of the disposal time. Sulphide is provided by microbial reduction of SO₄²⁻ (suppressed by the swelling pressure of the bentonite clay) and by dissolution of S²⁻ from FeS and FeS₂. Although SO₄²⁻ itself could in principle corrode copper to Cu₂S at low pH and high [Cl⁻], such conditions are highly unlikely and the slow kinetics would prevent SO₄²⁻ from corroding copper under the operational time of the repository.⁹⁵ Nevertheless, concerns have been raised that some S_yO_xⁿ⁻-species present in the groundwater may activate the corrosion of copper.¹³⁵ However, among the sulphur species, only sulfides are generally considered to be present in large enough concentrations to be of concern.⁹⁵ The corrosion of copper under real bedrock conditions, similar to those at the Forsmark site, has been studied for miniature copper canisters up to 10 years. In large, these studies corroborates the initial picture obtained from the modeling.^{188–190}

The above suggests that the oxidation by HS⁻ will be the most important corrosion process during the lifetime of the copper canister. This has long been

^{viii} Also note that, upon disposal, the copper surface will already be covered by an (hydr)oxide film. The surface structure at the on-set of oxidation is described elsewhere.^{72,185–187}

recognized and the engineering barriers of the repository are designed accordingly; the 50 mm thick copper canister is expected to corrode only a few mm over a period of 1 million years given a *homogenous* HS^- corrosion, pessimistic assumptions regarding the activity of sulphate reducing bacteria and including the initial oxygen-rich phase.^{105,184} The prevailing question is instead: just how homogeneous/inhomogeneous will the corrosion be?

Local corrosion and stress corrosion cracking can only take place if a passivating protecting oxidized film is formed on the copper surface.^{191,192} If the film is active the corrosion will instead be homogeneous. The initially formed oxide film (predominantly cuprite) is possible passive, but is expected to be converted to an active sulphide film by the anionic exchange reaction $\text{Cu}_2\text{O} + \text{HS}^- \rightarrow \text{Cu}_2\text{S} + \text{OH}^-$.^{191,193,194} This reaction is discussed further in **Paper V** and under section 4.1.4. The validity of the assumption that the sulphide film is active resides on the documented formation of a porous and not a compact Cu_2S film under the assumed HS^- and Cl^- concentrations of the repository.^{195–198} The possibility of localized corrosion is, however, still a question under consideration.^{199,ix}

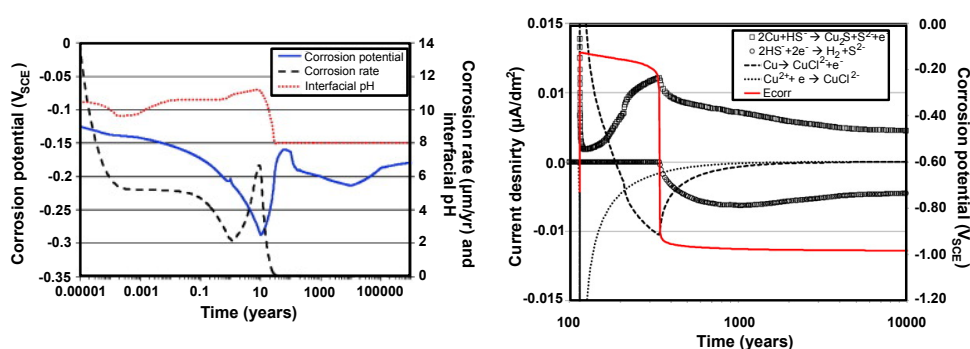


Figure 7. Modeled corrosion progression under bedrock conditions similar to the Forsmark site. Left figure: Canadian bedrock conditions. Reprint with permission from King et al.⁹⁵ Copyright 2013 Elsevier B.V. Right figure: Bedrocks of Olkiluoto, Finland. Note the 115 years lag phase due to the initial dry period. Reprint with permission from King et al.¹⁸⁴ Copyright 2011 Institute of Materials, Minerals and Mining.

^{ix} Note that on a sufficiently local scale, essentially all forms of corrosion are localized. The difference between the term general and localized corrosion used here is only meaningful on a more macroscopic scale where the local contributions in general corrosion are on the average constant whereas localized corrosion is not. One can also talk about the *degree of localization*, where a high degree of localization may, for instance, yield pitting.

3. Overview of computational methods

This chapter covers the computational methods used in this thesis. This comprises their theoretical foundation and link to experimental techniques and observables.

3.1. Computational chemistry

The study of chemistry resides on three pillars – experiments, theory and computations. Experiments observe chemistry in reality, theory forms laws and theorems based on observations and scientific reasoning, whereas computations make predictions and explanations from more or less exact models. The quality and applicability of the modeling depend largely on the approximations used.

In this thesis, both quantum chemical and classical modeling have been conducted. The modeling has covered molecules and crystalline solids, main group elements as well as transition metal compounds in gas phase and in solution. The multitude of systems and environments covered has demanded broad computational considerations. For instance, relatively dissimilar computational frameworks are commonly used for molecular and crystalline material, although they are governed by the same underlying principles. In addition, light elements such as oxygen or hydrogen can be accurately modeled by non-relativistic methods, while relativistic effects must be considered for heavier elements such as platinum or gold. An important aspect in modeling is, furthermore, the availability of computational resources. For the study of chemistry, quantum mechanics (QM) is one of our most accurate theories, but prohibitively computationally demanding in its exact form for most systems of any practical interest. Hence, approximate methods must be used. These will strive to maximize the accuracy while minimizing the computational cost. To date, the most popular families of approximate QM methods stem from two different theoretical approaches – wave function theory (WFT) and density functional theory (DFT).

The differences and specifics of the computational methods employed in this thesis are given in the following sections (3.1.1-3.1.9) including a general theoretical background based on refs. 200–203.

3.1.1. Introduction to quantum chemistry and wave function theory

The behavior of most physical system can be described by quantum theory including the theories of quantum mechanics, quantum electrodynamics and quantum fields. Within these theories, the Dirac equation is a corner stone, and a fundamental basis for the study of molecular and condensed phase systems. Since the Dirac equation is consistent with both the laws of quantum mechanics as well as special relativity, it can be used to study systems comprising heavy atoms (e.g.

transition metals) where the speed of the core electrons is approaching the speed of light. The Dirac equation reads:

$$\left(\beta mc^2 + c \left(\sum_{n=1}^3 \alpha_n p_n \right) \right) |\Psi(\mathbf{r}, t)\rangle = i\hbar \frac{\partial}{\partial t} |\Psi(\mathbf{r}, t)\rangle \quad (3.1)$$

Above, the many-body *wave function* $\Psi(\mathbf{r}, t)$ is a four-component function (a bispinor) of the space-time coordinates \mathbf{r} and t . The p_n s are the three momentum components ($p = m\nabla^2$), \hbar is Planck's constant divided by 2π , and c and m are the speed of light and the electron mass, respectively. The α and β are two 4 by 4 matrices. Unfortunately, it is not possible to solve the Dirac equation analytically for systems comprising more than two particles. Consequently the equation has to be solved numerically and approximately for most systems. The same applies to the closely related, and non-relativistic, Schrödinger equation (*vide infra*). However, even approximate methods for solving the Dirac equation are often prohibitively expensive (computationally) for most systems of chemical interest.^x By omitting relativistic factors, the computational expense can be largely decreased. This procedure reduces the Dirac equation to the *time-dependent* Schrödinger equation:

$$\hat{H}|\Psi(\mathbf{r}, t)\rangle = i\hbar \frac{\partial}{\partial t} |\Psi(\mathbf{r}, t)\rangle, \quad (3.2)$$

where \hat{H} is the Hamilton operator (*vide infra*) and $\Psi(\mathbf{r}, t)$ is reduced to a single component. For chemical applications, the above is usually a reasonable approach; although relativistic effects often have an indirect chemical importance – especially for the chemistry of the heavier elements – chemical interactions are, by and large, restricted to the non-relativistic valence electrons. Therefore the relativistic factors can usually be omitted or treated approximately.

Further simplifications may be invoked for systems that are describable in a time-independent framework (an exception to this is e.g. the study of irradiation effects). The *time-independent* Schrödinger equation reads:

$$\hat{H}\Psi(\mathbf{r}) = E\Psi(\mathbf{r}) \quad (3.3)$$

In atomic units ($m_e = \hbar = e = k_e = 1$), the Hamiltonian (\hat{H}) for a N -electron and M -nuclei system reads:

^x Approximate relativistic methods to the Dirac equation are, e.g., the zeroth-order regular approximation (ZORA)^{204,205} and the second order Douglas-Kroll-Hess (DKH) method.^{206–208}

$$\hat{H} = -\sum_{i=1}^N \frac{\nabla_i^2}{2} - \sum_{A=1}^M \frac{\nabla_A^2}{2m_A} - \sum_{i=1}^N \sum_{A=1}^M \frac{Z_A}{r_{iA}} + \sum_{i=1}^N \sum_{j>i}^N \frac{1}{r_{ij}} + \sum_{A=1}^M \sum_{B>A}^M \frac{Z_A Z_B}{R_{AB}} \quad (3.4)$$

It describes the energetics of the studied system and includes, from the left to the right, the kinetic energy terms of the electrons and nuclei (with the atomic masses and charges m_A and Z_A), the electrostatic nucleus-electron attraction as well as the electron-electron and nucleus-nucleus repulsion. Similar to the Dirac equation – and as will be detailed further below – the Schrödinger equation has to be solved approximately for all but the very smallest systems (e.g. the H atom).

Solving the Schrödinger equation is usually associated with finding the many-body wave function, Ψ , (in DFT the density, ρ) which corresponds to the lowest energy of the system. This is based on the *variational principle* that states that any approximate wave function will be associated with a higher (or equal) energy in comparison to the true wave function. (Note, however, that not all post Hartree-Fock quantum chemical methods follow the variational principle, *vide infra*). The correct wave function describes all ground state properties of the system; provided with Ψ we can compute the expectation value $\langle A \rangle$ of any physically measurable quantity given the appropriate Hermitian operator \hat{A} ,

$$\langle A \rangle = \frac{\langle \Psi | \hat{A} | \Psi \rangle}{\langle \Psi | \Psi \rangle} \quad (3.5)$$

If $\hat{A} = \hat{H}$, i.e. the total energy operator, eq. 3.5 gives us the total energy of the system. Other examples are the dipole operator, $\hat{A} = q\mathbf{r}$, or the total spin operator, \hat{S}^2 .

There is a complete set of Ψ_i solutions (eigenstates) that satisfy the Schrödinger equation, where the ground state is denoted Ψ_0 . Any conceivable state, Φ , of the system can be formed as a superposition, linear combination, of Ψ_i :

$$\Phi = \sum_i c_i \Psi_i \quad (3.6)$$

The wave function is normalized so that the probability of finding a specific electron anywhere in space is unity. The probability density (also known as charge or electron density), $\rho(\mathbf{r})$, is given by multiplication of the wave function with its complex conjugate as $\rho(\mathbf{r}) = \Psi^*(\mathbf{r})\Psi(\mathbf{r}) = |\Psi(\mathbf{r})|^2$. From this the probability $P(\mathbf{r})$ of finding an electron in an infinitesimal volume element $d\mathbf{r}$ is given by:

$$P(\mathbf{r}) = |\Psi(\mathbf{r})|^2 d\mathbf{r} = \rho(\mathbf{r}) d\mathbf{r} \quad (3.7)$$

In the general formulation, the wave function Ψ of a many-body polyatomic system is an intricate function of the nuclear (\mathbf{R}) and electronic coordinates (\mathbf{r}),

$\Psi = \Psi(\mathbf{R}, \mathbf{r})$. Strictly, the nuclear and electronic parts are mutually dependent and inseparable. This renders mathematical expressions that can only be solved analytically for systems containing up to two bodies. Below, approximate methods for solving the Schrödinger equation for chemically relevant systems will be discussed.

The Born-Oppenheimer approximation

The first approximation that is normally introduced is the so-called Born-Oppenheimer (BO) approximation. This assumes that the electronic and nuclear parts of the wave function can be separated: $\Psi = \Psi_{\text{nuc}}(\mathbf{R})\Psi_{\text{el}}(\mathbf{r}, \{\mathbf{R}\})$. This is generally a very good approximation due to the fact that the mass (and consequently the kinetic momentum) of the nuclei and electrons differ by a factor of 10^3 to 10^5 .^{xi} Hence the electrons can be regarded as moving in a static field created by stationary nuclei. The above means that we can solve the electronic part of the Schrödinger equation separately, with the nuclear positions entering the equation merely as parameters. The nuclear contribution can be added at a later stage, thus severely reducing the complexity of the posed problem to:

$$\hat{H}_{\text{el}}\Psi_{\text{el}} = E_{\text{el}}\Psi_{\text{el}} \quad (3.8)$$

with

$$E_{\text{tot}} = E_{\text{el}} + E_{\text{nuc}} \quad (3.9)$$

and

$$\hat{H}_{\text{el}} = - \sum_{i=1}^N \frac{\nabla_i^2}{2} - \sum_{i=1}^N \sum_{A=1}^M \frac{Z_A}{r_{iA}} + \sum_{i=1}^N \sum_{j>i}^N \frac{1}{r_{ij}} \quad (3.10)$$

The BO-approximation leads to the conception of potential energy surfaces (PES) where each nuclear geometry is associated with a potential energy, $E_{\text{tot}}(\Psi_{\text{el}}, \mathbf{R})$. By studying the PES for various nuclear coordinates, we can derive the nuclear contribution to the total energy, including vibrational frequencies and thermochemical corrections to enthalpies and free energies. It must be stressed that the BO-approximation is central to both theoretical as well as general chemistry: as a matter of fact, a large portion of our conceptual framework for rationalization of chemical process relies on the BO-approximation. Without it, concepts such as bond distances and transition states would be blurred and essentially meaningless.

^{xi} Mathematically the correctness of the BO approximation entails that the first and second derivative of the separated wave function with respect to the nuclear positions are small.

The orbital approximation

Despite the introduction of the BO-approximation, the problem of solving the Schrödinger equation remains unmanageable for most systems. This is due to the mutual dependency of the N electrons. Similar to the BO-approximation, a possible ansatz is thus to assume that also the electrons can be treated separately as one-electron wave functions, χ_i , e.g. as:

$$\Phi_{el}^{HP}(\mathbf{r}_1, \dots, \mathbf{r}_N) = \prod \chi_i(\mathbf{r}_i, \xi) \quad (3.11)$$

with

$$\chi_i(\mathbf{r}_i, \xi) = \begin{cases} \psi_i(\mathbf{r}_i)\alpha(\xi) \\ or \\ \psi_i(\mathbf{r}_i)\beta(\xi) \end{cases} \quad (3.12)$$

where $\psi_i(\mathbf{r})$ is the spatial part of the one-electron wave function, i.e. a space orbital, whereas $\alpha(\xi)$ and $\beta(\xi)$ are the two spin basis functions that correspond to the spin eigenvalues $+1/2$ and $-1/2$ of the spin operator. The above ansatz, a so-called Hartree product, would, however, yield a symmetric wave function whereas the Pauli principle dictates that the Schrödinger equation must result in an antisymmetric solution, i.e. $\Psi(i,j) = -\Psi(j,i)$, with respect to a permutation of two arbitrary electrons i and j . Therefore, a commonly used, and antisymmetric, ansatz is a Slater determinant normalized by $\sqrt{N!}$:

$$\Phi_{el}^{SD}(\mathbf{r}_1, \dots, \mathbf{r}_N) = \frac{1}{\sqrt{N!}} \begin{vmatrix} \chi_1(\mathbf{r}_1) & \chi_2(\mathbf{r}_1) & \cdots & \chi_N(\mathbf{r}_1) \\ \chi_1(\mathbf{r}_2) & \chi_2(\mathbf{r}_2) & \cdots & \chi_N(\mathbf{r}_2) \\ \vdots & \vdots & \ddots & \vdots \\ \chi_1(\mathbf{r}_N) & \chi_2(\mathbf{r}_N) & \cdots & \chi_N(\mathbf{r}_N) \end{vmatrix} \quad (3.13)$$

The quantum nature of molecular or condensed phase systems further dictates that the available single electron states within the system resort to mutually orthogonal and discrete energy levels. Due to the Pauli exclusion principle (a consequence of the fermionic nature of the electrons) two electrons cannot occupy the same spin-state. Accordingly the wave function describes how the electrons are configured in the system into different electronic shells (i.e. different principal quantum numbers $n=1,2,3,\dots$), different orbital types (e.g. s , p and d orbitals, i.e. different angular quantum numbers, l) with different orientation (e.g. $2p_x$, $2p_y$ and $2p_z$, i.e. different magnetic quantum numbers, m) and different spin (α or β).

Although we have now separated the individual electronic contributions, at this stage the one-electron wave functions, χ_i , also known as orbitals (or, more correctly, as spin-orbitals), are still explicitly dependent on the positions and

momentum of the remaining $N-1$ electrons. Strategies to overcome this problem will be outlined below under the Hartree-Fock (HF) theory section. First we shall, however, direct some focus on the orbitals and their construction.

Orbitals and basis sets

In order to discuss the molecular orbitals, i.e. the one-electron solutions to the Schrödinger equation, we must first present some general aspects resulting from the computational implementations of the WFT. In the most general case, the one-electron wave functions $\chi_i(\mathbf{r},\xi)$ are complex and span a complete space of solutions. In practice, we are, however, usually constraining the possible solutions to a limited subspace in order to speed up calculations and/or to assure that the optimized wave function obeys certain physical or mathematical rules. Firstly, the wave function is typically restricted to real, non-complex, solutions. In the *general Hartree-Fock theory* (GHF), the α and β spin functions are allowed to mix in the construction of the $\chi_i(\mathbf{r},\xi)$. However, the most common approach is to refrain from mixing the spin functions. Variants of the latter include the *spin-unrestricted Hartree-Fock theory* (UHF), where the α and β orbitals are optimized independently, and *spin-restricted Hartree-Fock theory*, where the spatial part of the α and β spin orbitals are set equal. If the studied system is in a singlet spin state, the spin-restricted Hartree-Fock is said to be *closed-shell* and referred to as RHF. If the spin-restricted system comprises unpaired electrons, e.g. a spin doublet, it instead has an *open-shell* electronic configuration (ROHF). Most calculations in the current thesis are either based on the restricted or the unrestricted formalisms.

In order to determine the solution to the Schrödinger equation, the standard procedure is to express the wave function as a linear combination of a pre-defined set of basis functions, ϕ_μ , that form a so-called basis set:

$$\psi_i(\mathbf{r}) = \sum_{\mu} c_{\mu i} \phi_{\mu}(\mathbf{r}) \quad (3.14)$$

Accordingly, by the end of a calculation, the wave function is described by a number of optimized expansion coefficients, $c_{\mu i}$. Given a non-complete basis set, the above is a further constraint to the possible solutions because we limit ourselves to the subspace spanned by the basis set of choice. Since it is virtually impossible to perform calculations with a complete basis set, the quality of a calculation is largely dependent on the quality of the truncated basis set applied. Hence it is an important task to construct sufficiently flexible whilst computationally efficient basis sets.

Common basis sets employed in molecular theory are Gaussian type orbitals (GTO). These are centered on each atom and are constructed to mimic atomic

orbitals (including s , p , d , and f orbitals, and so on). The combination of these to form molecular orbitals is known as LCAO (linear combination of atomic orbitals) method. Gaussian type basis functions [of the form $\exp(-r^2)$] are chosen primarily for computational reasons, whereas atomic orbitals are more correctly described by Slater type functions [$\exp(-r)$]. Although less popular, Slater type basis sets (STO) are also used to some extent in computations. Due to the incorrect radial shape of Gaussian functions, GTO basis functions are typically constructed as contracted functions represented by a number of primitive GTOs. By contracting the primitive functions (i.e. adding multiple functions with only one shared $c_{\mu i}$), the number of expansion coefficients to be optimized can be largely reduced, hence minimizing the computational cost without severely reducing the accuracy. In the GTO basis sets, the core states normally have to be represented by a comparable large number of contracted GTOs, e.g. six in the popular 6-31G Pople style basis set for light elements (see discussion below for the case of relativistic core electrons). In the same basis set, the valence states are constructed by a doubly split (double- ζ) valence including one set of three primitive GTOs and one uncontracted GTO. The quality of the basis set can be improved by further splitting the valence (to triple- ζ , quadruple- ζ and so on), and by augmenting the basis set with polarizing functions of higher angular momentum, and/or diffuse functions with small exponential coefficients.

In parallel to the development of molecule theory, the solid-state materials science community has developed a slightly alternative practice compared to the above. Due to the (semi-)infinite character of many solids, these systems are most efficiently treated in a periodic fashion where the electronic states are represented by *plane-wave* basis sets:

$$\phi_{\mu}(\mathbf{r}) = \frac{1}{\Omega} e^{i\mathbf{G}_{\mu}\mathbf{r}} \quad (3.15)$$

Where Ω is a constant and \mathbf{G}_{μ} is a vector in reciprocal space (*vide infra*, section 3.1.5). The size of the basis set is determined by an arbitrary energy cut-off, E_{\max} , as:

$$E_{\max} = \frac{G_{\max}^2}{2} \quad (3.16)$$

Close to the cores, the wave function oscillates rapidly. Thus very large plane-wave cut-offs have to be used to correctly describe these states rendering very expensive calculations. Therefore the core regions are usually represented by standardized potentials including contributions from the nuclei and core electrons, for instance

via the projector augmented wave^{xii} (PAW) potential method.^{209,210} For heavier atoms these PAW potentials include the relativistic effects of the electronic core states, thus any calculation implicitly accounts for relativity in a frozen core manner (this whereas the fully correct approach would have been to also allow the fixed core potential to relax within the field created by the valence electrons). Similar methods are employed for atom-centered basis sets (e.g. GTOs); in molecular theory the core states of the heavier atoms are commonly represented by frozen orbitals or fixed potentials via so-called *pseudo potentials* or *effective core potentials* (ECP) that have been optimized to work well together with specific basis-set families.

The molecular orbitals can be used to estimate atomic and molecular properties as discussed further in sections 3.4 and 4.2. Two basic theorems are those of Koopmans and Janak. According to the Koopmans' theorem,²¹¹ the eigenvalues of the occupied orbitals represents their ionization energies ($-\epsilon_i \approx I_i$). Similarly the eigenvalues of the virtual (unoccupied) orbitals estimates their electron affinities ($-\epsilon_i \approx EA_i$). In this fashion one can estimate spectral features of atoms, molecule and materials e.g. including UV/VIS adsorption energies and band gaps. Janak, furthermore, showed that the orbital eigenvalues are connected to the total energetic change of the system with respect to the orbital occupation (n_i) as:²¹²

$$\epsilon_i = \frac{\partial E}{\partial n_i} \quad (3.17)$$

3.1.2. Hartree-Fock theory

Hartree-Fock (HF) theory describes the most common approximate WFT approach for accounting for the electron-electron interaction. It is the standard starting-point of most wave function based methods. HF is also closely related to the popular DFT Kohn-Sham approach and implemented in all hybrid DFT methods. The advantage of HF is that it allows us to reformulate the many-particle problem in terms of a system of one-electron equations that can be solved comprehensible by a suitable computer algorithm.

The trick introduced in HF is to treat the electron-electron interactions in a mean-field approximation. Thereby each electron is assumed to interact with the electronic field created by the *mean* distribution of the other electrons. Hence we are neglecting the correlated motions of the electrons (giving rise to a small but

^{xii} Note that although PAW pseudo potentials treat the core electrons in a 'frozen core' manner, the all-electron wave function is available via a linear transformation.²⁰⁹

chemically significant correlation error, *vide infra*). Through this approximation we can formulate the electronic Schrödinger equation for each individual electronic state in terms of one-electron Fock-equations on the form (for the first electron):

$$\hat{f}(i)\chi_a(i) = \epsilon_a\chi_a(i) \quad (3.18)$$

With the Fock operator $\hat{f}(1)$:

$$\hat{f}(i) = -\frac{1}{2}\nabla_i^2 - \sum_{A=1} \frac{Z_A}{\mathbf{R}_{iA}} + v^{\text{HF}}(i) \quad (3.19)$$

where $v^{\text{HF}}(1)$ is an effective one-electron operator describing the electrostatic mean field experienced by an electron in the i :th orbital due to the presence of the other electrons. v^{HF} consists of the classical coulomb operator $J(1)$ and the quantum mechanical exchange operator $K(1)$ that is a result of the antisymmetric character of the wave function:

$$v^{\text{HF}}(i) = \sum_b [J_b(i) - K_b(i)] \quad (3.20)$$

with

$$J_b(i) = \int |\chi_b(j)|^2 r_{ij}^{-1} d\mathbf{r}_j \quad (3.21)$$

and

$$K_b(i)\chi_a = \int [\chi_b^*(j)r_{ij}^{-1}\chi_b(j)]\chi_a(i)d\mathbf{r}_j \quad (3.22)$$

In addition, the $v^{\text{HF}}(i)$ of any electron depends implicitly on its own one-electron wave function. Hence the problem has to be solved iteratively starting from an initial guess. The wave function is updated until some stipulated convergence criterion(s) is met (e.g. an energy cut-off and/or change in the orbital density). This iterative procedure is referred to as solving the problem self-consistently in the field created by the optimized electronic configuration, i.e. a self-consistent field (SCF) calculation.

As described previously, the orbitals are constructed as linear combinations of a set of reference functions, i.e. the basis set. By inserting the basis set equation (eq. 3.14) into the Fock equation (eq. 3.19) and multiplying by $\phi_v^*(i)$ from the left we get:

$$\sum_{\mu} c_{\mu a} \int \phi_{\nu}^*(i) \hat{f}(i) \phi_{\mu}(i) d\mathbf{r} = \epsilon_a \sum_{\mu} c_{\mu a} \int \phi_{\nu}^*(i) \phi_{\mu}(i) d\mathbf{r} \quad (3.23)$$

This is known as the Roothan–Hall equations, and can, for the full system, be expressed as

$$\mathbf{FC} = \mathbf{SC}\epsilon \quad (3.24)$$

In the above \mathbf{F} is the Fock (operator) matrix, \mathbf{C} is a matrix including the basis set expansion coefficients, and \mathbf{S} is the orbital overlap matrix. The spin-orbital eigenvalues are given in the diagonal matrix ϵ . The Roothan-Hall system of equations is nowadays routinely solved in standard quantum chemical codes.

3.1.3. Post Hartree-Fock methods and correlation energy

The origin of the largest error in the HF method can be traced back to the electron mean field approximation where the mutual correlation in the electron movements is omitted. Effectively this is, however, only true for the electrons of opposite spins; the antisymmetry constraint invoked by the Slater determinant fortunately results in the exact and full recovery of the correlation of electrons of the same spin. This is known as electron *exchange* (or Fermi exchange), with the associated *exchange energy* E_X . The remaining energy difference between the exact energy (within the basis set limit) and the calculated energy in HF is referred to as the *correlation energy* (or Coulomb exchange energy), E_C :

$$E_C = E_{\text{exact}} - E_{\text{HF}} \quad (3.25)$$

The correlation energy is small compared to other energy contributions, but of the same magnitude as typical chemical processes and thus limits the applicability of the HF method. In addition, the correlation energy varies largely with the number of electrons of a system, which for example means that HF cannot treat the various compounds of a dissociation reaction on an equal footing. This is known as size-inconsistency. To remediate the above a multitude of elaborate methods to retrieve the correlation energy *a posteriori* of a HF calculation have been proposed. These include the most accurate theoretical methods for studying chemical systems to date, but typically suffers from bad scaling with system size and thus a (very) large computational cost.

The post HF methods have not been employed to any extent in this thesis work and will only be covered breathily. These methods are described in detail elsewhere.²¹³ In short, the post HF methods reside to methods based on perturbation theory, e.g. the Møller-Plesset (MP) methods, or to methods based on in-mixing of virtual orbitals in the wave function by expanding the ground state

determinant via linear combination of excited-state determinants. The latter includes e.g. the configuration interaction (CI) and coupled cluster (CC) methods. The outlined methods are in principle exact, in the limit of the employed basis set. Full-CI considering all possible excitations and a complete basis set would be the ultimate standard. In any practical application the employed method must, however, be truncated resulting in a residual error. Common truncations include MP2 and MP4 (MP truncated to second and forth order terms), and CCSD(T). The latter represents CC with single and double excitations as well as triplet excitations added by perturbation. The CCSD(T) is widely considered the golden standard of practical computational chemistry against which other more approximate methods can be benchmarked. The truncated methods above are still prohibitively demanding and scales as e.g. N^5 [MP2] and N^7 [CCSD(T)] with the size of the basis set. This can be compared to Hartree-Fock, which scales as $<N^4$. Approximate methods to speed up the computations with a minimal compromise on the accuracy have been presented lately [e.g. DLPNO-CCSD(T)²¹⁴] but will not be considered here.

In addition to the above, one often separate between *dynamic correlation* – i.e. the picture described above where the motions of the electrons are correlated – and *static correlation* – originating from a (close to) degeneracy of different electronic configurations of the system. The latter is essentially a defect that comes from the use of a single HF Slater determinant as reference state. Whereas the MP, CI and CC methods can effectively retrieve dynamic correlation effects, static correlation often demands the introduction of, not only excitation determinates, but also a larger set of ground state reference determinants. This is for instance the case in the MRSCF method (multi-configurational self-consistent field). By combination of MRSCF with *a posteriori* corrections via CI, known as MRCI, or by perturbation theory, e.g. complete active space perturbation theory (CASPT2) or reduced active space SCF (RASSCF), one is equipped with methods that can handle even the most difficult cases in theoretical chemistry, although at a very large computational expense.

3.1.4. Density functional theory

In 1964 Hohenberg and Kohn²¹⁵ published a seminal paper presenting the mathematical proof that the ground state properties of a non-degenerate^{xiii} molecular species are uniquely defined by its electron density $\rho=\rho(\mathbf{r})$.^{xiv} The ground state energy, E_0 , can be determined by:

$$E_0 = E_0[\rho(\mathbf{r})] \equiv \int V_{\text{ext}} \rho(\mathbf{r}) + F[\rho(\mathbf{r})] \quad (3.26)$$

where V_{ext} is the external potential that the electrons experience from the nuclei, and $F[\rho(\mathbf{r})]$ is the universal functional^{xv} embodying the kinetic energy $T[\rho(\mathbf{r})]$ of the electrons and the electron-electron interaction energy $E_{\text{ee}}[\rho(\mathbf{r})]$. On the basis of the above theorem, an alternative method to the wave function based approaches was established – *density functional theory* (DFT). In comparison to WFT methods, DFT has the benefit of depending merely on three spatial coordinates ($\mathbf{r}=\text{x,y,z}$) for describing the many-body interactions. This immensely reduces the computational effort compared to WFT where $4n$ electronic coordinates (three spatial and one spin coordinate)^{xvi} of the n electrons must be accounted for. The low computational cost in combination with sufficient accuracy explains^{xvii} the popularity of DFT and its approximations in modern computational chemistry and physics.

According to the theorems of Hohenberg and Kohn, DFT is variational meaning that any approximate energy E_{approx} must be larger than the exact energy E_{exact} . The exact energy is determined by the energy functional $E[\rho(\mathbf{r})]$ of eq. 3.26. Unfortunately the correct form of $E[\rho(\mathbf{r})]$ is unknown, why approximate methods must be applied. Methods deviating from the exact theoretical formulation of DFT are formally known as density functional approximation (DFA), but DFT is often used synonymously also to the latter. While, in DFT, the electron-electron repulsion and electron-nuclei attraction are readily expressed using classical Coulomb interactions (*vide infra*), no similar expressions based on $\rho(\mathbf{r})$ have to date been formulated for the electronic exchange and correlation, nor for the electron kinetic energy.

^{xiii} The scope of applicability of DFT was later extended to cover also species with degenerate ground states by Levy.^{216,217}

^{xiv} An additional constraint is that the density is V -representable.²¹⁵

^{xv} A functional is an operator that takes a function as input and outputs a scalar.

^{xvi} In applied DFT, orbitals are usually reintroduced and the cost is approximately that of HF.

^{xvii} DFT's main benefit is that the correlation energy is (partly) included at the cost of HF.

To circumvent the problems of DFT outlined above, Kohn and Sham developed a new formalism (KS-DFT)²¹⁸ that reintroduces N explicit but fictitious KS-electrons that are mutually non-interacting while still sensing the nuclear attraction. The density of these electrons is chosen such that $\rho^{\text{KS}} = \rho^{\text{exact}}$ with $\rho^{\text{KS}}(\mathbf{r}) = \sum_i |\psi_i^{\text{KS}}(\mathbf{r})|^2$. The one-electron KS wave functions, ψ_i^{KS} , are determined by solving the Kohn-Sham Schrödinger equation under the constraints that the KS-orbitals are mutually orthogonal and that the number of electrons, N , is constant. The KS equation reads (in atomic units):

$$\left(-\frac{\nabla^2}{2} + V_{\text{eff}}[\rho(\mathbf{r})] \right) \psi_i^{\text{KS}} = \varepsilon_i \psi_i^{\text{KS}} \quad (3.27)$$

In the above, $V_{\text{eff}}[\rho(\mathbf{r})]$ is an effective potential that consist of the classical electron-electron repulsion ($V_{\text{EE}}[\rho(\mathbf{r})]$) and electron-nuclei attraction ($V_{\text{ext}}[\rho(\mathbf{r})]$), as well as the quantum mechanical exchange-correlation potential ($V_{\text{xc}}[\rho(\mathbf{r})]$), via:

$$V_{\text{eff}}[\rho(\mathbf{r})] = V_{\text{EE}}[\rho(\mathbf{r})] + V_{\text{ext}}[\rho(\mathbf{r})] + V_{\text{xc}}[\rho(\mathbf{r})] \quad (3.28)$$

with

$$V_{\text{EE}}[\rho(\mathbf{r}')] = \int \frac{\rho(\mathbf{r}')}{|\mathbf{r} - \mathbf{r}'|} d\mathbf{r}' \quad (3.29)$$

and

$$V_{\text{ext}}[\rho(\mathbf{r})] = - \sum_A \frac{Z_A}{|\mathbf{r} - \mathbf{R}_A|} \quad (3.30)$$

$V_{\text{xc}}[\rho]$ is in reality a rest term that indeed contains contributions from electron exchange and correlation, but also has contributions from the residual of the electron kinetic energy arising from the fact that the fictions KS-electrons behave differently than real electrons, as well as from the self-interaction^{xviii} of the electrons that is inherent in DFT. Based on the exchange-correlation energy (xc)-functional, E_{xc} , $V_{\text{xc}}[\rho(\mathbf{r})]$ is defined as:

$$V_{\text{xc}}[\rho(\mathbf{r})] = \frac{\partial E_{\text{xc}}[\rho(\mathbf{r})]}{\partial \rho(\mathbf{r})} \quad (3.31)$$

The final energy is obtained self-consistently from an initial trial density by:

^{xviii} Each electron interacts with $\rho(\mathbf{r})$ that is a function of all electrons, including the electron itself. This leads to the self-interaction error.

$$E[\rho(\mathbf{r})] = \sum_i^N \varepsilon_i - \int \left(\frac{1}{2} V_{EE}[\rho] + V_{XC}[\rho] \right) \rho(\mathbf{r}) d\mathbf{r} + E_{XC}[\rho] \quad (3.32)$$

The problem in DFT (and DFA) now amounts to finding the correct form of (or the best approximation to) the unknown E_{XC} . Note, furthermore, that the Born-Oppenheimer approximation applies also in DFT, and the nuclei-nuclei repulsion ($E_{\text{nuc}}[\rho]$) and thermal corrections can be added to the total energy at a later stage.

Exchange-correlation functionals

The exchange-correlation energy in DFT is small compared to the other components, but important for the study of chemical systems. Several approximations to the E_{XC} have been suggested. Perdew has outlined a hierarchical categorization of these referred to as *Jacob's ladder*.²¹⁹ In general terms the simplest and least accurate xc-functionals are found in the bottom of the ladder and, as we reached higher *rungs* (levels) the complexity and accuracy increases. For most xc-functionals, the E_{XC} is divided into an exchange, E_X , and a correlation part, E_C , with $E_{XC}=E_X+E_C$. In the general case $E_X > E_C$.

The first rung of Jacob's ladder includes the simplest xc-functionals of practical use, the local (spin) density approximation, L(S)DA, functionals, e.g. the VWN functional.²²⁰ In L(S)DA functionals the energy is assumed to depend only on the local density and is valid in cases of slowly varying densities. The second and third rung of the Jacob's ladder introduces a semi-local dependency on the density and KS-orbitals. Generalized gradient approximation (GGA) xc-functionals of the second rung (e.g. PBE²²¹) includes besides the local electron density also its gradient. Third rung meta-GGA functionals (e.g. TPSS²²²) adds considerations of the kinetic energy density, i.e. the Laplacian of the KS orbitals.

Higher rungs include hyper-GGA and hybrid-GGA (forth rung) that account for the non-locality of the occupied orbitals, whereas in the fifth rung (e.g. RPA^{223,224}) also unoccupied orbitals are considered. Hyper GGAs and hybrid functionals recovers the full (or parts of the full) exchange energy. In the case of hybrid functionals a common procedure is to mix in a certain percentage of exact exchange from Hartree-Fock calculations^{xix} besides the GGA E_X . Hybrid functionals comprises some of the most common functionals including PBEO²²⁵ (PBE with 25% HF E_X) as well as the B3LYP^{226,227} functional (20% HF). For the sake of illustration, the functional form of the PBEO xc-functional is given below:

^{xix} Performed on the KS wave function.

$$E_{XC}^{PBE0} = \frac{1}{4}(E_X^{HF} + 3E_X^{PBE}) + E_C^{PBE} \quad (3.33)$$

On top of this exist a number of intermediate xc-functionals that cannot be unambiguously be assigned to any of the rungs of Jacob's ladder. Notable examples are meta-hybrid functionals (e.g. M06-2X²²⁸), the double-hybrid functionals (e.g. B2PLYP²²⁹) that includes both HF E_X and MP2 E_C corrections, as well as the range-separated HSE functionals^{230,231} and the long-range corrected functionals (e.g. CAM-B3LYP²³²) where the amount of HF admixture depends on the distance to the nucleus. In addition, few functionals are suited for studies of dispersion effects, why dispersion corrections according to e.g. Grimme's D3 scheme²³³ or the vdW methods of Dion et al.²³⁴ are often added to the energy evaluations. The BEEF-vdW functional includes dispersion and further makes use of a plethora of functionals in order to obtain error estimates by the use of Bayesian statistics.²³⁵ Furthermore, in materials science a common problem for studies of e.g. transition metal oxides is the incorrect assignment of strongly correlated semiconducting or insulating materials as conductors. This is mainly due to the self-interaction error in e.g. GGA or LDA functionals that promotes electron delocalization. By adding a so-called *Hubbard correction* (+U)²³⁶ to the localized states (primarily metal centered *d*- or *f*-states) this problem can be empirically remedied by e.g. the method of Dudarev et al.²³⁶

$$E_{\text{DFT}+U} = E_{\text{DFT}} + \frac{(U-j)}{2} \sum_{\sigma} \left[\left(\sum_j \rho_{jj}^{\sigma} \right) - \left(\sum_{j,l} \rho_{jl}^{\sigma} \rho_{lj}^{\sigma} \right) \right] \quad (3.34)$$

where σ is the spin and ρ_{jl} the *d(f)*-electron density matrix. U and j represents the spherically average of the matrix elements of the screened Coulombic electron interaction.

To conclude, DFT (or, to be correct, DFA) calculations can provide high accuracy results for large atomic systems that in many cases are of similar, or better, quality as advanced WFT calculations but at the approximate cost of HF. However, DFT has its limitations especially for the study of near-degenerate compounds of multi-configurational character. Ideally, and if possible, DFT results should be compared to higher-level WFT calculations when the results are in doubt.

3.1.5. Band structure theory

A large part of the current thesis encompasses computations of the properties and chemistry of material surfaces. Although the same physical laws govern both molecules and solid-state materials, there are some geometrical and electronic differences that make it suitable to study materials and molecules within different frameworks. In particular, the (semi)-infinite character of the crystalline materials makes it more efficient to employ periodic boundary conditions and expand the wave function on a plane-wave basis set instead of the molecular approach where linear combinations of atom centered basis functions are used (LCAO, *vide supra*). The reason for this is that small repeating unit cells build up crystalline materials, which by the use of periodic symmetry operations can be efficiently translated to describe the entire extended material (see section 2.1.5).

The semi-infinite character of materials also gives rise to their band structure. When the atoms combine in the crystal lattices, the atomic orbitals overlap leading to new electronic states, especially for the valence electrons. According to the Pauli principle, the electrons cannot occupy the same state, why these are discretized. Due to the large number of electrons in the crystal, these states are only infinitesimally separated (energetically), which qualitatively leads to the formation of a continuum of states, *bands*. Some bands are localized on specific atoms or regions, whereas many are highly delocalized over the whole material. At zero K, electrons occupy states up to the *Fermi level*, E_F . E_F is located in the middle of the conduction (lowest unoccupied states) and valence bands (highest occupied states) – strictly E_F is the energy level that has a 50% probability of being occupied at zero K (which does not necessarily have to be a real energy level). For a metallic material, which by definition is an electrical conductor, the valence band smoothly overlaps the conduction band, whereas for semi-conductors and insulators the bands are separated by a *band gap*. Insulators are distinguished from semi-conductors by a larger band gap.

According to the Bloch theorem²³⁷ the wave function of an electron in an infinite crystal can be written as a product of a plane-wave and a periodic function ($\mu_{n\mathbf{k}}$) describing the periodicity of the crystal lattice

$$\psi_j = e^{i\mathbf{k}\cdot\mathbf{r}} \mu_{n\mathbf{k}}(\mathbf{r}) = e^{i\mathbf{k}\cdot\mathbf{r}} \mu_{n\mathbf{k}}(\mathbf{r} + \mathbf{a}) \quad (3.35)$$

Here \mathbf{k} is the wave vector and $\mathbf{a}=(a_x, a_y, a_z)$ gives the length of the unit cell (lattice constants) in the three spatial directions x, y, and z. The wave function can be expanded on a plane-wave basis (*vide supra*) as:

$$\psi_{j,\mathbf{k}} = \sum_{\mathbf{G}} c_{j,(\mathbf{k}+\mathbf{G})} e^{i(\mathbf{k}+\mathbf{G})\cdot\mathbf{r}} \quad (3.36)$$

with \mathbf{G} being the reciprocal lattice vector and where $c_{j,(\mathbf{k}+\mathbf{G})}$ are the plane-wave expansion coefficients. By the above procedure only the limited number of electrons of the unit cell has to be accounted for rather than the infinite number of electrons of the entire crystal. Yet, in order to fully describe the crystalline system, the whole \mathbf{k} -space^{xx} (momentum space or reciprocal space) must be sampled including infinitely many \mathbf{k} -values (\mathbf{k} -points). Unique wave functions are, however, only found for \mathbf{k} -points in the interval $-\pi/\mathbf{a} \leq \mathbf{k} \leq \pi/\mathbf{a}$ comprising the *first Brillouin zone* (FBZ). Furthermore, the electron configuration varies smoothly over \mathbf{k} -space. Therefore the computational effort can be reduced by numerical sampling of the FBZ using a discrete mesh of \mathbf{k} -points via e.g. the Monkhorst-Pack sampling scheme,²³⁹ and by taking advantage of unit cell symmetry. This has the benefit that the integration over the BZ turns into a sum of contributions from irreducible \mathbf{k} -points suitable weighted by their relative contributions. The above leads to an error where the finer the employed \mathbf{k} -mesh is, the more accurate are the calculations. Hence convergence of a studied property should be checked with respect to the quality of the \mathbf{k} -mesh.

3.1.6. Molecular mechanics and other (semi)-empirical methods

The calculations of molecular and condensed phase systems can be sped up in comparison to WFT and DFT calculations by the use of further approximate methods. This is often attractive if long time scales are to be studied in molecular dynamics (MD) simulations (*vide infra*), or if one is interested in studying very large systems. Such methods include e.g. the tight-binding model traditionally used in solid-state computations²⁴⁰ or the semi-empirical PM3²⁴¹ and AM1²⁴² QM methods.

Another popular approach is to treat the atom as classical physical entities, and thereby omitting the explicit treatment of electrons. In the molecular mechanics (MM) methods, one derives so-called *force fields* that describe the energetics of the molecules and atoms under study. Traditional force fields does not allow for the formation or cleavage of covalent bonds (nor the transfer of electrons), why one is restricted to the study of weak non-covalent interactions. This is suitable if one, e.g., is interested in studying protein folding or for sampling of the configuration space of a molecule. Traditional force fields include energy terms such as²⁴³

$$E_{\text{FF}} = E_{\text{stretch}} + E_{\text{bend}} + E_{\text{torsion}} + E_{\text{el}} + E_{\text{vdW}} + E_{\text{cross}} \quad (3.37)$$

^{xx} From the atomic orbital perspective, \mathbf{k} -space can be seen as a smooth transition between the limits of completely bonding to completely antibonding orbital combinations.²³⁸

Each term is represented by a classical physical relation and often optimized to describe a particular sort of system (e.g. proteins) accurately. A bond stretch (ΔR_{AB}) between two atoms could e.g. be represented by a spring with the constant k_{AB} as:

$$E_{\text{bend}}(\Delta R_{AB}) = k_{AB}(\Delta R_{AB})^2 \quad (3.38)$$

More elaborate force fields exist, e.g. the effective fragment potential (EFP1²⁴⁴) method where the potential (commonly water) is polarizable. EFP1 works particularly well for so-called QM/MM calculations (see **Figure 8**) where a part of the system is treated by QM (for instance comprising a region where we want to study covalent bond breakage) and a MM part including the water solvent. EFP1 terms derived from previous QM calculations representing Coulombic interactions, polarization, Pauli repulsion and (implicitly) charge-transfer seamlessly enter the QM Hamiltonian as one electron terms.²⁴⁴

Reactive force fields that allow for the study of reactions in MM have been parameterized in later years. This demands accurate descriptions of TS regions. This adds complexity to the force field since the TS often differ largely from the ground state structure, and thus demands a flexible functional form of the force field. In the ReaxFF reactive force field this is achieved by creating the force field based on bond-order terms between all atoms of the simulation cell (within a certain cut-off).²⁴⁵

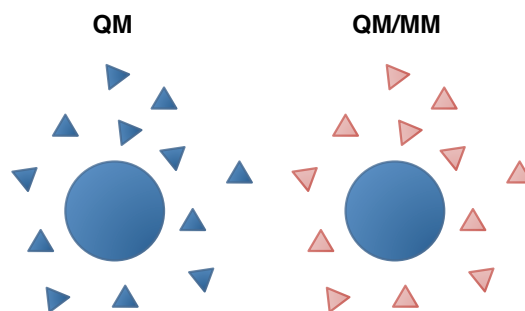


Figure 8. Illustrating the difference between a full QM and a QM/MM calculation. Dark-blue species are treated by full QM. The solute (round) is always treated by full QM whereas the pink solvent molecules (triangular) of the QM/MM calculation are represented by MM force fields.

3.1.7. Solvation models

Chemistry is often performed in solution phase. Nonetheless the majority of the quantum chemical calculations have traditionally been performed in gas phase (*in vacuo*). This is due to the complexity added by accounting for solvation effects in QM calculations. Nowadays, effective methods for describing solvation effects are, however, available in most computational programs.

Models for describing solvation effects in computational chemistry can broadly be sorted under two categories: *implicit* and *explicit* models. In the explicit models, a number of discrete solvent molecules are added to the model systems. These can either be represented at the same level of theory as the solute molecule, or described by a method of lower sophistication. One could e.g. describe the solvent with a smaller basis set than the solute. Alternatively the solvent could be represented by a MM force field resulting in a QM/MM calculation as illustrated in **Figure 8**. The explicit solvent models have the disadvantage that a large number of solvent configurations have to be sampled. Thereby the computational effort grows quickly with the number of included solvent molecules. Thus one usually strives to use as few explicit molecules as possible, possibly in combination with the implicit methods described below.

The implicit models represent the solvent by a polarizable continuum with a dielectric constant ϵ . If the continuum and the solute are allowed to be mutually polarized iteratively the methods are described as self-consistent reaction field (SCRF) methods.²⁴⁶ These comprise e.g. the popular IEF-PCM^{247,248} (integral equation formalism polarizable continuum model) and COSMO²⁴⁹ (conductor-like screening model) methods. The free energy in solution is described by:

$$\Delta G_{\text{solv}} = \Delta G_{\text{cavity}} + \Delta G_{\text{dr}} + \Delta G_{\text{el}} \quad (3.39)$$

Where the ΔG_{cavity} is the energy change associated with creating a cavity in the solvent for the solute. The size of the cavity may e.g. be determined by overlapping atom-centered spheres created by empirically scaled atomic radii. ΔG_{dr} is a dispersion-repulsion term. ΔG_{cavity} and ΔG_{dr} are parameterized based on the cavity surface area whereas the ΔG_{el} is determined by the modified Hamiltonian:

$$\hat{\mathbf{H}} = \hat{\mathbf{H}}_0 + \phi(\mathbf{r}) \quad (3.40)$$

where $\hat{\mathbf{H}}_0$ is the unmodified electronic Hamiltonian of the solute and $\phi(\mathbf{r})$ is the electrostatic potential of the polarizable solvent model. The electrostatic effect is accounted for by dividing the cavity surface into fragments, *tesserae*, associated with a partial charge density $\sigma_s(\mathbf{r}_s, \epsilon)$ that depends on the dielectric constant of the medium and of the charge density of the solute. From this, one can compute the electrostatic potential due to the continuum model by:

$$\phi_s(\mathbf{r}) = \int \frac{\sigma_s(\mathbf{r}_s, \varepsilon)}{\mathbf{r} - \mathbf{r}_s} d\mathbf{r}_s \quad (3.41)$$

In the COMSO model, the dielectric constant is set to infinity outside of the cavity surface and the resulting surface charges $\sigma_s^*(\mathbf{r}_s)$ must be scaled by a function of ε , $f(\varepsilon)$, to retrieve the correct surface charges ($k=0.5$ in the original formulation²⁴⁹):

$$f(\varepsilon) = \frac{\varepsilon - 1}{\varepsilon + k} \quad (3.42)$$

$$\sigma_s(\mathbf{r}_s, \varepsilon) = f(\varepsilon)\sigma_s^*(\mathbf{r}_s) \quad (3.43)$$

Charge spill resulting from the overlap of electron density and the continuum can be compensated for by the suggestions of Klamt and Jonas.²⁵⁰

Traditionally, continuum models for periodic plane-wave calculations have not been extensively used. Recent methods have, however, been suggested also for these kind of calculations e.g. the VASPsol method.²⁵¹

3.1.8. Molecular dynamics

Whereas real chemical systems are dynamic, the picture obtained from studying a reaction via standard QM calculation of ground and transition states is highly stationary. This approach can, nevertheless, yield a sufficient description of a reaction given that the states are well represented by single atomic configurations. In other cases, averages over ensembles of states have to be studied by sampling over a larger part of the configuration space of the system. Monte-Carlo simulations can achieve this as described elsewhere.²⁰¹ Alternatively *molecular dynamics* (MD) simulations can be used where deterministic trajectories of the dynamic movement of the particles of the system are studied. The dynamics of the system is followed by assigning initial velocities to the particles and solving Newton's equation of motion:

$$\mathbf{F} = -\frac{dE}{d\mathbf{r}} = \mathbf{m}\mathbf{a} \quad (3.44)$$

The problem of evolving the system can be formulated based on the current and previous time frames via the use of a Taylor expansion to second order with respect to a small change in time (Δt). This is known as the Verlet algorithm:²⁵²

$$\mathbf{r}_{i+1} = (\mathbf{r}_i - \mathbf{r}_{i-1}) + \mathbf{a}_i(\Delta t)^2 \quad (3.45)$$

With the acceleration:

$$\mathbf{a}_i = -\frac{1}{m_i} \frac{d\mathbf{v}_i}{d\mathbf{r}_i} \quad (3.46)$$

In MD simulations it is important to make sure that the Δt is shorter than the fastest fundamental motion of the system. If this is the vibration of H atoms, the Δt is commonly set to around 1 fs. Different ensembles can be sampled. If e.g. the number of particles (N), the volume of the simulation cell (V) and the total energy (E) is kept constant for the system during the course of the simulation, we sample the *NVE*- or *microcanonical ensemble*. If instead the temperature (T) is constant the *NVT*- or *canonical ensemble* is sampled. One can controlled the temperature of the cell by rescaling of the velocities or by energy exchange with a so-called thermostat (a heat bath of a given temperature), e.g. the Berendsen²⁵³ or Nosé-Hoover thermostat.^{254,255}

In MD simulations periodic boundary conditions are common, but for some cases it can be more appropriate to use e.g. spherical boundary conditions.^{256,257} This allows for the inclusion of a smaller number of species in the simulation, attractive for the study of solute-solvent interactions in e.g. QM/MM simulations. Under spherical boundary conditions, a central constraining potential U_{const} is applied to keep the particles within a certain distance (R) from the center (R_{center}):

$$U_{\text{const}}(\mathbf{r}) = k[(\mathbf{r} - R_{\text{center}}) - R]^2 \quad (3.47)$$

k is a force constant and R is usually chosen so as to set the density of the simulation cell to a given value.

3.1.9. Optimization procedures

Studying the PES (potential energy surface) in computational chemistry often amounts to finding stationary point structures corresponding to stable or metastable ground or transition states. Optimization to a local minimum is fairly straightforward and is usually achieved via the use of either the *steepest-decent*, *conjugate gradient* or *Newton-Raphson* methods in computational chemistry codes. Methods avoiding the use of explicit calculations of the second order derivative matrix, the Hessian \mathbf{H} , of the system are generally most effective but may occasionally suffer from convergence problems.

TS calculations are more demanding because TS structures by definition (in TST) have one, and only one, imaginary vibrational frequency. The methods for finding TS can be divided into local and interpolation methods. For the local methods calculations of the Hessian are necessary and we have to provide the algorithm with a good guess of the TS structure. The interpolation methods use at least two start structures, one on the product and one on the reactant side of the

TS. These are interpolated to form the TS. An example of the latter approach is the Nudge-elastic band method.²⁵⁸

Other methods for structure identification are Monte-Carlo or MD simulations. In the simulated annealing (SA) procedure, low-energy structures are identified by first performing a MD simulation at high temperature and then slowly reducing the temperature to low temperatures. In this way we increase our chances to find the lowest energy structures of the system since the high temperature allows the structures to visit a larger part of the configuration space. SA can be useful for identifying global minimum for complex systems with a multitude of local minima.

3.2. *Ab initio* atomistic thermodynamics

The procedures of deriving thermodynamic properties from *first principles*, such as WFT or DFT,^{xxi} are jointly referred to as *ab initio atomistic thermodynamics*. It resides on the fact that the thermodynamic properties G , S , U and H are state functions and can be expressed as sums of the contributions from the subsystems. Therefore the atomic subsystems can be evaluated separately by quantum mechanical methods and their joint contribution added in order to estimate the thermochemistry of various states, e.g. to evaluate the ΔG of a reaction by comparing the sum of the G 's of the products to the sum of the G 's of the reactants.

In order to account for thermochemical effects in computational chemistry we have to estimate statistical ensembles and partition functions. This corresponds to identifying all accessible (and significant) states of the system and to determine their energies. While this is a demanding task for any system, the complexity quickly grows with the size of the system. For a solvent phase, for instance, a very large number of intra- and intermolecular configurations have to be evaluated. Molecular dynamics (MD, section 3.1.8) simulations are one way to sample the configuration space. In gas phase we only have to consider the rotational, translational, electronic, vibrational and conformational (from symmetry) states as discussed below.

The following is based on statistical mechanics and thermochemical relationships as described in the literature.^{259–261} The Gibbs free energy can be expressed in terms of statistical partition functions, Q , of the system:

$$G = U + pV - TS = \sum_i \mu_i N_i = -kT \ln Q + pV \quad (3.48)$$

^{xxi} Strictly speaking DFT is only *ab initio* if used without semi-empirical parameters.

Similarly for the Helmholtz free energy:

$$A = -kT \ln Q \quad (3.49)$$

where the total partition function is:

$$Q = \frac{1}{N!} q^N \quad (3.50)$$

and q is a product of the individual translational, vibrational, rotational, symmetrical and electronic contributions of each considered subsystem:

$$q = q^{trans} q^{rot} q^{vib} q^{el} q^{sym} \quad (3.51)$$

Furthermore (under constant temperature, pressure and number of particles):

$$\mu = kT(\ln N + 1 - \ln q) \quad (3.52)$$

Assuming an ideal gas of pressure p :

$$q^{trans} = \left(\frac{2\pi m}{h^2} \right)^{\frac{3}{2}} T^{\frac{5}{2}} \frac{nR}{p} \quad (3.53)$$

By employing the rigid-rotor and harmonic oscillator approximations we get:

$$q^{rot} = 8\pi^2 \left(\frac{2\pi kT}{h^2} \right)^{\frac{3}{2}} (\mathbf{I}_A \mathbf{I}_B \mathbf{I}_C)^{\frac{1}{2}} \quad (3.54)$$

where \mathbf{I}_A , \mathbf{I}_B and \mathbf{I}_C are the moments of inertia. In addition:

$$q^{vib} = \prod_i \left[e^{-\frac{h\omega_i}{2kT}} \left(1 - e^{-\frac{h\omega_i}{2kT}} \right)^{-1} \right] \quad (3.55)$$

In the above ω_i are the harmonic vibrational frequencies of the studied compound. These can be determined from the mass-weighted Hessian \mathbf{H} of the system (obtained numerically or analytically) by first projecting out the rotational and translational modes leaving $3M-6$ (M =number of atoms) frequencies > 0 for a non-linear molecule ($3M-5$ for a linear). For a crystalline surface we assume rigidity of the system is assumed, why translation and rotation effects vanishes. The $3M-3$ optical phonon modes are usually considered, while the acoustic modes (the three modes of lowest frequency) are often omitted and projected out. The out-projected Hessian is diagonalized yielding λ_i eigenvalues that are related to the vibrational frequencies as (c is the speed of light):

$$\omega_i = \frac{\sqrt{\lambda_i}}{2\pi c} \quad (3.56)$$

Assuming that the first electronic excited state is energetically inaccessible, the electronic partition function is given by:

$$q^{el} = v_0 e^{-\frac{E_0}{kT}} \quad (3.57)$$

with $v_0=2S+1$, i.e. the spin-multiplicity. Lastly the number of symmetrically unique conformations that a compound can adopt determines the symmetry correction. The correction is expressed in terms of the rotational symmetry number σ :

$$q^{sym} = \frac{1}{\sigma} \quad (3.58)$$

The Gibbs free energy from a DFT or WFT calculations can be determined from the electronic energy E_{el} of a system corrected by the thermal contributions from above:

$$G = E_{el} + \Delta G^{trans} + \Delta G^{rot} + \Delta G^{vib} + \Delta G^{el} + \Delta G^{sym} \quad (3.59)$$

On top of this one could add corrections for converting from gas to condensed phase (see 3.1.7), and corrections from the sampling of the configuration space. Converting to arbitrary pressures and concentrations is carried out based on the equations of section 2.1.1. For example the reaction free energy at standard state, ΔG° , may be converted to the free energy ΔG^* of an arbitrary state by:

$$\Delta G^* = \Delta G^\circ + \sum_i \Delta \Delta G_i^{\circ \rightarrow *} \quad (3.60)$$

$$\Delta \Delta G_i^{\circ \rightarrow *} = -c_i RT \ln[\{i\}^*/\{i\}^\circ] \quad (3.61)$$

Where $\{i\}^*$ ($\{i\}^\circ$) is the activity or fugacity of compound i in the new (standard) state and c_i is the stoichiometry coefficient that is positive for a reactant and negative for a product. Note that in the standard state $\{i\}^\circ$ is 1 bar (≈ 0.041 M) in gas phase and 1 M in solution.

3.3. Estimations of surface properties

A large focus is directed towards the computing of surface properties in this thesis, in particular adsorption characteristics. Some basic considerations are given below.

First follows a few words on the choice of model. Common models for surfaces are periodic *slabs* or non-periodical *cluster* models.^{xxii} Both have advantages and disadvantages. The use of cluster models allows for the employment of a plethora of computationally elaborate methods including hybrid DFT or post-HF methods and other methods from molecular quantum mechanics codes, including also well-established solvation models. By the use of cluster models one avoids the spurious interaction between periodic images of neighboring unit cells or interslab interactions. However, the semi-infinite character of surfaces is lost and convergence towards bulk properties is often slow with cluster size. A possibility is to embed the cluster; e.g. via termination by hydrogen or hydroxyl groups, or by embedding in a lattice of point charges.

For slab models it is important to take action in order to avoid unwanted interaction between periodic mirror images. This often results in the need to use large supercells,^{xxiii} especially when considering adsorbate interactions. Effectively this means that one should always check that a studied property has converged with respect to i) surface supercell size, ii) the number of atomic layers in the slab model and iii) the vacuum distance between slabs. Spurious dipolar interactions between periodic surface slab images decay slowly with the vacuum distance, why addition of dipolar corrections is sometimes preferable over large slab separations.^{262,263}

3.3.1. Surface related properties and phenomena

Surface properties are closely connected to the surface's geometric and electronic structure. The surface energy of a material varies largely with the surface structure and composition, dictating e.g. its wettability, adsorbate affinities and conductivity. This is interlinked with the electronic configuration of the surface that can be described by its band structure and density of states (DOS) – i.e. its wave function. The band gap is estimated by the energy difference between the

^{xxii} A slab consists of n layers of a solid crystal unit cell extended as a 2D surface in the lateral dimensions and separated by a vacuum distance in the surface normal directions, i.e. a 2D model represented in a 3D framework. A cluster model is an isolated, non-periodic model often consisting of a cutout of the surface crystal structure.

^{xxiii} The supercell is the simulation cell. It consisting of extended unit cells, e.g. 2×2 in the surface dimensions and $\times 10$ in surface normal direction including slab layers and the vacuum region.

highest occupied state of the valence band and the lowest unoccupied of the conduction band. Some other important aspects and properties are i) surface coverage, ii) adsorbate affinity and iii) the surface work function. The surface coverage is defined somewhat arbitrarily but gives, by and large, a measure of the number of occupied adsorption sites compared to the maximum available sites on the surface. The adsorbate affinity, or adsorption (interaction) energy, is given by the energy difference between the adsorbate–surface (s – a) adduct and the free compounds (s , a), i.e.:

$$\Delta E_{ad} = E_{s-a} - (E_s + E_a) \quad (3.62)$$

Note that the adsorption energy and interaction energies are sometimes defined with opposite signs. The work function, ϕ , is the minimum work needed to remove an electron from the Fermi level (E_F) and placing it in the vacuum region in close proximity to the surface. The latter gives a measure of the redox properties of a given surface.

Concerning molecule-surface interactions, these can be understood by analysis of the wave function of the adsorbate and the substrate prior to and after adsorption. The interaction usually leads to large perturbations in the case of chemisorption, whereas physisorption is associated with a smaller rearrangement of the wave functions. The favored adsorption position and the bond strengths can largely be rationalized by the local orbital-band overlap, as well as by the occupation and distribution of electron energy levels of the interaction compounds.⁶⁶ Adsorbate-surface interactions will be further discussed in section 3.4.5 and chapter 4. More comprehensive accounts of surface properties are given elsewhere.²⁶⁴

3.3.2. X-ray photoemission spectroscopy (XPS)

DFT can be used to estimate spectral features from many kinds of spectroscopic methods including X-ray photoelectron spectroscopy (XPS). XPS is a useful technique; not least so for the study of surface characteristics, surface composition and adsorbate interactions. XPS measures differences in core-level ionization energies, which is obtained by exposing the sample to monochromatic and ionizing X-ray irradiation of energy $h\nu$. For chemical and elemental analysis, we are interested in the binding energy (BE) of the core electrons of the sample. One can obtain the BE by measuring the kinetic energy (E_{kin}) of the knocked-out electrons and subtracting that from the energy of the incident radiation by: ^{265,266}

$$\text{BE} = h\nu - E_{\text{kin}} \quad (3.63)$$

The binding energy will vary with the type of atom, the studied core state as well as the chemical environment of the atom: the latter is known as the *chemical shift*. By comparing the chemical shifts within or in-between different samples we can draw conclusions about the state and chemical composition of the sample: for instance what elements are present on the surface, what kind of species is adsorbed and if the surface is reconstructed or not. However, the analysis demands prior knowledge of the system under study and comparison to reference data. For this purpose DFT calculations are commonly used as a guiding tool.^{265,266}

The standard approaches to calculate the BE and the chemical shifts are divided into approximations including initial state and final state effects, or both of them. Whereas the initial state effects are intrinsic properties of the ground state of the system, final state effects accounts for the relaxation of the ionized system in order to shield the created core ion. In this thesis both final and initial state effects have been accounted for by performing two separate calculations, one of the initial state and one of the final state. The energy difference gives the BE. On an absolute scale errors in the BE's obtained by DFT can be quite large (up to 1 eV) and thus the computed BEs are often unreliable. Relative shifts between different samples are, nevertheless, determined with a much better precision. (Note that a certain DFT xc-functional sensitivity have been reported.²⁶⁷) The reported XPS data in this thesis are exclusively relative BE, also known as core-level shifts (CLS), determined by:

$$\text{CLS} = \text{BE}(X) - \text{BE}(\text{ref}) = (E_x^* - E_x) - (E_{\text{ref}}^* - E_{\text{ref}}) \quad (3.64)$$

Above E and E^* represents the initial and final state energies for an arbitrary atom X compared to a reference (ref). For samples with a common initial state the above equation simplifies to:²⁶⁸

$$\text{CLS} = E_x^* - E_{\text{ref}}^* \quad (3.65)$$

This is, for instance, the case when comparing different atoms of the same surface. For metallic systems, the final state is most commonly approximated by exciting a core electron to the Fermi level of the conduction band. While this is a good approximation for metals (that have no band gap), oxides and other insulators/semi-conductors should not be treated in this fashion because of their band gaps. This can also be understood in terms of final-state core-hole screening effects where the delocalized electron of a metal effectively screens the cationic core, whereas the same process is less effective for oxides that have more localized electronic states. Therefore the final state of a metal can be conveniently approximated by an excited state, while for an oxide, with poorer screening, this approximation is qualitatively wrong and the method of choice for oxides is to remove one electron from the system completely. This will generate a net positive

charge, which is compensated for in periodic calculations by applying an opposing and homogenous jellium potential.²⁶⁹ In periodic calculations special considerations have to be applied also in the generation of an ionic core state due to the use of PAW potentials to represent the core electrons. This problem can be overcome by generating special PAW potentials for these states and reevaluating the local electrostatic potential.^{270,271}

3.3.3. Scanning tunneling microscopy (STM)

Scanning tunneling microscopy (STM) is an experimental technique for surface imaging. STM studies variations in the tunneling current between a surface and a small probe tip of the instrument. Given a sufficiently sharp probe, STM has the capacity to provide atomically resolved surface images. By applying a bias voltage to the probe one can either map occupied (+ voltage) or unoccupied states (- voltage) of the sample. By this technique one may, for instance, study reconstruction patterns of surfaces or adsorbate positions, orientation and states – including e.g. studies of water/hydroxyl structures on metal surface.²⁷²

The simulated STM images of this thesis were generated using to the Tersoff-Hamann method.²⁷³ According to this method, the STM current is taken as the local density of states (LDOS) at the position of the simulated probe tip. The LDOS includes all states ranging from the Fermi level to a given bias. Ideally, the computational bias voltage should match the experimental conditions. However, due to inherent differences between DFT computations and experiments (e.g. differences in experimental and computed band-gaps are common), a shift in the computational bias are sometimes necessary in order to reproduce experimental results. Variations in the STM current density can be accounted for by adjusting the simulated surface-probe distance. In practice this may be achieved by probing the LDOS at different isodensity contours of the studied surface.

3.4. Quantum chemical interaction and reaction descriptors

Although the modern computational toolbox comprises sophisticated methods that are able to accurately predict chemical properties, they generally suffer from two major drawback; i) a large computational cost, and ii) a lack of theoretical transparency. For this reason simpler methods and concepts can serve as valuable options for rationalization of chemical reactivity and intermolecular interactions.

Many qualitative methods attempt to extrapolate interaction behavior based on the ground state properties of the interacting compounds, see **Figure 9**. Whereas the entire PES should ideally be studied for a comprehensive understanding, the ground state approach is often remarkable useful. It does naturally have its limitations, especially for cases where the interaction leads to significant changes in electronic or geometrical structures. Regardless, when employed carefully, ground state quantities (descriptors) obtained from e.g. quantum chemical calculations can be powerful for predicting and explaining chemical behavior. Some of the most common and useful concepts from molecular and condensed phase theory are discussed in the following sections. When comparing descriptors it is, furthermore, important to keep in mind if they are *global* or *local*. A global descriptor describes a property for the compound as a whole entity, whereas a local descriptor provides information resolved for different regions of a compound.

3.4.1. Frontier molecular orbital theory and Fukui functions

In the frontier molecular orbital (FMO) theory²⁷⁴ chemical reactions are rationalized on the basis of the *highest occupied molecular orbital* (HOMO) and *lowest unoccupied molecular orbital* (LUMO) of the interacting compounds at their ground states. This can be motivated by perturbation theory by expanding the energy of the interacting species to second order as (in an atom-based framework):^{275,276}

$$\Delta E = - \sum_{A,B}^{\text{atoms}} (\rho_A + \rho_B) \langle \Phi_A | \mathbf{V} | \Phi_B \rangle \langle \Phi_A | \Phi_B \rangle + \sum_{A,B}^{\text{atoms}} \frac{Q_A Q_B}{R_{AB}} + \left(\sum_{i \in A}^{\text{occ. MO}} \sum_{a \in A}^{\text{vir. MO}} + \sum_{i \in B}^{\text{occ. MO}} \sum_{a \in A}^{\text{occ. MO}} \right) \frac{2 (\sum_{\alpha}^{\text{AO}} c_{\alpha i} c_{\alpha a} \langle \Phi_{\alpha i} | \mathbf{V} | \Phi_{\alpha a} \rangle)^2}{\epsilon_i - \epsilon_a} \quad (3.66)$$

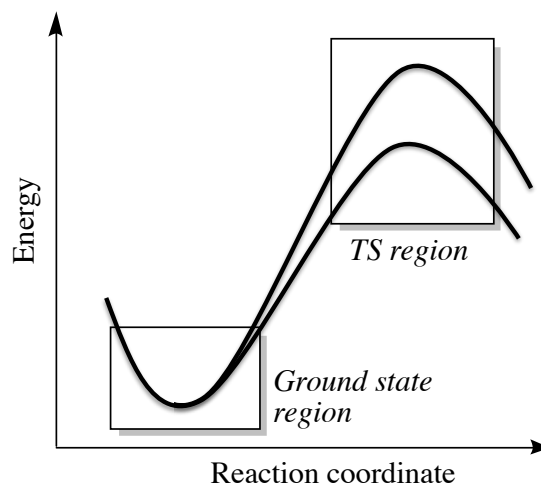


Figure 9. Illustrating the use of ground state properties for estimation of chemical reactivity. Small differences in the ground states of two compounds are extrapolated to reflect the behavior of their transition states. Readopted with permission.²⁰¹ © 2007 John Wiley & Sons, Ltd.

A and B represents atoms on the two interacting compounds, respectively. \mathbf{V} is an operator containing the potential energy contributions from the two molecules, ρ and Q give the atomic charge density and atomic net charge (*vide infra*), Φ represents atomic orbitals and ε corresponds to orbital eigenvalues. The first term of eq. 3.64 characterizes the steric or Pauli repulsion between the overlapping electron densities, the second term represents the classical Coulomb interactions, whereas the third term reflects the stabilizing effect of orbital mixing (charge transfer) and sums over all intermolecular occupied and virtual orbital interactions.

For a charge-transfer controlled interaction the third term of eq. 3.66 will dominate, while an electrostatically controlled interaction (e.g. between two polar species) will be dominated by the second term. In FMO theory, everything but the third term is neglected and the charge-transfer contribution is reduced to the interaction between the HOMO of the electron-donating compound (the nucleophile) and the LUMO of the electron-accepting compound (the electrophile). This is a considerable simplification since the contributions from the other orbitals as well as the sterics and Coulomb terms are typically much larger than the HOMO-LUMO contribution. However, the frontier orbitals can often reflect the underlying properties that govern reactivity of a compound. Hence one has found that the interactions can be rationalized by the density distribution of the HOMO and LUMO orbitals over the molecules; a site of large orbital density is more susceptible to interactions. In line with eq. 3.66 one has also found that

interactions are favored by a small energetic difference between the HOMO of the nucleophile and the LUMO of the electrophile. This type of analysis is particularly useful for molecules with small HOMO-LUMO gap and soft interactions. For hard-hard interactions (species with large HOMO-LUMO gaps) the frontier orbitals are poor descriptors. Instead atomic partial charges (section 3.4.2) or the electrostatic potential (section 3.4.3) are suitable choices. Two multi-orbital descriptors that extend the HOMO and LUMO concepts and capture a larger portion of the charge transfer contribution are the average local ionization energy and the local electron attachment energy discussed in section 3.4.4 and 4.2.1.

A concept that is closely related to FMO is the Fukui function, $f(\mathbf{r})$:^{275,277}

$$f(\mathbf{r}) = \left(\frac{\partial \rho(\mathbf{r})}{\partial N_{\text{elec}}} \right)_{V(\mathbf{r})} \quad (3.67)$$

Upon reaction, the electronic density of a compound is usually redistributed. The Fukui function identifies sites where the density is more easily perturbed and hence more prone to react. Two versions of $f(\mathbf{r})$ exist for closed shell compounds, one where density is added [$f_+(\mathbf{r})$] and one where density is removed [$f_-(\mathbf{r})$]. These can be written in difference form and on molecular orbital form:

$$\begin{aligned} f_+(\mathbf{r}) &= \rho_{N+1}(\mathbf{r}) - \rho_N(\mathbf{r}) = \psi_{\text{LUMO}}^2(\mathbf{r}) + \sum_{i=1}^{N_{\text{elec}}} \frac{\partial \psi_i^2(\mathbf{r})}{\partial n_i} \\ f_-(\mathbf{r}) &= \rho_N(\mathbf{r}) - \rho_{N-1}(\mathbf{r}) = \psi_{\text{HOMO}}^2(\mathbf{r}) + \sum_{i=1}^{N_{\text{elec}}-1} \frac{\partial \psi_i^2(\mathbf{r})}{\partial n_i} \end{aligned} \quad (3.68)$$

In a frozen orbital picture, the $f_+(\mathbf{r})$ [$f_-(\mathbf{r})$] reduce to the LUMO [HOMO] terms.

3.4.2. Atomic partial charges

Assigning partial charges to atoms in molecules or materials is a popular practice in physical chemistry, this despite the lack of a theoretical or experimental motivation for their accidental existence. Regardless, if properly handled, atomic charges can be used to qualitatively comprehend certain chemical characteristics, e.g. for identification of sites of interaction, to understanding charge-transfer and even, to some degree, to rank interaction propensities of chemical compounds. Various schemes for assigning atomic charges have been developed over the years including Mulliken,²⁷⁸ Löwdin,²⁷⁹ Hirshfeld²⁸⁰ (and the updated CM5²⁸¹ and CM5M²⁸¹ methods), Bader²⁸² and Merz-Kollman-Singh (MKS) charges that are based on fitting charges to match the surface electrostatic potential,^{283,284} as well as charges obtained from natural population analysis (NPA).²⁶ The NPA charges are included in the NBO analysis schemes.²⁵⁻²⁸

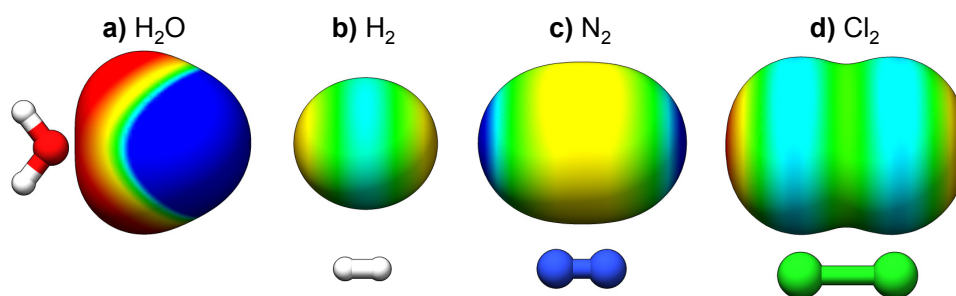


Figure 10. Electrostatic potential of H_2O , H_2 , N_2 and Cl_2 determined at the 0.001 isodensity contour. Color scale in kcal mol^{-1} (centered at): red=25, yellow=7.5, green=0, cyan=-3.5, blue=-7.5.

3.4.3. The surface electrostatic potential

A central property in this thesis is the electrostatic potential, $V(\mathbf{r})$. $V(\mathbf{r})$ has been used extensively for the analysis and understanding of e.g. molecular interactions, chemical reactivity, hydrogen bonding and biological recognition interactions.^{285–287} Unlike atomic partial charges, the electrostatic potential is a rigorously defined property and a physical observable that may be derived from both experimental data (e.g. via X-ray diffraction techniques) or by computational methods.²⁸⁵ The $V(\mathbf{r})$ at the spatial coordinate \mathbf{r} of a polyatomic compound is defined by:

$$V(\mathbf{r}) = \sum_A \frac{Z_A}{|\mathbf{R}_A - \mathbf{r}|} - \int \frac{\rho(\mathbf{r}') d\mathbf{r}'}{|\mathbf{r}' - \mathbf{r}|} \quad (3.69)$$

In eq. 3.69, Z_A is the charge of the A^{th} nucleus whereas $\rho(\mathbf{r})$ is the electron density function. The first term of the above expression originates from the nuclei and is thus always positive. The second term is always negative and corresponds to the electronic contribution. Therefore, the sign of the electrostatic potential at a given point will tell which term that dominates at a given point of the compound.

Following the early suggestion by Bader, Politzer and coworkers^{287–289} have demonstrated that a useful approach to evaluate the $V(\mathbf{r})$ property for the study of molecular interactions is to compute it on a molecular surface of constant density, an isodensity surface. When evaluated on an isodensity surface, the surface electrostatic potential is denoted $V_s(\mathbf{r})$. The isosurface is typically chosen within the density range of 0.001 to 0.004 atomic units (a.u. = electrons bohr⁻³). The latter gives a surface positioned somewhat closer to the molecular core than surfaces constructed by the van der Waals radii of the atoms that constitute the molecule whereas the former isosurface is marginally more diffuse than the van der Waals surface. For weak interactions the choice of isosurfaces reflects the expected interaction distances fairly well. However, for reactions leading to

covalent bonding the atomic separations will be even smaller. It has, nevertheless, been found that many reactions are directed by early interactions and that the use of e.g. the 0.001 a.u. isosurface is indeed a suitable choice. When comparing different interaction sites, the evaluation at an isodensity surface has the added advantage of resulting in an approximately constant Pauli repulsion thus simplifying the analysis. **Figure 10** shows example of the surface electrostatic potential evaluated on the 0.001 a.u. isosurface of H₂O, H₂, N₂ and Cl₂ molecules.

For estimations of the position and strength of an interaction, one often make use of local extremes in the $V_S(\mathbf{r})$: local maxima, $V_{S,\max}$, and local minima, $V_{S,\min}$,^{xxiv} correspond to sites susceptible to interactions with nucleophiles (Lewis bases) and electrophiles (Lewis acids) respectively. $V_{S,\max}$, or rather electron depleted areas of relatively high electrostatic potential, are sometimes denoted σ - or π -holes^{xxv} depending on if they are located in the extension of (σ) or perpendicular to (π) an intramolecular bond.^{290,291} Correlations have been found between the magnitude of $V_{S,\max}$ or $V_{S,\min}$ and the strength of the interaction. The interaction energy, ΔE_{INT} , can be estimated by placing a test charge q at the position \mathbf{r} of the local surface extreme, $\Delta E_{\text{INT}} \approx qV_S(\mathbf{r})$. The test charge q is most commonly chosen as 1 or -1 depending on the type of interaction studied. On the basis of perturbation theory one can, furthermore, show that $qV_S(\mathbf{r})$ gives the first order contribution to the interaction energy (see section 2.1.3). A second order polarization correction to $V(\mathbf{r})$, known as $P(\mathbf{r})$, have been defined as:²⁹²

$$P(\mathbf{r}) = \sum_i^{\text{occ.}} \sum_a^{\text{vir.}} \frac{1}{\varepsilon_i - \varepsilon_a} \left[\sum_\mu \sum_\nu c_{\mu i} c_{\nu a} \int \frac{\phi_\mu(\mathbf{r}') \phi_\nu(\mathbf{r}') d\mathbf{r}'}{|\mathbf{r}' - \mathbf{r}|} \right]^2 \quad (3.70)$$

It has been found³⁸ that a dual descriptor of $qV(\mathbf{r}) + q^2P(\mathbf{r})$ is better suited than $V(\mathbf{r})$ for studies of strong nucleophiles and electrophiles leading to formation of covalent bonding, for instance in aromatic substitutions and reactions of vinylic compounds. However, the computation of $P(\mathbf{r})$ is considerable more demanding than the computation of $V(\mathbf{r})$, why $P(\mathbf{r})$ is seldom used. The $\tilde{I}(\mathbf{r})$ property discussed below (section 3.4.4) is more readily computed. $\tilde{I}(\mathbf{r})$ has been shown to correlate with the local polarizability of a compound and can potentially be used *in lieu* of $P(\mathbf{r})$.^{293,xxvi}

^{xxiv} Note, however, that the spatial minima of $V(\mathbf{r})$, V_{\min} , sometimes are better descriptors than the surface minima for estimations of nucleophilic interactions, e.g. for the estimation of H-bond acceptor strengths.³⁸

^{xxv} A corresponding concept, σ -lumps, is introduced for $V_{S,\min}$ in **Paper XI**.

^{xxvi} This is not always true, however, and Brinck³⁴ has found that $\tilde{I}(\mathbf{r})$ and $P(\mathbf{r})$ in many cases instead are complementary properties.

The variations of $V(\mathbf{r})$ for a chemical compound can be understood by the derivation from an atomic perspective. The electrostatic potential of an atom in its ground state is (on the average) spherically symmetric, everywhere positive and goes toward zero at increasing distances from the nuclei. Upon formation of bonds, the electron density is redistributed leading to regions of both positive and negative potential. For a non-polar, covalently bound molecule such as H_2 , this leads to an accumulation of electron density in the bonding region, and a corresponding depletion of density in the extensions of the bonds at the two ends of the molecule. The result is two $V_{\text{S,max}}$, one at each end of the molecule and in a band-shaped $V_{\text{S,min}}$ over the bonding region (**Figure 10.b**). For the N_2 molecule, the surface electrostatic potential is reversed due to the electron lone pairs along the extensions of the N-N bond. Thus $V_{\text{S,min}}$ are located at both ends of the N_2 molecule with a positive region in-between (**Figure 10.c**). In the H_2O molecule the bonds are polarized leading to accumulation of electron density on the electronegative O atom and corresponding $V_{\text{S,min}}$ over the electron lone pairs, and depletion of density over the H atoms with corresponding $V_{\text{S,max}}$ (**Figure 10.a**). The kind of information presented above can be used to rationalize interactions. For instance have the magnitudes of $V_{\text{S,min}}$ and $V_{\text{S,max}}$ of different H-bonding molecules and Brønsted acids been used to estimate their interaction affinities and $\text{p}K_{\text{A}}$.^{294,295}

Figure 10.d shows the surface electrostatic potential of the Cl_2 molecule. Here the electronic structure gives rise to an interesting $V_{\text{S}}(\mathbf{r})$ profile. Similar to N_2 a band shaped area of positive potential is located over the bonding region surrounded by areas of negative potential at the atoms. However, the lone pairs of Cl_2 are not located at the extensions of the bond but according to a sp^3 hybridization. Hence, negative surface potential is observed as a ring around the atoms, with a depletion of electron density along the extension of the Cl-Cl bond and thus a corresponding $V_{\text{S,max}}$ at the two ends of the molecule. This kind of $V_{\text{S}}(\mathbf{r})$ profile has been found to be a general feature of single coordinated halogen atoms ($\text{X}=\text{Cl}$, Br , and I) and rationalizes the propensity of the electronegative halogen atoms to interact with electron donors. This e.g. explains the crystal structure of Cl_2 (that forms a L-shaped dimer)^{38,296,297} as well as the formation of halogen bonds between halogenated compounds and electron donors such as the carbonyl O atom of acetone,^{53,54,298} see also section 2.1.4 and 4.2.

3.4.4. The average local ionization energy

The $V_s(\mathbf{r})$ is an excellent tool for analysis of non-covalent interactions that are governed by electrostatics, but lacks the ability to reflect charge redistribution effects. In 1990 Sjöberg et al.³⁷ introduced a new property, the local average ionization energy $[\bar{I}(\mathbf{r})]$, which complements the electrostatic potential for interactions that are not purely electrostatic but largely controlled by charge-transfer and polarization. $\bar{I}(\mathbf{r})$ is rigorously defined within HF and DFT via:

$$\bar{I}(\mathbf{r}) = - \sum_{i=1}^{\text{HOMO}} \frac{\varepsilon_i \rho_i(\mathbf{r})}{\rho(\mathbf{r})} \quad (3.71)$$

where ε_i is the energy of the i^{th} orbital and $\rho(\mathbf{r})$ is the electron density function. The summation runs over all occupied orbitals. In HF, the $\bar{I}(\mathbf{r})$ property is motivated by Koopmans' theorem and gives a local measure of the cost of removing electron density from a molecule (particle or surface), i.e. a local ionization energy averaged over all orbitals. Accordingly, $\bar{I}(\mathbf{r})$ has been found to reflect the local susceptibility towards interactions/reactions with electrophilic (Lewis acidic) species. This has e.g. been demonstrated by studies of electrophilic aromatic substitution reactions and aqueous acidity.^{37,294,299–302} In particular, $\bar{I}(\mathbf{r})$ has proven well suited for studies of reactions in solution where the electrostatic contributions are partly shielded.

Although $\bar{I}(\mathbf{r})$ and $V(\mathbf{r})$ can be used as complementary properties, one has found that they are often correlated. This can be understood by decomposing $\bar{I}(\mathbf{r})$ via:^{303,xxvii}

$$\bar{I}(\mathbf{r}) = - \frac{t_s(\mathbf{r})}{\rho(\mathbf{r})} + V(\mathbf{r}) + V_{\text{xc}}(\mathbf{r}) \quad (3.72)$$

One thus finds that $\bar{I}(\mathbf{r})$ indeed depends on the electrostatic potential, but also on the exchange-correlation potential, $V_{\text{xc}}(\mathbf{r})$, as well as on the local kinetic energy density, here defined as $t_s(\mathbf{r}) = -1/2 \sum_i^{\text{occ}} \psi_i^*(\mathbf{r}) \nabla^2 \psi_i(\mathbf{r})$. The latter is connected to the local electron temperature $T(\mathbf{r})$ via $2/3 t_s(\mathbf{r}) / \rho(\mathbf{r}) = kT(\mathbf{r})$. From eq. 3.72 it is clear that $\bar{I}(\mathbf{r})$ not only accounts for the electrostatics capacities of a compound, but also its ability to participate in charge-transfer via electron donation. In addition it has been found that $\bar{I}(\mathbf{r})$ correlates with the local polarizability of a compound.²⁹³ Compared to the FMO theory, $\bar{I}(\mathbf{r})$ is likely to capture a larger portion of the interaction energy since all donor orbitals are considered.

^{xxvii} This means that $\bar{I}(\mathbf{r})$ can be expressed purely as a function of the electron density.

As in the case of $V(\mathbf{r})$, $\bar{I}(\mathbf{r})$ is often evaluated on an isodensity surface (typically 0.001 a.u.), denoted $\bar{I}_s(\mathbf{r})$. Local surface minima, $\bar{I}_{s,\min}$, corresponds to nucleophilic sites of the studied species. An inherent limitation of $\bar{I}(\mathbf{r})$ is that it cannot be used for predictions of electrophilicity; this whereas $V_s(\mathbf{r})$ is suitable for the study of both electrophilicity and nucleophilicity. To remedy the above, we have, during the course of this thesis work, introduced an analogous property to $\bar{I}(\mathbf{r})$ that is applicable for the study of a compound's electrophilic character. This property is called the local electron attachment energy, $E(\mathbf{r})$, and will be properly defined under section 4.2.1.

3.4.5. Other concepts for describing bonding and interactions

There are many other quantum chemically derived descriptors for estimations of chemical interactions, a few of them will be introduced below included quantities from the field of conceptual DFT as well as the d -band model of Hammer and Nørskov for rationalization of interactions with metal surfaces. Other quantum chemical and non-quantum chemical descriptors not further discussed include the use of surface energy³⁰⁴ or the number of outer electrons³⁰⁵ to predict reactivity of metal and oxide surfaces, as well as the use of coordination numbers or effective coordination numbers to predict adsorption sites of particles and surfaces.^{306–308}

Conceptual DFT

In conceptual DFT, electronegativity (χ) and chemical hardness (η) are defined as:³⁰⁹

$$\chi = -\mu = \left(\frac{\partial E}{\partial N} \right)_{V(\mathbf{r})} \quad (3.73)$$

$$\eta = \left(\frac{\partial^2 E}{\partial N^2} \right)_{V(\mathbf{r})} = \left(\frac{\partial \mu}{\partial N} \right)_{V(\mathbf{r})} \quad (3.74)$$

with μ being the chemical potential. From Koopmans' theorem²¹¹ and by using finite differences, the above can be rewritten in terms of the frontier molecular orbitals:³⁰⁹

$$\chi = -\frac{\varepsilon_{\text{HOMO}} + \varepsilon_{\text{LUMO}}}{2} \quad (3.75)$$

$$\eta = \varepsilon_{\text{LUMO}} - \varepsilon_{\text{HOMO}} \quad (3.76)$$

Following the suggestion of Maynard and coworkers,³¹⁰ Parr et al.³¹¹ defined the electrophilicity index descriptor from the above quantities as:

$$\omega = \frac{\chi^2}{2\eta} = \frac{(\varepsilon_{\text{HOMO}} + \varepsilon_{\text{LUMO}})^2}{4(\varepsilon_{\text{LUMO}} - \varepsilon_{\text{HOMO}})} \quad (3.77)$$

This can be motivated by a second order expansion of the energy with respect to charge transfer from an infinite electron bath until $(\Delta E/\Delta N)=0$. A local version of this, ω_k includes the Fukui $f_+(\mathbf{r})$ function:

$$\omega_k = \omega f_+(\mathbf{r}) \approx \omega \rho_{\text{LUMO}}(\mathbf{r}) \quad (3.78)$$

These descriptors have shown correlation with chemical properties,³⁰⁹ e.g. reactivity including nucleophilic addition to activated carbon-carbon double bonds.³¹²

The *d*-band model

The *d*-band model of Hammer and Nørskov³¹³ is widely used for assessment of catalytic activity of transition metal surfaces.^{314–317} In its most common practice, the *d*-band model links differences in the *d*-band center with respect to the Fermi level ($\varepsilon_d - E_F$) of congeneric^{xxviii} transition metal substrates to differences in molecular adsorption affinities of the surfaces.³¹⁴ Adsorption affinities and catalytic activity are known to correlate for simple reactions.^{314,xxix} This can be exploited in the rationalization of and screening for catalytic material, where the ideal adsorption strength is typically a compromise between different surface processes, why it is often found in the intermediate adsorption strength range. Since the *d*-band center is readily calculated by DFT, large data series of transition metals and alloys can be scanned in order to identify new catalytic materials.^{314,321} For more complex catalytic processes more involved microkinetic models should be formulated where $(\varepsilon_d - E_F)$, or computed adsorption energies, can be used to estimate different elementary rate-constants and the effects of temperature and pressure assessed by a Sabatier type of analysis.³¹⁴

^{xxviii} Typically the compared surfaces should have the same general crystal structure and the same crystallographic facet, e.g. (111). Nørskov and coworkers distinguish between electronic effects captured by e.g. the *d*-band model, and geometric effects due to e.g. structural differences between different surface facets.³¹⁴

^{xxix} This is based on the use of scaling relations such as the Brønstedt-Evans-Polanyi (BEP) relationships^{319,320} that link adsorption energies to TS barriers.

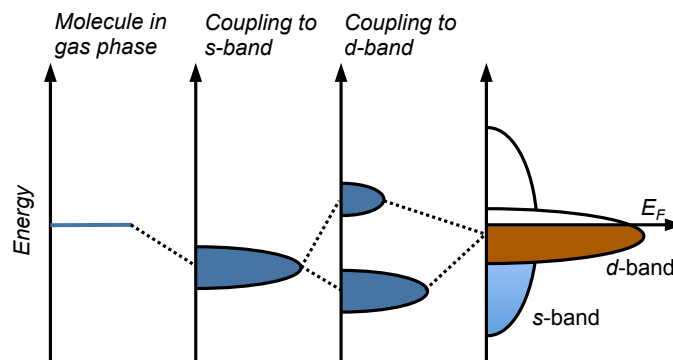


Figure 11. Coupling of an adsorbate orbital to the metal substrate's *s*- and *d*-bands. Adapted with permission from Hammer et al.³¹⁸ Copyright 2000 Elsevier Inc.

The success of the *d*-band model can be theoretically rationalized. Upon interaction between an adsorbate and a substrate their initial wave functions become perturbed; due to the Pauli repulsion the adsorbate and substrate orbitals are for instance mutually reorthogonalized. In addition, orbital mixing leads to new electronic states that usually leads to bonding. Electrostatic interactions and dispersive effects also determine the bonding strength. Using a frozen density ansatz, Hammer and Nørskov³¹³ have showed that changes in the adsorption energy (δE_{INT}) for similar surfaces can be expressed by differences in the one-electron energies ($\delta \varepsilon_{\text{1el}}$, i.e. differences in the orbital/band eigenvalues) and differences in the adsorbate-metal electrostatic interaction ($\delta E_{\text{es,A-M}}$) as

$$\delta E_{\text{INT}} = \delta \varepsilon_{\text{1el}} + \delta E_{\text{es,A-M}} \quad (3.79)$$

Hence, changes in interaction energies between different surfaces can (partly) be understood by differences in the substrate band structure. Considering an approaching adsorbate, it will couple with the wide *s*(*p*)-band and with the more compresses *d*-band of the metal substrate as illustrated in **Figure 11**. The interaction with the *s*(*p*)-band typically broadens and shifts the adsorbate energy levels whereas interaction with the *d*-band will render a split in the adsorbate states into bonding and anti-bonding states. A basic, but non-rigorous, approximation in the *d*-band model is that the interaction with the *s*(*p*)-band is independent of the metal and hence constant. Consequently the interaction energy can be approximated by contributions solely from the *d*-band. Via the Newns-Anderson model^{322,323} one, furthermore, find that the *d*-band contribution to a first approximation can be estimated by the position of the *d*-band center relative to the Fermi level.³¹⁴ Thus δE_{INT} in the comparison between similar surfaces can be expressed as:

$$\delta E_{\text{INT}} \approx \delta E_d \propto \delta(\varepsilon_d - E_F) \quad (3.80)$$

The position of the d -band center reflects its occupation; as the center is shifted downwards, the filling is increased and more anti-bonding states become occupied, which further explains the correlation with adsorption energies. However, the d -band model has its deficiencies,^{315,324–326} Some could potentially be remedied by considering not only the d -band center but also its shape,³²⁷ or by slightly expanding the method. The d -band *center* model does for instance work best for comparison within periods and not down groups of the periodic table. This is partly due to the neglect of Pauli repulsion and can be resolved by including the coupling matrix element V_{ad} .³¹⁴ Some deficiencies are, however, inherited. Of natural reasons the d -band model is not well suited for describing interactions where d -orbitals are not involved. In addition the d -band model normally fails for characterization of oxides and other non-conducting surfaces.^{305,315,328}

4. Summary of the research

The research conducted during the course of this thesis project is summarized in the following chapter. The two major research areas covered – interaction and reaction theory and the behavior of copper-based materials – are discussed separately. Nevertheless, as will be continuously pointed out, the two overlap in several aspects.

The computations in this thesis have been carried out using commercial and academic software comprising the Gaussian 09,³²⁹ Orca,³³⁰ Jaguar,³³¹ ADF,³³² GAMESS,^{333,334} Turbomole,³³⁵ TERACHEM,^{336,337} and VASP^{338–342} quantum chemical program packages.

4.1. The behavior of copper-based materials

(Papers I–VI)

As outlined in the previous chapters, copper-based materials have widespread applications. Copper is also attractive in many emerging applications due to its high abundance, low cost and favorable environmental properties compared to many heavy metals presently in use today. Most of the studies herein were motivated by the need to better understand the mechanisms of copper corrosion in a future repository for SNF in Sweden. However, the results are universal and can equally well be applied in other scientific areas such as heterogeneous catalysis, nanotechnology or basic surface science and chemistry.

4.1.1. Aqueous solvation and oxidation of the Cu₇ nanocluster

Papers I–II examined the interplay between the Cu₇ nanocluster and water where Cu₇ is the smallest 3D cluster of copper (**Figure 12**). Although Cu₇ has only been experimentally observed in inert matrices^{343–345} and not in water solutions, it serves as an useful model for the study of solvation effects on nanoparticles and clusters. It is also a suitable system for the evaluation of computational solvation models for describing copper (and possible other TM) nanomaterial in aqueous environment. Due to its small size Cu₇ is, furthermore, a convenient model system for mechanistic testing that can be translated to similar systems of e.g. larger size. Irrespective of whether or not Cu₇ dispersed in aqueous media is stable in a real situation, a considerable part of the results presented here are thus largely transferable to other systems. From the perspective of copper corrosion, our findings are relevant in e.g. the hypothesis testing concerning nanostructured

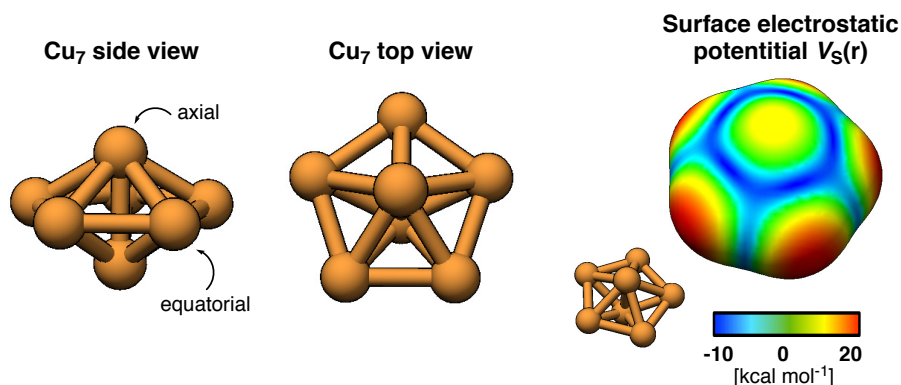


Figure 12. Structure of the bipyramidal D_{5h} Cu_7 nanocluster from different angles as well as the surface electrostatic potential evaluated on the 0.001 a.u. isodensity surface and determined on the PBE0/LACV3P**++ level of theory.

copper materials and if these can contribute to the formation of hydrogen gas upon immersion of copper samples in pure, oxygen free water (see section 2.2.5). The main points considered in **Papers I-II** can be summarized as:

- Comparison of solvation models for the efficient and accurate study of Cu compounds in aqueous environments (in particular in **Paper II**).
- Evaluation of the mechanism of Cu_7 water oxidation (**Paper I**).
- Oxidation thermodynamics of Cu_7 and its potential relation to corrosion of metallic copper under anoxic conditions (**Paper I and II**).

Solvation effects

We shall begin by discussing solvation effects. Despite the fact that copper and other transition metal (TM) nanomaterial are exposed to humid or aqueous environments in countless applications,³⁴⁶ the TM NP-water interactions are rather poorly characterized, as discussed in **Paper II**. (Water-TM NP interactions are further elaborated on in section 4.2.4 and **Papers IX-XII** of this thesis). From a computational point of view there is a surprising lack of consensus regarding the appropriate approach for studying solvation effects on TM NP. This in particular regarding whether or not the computationally efficient implicit solvation models can be used for TM NP in the same extent as for compounds comprising only main group elements. Various general aspects of TM compounds that should be considered when studying solvent-solute interactions are for example:

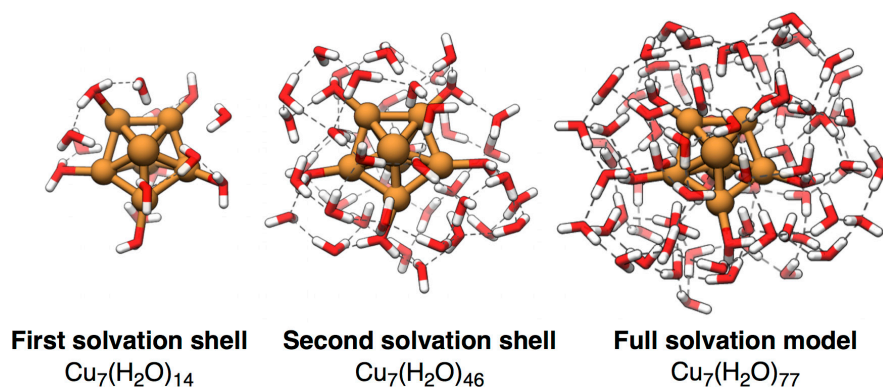


Figure 13. Showing to the first (left) and second solvation shells (middle) and the full $\text{Cu}_7(\text{H}_2\text{O})_{77}$ nanodroplet structure (right). Reproduced with permission from Stenlid et al.¹⁵¹ Copyright 2016 American Chemical Society.

- TM atoms can adopt different oxidation states adding complexity to the parameterization of the model.
- TM atoms and ions often form anisotropic interactions with the solvent (e.g. Jahn-Teller effects in TM ion-complexes³⁴⁷).
- TM NP atoms are under-coordinated and likely to form relatively strong bonds with the solvent (chemisorption rather than physisorption).³⁴⁸

All of the above are notoriously difficult or impossible to capture by implicit models. Thus it is not obvious that implicit models can or should be directly employed on TM NPs. Rather it is likely that an inner shell of chemisorbed solvent molecules must first be included, outside of which one can employ the implicit solvent model as a mixed cluster/continuum model³⁴⁹ if one so desire. This picture was corroborated by the studies of **Paper I** and **II** using three types of solvation models:

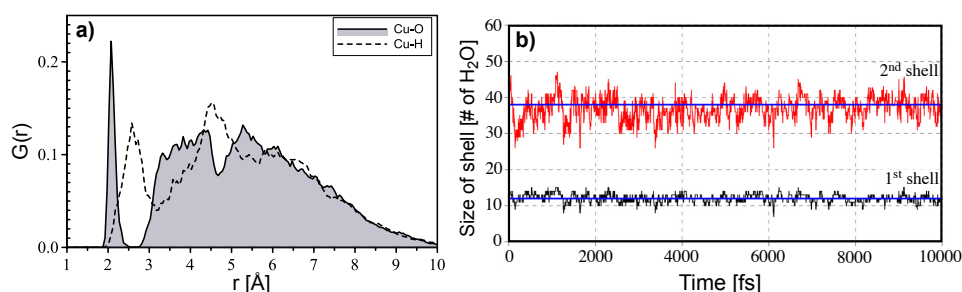


Figure 14. In a) Radial distribution function $[G(\mathbf{r})]$ for the Cu-O and Cu-H distances of Cu_7 in a 77 H_2O water cluster studied by QM-MD. In b) Solvation shell size over time for the same simulation. The blue lines in b) represents the shell size. Reproduced with permission from Stenlid et al.¹⁵¹ Copyright 2016 American Chemical Society.

- Implicit continuum models: IEF-PCM (**Paper I**) and COSMO (**Paper II**)
- Explicit models using full QM calculations (**Paper I-II**)
- Explicit models with MM EFP1 potentials for the solvent molecules (**Paper II**)

An additional question is: if we indeed need to include an inner sphere of explicit solvent molecule, how big does this sphere have to be? To evaluate this $\text{Cu}_7(\text{H}_2\text{O})_n$ cluster models comprising altogether 77 water molecules (or equivalent, *vide infra*) were constructed in **Paper II**. These were based on a set of hydroxylated and water covered $\text{Cu}_7(\text{OH})_x(\text{H}_2\text{O})_y$ *core structures* identified in **Paper I** that were used for the evaluation of the oxidation thermodynamics of Cu_7 in water as discussed further below. Low-energy solvation structures as well as the first and second solvation shells could be extracted from QM/MM-MD and full QM-MD simulations of the $\text{Cu}_7\text{-H}_2\text{O}$ clusters (structure examples are given in **Figure 13**).^{xxx} The overall conclusions are that:

- An innermost shell comprising H_2O molecules in direct contact with the Cu_7 core ($x\text{OH}_{\text{ad}}$ included in the core) is sufficient to capture the full solvation effect as compared to the larger clusters.
- The inner solvation shell grows with the number of OH_{ad} comprising 14 H_2O for the non-hydroxylated cluster and 21 H_2O for the $\text{Cu}_7(\text{OH})_7$ cluster.
- The QM-MD simulations were found to be a better tool than QM/MM-MD for identification of low-energy solvation structures.

A more detailed discussion on the solvation and its dynamics will now follow. Firstly focus will be directed towards the neutral non-hydroxylated Cu_7 cluster, before turning to the hydroxylated clusters for a general discussion in relation to the presentation of the thermodynamics of the aqueous Cu_7 oxidation.

In **Papers I-II** we found that the Cu_7 cluster has a rich interaction behavior with H_2O .^{xxxi} Cu_7 consists of two symmetrically unique atoms – a five-fold degenerate equatorial site and a two-fold degenerate axial site. The axial sites carry the largest parts of the spin density (Cu_7 is a spin doublet) but are associated with significantly lower H_2O adsorption energy in comparison to the equatorial

^{xxx} The MD simulations were run under 10 ps using stiff spherical boundary conditions to mimic an NVT-ensemble. The QM-MD was run at 350 K in TERACHEM^{336,337} using the PBE/pVDZ^{221,350} combination. The QM/MM-MD was conducted in GAMESS^{333,334} using PBEo/LACVP*^{+225,351} for the QM region (the *core structures* as defined in the text) and the EFP1 DFT- H_2O potential²⁴⁴ for the MM region.

^{xxxi} The initial adsorption behavior of H_2O onto Cu_7 was investigated in **Paper I** at the PBEo/LACV3P**+//LACVP*+ level of theory in both gas and condensed phase (by IEF-PCM) in Go9.³²⁹

sites. The difference in adsorption energy amounts to 0.14 (0.11) eV in gas (condensed) phase. This can be rationalized by the electrostatic potential [$V_s(\mathbf{r})$] at the adsorption sites where the axial atoms have larger $V_{s,\max}$ in comparison to the equatorial atoms (**Figure 12**). Areas of negative electrostatic potential ($V_{s,\min}$) are found in the bridge and hollow sites in between the atoms. This is in line with the tendency of H_2O H-down and H_{ad} interactions at these sites as identified in both **Paper I** and **II**. Adsorption of up to four, and possible five, H_2O atoms was found exergonic ($\Delta G < 0$) onto Cu_7 in **Paper I**, all at equatorial sites. H_2O was, furthermore, found to preferentially adsorb onto another H_2O rather than onto the axial Cu atom thereby suggesting that the axial sites are hydrophobic. This picture was, however, slightly altered in **Paper II**; during the course of the MD simulations, H_2O binds O-down towards one of the axial atoms but H-down in the vicinity of the other axial Cu. The Cu-O interaction at the axial atom is, nevertheless, somewhat longer than at the equatorial sites. Although H_2O may thus bind O-down towards the axial Cu sites, the conclusion remains that axial sites are less prone to interaction with H_2O than the equatorial. Additional features of the H_2O - Cu_7 interaction that could be identified from the MD simulations in **Paper II** are the abovementioned H-down interactions and the observation that more than one H_2O can fit to the same equatorial adsorption site.

The Cu_7 - H_2O interaction behavior was further analyzed by the use of time-averaged statistics from the MD simulations. **Figure 14.a** shows the radial distribution function (RDF) for the Cu-O and Cu-H distances averaged over the final 5 ps of the QM-MD simulation of Cu_7 . The first peaks of the RDF show that the O-Cu interactions with Cu are, on the average, closer than the H-Cu interactions. O stays within a fairly limited distance whereas H seems to fluctuate over larger bonding distances, indicating a weaker bond for H-down adsorption than for O-down. The first RDF peak was used to define the first solvation shell – all molecules that have an O (or an H) in the first RDF peak are considered to belong to the first shell. The second shell is not clearly defined because of the diffuse second RDF peak. Instead the second shell was taken as the H_2O molecules at H-bonding distance (here $< 2\text{\AA}$) from the first shell. **Figure 14.b** shows the number of H_2O molecules in the first and second solvation shell of Cu_7 over the course of the simulation yielding on the average 12 H_2O molecules in the first shell and 38 in the second. Similar analysis where performed for the remaining, hydroxylated Cu_7 -clusters. Analysis of the root mean square deviations of the positions of the O atoms in the two solvation shells indicate that the second shell is more mobile and less tightly bound than the first shell. It also indicates that the mobility of the solvation shell becomes reduced as the degree of surface hydroxylation of the Cu-cluster is increased indicating stronger OH_{ad} - H_2O and H_2O -Cu(I) bonds than H_2O -Cu(0) bonds.

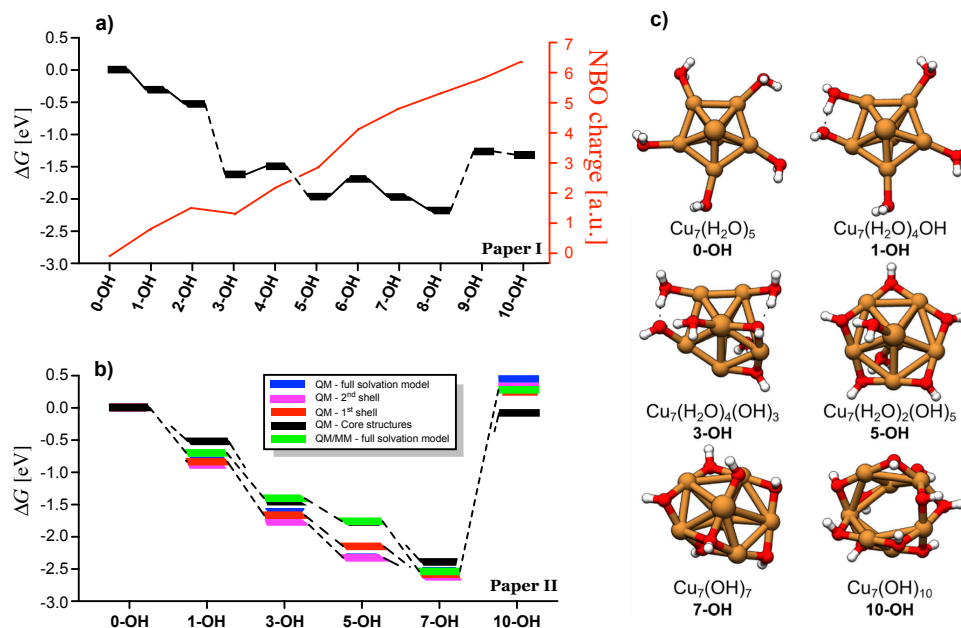
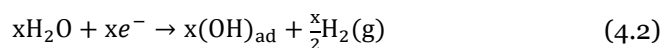
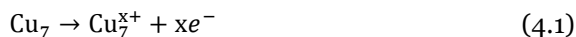


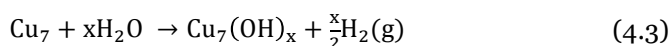
Figure 15. Included in a) are the Gibbs free energy variations for the aqueous oxidation of Cu_7 as reported in **Paper I** for the case of IEF-PCM solvation. Shown is also the increase in NBO charge of the Cu_7 core with the level of oxidation. In b) are the Gibbs free energy for the Cu_7 oxidation shown for the different considered water solvation models from **Paper II**. Figure c) displays a selection of hydroxylated Cu_7 core structures identified in **Paper I** and used in both studies. A hydrogen gas pressures corresponding to the annual mean tropospheric partial pressure¹⁴² of 0.531 μbar . Figure b) and c) are reproduced with permission from Stenlid et al.¹⁵¹ Copyright 2016 American Chemical Society.

Thermodynamic limit of oxidation

The aqueous oxidation of the Cu_7 cluster is described by the redox reactions:



That is combined to the total reaction:



In **Paper I**, the step-wise oxidation reactions was investigated^{xxxii} for structures comprising $x=0,1,2,\dots,10$ (see **Figure 15.c.** for a selection of these *core structures*). This yielded the results presented in **Figure 15.a** for the aqueous oxidation of Cu_7 . Here the overall conclusion was that the oxidation stops at a state corresponding roughly to a Cu(I)OH species, more precisely $\text{Cu}_7(\text{OH})_8$. From NBO analysis, the charge of the Cu_7 core can be seen to grow increasingly more positive with the surface hydroxylation in an essentially linear relation. We can also note an odd-even oscillation in the energies. This is a common feature in NP science and can here be traced to the electronic structure of the clusters. The low-energy structures of odd OH numbers correspond to a favorable closed shell singlet electronic structure, while the even numbers have a doublet multiplicity.

A prevailing question after **Paper I** was whether or not the employed solvation model with 5-10 explicit water/hydroxyl groups and implicit IEF-PCM solvation is accurate enough to support the conclusions regarding the Cu_7 oxidation? This was investigated in **Paper II**. As outlined above, the solvation model was increased by adding up to a total of 77 H_2O molecules [or $(77-x)\text{H}_2\text{O} + x\text{OH}$] in **Paper II** for a selection of the hydroxylated Cu_7 core structures of **Paper I**. This comprised the structures with $x\text{OH}_{\text{ad}}$, $x=0, 1, 3, 5, 7$, and 10. Low-energy structures from the QM-MD and QM/MM-MD simulations were extracted and relaxed.^{xxxiii} For the QM-MD, structures of the first and second solvation shell were also cut out and relaxed. Final energies were determined^{xxxiv} and compared with each other and to the results of **Paper I** as is shown in **Figure 15.b**. The conclusions are that the main trends for the aqueous oxidation of Cu_7 are captured at all the considered levels of theory and solvation;^{xxxv} namely that the oxidation is favorable up until a Cu(I)OH species. However, there are some clear differences in the details between the implicit and explicit solvation models, in particular regarding the more hydroxylated states. For these states the hydrogen

^{xxxii} At the PBE0/LACV3P**++//LACVP*+ level of theory^{225,351,352} in gas phase and condensed phase with IEF-PCM solvation in Go9.³²⁹

^{xxxiii} The QM/MM structural optimizations were carried out in GAMESS^{332,333} at the PBE0/LACVP*+ level of theory^{225,350} for the QM region (including the *core structures* of **Figure 15**) and ECP1 (H_2O -DFT)²⁴⁴ for MM region embedded in IEF-PCM solvation. For the full QM calculations PBE0 with Grimme's D3²³³ dispersion corrections and Becke-Johnson damping (BJ) were used, employing the RIJCOSX algorithm and the def2-SVP/J basis set including Los Alamos ECP in Orca.³²⁹

^{xxxiv} The QM/MM final energies were obtained at the QM PBE0/LACV3P**++ and MM ECP1 (H_2O -DFT) level^{225,350,351} with IEF-PCM solvation in GAMESS.^{332,333} The final energies for the full QM structures PBE0-D3(BJ)/def2-TZVP (COSMO) level in Orca.³²⁹

^{xxxv} Also the gas phase calculations of **Paper I** results in the same favored oxidation state.

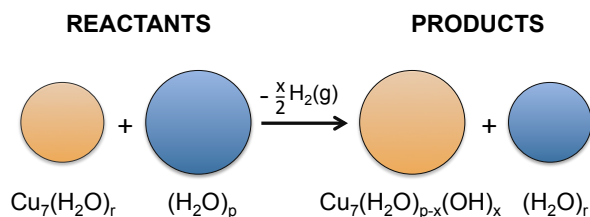


Figure 16. Cluster size consistency concept for the oxidation reaction between clusters of $\text{Cu}_7(\text{OH})_x(\text{H}_2\text{O})_{n-x}$ clusters of different sizes. Reproduced with permission from Stenlid et al.¹⁵¹ Copyright 2016 American Chemical Society

bonding of the explicit solvent molecules cannot be fully captured by the continuum models. Thus the recommendation for the study of similar systems comprising TM-based nanomaterial is to use a mixed cluster/continuum model including an explicit first solvation sphere.

A note of caution should, however, be included for the use of solvation shell structures. For the first and second shell structures of **Figure 15**, the number of water molecules included in the shells for the different states of oxidation varies. The differences introduced a problem in the evaluation of the relative energies for the oxidation process of **Figure 15.b**. This since implicit models are known to treat large H-bonding systems on an unequal footing due to the structural flexibility³⁴⁹ of the system. Accordingly a new concept was developed to account for the size-differences of the clusters. This is referred to as the *cluster size consistence* (CSC) concept, see **Figure 16**. Here a reference $(\text{H}_2\text{O})_n$ ($n=p$ from the product Cu cluster, and $n=r$ for the reactant) cluster is introduced on each side of the reaction where the size of the $(\text{H}_2\text{O})_n$ cluster is chosen as to match the size of the $\text{Cu}_7(\text{OH})_x(\text{H}_2\text{O})_{n-x}$ cluster on the other side. Thereby the number of atoms is kept constant over the reaction, as is the number of clusters of the same size. Note that the non-hydroxylated $\text{Cu}_7(\text{H}_2\text{O})_r$ cluster is always chosen as references reactant in this work, meaning that a $(\text{H}_2\text{O})_r$ cluster will always be added on the product side.

Concerning the potential connection between the aqueous oxidation behavior of the Cu_7 nanocluster and the experimentally proposed copper corrosion under anoxic corrosion discussed in section 2.2.5, some comments are included below. The central question is: can nanosized copper explain the observations of elevated H_2 partial pressures (orders of magnitude larger than the equilibrium pressure) upon immersion of metallic Cu(s) in anoxic water?

The Cu_7 nanoparticle reaches a favored oxidation state of Cu(I) in water as discussed above. Similar DFT studies of water on e.g. the Cu(110) surfaces find that also surfaces are hydroxylated but only to the extent that a mixed 50:50 OH/ H_2O ML is formed on Cu(110).^{154–156} This can be translated to a mixed

Cu(I)/Cu(O) state of the outermost copper atoms. Thus Cu₇ yields a more oxidized state than is predicted for metallic copper. This can be used in the assessment of copper corrosion by the hypothesis that n Cu surface layers are converted to dispersed hydroxylated Cu(I) NP, hence assuming that Cu₇ can represent all copper NPs.

From the reported hydrogen pressures and the experimental specifics of Hultquist et al.,¹⁴⁸ one arrives at a Cu(I)OH-NP concentration of ~6 mgL⁻¹. This is based on the consumption of 20 Cu(110) ML of copper as discussed in connection to the introduction of the *surface hypothesis* in section 2.2.5. We can compare this to the recently reported ~6 µgL⁻¹ Cu content in pure anoxic water for a sample in contact with copper foils for 29 months.¹⁶² Based on this comparison, nanoparticles are unlikely to have major contribution to the possible production of H₂ gas upon immersion of copper in pure O₂-free water. Similar conclusions have been reached in other studies.¹⁷⁹

Mechanism of oxidation

In the evaluation of the oxidation thermodynamics above, it was assumed that the kinetics is not a limiting factor. This assumption was controlled in **Paper I** for the first cycle of H₂O dissociation, surface hydroxylation and H₂ evolution (see **Figure 17.a**). It was found that the reaction kinetics is very slow with a ΔG^\ddagger barrier of ~1.2 eV in condensed phase. This is for the case when only one explicit assisting H₂O molecule is considered. The barrier is, however, lowered to ~1.0 eV when a second H₂O molecule assist in the dissociation (**Figure 17.b**), which is still a rather slow reaction at room temperature but of the same magnitude as reported barriers on copper surfaces.^{76,163,355,356} We can therefore conclude that reaching the equilibrium in aqueous oxidation of copper is most likely a slow process.

H₂O dissociation was identified as the rate-limiting step. Using NBO analysis,³⁵⁷ we were able to characterize this is a redox step: an electron is transferred from the Cu₇ cluster to the H_{ad}+OH_{ad}⁻, i.e. the products of the dissociated H₂O molecule. In the full formation of H₂(g) and 2OH_{ad}⁻ from the dissociation of two H₂O molecules, the second H₂O dissociation occurs by the direct association of the H of the dissociating H₂O with an adjacent H_{ad}. Again NBO analysis was used to aid in the rationalization; whereas the H_{ad} in fact can be seen as a hydride radical with a slightly negative charge, H in H₂O has a positive NBO charge. These two attract each other giving rise to a second redox reaction where an electron is abstracted from Cu₇ to yield H₂ that desorbs as H₂(g). Thus,

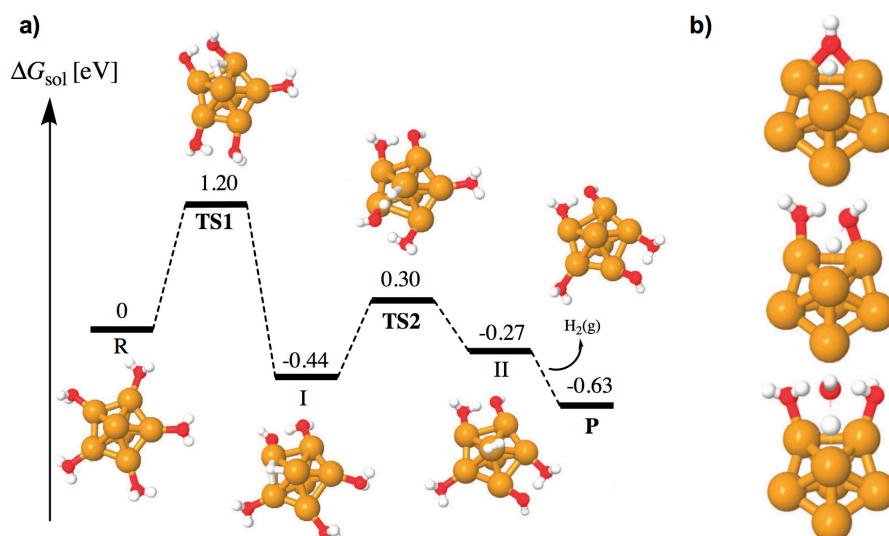


Figure 17. In a): Full mechanism^{xxxvi} for the first cycle of H₂O dissociation, surface hydroxylation and H₂ evolution on the Cu₇ cluster model assuming the annual mean tropospheric H₂ pressure¹⁴² of 0.531 μbar. Note that more details are included in the original paper (**Paper I**). In b): Comparison of the TS structure for the rate-limiting step of H₂O dissociation assisted by zero (top), one (middle) and two (bottom) H₂O molecules. Colors: Cu in orange, O in red and H in white. Readopted from Stenlid et al.¹⁵⁰

altogether, gaseous H₂ and a Cu₇²⁺ nanocluster 2OH_{ad} are formed. The second step has a lower barrier than the first step, ~0.7 eV, which can be reduced to ~0.4 eV by the assistance of additional H₂O molecules.

4.1.2. The surface structure and properties of Cu₂O

The atomic structure and composition of surfaces largely dictate their properties. Even small structural differences can have significant impact. The clearest example is perhaps the dissimilar properties of surfaces cut at different crystallographic planes of the same material. The low-index (111), (110), and (100) surfaces of copper for instance have different redox properties and do not share the same electrochemical work functions nor chemical activity. Even for the same surface facet minor differences in atomic composition can change the chemical

^{xxxvi} Investigated at the PBE0/LACV3P^{***}+/LACVP*+ level of theory^{225,351,352} with IEF-PCM solvation in Go9.³²⁹

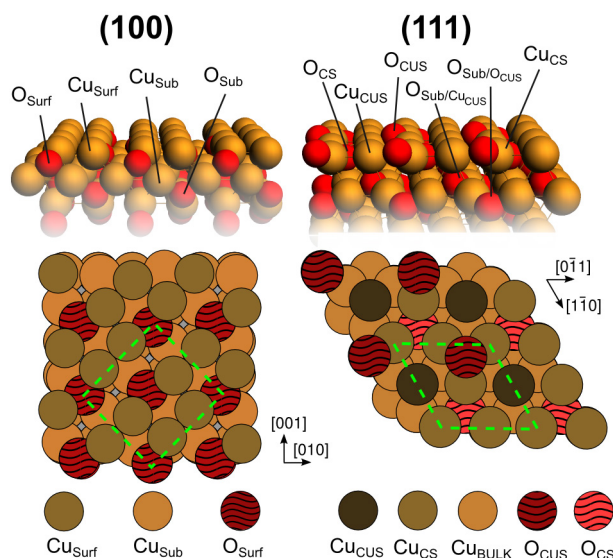


Figure 18. Surface structures of the unreconstructed Cu-terminated $\text{Cu}_2\text{O}(100)$ and stoichiometric $\text{Cu}_2\text{O}(111)$ surface facets. Reprint from Stenlid et al.¹⁵³

properties of the surface largely. An example of the latter is the $\text{Cu}_2\text{O}(111)$ surface studied to some extent in this thesis (**Paper V-VI**). For this surface the presence or absence of a single atom type (Cu_{CUS} , *vide infra*) on the surface will e.g. significantly alter its molecular adsorption affinities, catalytic efficiency and wettability. This part of the thesis will primarily address the surface termination of the $\text{Cu}_2\text{O}(100)$ surface facet based on the investigation in **Paper III**, with a short account of the (111) surface.

Figure 18 shows the unreconstructed surface structures of the Cu-terminated $\text{Cu}_2\text{O}(100)$ and the stoichiometric $\text{Cu}_2\text{O}(111)$ surface facets. These will serve as starting points in the following discussion. Both surface facets have previously been studied extensively, experimentally as well as computationally, in vacuum or under the exposure to molecular species. Computational studies suggest that $\text{Cu}_2\text{O}(111)$ is the most stable low-index Cu_2O surface.^{358,359}

Before discussing our results from **Paper III** on the surface structure of the Cu-terminated (100) facet of Cu_2O , the current knowledge concerning the $\text{Cu}_2\text{O}(111)$ facet's structure and composition will be briefly addressed. Experimentally, a $(\sqrt{3} \times \sqrt{3})R30^\circ$ reconstruction is the most commonly observed surface phase under UHV (ultra-high vacuum) structure mixed with (1×1) minority areas.³⁶⁰ The ideal and stoichiometric (1×1) surface contains coordinatively saturated (CS) and unsaturated (CUS) Cu and O atoms; a layer of

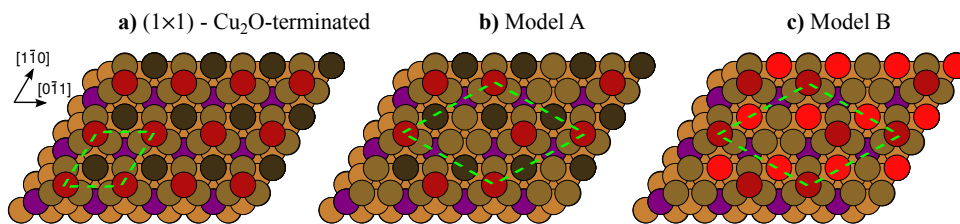


Figure 19. Surface structure of the $\text{Cu}_2\text{O}(111)$ facet. Included in a) is the stoichiometric (1×1) structure [note that the Cu_{CUS} -vacant (1×1) structure is formed by removing all Cu_{CUS} atoms]. In b) is the model A and in c) is the model B $(\sqrt{3} \times \sqrt{3})R30^\circ$ surfaces shown. Coloring: Cu_{CUS} (dark brown), Cu_{CS} (beige), bulk Cu (orange), O_{CUS} (deep red), O_{CS} (purple), and bulk O (bright red). Reproduced from Besharat et al.,³⁵⁹ with permission of AIP Publishing

Cu_{CUS} and Cu_{CS} atoms are sandwiched between the outermost O_{CUS} and lower-lying O_{CS} atoms. The unsaturated atoms are believed to play a crucial role in the catalytic activity of Cu_2O .³⁶¹ The presence or absence of unsaturated atoms on the $\text{Cu}_2\text{O}(111)$ surface under different conditions is, however, a matter of ongoing investigation and different surface models for the (1×1) and $(\sqrt{3} \times \sqrt{3})R30^\circ$ domains have been suggested. Whereas the $(\sqrt{3} \times \sqrt{3})R30^\circ$ pattern is generally attributed to $\frac{1}{3}$ ML O_{CUS} vacancies, 1 ML Cu_{CUS} -vacant models have been considered for both the (1×1) and $(\sqrt{3} \times \sqrt{3})R30^\circ$ surface domains. In summary, these four models are plausible (see also **Figure 19**):

- Stoichiometric (1×1)
- Cu_{CUS} -vacant (1×1)
- Model A = $(\sqrt{3} \times \sqrt{3})R30^\circ$ with $\frac{1}{3}$ ML O_{CUS} vacancies
- Model B = $(\sqrt{3} \times \sqrt{3})R30^\circ$ with $\frac{1}{3}$ ML O_{CUS} and 1 ML Cu_{CUS} vacancies

Computational studies using GGA functionals suggest that the Cu_{CUS} -vacant (1×1) surface structure is favored for all reasonable oxygen pressures.^{358,359} Employing more elaborate hybrid (HSE06^{230,231,362,363}) functionals, Nilius et al.³⁶⁴ have revised this picture by suggesting that the stoichiometric (1×1) surface becomes more stable than the Cu_{CUS} -vacant under oxygen lean conditions. Final consensus is, nonetheless, yet to be reached with regards to the composition and structure of the (111) facet of Cu_2O . The final answer, if ever found, may well be a mixed composition. Some indications on the possible surface structure are provided in **Paper VI** from the study of methanol adsorption and decomposition.

For the $\text{Cu}_2\text{O}(100)$ surface facet, a Cu-terminated structure is anticipated under oxygen lean conditions, whereas an ideal O-terminated (1×1) structure is adopted at elevated oxygen partial pressures (**Figure 20.d**). The Cu-terminated surface was given most attention in the papers of this thesis. Depending on the

preparation procedure, the surface reconstructs under oxygen lean ultra high-vacuum conditions forming ordered (1×1) and $c(2\times 2)$ structures. The dominating phase is, however, a phase that was previously interpreted³⁶⁵ as an oblique $(3\sqrt{2}\times\sqrt{2})R45^\circ$ [consisting of two 90° rotational domains of a $(1,0;1^{1/2},1^{1/2})$ matrix] structure. The latter structure was revised in **Paper III** providing clear evidence of a surface structure with a $(3,0;1,1)$ [matrix notation] unit cell with two 90° rotational domains based on both low-energy electron diffraction (LEED) and scanning tunneling microscopy (STM). The atomic arrangement and composition of the $\text{Cu}_2\text{O}(100)$ facet was investigated by DFT in **Paper III** in comparison to the experimental data, which also included X-ray photoemission spectroscopy (XPS) results.

Figure 20.a-e shows a selection of different surface terminations of $\text{Cu}_2\text{O}(100)$ considered in **Paper III**. Firstly, the unreconstructed (1×1) surface was optimized^{xxxvii} in the normal direction only, yielding a minor contraction and

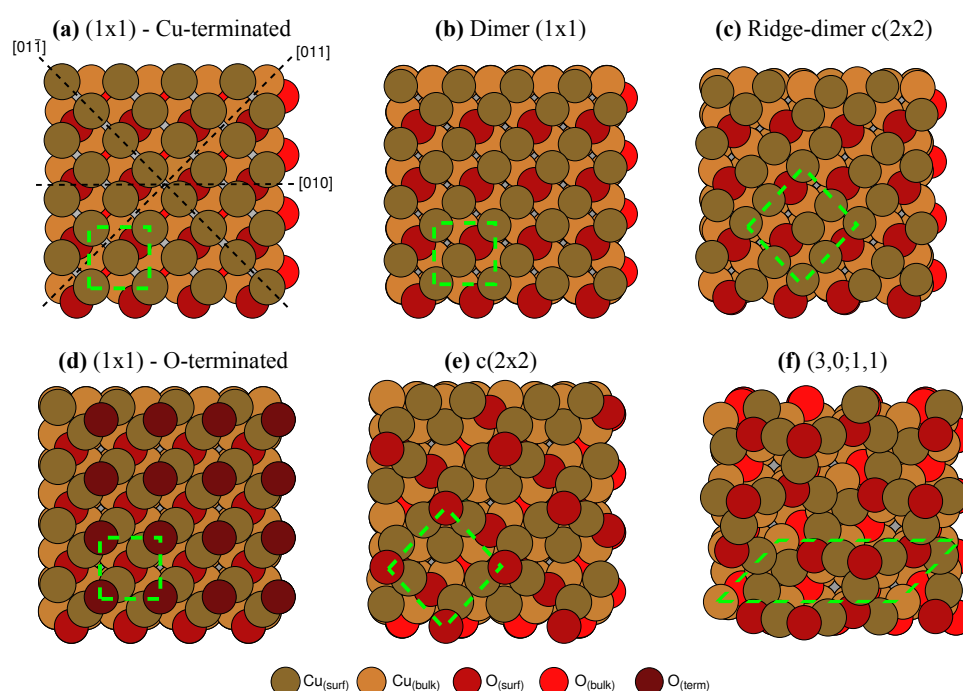


Figure 20. Showing different surface terminations of $\text{Cu}_2\text{O}(100)$. Reproduced with permission from Soldemo et al.³⁶⁶ Copyright 2016 American Chemical Society.

^{xxxvii} The calculations were carried out at the PBE-D3(BJ)+U level of theory^{221,233,354} using periodic slab models in the VASP^{338–342} software package.

Table 1. Surface energies (γ) and dipole moments (μ) for different Cu-terminated $\text{Cu}_2\text{O}(100)$ surface structures.

Unit cell	Structure	γ [eV \AA^{-2}]	μ [mD \AA^{-2}]
(1 \times 1)	unrelaxed ^{a)}	0.089	15.0
(1 \times 1)	contracted ^{b)}	0.088	(-) ^{c)}
(1 \times 1)	dimer ^{d)}	0.075	14.0
c(2 \times 2)	ridge-dimer ^{e)}	0.073	12.0
c(2 \times 2)	low-energy ^{f)}	0.071	10.3
(3,0;1,1)	low-energy ^{f)}	0.071	7.2

^{a)} As cut from the crystal structure, ^{b)} relaxed in the surface normal direction, ^{c)} Not computed. ^{d)} Cu^+-Cu^+ dimers in the [011] direction, ^{e)} Cu^+-Cu^+ dimers in the [011] and [01 $\bar{1}$] direction, ^{f)} identified from simulated annealing MD.

energy gain. Upon lifting of the lateral constraints this surface relaxes to form Cu^+-Cu^+ dimers in the [011]-direction. Further relaxation of the Cu^+ ions was observed upon also lifting the structural symmetry. This led to dimerization also in the [01 $\bar{1}$]-direction yielding the *ridge-dimer* c(2 \times 2) structure of **Figure 20.c**. The Cu-terminated $\text{Cu}_2\text{O}(100)$ surface is polar and it was found that the reconstruction is largely driven by a lowering of the surface dipole moment. Going from the unreconstructed (1 \times 1) to the dimer and ridge-dimer structures, the dipole moment decreases gradually accompanied by a reduction of the surface energy as reported in **Table 1**. Structures of even lower energy could be identified from simulated annealing (SA-MD) simulations where the temperature was varied in three steps; initial ramping from 0 K to 800 K, followed by a period of constant 800 K before slowly reducing the temperature to 300 K. This led to the identification of considerably less ordered structures for the c(2 \times 2) and (3,0;1,1) unit cells, but with reduced dipole moments and lowered surface energies. The SA-MD (3,0;1,1) structure is the structure of lowest surface energy of all the considered structures closely followed by the SA-MD c(2 \times 2) structure. However, the differences in surface energy between the SA-MD structures and the dimer structure are small enough to allow for the lifting of the surface reconstruction back to more ordered surface stabilized by adhered (polar) molecular adsorbents (see section 4.1.3), and for the coexistence of different surface phases of different structures at elevated temperature, as observed experimentally.

STM images were simulated and XPS core-level shifts calculated for the different surfaces according to the procedures outlined in section 3.3.2 and 3.3.3. **Figure 21** includes the resulting simulated and experimental STM-images for the oxygen covered surface and the low-energy SA-MD structures. The simulated and experimental images are in good agreement. The experimental O 1s XPS spectrum

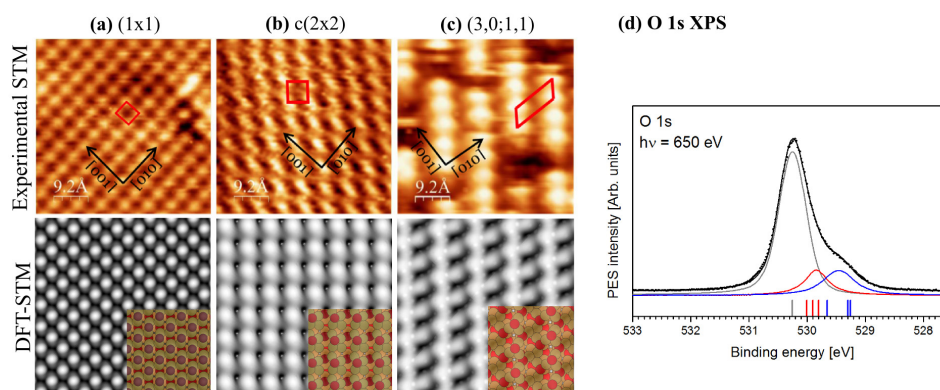


Figure 21. Experimental and simulated STM images for the O-terminated $\text{Cu}_2\text{O}(100)$ surface in a), the low-energy $c(2\times 2)$ and $(3,0;1,1)$ SA-MD surfaces in b) and c). d) shows a XPS spectrum of the $\text{Cu}_2\text{O}(100)$ with fitted bulk (black) surface (blue) and subsurface (red) components from DFT. Reproduced with permission from Soldemo et al.³⁶⁶ Copyright 2016 American Chemical Society.

in **Figure 21** shows a shoulder at lower binding energies originating from the surface atoms. Our calculated core-level shifts suggest that the shoulder has contributions from surface and subsurface atoms in a second layer. The structures identified in **Paper III** are used as templates for molecular interactions in **Paper IV-VI**.

4.1.3. Molecular interactions at the Cu_2O surface

The molecular interactions behavior of cuprite is central to e.g. its catalytic performance, but also in relation to the corrosion behavior of copper. This since cuprite is one of the most common corrosion products of copper.⁷¹ As discussed in section 2.2, corrosion processes will result in an oxide film on the surface of copper waste canister surface during the initial phase of the proposed enclosure of the SNF in Sweden. The study of the copper oxide is also of importance for the debate of whether or not copper corrodes in oxygen free, in particular since Hultquist et al.^{119,120,148} report the use of an ‘as received’ copper foil in their experiments (see section 2.2.5), which implies an oxide covered surface. Accordingly it is of importance to characterize the $\text{Cu}_2\text{O}\text{-H}_2\text{O}$ interface to gain a better understanding of the corrosion behavior of the copper canister. $\text{Cu}_2\text{O}\text{-H}_2\text{O}$ interactions at the (100) and (111) surface facets of Cu_2O are addressed in **Papers IV-V**. **Paper VI** discusses the interaction of the methanol molecule on the same surfaces. Water and methanol behave similarly at the surfaces in many aspects. Comparison between the two molecules favors the general understanding of the Cu_2O surfaces’ atomic structures and chemical properties.

Water

The structure and composition of the water interface of the Cu-terminated Cu₂O(100) are studied in detail by the combination of DFT^{xxxviii} and O 1s XPS in **Paper IV**. Both methods suggest that H₂O partly dissociates upon surface adsorption. It was found that a mixed H₂O-OH adsorption layer forms at larger H₂O coverage and a pure OH layer at lower total coverage; from the XPS data the amount of H₂O and OH at the surface was deduced as a function of temperature, see **Figure 22**. H₂O and OH coexist at the surface at low temperatures and a maximal OH coverage of 0.43 ML^{xxxix} is reached at 178 K.^{xl} At the same temperature all H₂O molecules have become evaporated. The clean surface is recovered and all OH are desorbed at 573 K. Most likely the desorption of OH take place via either OH_{ad} disproportionation [$4\text{OH}_{ad} \rightarrow 2\text{H}_2\text{O}(\text{g}) + \text{O}_2(\text{g})$] or by OH_{ad} reassociation vid surface residing H_{ad} [$\text{OH}_{ad} + \text{H}_{ad} \rightarrow \text{H}_2\text{O}(\text{g})$]. The identified maximum surface hydroxylation of 0.43 ML is larger than the maximum 0.1 ML previously suggested by a 1991 study of Cox and Schulz.³⁶⁷ We note, however, that the data of Cox and Schulz does not contradicts our results, but that they arrive at another interpretation possible due to the usage of less refined analysis methods.

H₂O interaction with Cu₂O(100) lifts its vacuum (3,0;1,1) reconstruction to generate a close to unreconstructed (1×1) surface structure. The unreconstructed surface is stabilized by OH_{ad} and H_{ad} positioned in the Cu⁺-Cu⁺ bridge positions, which are the natural positions for O atoms in the extended crystal structure. The OH_{ad} and H_{ad} interactions with Cu⁺ prevent Cu⁺-Cu⁺ dimerization. H₂O also prefers to sit in the Cu⁺-Cu⁺ bridge positions. In contrast to the case of OH_{ad} and H_{ad}, the surface underneath H₂O adopts the Cu⁺-Cu⁺ dimer structure of the c(2×2)-reconstructed surfaces in **Figure 20**, why the Cu₂O(100) substrate surface can be described as a mixed (1×1)/c(2×2) structure underneath a mixed H/OH/H₂O adsorption layer (see **Figure 23**).

Furthermore, H₂O adsorption and dissociation on Cu-terminated Cu₂O(100) coupled to H₂(g) formation were studied by DFT as outlined in **Figure 24**. It was found that dissociative H₂O adsorption to OH_{ad}+H_{ad} is favored over molecular adsorption at low total surface coverage (0.25 ML). Continued

^{xxxviii} The calculations were carried out at the PBE-D3(BJ)+U level of theory^{221,233,354} using periodic slab models in the VASP^{338–342} software package. Comparisons to the results with the pure PBE, PBE-D3 (without +U) and hybrid HSE06-D3^{230,231,362,363} were performed with the conclusion that the same overall trends are obtained at the different levels of theory.

^{xxxix} A monolayer (ML) is here defined as one H₂O per surface Cu atom.

^{xl} Upon annealing of a surface dosed with 3 L (L = 1 s × 10⁻⁶ torr) of water at 100 K.

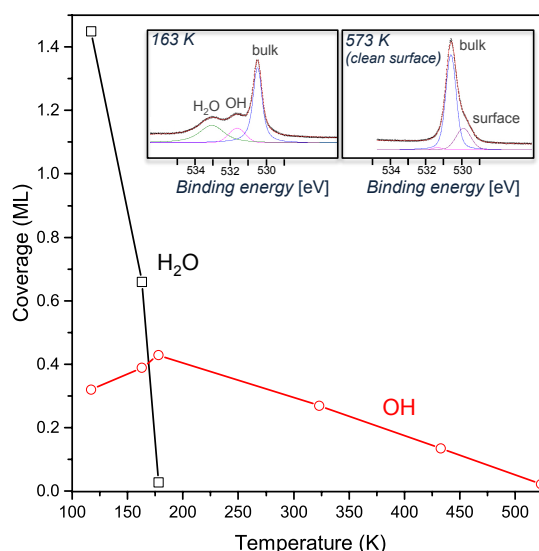


Figure 22. H₂O and OH coverage as a function of temperature estimated from XPS O 1s-data in **Paper IV**. Insert shows XPS O 1s spectra at different temperatures. Based on spectra obtained at 3 L H₂O dose ($L = 1\text{ s} \times 10^{-6}$ torr) at 100 K and subsequent annealing at the indicated temperatures (squares and circles). Note that the surface reconstruction shoulder seen at 573 K is not present on the H₂O/OH covered surface indicating that the adsorbate lifts the surface reconstruction. Adopted from Stenlid et al.¹⁵² with permission from the PCCP owner societies.

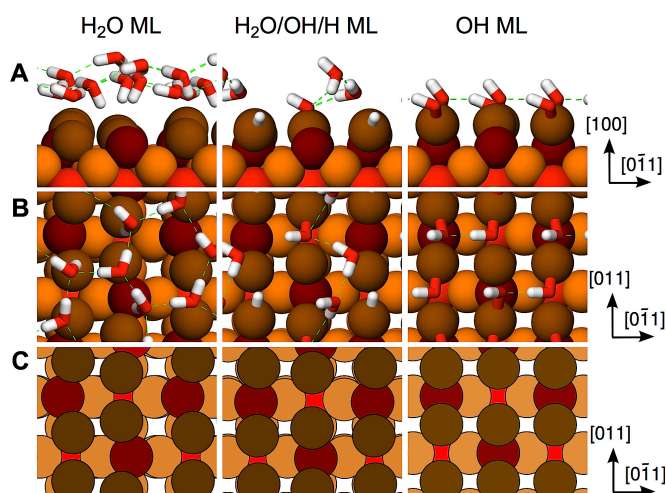


Figure 23. Surface and adsorbate structures. As a water ML is adsorbed and dissociated, the Cu₂O(100) substrate surface reconstruction is lifted. Reproduced from Stenlid et al.¹⁵² with permission from the PCCP owner societies.

dissociation to O_{ad} and $2H_{ad}$ [or to $H_2(g)$] is, however, disfavored. At intermediate coverage (0.25 and low temperatures, a mixed H_2O -OH state with surface H_{ad} is slightly more exergonic than formation of a purely hydroxylated state (i.e. 0.5 ML OH_{ad}) accompanied by $H_2(g)$ generation (Assuming the annual tropospheric mean H_2 partial pressure of 0.531 μ bar.¹⁴²). Higher temperatures and low H_2 partial pressures favor the hydroxylated state, in agreement with the XPS results.

For larger total surface coverage (up to 1 ML) we concluded that the continued dissociation, beyond 0.25 ML OH coverage at low temperatures and 0.5 ML OH_{ad} at elevated temperatures, is disfavored. This can be rationalized in terms of i) a surface over-crowding (i.e. lack of adsorption positions) when forming additional OH_{ad} and H_{ad} , ii) Coulombic repulsion by adjacent OH_{ad} groups and iii) by favorable H-bond interactions with adsorbed H_2O . Thus the DFT results (see insert of **Figure 24**) suggest a degree of surface hydroxylation of 0.25-0.5 ML, comparing well with the experimental results. The H_2O adsorption behavior onto a clean Cu-terminated $Cu_2O(100)$ surface can thus be described as dissociative up to 0.25-0.5 ML of OH depending on the ambient conditions, and molecular at larger coverage.

The possibility of OH coverage below 0.25 ML was considered by the use of a larger surface unit cell [$p(2\times 2)$] that allowed for a finer discretization of the surface states (see **Figure 25**). This resulted in the same favored dissociation states of 0.25-0.5 ML OH_{ad} as for the small unit cell [$c(2\times 2)$]. **Figure 25** also shows the Gibbs free energy for the various surface states when considering the effects of a second H_2O layer of water on top of the adsorption layer, forming a bilayer structure (BL). Although the BL acts stabilizing on the surface structures, and more so for the more hydroxylated states, the conclusion from above that the surface is covered by 0.25-0.5 ML OH_{ad} prevails. We further note that this is similar to the favored 0.4-0.5 ML OH_{ad} identified on the $Cu(110)$ surface.¹⁵⁴

The $Cu_2O(111)$ - H_2O interface was also studied in this thesis. **Paper V** contains result for the low coverage H_2O adsorption to the stoichiometric (1×1) $Cu_2O(111)$ surface indicating that dissociation is not favorable. In contrast, experiments for the $Cu_2O(111)$ surface with identical set-up to those discussed for the $Cu_2O(111)$ surface above suggest an approximate 0.25 ML of surface hydroxylation upon exposure to H_2O .¹⁷⁰ This is, in broad, consistent with the dissociation of one H_2O per O_{CUS} vacancy of a $(\sqrt{3}\times\sqrt{3})R30^\circ$ surface leading to OH_{ad} and H_{ad} another surface O_{CUS} . Since the surface structure is expected to be dominated by $(\sqrt{3}\times\sqrt{3})R30^\circ$ domains, it is reasonable that the stoichiometric (1×1) surface does not capture the experimental results.³⁶⁰ Nevertheless, (1×1) minority domains are always present on the surface, and the (1×1) domain is possible dominant under certain conditions. Therefore the results of **Paper V** are still largely relevant.

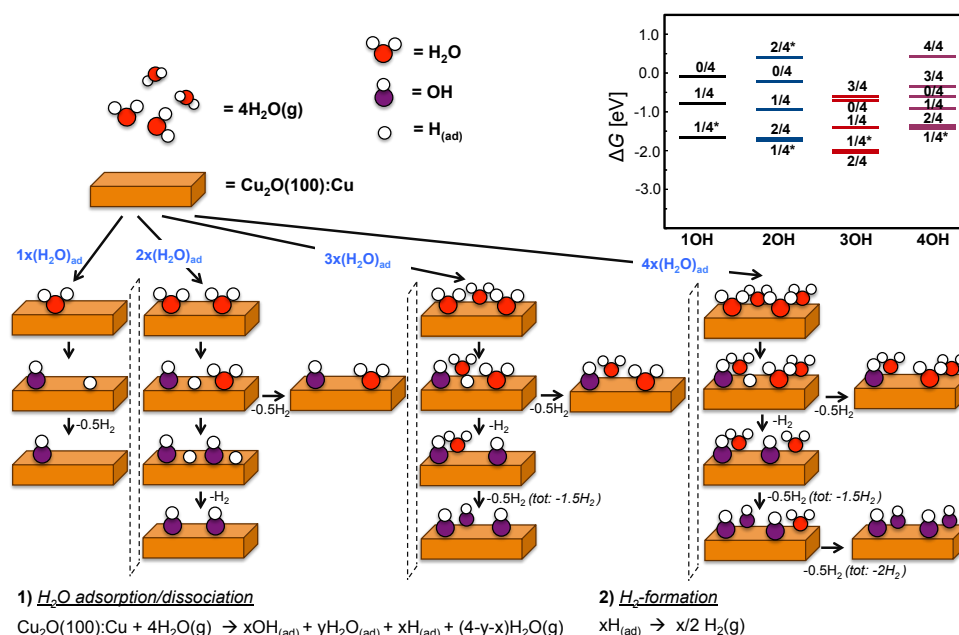


Figure 24. Sketch over the H_2O adsorption and dissociation interactions considered in **Paper IV**. The insert in the top right corner shows Gibbs free energies of the considered states at 298.15 K and $p_{H_2}=0.531 \mu\text{bar}$ (i.e. the tropospheric annual mean¹⁴²). Adopted from Stenlid et al.¹⁵² with permission from the PCCP owner societies.

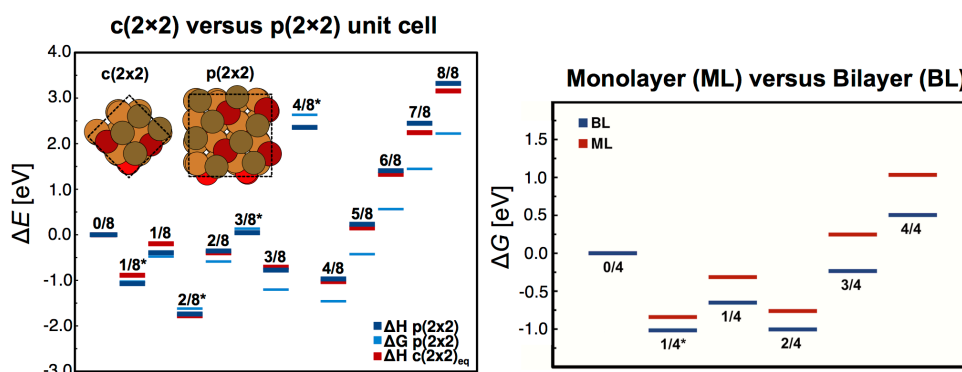


Figure 25. Shows water adsorption and dissociation Gibbs free energies ($E=G$) and reaction enthalpies ($E=H$) at 298.15 K and $p_{H_2}=0.531 \mu\text{bar}$ (i.e. the tropospheric annual mean¹⁴²) on the $Cu_2O(100)$ surface. To the left is the reaction evaluated on the $c(2 \times 2)$ and the larger $p(2 \times 2)$ unit cells compared. The right figure compares the reaction free energies obtained for monolayer and bilayer OH/ H_2O structures. The asterisk (*) marks a H_{ad} dissociation product, whereas $H_2(g)$ is otherwise assumed. Adopted from Stenlid et al.¹⁵² with permission from the PCCP owner societies.

Methanol

Methanol adsorption and dehydrogenation at the (100) and (111) facets of Cu₂O were investigated in **Paper VI**. XPS, sum-frequency generation spectroscopy (SFG) and DFT studies^{xli} were combined. The main DFT results are summarized in **Table 2**. Experimentally it is found that the (111) leads to further methanol dehydrogenation than the (100) surface. This can also be expressed as a larger selectivity for formaldehyde formation on the (100) surface and an increased formation of CO and CO₂ on the (111) surface. The differences can be understood from the surface structures, and the larger diversity of surface sites and the availability of surface O atoms to store H_{ad} on the (111) surface.

The molecular adsorption energy for methanol was found to be of similar magnitude on both surface facets. The initial dissociation of the RO-H bond is, however, considerably more exothermic on the (100) facet compared to the (111), although more extended dehydrogenation is overall more beneficial on the (111) surface as explained below. These results are analogous, energetically and structurally, to the case of water adsorption and dissociation on the same surface facets (see e.g. **Paper IV** and **V**). Similar to the case of water, methanol lifts the surface reconstruction of the (100) facet. Formation of formaldehyde from methoxy is weakly endothermic but attainable at elevated temperatures on both surfaces. On the (100) surface, the continued dehydrogenation beyond formaldehyde is hampered by the lack of sites to store H_{ad} (extrapolating to a high coverage scenario from the studied low coverage) and by a relatively strong Cu-H bond that slows down H₂ formation leading to overcrowding of the surface. On the (111) surface, the situation is different and the O_{CUS} atoms (and possible O atoms exposed at the Cu_{CUS} vacancy) serve as effective transient adsorption sites for H_{ad} before formation of H₂ (or H₂O) and subsequent desorption, as suggested by the XPS data. Where available, calculated and experimental core-level shifts could be linked for the surface structures as discussed in detail in the original text of **Paper VI**. See adsorption structures in **Figure 26**.

Our results can further be used to (possibly) shed some light on the puzzle of the Cu₂O(111) surface structure (section 4.1.2). It was found that only surfaces with O_{CUS} vacancies could lead to the exothermic RO-H dissociation behavior of methanol expected based on the experimental results. The exposed Cu_{CS} atoms at the O_{CUS} vacancy form a favorable adsorption site for a methoxy group. This is also the preferred site at the model B surface, whereas Cu_{CUS} is slightly more favored for model A. Of the two ($\sqrt{3}\times\sqrt{3}$)R30° surface structures, methanol dissociation is

^{xli} The calculations were carried out at the PBE-D3(BJ)+U level of theory^{221,233,354} using periodic slab models in the VASP^{338–342} software package.

exothermic (by -0.6 eV) on the model B surface, but slightly endothermic (by 0.2 eV) on the model A surface. Thus the results are in favor of a model B surface. However, the endothermicity of 0.2 eV for the model A surface is too small to rule out this structure or the possibility that both surface structures coexists. This in particular considering the level of approximation in the reported DFT data with regards to e.g. the omission of thermochemical effects and the emphasis on low surface coverage.

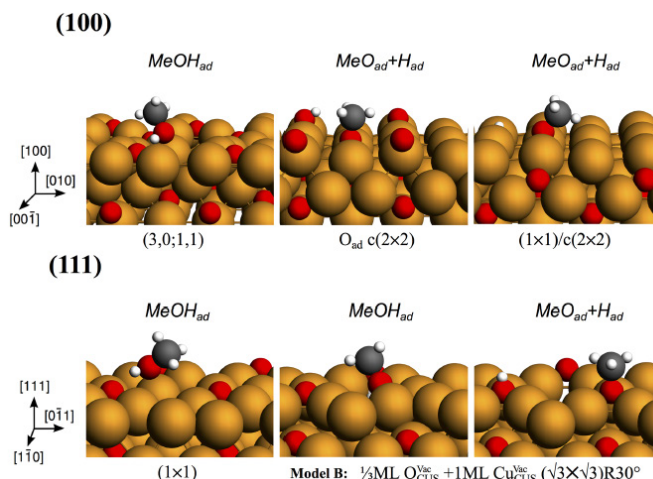


Figure 26. A selection of methanol adsorptions and dissociation structures on the $\text{Cu}_2\text{O}(111)$ and (100) surface facets. Reproduced from Besharat et al.,³⁶⁸ with permission of AIP Publishing.

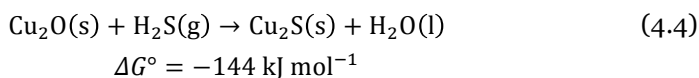
Table 2. Preferred adsorption sites for methanol, methoxy and H_{ad} as well as molecular and dissociative adsorption energies for the considered surface termination of the (100) and (111) surface facets of Cu_2O . Readopted from Besharat et al.³⁶⁸

Surface	Preferred adsorption site			Adsorption energy [eV]	
	Methanol	Methoxy	H_{ad}	Molecular	Dissociative
(100)					
c(2×2)	Cu bridge	Cu bridge	Cu bridge	-0.8	-2.3
(3,0;1,1)	Cu trimer	Cu trimer	Cu trimer	-0.7	0.3
(111)					
Ideal-(1×1)	Cu_{CUS}	Cu_{CUS}	$\text{Cu}_{\text{CUS}}/\text{O}_{\text{CUS}}$	-0.9	-0.4
$\text{Cu}^{\text{vac}}-(1\times 1)$	Cu^{vac}	Cu^{vac}	O_{CUS}	-0.8	0.0
Model A ^{b)}	Cu_{CUS}	Cu_{CUS}	O_{CUS}	-1.2	-1.0
Model B ^{c)}	Cu^{vac}	O^{vac}	O_{CUS}	-0.8	-1.4

a) ridge-dimer structure, b) $(\sqrt{3}\times\sqrt{3})R30^\circ$ with $\frac{1}{3}$ ML O_{CUS} , c) $(\sqrt{3}\times\sqrt{3})R30^\circ$ with $\frac{1}{3}$ ML O_{CUS} and 1ML Cu_{CUS} vacancies.

4.1.4. Sulphidation of Cu₂O

One of the critical premises for the safe disposal of SNF in Sweden is the slow and uniform sulphide-induced corrosion of the copper waste container. For the main part of the repository lifetime this is the anticipated behavior (see section 2.2.6.). The uniform corrosion resides on the formation of an active corrosion film on the copper surface. Under the conditions expected in the Swedish nuclear waste repository, the formed sulphide film (chalcocite, Cu₂S) is predicted to be porous and active. During the initial stage of the repository the copper surface will, however, be covered by a (hydr)oxide film due to the prehandling of the canister in oxygen containing environments, and due to reactions with oxygen trapped in the bore-holes. The (hydr)oxide film could possibly be passive, which could lead to undesired, and potentially critical, localized corrosion. The conversion of the oxide (mainly Cu₂O, but also chloride containing hydroxides such as paratacamite) to chalcocite is thermodynamically favorable for oxygen lean conditions and fast in aqueous media.^{193,194,369} Therefore the oxide film is not expected to be present for more than a short period of the repository lifetime with minor risks for critical damage. The overall Cu₂O to Cu₂S conversion reaction reads:¹³⁸



The detailed understanding of the conversion mechanism is, however, incomplete and a correct description at the atomic scale mechanism is lacking.³⁷⁰ The comprehensive understanding of this mechanism is important in order to evaluate the risk for localized copper corrosion in the SNF repository. **Paper V** of this thesis has examined the initial stages of the Cu₂O–Cu₂S conversion setting the grounds for future and more complete studies.

An important step in the Cu₂O–Cu₂S conversion will doubtlessly be the adsorption of a sulphide species onto the surface. For this reason, the adsorption of gaseous H₂S was considered. Interaction with dissolved HS⁻ or S²⁻ is another possibility. However, during the initial period of the waste repository it is, due to low ground water flow and prolonged resaturation of the bentonite buffer, likely that the copper surface will be in contact with a gas phase, at least in a fraction of the drill holes. In any case, H₂O will play an important role; partly because it is a by-product in the Cu₂O–Cu₂S conversion, partly because it inevitable will be present on the oxide surface in some form due to its abundance in the bedrock. The presence of H₂O has the potential to be either kinetically hampering or mitigating for the conversion reaction. Upon adsorption of sulphides to the surface, dissociation is a plausible subsequent step preceding O²⁻–S²⁻ lattice replacement. The dissociation (and association) of H₂O will also be of significance

for the overall reaction. The adsorption and dissociation behavior of H_2S and H_2O on the $\text{Cu}_2\text{O}(100)$ and $\text{Cu}_2\text{O}(111)$ surfaces^{xliii} are summarized in **Figure 27** on the basis of the results of **Paper V**. The results for H_2O onto the $\text{Cu}_2\text{O}(100)$ surface are essentially identical to those in **Paper IV**.

Some general conclusions can be drawn with regards to the behavior of H_2O versus H_2S , as well as for the (100) versus (111) surfaces. Note, firstly, that the ideal (1×1) surface is considered for the $\text{Cu}_2\text{O}(111)$. This is one of the plausible surface terminations of $\text{Cu}_2\text{O}(111)$, but the (111) surface structure is to date not fully resolved (see section 4.1.2 and 4.1.3). The ridge-dimer reconstruction of $\text{Cu}_2\text{O}(100)$ is lifted upon H_2O and H_2S dissociation yielding an essentially unreconstructed (1×1)/c(2×2) substrate surface (*cf.* section 4.1.3). Comparison of the adsorption behavior of the two surfaces shows that $\text{Cu}_2\text{O}(100)$ binds the H_2O and H_2S species stronger than the (111) surface. The (100) surface promotes H_2O dissociation to $\text{H}+\text{OH}^-$ whereas H_2O dissociation is endergonic on the (111) surface. H_2S dissociation to $2\text{H}+\text{S}^{2-}$ is exergonic on both surfaces.^{xliiii}

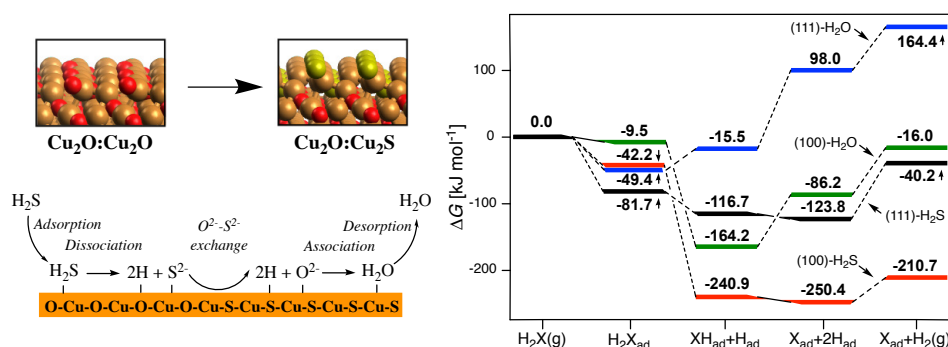
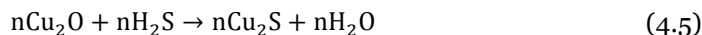


Figure 27. The scheme to the left shows a possible mechanism for the $\text{Cu}_2\text{O}-\text{Cu}_2\text{S}$ conversion reaction. The rightmost figure shows the Gibbs free energies ($\Delta G = \Delta E_{\text{el}} + nRT \ln[p_x]$, $n = -1$ for $x = \text{H}_2\text{O}$ and H_2S , $n = 1$ for $x = \text{H}_2$) for the adsorption and dissociation processes of H_2O and H_2S onto the $\text{Cu}_2\text{O}(100)$ and $\text{Cu}_2\text{O}(111)$ surfaces. Assumptions: $p_{\text{H}_2\text{O}} = p_{\text{H}_2\text{S}} = 1 \text{ bar}$, $p_{\text{H}_2} = 0.531 \mu\text{bar}$. Readopted from Stenlid et al.¹⁵³

^{xliii} The Cu-terminated c(2×2) ridge-dimer reconstructed surface of (100) and the stoichiometric (1×1) surface terminations where considered for the Cu_2O substrate. The calculations were carried out at the PBE-D3(BJ)+U level of theory^{221,233,354} using periodic slab models in the VASP^{338–342} software package.

^{xliiii} Adsorption of H_2O and H_2S takes place at Cu-Cu bridges on the (100) surface – the dissociation products favor the same sites. On the (111) surfaces, the unsaturated Cu (Cu_{cus}) and O (O_{cus}) atoms are the favored sites. H_2O and H_2S sit O/S-down over the Cu_{cus} site. H_2S sits parallel to the surface while H_2O forms a tilted angle (inline with the positions of the $V_{\text{S,min}}$ on their respective isodensity surfaces). H_{ad} preferentially binds to the O_{cus} , whereas OH^- , SH^- , O^{2-} and S^{2-} sits in bridge sites between Cu_{cus} and a saturated Cu atom (Cu_{cs}).

In order to determine the thermodynamic driving force for the sulphidation, the $O^{2-}-S^{2-}$ lattice replacement reaction was further considered by the overall reaction:



For the case of $n=1$ it was generally found that; i) it is not necessary to include explicitly adsorbed H_2O and H_2S to capture the trends in the replacement reaction, ii) replacement of the topmost O^{2-} is more beneficial than replacement of subsurface O^{2-} . The latter is reasonable considering that S^{2-} is a larger anion than O^{2-} and thus unlikely to fit seamlessly into the anionic lattice positions of Cu_2O . The replacement process accordingly leads to clear rearrangements of the crystal lattice locally around the S^{2-} . We further note that the experimental crystal lattices of Cu_2O and Cu_2S differ considerable (see section 2.2.2 and **Figure 4**).

For the continued reaction, with $n>1$ in eq. 4.5, we considered the replacement of the topmost surface atoms only. For $Cu_2O(111)$ this include both the outermost O_{CUS} , and the lower laying O_{CS} O^{2-} anions, whereas for $Cu_2O(100)$ all O^{2-} are equivalent. Reaction up to full surface replacement was tested resulting in the discrete sulphidation states of 0%, 25%, 50%, 75%, and 100% conversion. **Figure 28** shows structure examples for sulphidation of the $Cu_2O(111)$ surface as

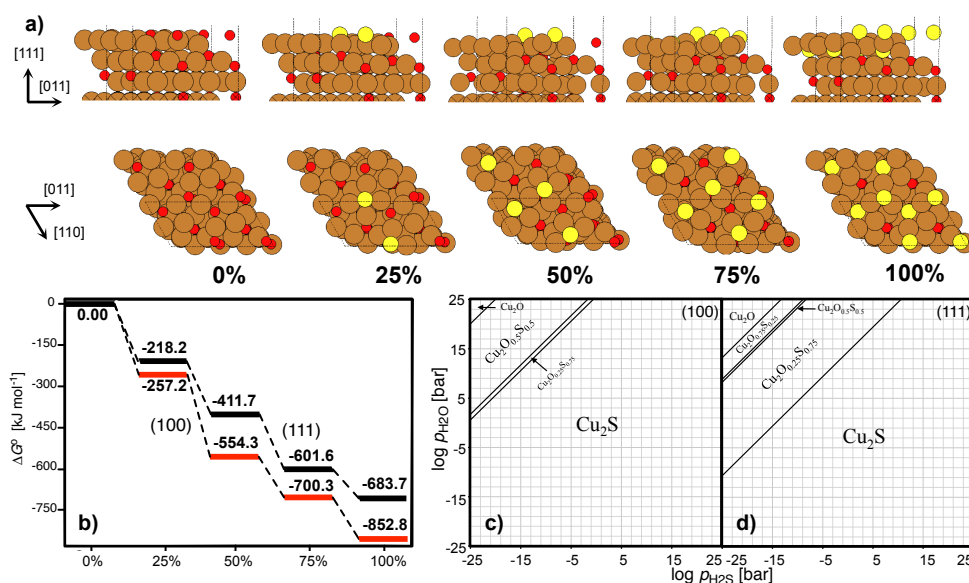


Figure 28. Showing in a) the step-wise sulphidation ($O^{2-}-S^{2-}$ replacement) structures of the $Cu_2O(111)$ surface. Figure b) displays the Gibbs free energy diagrams for the sulphidation of both the (100) and (111) facets assuming $p_{H_2O}=p_{H_2S}=1\text{bar}$, degree of sulphidation on x-axis. Figure c) and d) show the prevalent surface state at varied p_{H_2O} and p_{H_2S} partial pressures. The figure is readopted from Stenlid et al.¹⁵³

well as the sulphidation reaction energetics. Included in **Figure 28** are also $\log p_{\text{H}_2\text{S}} - \log p_{\text{H}_2\text{O}}$ phase-diagrams that show the prevalent (energetically favored) surface state under various conditions. In conclusion, sulphidation is exergonic for both the (100) and (111) surface facets with (100) being more susceptible to conversion. The sulfidation proceeds to full surface conversion for the conditions expected in the Swedish nuclear waste repository, in agreement with experiments.^{371,372} As stated above, the presented results encompass an initial investigation and future studies should for example consider a broader span of conditions, deeper conversion, additional mechanistic details and alternative surface terminations.

4.2. Interaction and reactivity analysis

(Papers VII-XIII)

This part of the thesis covers our work in the field of chemical interaction theory, including the development of new reactivity descriptors. In particular the use of the $V(\mathbf{r})$, $\tilde{I}(\mathbf{r})$ and $E(\mathbf{r})$ properties determined at electronic isodensity contours is discussed for predictions and rationalization of local and global reactivities and interaction affinities of various molecular, particle and crystalline compounds. For comparison, the $V(\mathbf{r})$, $\tilde{I}(\mathbf{r})$ and $E(\mathbf{r})$ quantities will be contrasted to the FMO, atomic partial charges and other popular ground state descriptors.

The derivation and theoretical foundation of the new property – the local electron attachment energy, $E(\mathbf{r})$ – introduced in this thesis is provided in section 4.2.1. (**Paper VII**). Its performance for rationalization of covalent and non-covalent molecular interactions is overviewed in sections 4.2.2-4.2.3. This particularly encompasses the study of electron deficient arenes and their substitution reactions with nucleophilic substances, as well as halogen bond interactions.

Chemical interactions not only take place between two molecular entities but also between molecules and material compounds. Motivated by the successes of the ground state properties of $V(\mathbf{r})$, $\tilde{I}(\mathbf{r})$ and $E(\mathbf{r})$ for characterizing molecular interactions and reactions, and inspired by the immense potential applications in materials science, we have readopted the theoretical framework for $V(\mathbf{r})$, $\tilde{I}(\mathbf{r})$ and $E(\mathbf{r})$ to suit transition metal compounds and periodic calculations. Some results for transition metal and transition metal oxide nanoparticles (and nanoclusters) are discussed in section 4.2.4, while extended surfaces are considered in section 4.2.5.

4.2.1. The local electron attachment energy

During the course of this thesis work (**Paper VII**) we have introduced a new ground state property for characterization of local electrophilicity, the *local electron attachment energy* denoted $E(\mathbf{r})$. Similar to its nucleophilic analog, $\bar{I}(\mathbf{r})$ (section 3.4.4), $E(\mathbf{r})$ is a complementary property to $V(\mathbf{r})$ (section 3.4.3) in that it is suited for the description of charge-transfer and polarization tendencies of interactions whereas $V(\mathbf{r})$ merely reflects the electrostatics. Surface $E(\mathbf{r})$ is denoted $E_s(\mathbf{r})$ and its minima, $E_{s,\min}$, marks electrophilic sites susceptible to interactions with electron-donors (Lewis bases/nucleophiles). Similar to the $\bar{I}(\mathbf{r})$ and $V(\mathbf{r})$ properties, $E(\mathbf{r})$ evaluated on isodensity contours of 0.001-0.004 a.u. of a compound were found suitable for the study of intercompound interactions.

The functional form of $E(\mathbf{r})$ is motivated by Janak's theorem²¹² and the piecewise linear energy dependence upon addition of electrons to atomic and polyatomic systems (*vide infra*).^{373,374} In analogy with $\bar{I}(\mathbf{r})$, $E(\mathbf{r})$ can be expressed as a summation over orbitals (in this case the virtual, unoccupied orbitals) normalized by the local occupied density $\rho(\mathbf{r})$. In its general form we refer to $E(\mathbf{r})$ as $E^{E_0}(\mathbf{r})$ with the definition:

$$E^{E_0}(\mathbf{r}) = \sum_{i=\text{LUMO}}^{\varepsilon_i < E_0} \frac{(\varepsilon_i - E_0)\rho_i(\mathbf{r})}{\rho(\mathbf{r})} \quad (4.6)$$

Here the summation runs from LUMO to orbitals up to a given energy offset, E_0 . In the above, ε_i are orbital eigenvalues with the corresponding orbital density function $\rho_i(\mathbf{r})$. The cut-off value for the considered ε_i is necessary in the above expression since all virtual orbitals will not contribute to attractive interactions (*vide infra*). In the applied form of $E(\mathbf{r})$, E_0 is usually set to zero with some exceptions (see e.g. periodic calculations below). This choice will be motivated in the following and leads to the expression:

$$E(\mathbf{r}) = E^{E_0=0}(\mathbf{r}) = \sum_{i=\text{LUMO}}^{\varepsilon_i < 0} \frac{\varepsilon_i \rho_i(\mathbf{r})}{\rho(\mathbf{r})} \quad (4.7)$$

The use of orbital eigenvalues is justified by Janak's theorem and the piecewise linear energy dependence for electron addition in generalized Kohn-Sham DFT (GKS-DFT). It can be demonstrated that the exact energy of an atomic or polyatomic system in an external potential $V_{\text{ext}}(\mathbf{r})$ is always a linear function of the fractional electron occupation when going from an integer occupation to the next.^{373,375} This means that the energy change upon addition of a fractional electron $\Delta N \leq 1$ to an M electron system is given by:

$$E(M + \Delta N) - E(M) = \Delta N \varepsilon_{\text{LUMO}} \quad (4.8)$$

The above can be generalized for the electron addition to an arbitrary orbital as:

$$E(M + \Delta n_i) - E(M) = \Delta n_i \varepsilon_i \quad (4.9)$$

For methods that obey the linear relationships of eq. 4.8 it follows that the LUMO energy corresponds exactly to the electron affinity ($\varepsilon_{\text{HOMO}} = -EA$). Analogous derivations can be conducted for electron removal yielding $\varepsilon_{\text{HOMO}} = -I$, where I is the ionization energy. Thus, although Koopmans' theorem²¹¹ ($\varepsilon_i \approx -EA_i$)^{xliv} strictly is not defined for DFT, we arrive at a similar conclusion within exact GKS-DFT methods. This is a significant conclusion since the prosperity of $E(\mathbf{r})$ in its proposed form resides on the principle that the ε_i of the virtual orbitals can estimate trends in electron affinities similar to the suggestions of Koopmans.

The above relationships also corroborate the choice of $E_0=0$ for exact GKS-DFT methods. Both Janak's theorem ($\partial E / \partial n_i = \varepsilon_i$),²¹² and the piecewise linear energy dependency relation show that only an orbital with negative eigenvalue binds a fractional electron. The addition of electrons to orbitals with $\varepsilon_i > 0$ will result in a positive (repulsive) energy change, why these states will not contribute to the attractive interaction. This motivates the choice of $E_0=0$. The cut-off can, furthermore, be interpreted as the free electron limit, where electrons in states of lower energy are bound, while electrons above the limit are unbound and behave as a free electron gas. In computations with infinite (large) basis sets there will be infinitely (very) many unbound states. By the introduction of the $E_0=0$ cut-off, all these states can be avoided yielding a computationally effective and physically sound property also for large basis sets.

In applied DFT, approximate methods are employed that generally deviates from the linear energy dependency upon addition of fractional electrons.^{373,375} Comparing the various functionals, it is found that hybrid functional shows better linearity than e.g. HF or GGA functionals.^{373,375} It can, furthermore, be (roughly) expected that an approximate method that provides accurate electron affinities and energies for charge-transfer interactions will give reasonable estimations to $E(\mathbf{r})$ with the cut off $E_0=0$. For finite systems, standard hybrid functionals such as B3LYP or PBE0 are known to yield accurate estimations of electron affinities. They also perform well for main group thermochemistry and kinetics for interactions involving significant charge-transfer components.³⁷⁶ Accordingly, we

^{xliv} $EA_i \approx -\varepsilon_i$ for virtual orbitals. Similarly $I_i \approx -\varepsilon_i$ for occupied orbitals. Koopmans's theorem is defined for HF theory and works best for occupied orbitals due to the cancellation of the correlation and orbital relaxation errors.

have found that the use of the B3LYP or PBE0 functionals for the evaluation of $E(\mathbf{r})$ in conjugation with $E_o=0$ yield good results for molecules and finite particles, often with excellent capability to predict electrophilic interactions and reactions (*vide infra*). For other DFT and QM methods, different cut-off values may be more appropriate. For instance, HF notoriously yields too diffuse virtual orbitals with positive eigenvalues, why a larger cut-off value may be suitable for $E(\mathbf{r})$ estimated from HF orbitals. For periodic solids it has been shown that the abovementioned piecewise linearity is reached for large unit cells even for xc-functionals that shows deviations for finite systems.^{377,378} This may grant the use of e.g. GGA functionals for estimations of $E(\mathbf{r})$ in periodic calculations.

Similar to $\tilde{I}(\mathbf{r})$, $E(\mathbf{r})$ can be decomposed into components associated with the local orbital electron kinetic energy density, $t_i(\mathbf{r})$, the electrostatic potential, $V(\mathbf{r})$, and the exchange-correlation potential, $V_{xc}(\mathbf{r})$, as:

$$E(\mathbf{r}) = \frac{1}{\rho(\mathbf{r})} \left[\sum_{i=\text{LUMO}}^{\varepsilon_i < 0} t_i(\mathbf{r}) - [V(\mathbf{r}) + V_{xc}(\mathbf{r})] \sum_{i=\text{LUMO}}^{\varepsilon_i < 0} \rho_i(\mathbf{r}) \right] \quad (4.10)$$

with $t_i(\mathbf{r}) = -1/2 \psi_i^*(\mathbf{r}) \nabla^2 \psi_i(\mathbf{r})$. Accordingly, $V(\mathbf{r})$ and $E(\mathbf{r})$ give complementary information; $V(\mathbf{r})$ describes the purely electrostatic component of an interaction whereas $E(\mathbf{r})$ also describes the interaction's charge-transfer and polarization characteristics.

It should, furthermore, be recognized that the $E(\mathbf{r})$ descriptor can be seen as a modified version of the local electron affinity descriptor [$EA_L(\mathbf{r})$] of Clark and coworkers^{379,380} that has been used for calculations of e.g. charge-transfer properties in organic field-effect transistors and as a descriptor in QSAR analysis for drug discovery.^{381,381,382} $EA_L(\mathbf{r})$ descriptor sums over *all* virtual orbitals, up to the total number of orbitals in the calculation (n_{orbs}), and is normalized by the total *virtual* density as:

$$EA_L(\mathbf{r}) = - \frac{\sum_{i=\text{LUMO}}^{n_{\text{orbs}}} \varepsilon_i \rho_i(\mathbf{r})}{\sum_{i=\text{LUMO}}^{n_{\text{orbs}}} \rho_i(\mathbf{r})} \quad (4.11)$$

Although the functional forms of the $E(\mathbf{r})$ and $EA_L(\mathbf{r})$ quantities are superficially similar, they differ profoundly in the details and physical consequences thereof. The first difference is the lack of energy cut-off in $EA_L(\mathbf{r})$. This leads to some severe disadvantages compared to $E(\mathbf{r})$. In particular $EA_L(\mathbf{r})$ is very sensitive to the size of the basis set and is therefore largely restricted to semi-empirical methods and minimal basis sets. This is certainly not attractive since we would typically like to treat the system with higher-level methods and larger basis sets for better accuracy in our calculations. Moreover, and regardless of the choice of basis set, $EA_L(\mathbf{r})$ will

include contributions from high-energy orbitals, which has little physical justification in the assignment of reactivity; for instance, due to contributions from high-energy σ^* -orbitals, $EA_L(\mathbf{r})$ analysis often lead to the incorrect conclusion that aromatic carbon atoms are unreactive (see e.g. section 4.2.2).

Another difference between $E(\mathbf{r})$ and $EA_L(\mathbf{r})$ is the use of virtual density in the denominator of $EA_L(\mathbf{r})$ whereas the total occupied density is used in $E(\mathbf{r})$. One of the advantages of the evaluation of properties on isodensity contours is that the repulsive terms originating in Pauli exchange is approximately constant over the isosurface.^{xlv} Thus the interaction propensities can be approximated by the variations in the evaluated surface property. This is no longer the case if denominators other than the occupied density are used. The functional form of $EA_L(\mathbf{r})$ will, moreover, often result in the assignment of high reactivity to regions of low total virtual density, which is contradicting the general rules from e.g. FMO theory that states that regions of high LUMO density are more prone to reactions.

In summary, a new electrophilicity descriptor, $E(\mathbf{r})$, have been proposed that can be used for estimations of charge-transfer and polarization capabilities of polyatomic compounds. Similar to $\bar{I}(\mathbf{r})$, $E(\mathbf{r})$ can be seen as an extension of FMO theory where multi-orbital contributions are considered instead of only the LUMO orbital. $E(\mathbf{r})$ also scales with the electrostatic potential, why variations in Coulombic interactions are likely to be captured. $E(\mathbf{r})$ is local in its nature and can thus be used to compare interaction and reaction propensities of different sites on the same compound, but also for the comparison of different compounds. Examples of the usage of $E(\mathbf{r})$ are given in the sections 4.2.2-4.2.5.

$E(\mathbf{r})$ for periodic calculations

In the following the functional form of $E(\mathbf{r})$ for periodic calculations is derived based on the details of **Paper XIII**. Due to the 3D infinite character of a typical periodic calculation, its electrostatic potential, $V^{\text{per}}(\mathbf{r})$, is shifted with respect to the absolute scale,³⁸³ $V^{\text{abs}}(\mathbf{r})$, of e.g. a molecular calculations.^{xlvi} The shift $\Delta V(\xi)$ varies with the system, ξ , because of differences in periodicity, structure, orientation and/or atomic composition. In summary:

^{xlv} For $E(\mathbf{r})$ and $\bar{I}(\mathbf{r})$ this can be expanded to include the whole exchange-correlation term.

^{xlvi} In the averaging of the electrostatic potential over a three-dimensionally infinite crystal an arbitrary constant falls out making the average potential ill-defined for such systems and dependent on the arbitrary choices one makes in the evaluation of potential.³⁸³ This does e.g. result in different shifts in different program codes for the same system, although the relative profiles of the electrostatic potential are identical.³⁸⁴ For a real, semi-infinite crystal or surface the electrostatic potential is, on the other hand, well defined.

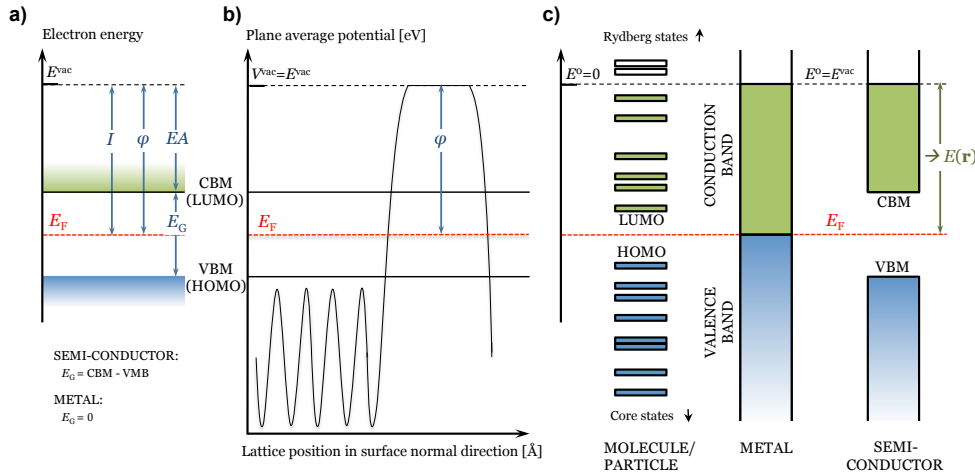


Figure 29. In a) is an overview of the relation between energy levels and surface concepts included. In b) are the planar average potential variations over a periodic slab model illustrated. Figure c) compares the evaluation of $E(\mathbf{r})$ for different kinds of compounds.

$$V^{\text{per}}(\mathbf{r}) = V^{\text{abs}}(\mathbf{r}) + \Delta V(\xi) \quad (4.12)$$

In addition, the eigenvalues of the one-electron states are shifted accordingly (the electron charge $q_e = -e = -1$ in atomic units):

$$\varepsilon_i^{\text{per}} = \varepsilon_i^{\text{abs}} - q_e \Delta V(\xi) \quad (4.13)$$

This poses a problem to the evaluation of $E(\mathbf{r})$, as well as $V(\mathbf{r})$ and $\tilde{I}(\mathbf{r})$, for periodic systems since a prerequisite for the intercompound comparison of these properties relies on the use of a common scale. A usual workaround is to simply shift the potential back to the absolute scale – or at least to a scale common for all the compared structures – by the use of a reference potential, V^{ref} .^{384–387} For a surface slab calculation with a sufficiently large vacuum region, this may be taken as the potential in the mid-point of the vacuum region, V^{vac} . Consequently:

$$V^{\text{abs}}(\mathbf{r}) \approx V^{\text{per}}(\mathbf{r}) - V^{\text{vac}} \quad (4.14)$$

Ideally $V^{\text{vac}} = \Delta V(\xi)$ with the corresponding energy for an electron in the vacuum region $E^{\text{vac}} = -qV^{\text{vac}}$. Since the charge of an electron is -1 in atomic units, $E^{\text{vac}} = V^{\text{vac}}$. **Figure 29.b.** shows the variations of the planar average electrostatic potential for a slab calculation in the surface normal direction.

One can further note that the vacuum level can be related to the surface concepts of the Fermi level (E_F), work function (ϕ), conduction band minimum (CBM=LUMO), valence band maximum (VBM=HOMO), the fundamental band

gap (E_G), and the surface ionization energy (I) as well as electron affinity (EA), see **Figure 29.a**. The work function may be determined by the relation:

$$\varphi = E^{\text{vac}} - E_F \quad (4.15)$$

The $E(\mathbf{r})$ for periodic calculations can now be reformulated through the shifting of the one-electron energies by the energy of the vacuum level (E^{vac}) and by summarizing over the energy levels from the Fermi level (E_F) up to E^{vac} since this represents the free electron limit (i.e. zero on the absolute scale):

$$E(\mathbf{r}) = \sum_{\substack{\varepsilon_i < E^{\text{vac}} \\ \varepsilon_i > E_F}} \frac{(\varepsilon_i - E^{\text{vac}})\rho_i(\mathbf{r})}{\rho(\mathbf{r})} \quad (4.16)$$

While the above is valid for a single \mathbf{k} -point case, we typically consider multiple \mathbf{k} -points in a periodic calculation. Therefore we must summarize over all \mathbf{k} -points (n_{kpt}) weighted by w_k that accounts for the degeneracy of symmetrically equivalent \mathbf{k} -points:

$$E(\mathbf{r}) = \sum_{k=1}^{n_{\text{kpt}}} \sum_{\substack{\varepsilon_i < E^{\text{vac}} \\ \varepsilon_i > E_F}} \frac{w_k(\varepsilon_{i,k} - E^{\text{vac}})\rho_{i,k}(\mathbf{r})}{\rho(\mathbf{r})} \quad (4.17)$$

For a spin-polarized calculation we must also add a summation over the σ spin states α and β by:

$$E(\mathbf{r}) = \sum_{\sigma=\alpha}^{\beta} \sum_{k=1}^{n_{\text{kpt}}} \sum_{\substack{\varepsilon_i < E^{\text{vac}} \\ \varepsilon_i > E_F}} \frac{w_{k,\sigma}(\varepsilon_{i,k,\sigma} - E^{\text{vac}})\rho_{i,k,\sigma}(\mathbf{r})}{\rho(\mathbf{r})} \quad (4.18)$$

Figure 29.c compares the evaluation of $E(\mathbf{r})$ of molecules, metals and semiconductors.

In a very similar manner to the above, we can write the spin-polarized form of $\bar{I}(\mathbf{r})$ for periodic calculations as:

$$\bar{I}(\mathbf{r}) = - \sum_{\sigma=\alpha}^{\beta} \sum_{k=1}^{n_{\text{kpt}}} \sum_{i=1}^{E_F} \frac{w_{k,\sigma}(\varepsilon_{i,k,\sigma} - E^{\text{vac}})\rho_{i,k,\sigma}(\mathbf{r})}{\rho(\mathbf{r})} \quad (4.19)$$

The latter has not been evaluated in the presented thesis work, but is anticipated to find future uses.

4.2.2. Nucleophilic reactions with electron deficient arenes and C=C bonds

The applicability of the $E(\mathbf{r})$ property for predictions and rationalization of molecular reactivity was assessed in **Papers VII-VIII** by the study of nucleophilic reactions of electron deficient arenes and conjugated C=C double bonds. As a first example conjugate addition of nucleophilic piperidine to a series of benzylidenemalononitriles (BMNs) was considered. **Figure 30** shows $E_s(\mathbf{r})$ evaluated^{xlvi} on the 0.004 isosurface^{xlvi} of BMN. The $E_{s,\min}$ of the largest magnitude is located at the β -carbon of the C=C bond marking this as a plausible site for interactions with nucleophilic reactants, in agreement with experimental results.³⁸⁸ Comparing the β -carbon $E_{s,\min}$ for the series of BMNs shown in **Figure 30** to experimental reactivity data with piperidine as nucleophile, we have found good linear correlation with a coefficient of correlation (R^2) of 0.917. The 4-NMe₂ is an outlier, which has previously been attributed to deviant solvation behavior.³¹² Excluding 4-NMe₂ from the trend gives a $R^2=0.975$ showing that clearly $E(\mathbf{r})$ can be used to reproduce reactivity trends.

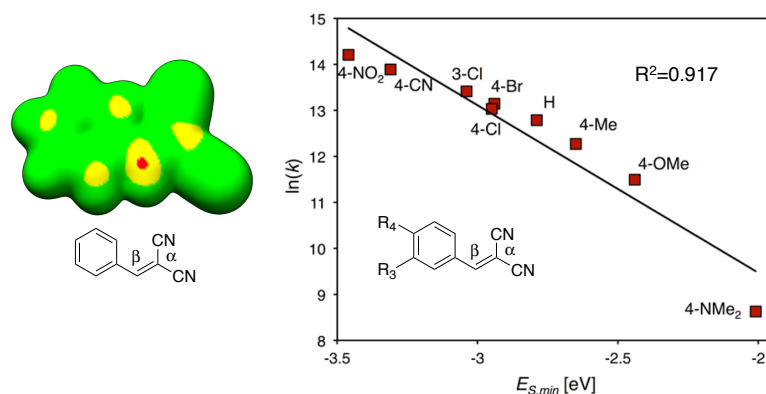


Figure 30. To the left is the $E_s(\mathbf{r})$ property evaluated at the 0.004 a.u. isodensity surface of benzylidenemalononitriles (BMN) shown. Coloring in eV: red $< -2.6 < \text{yellow} < -0.8 < \text{green}$. The right figure displays the linear correlation plot for $E_{s,\min}$ at the β position versus the logarithm of the experimental rate constants³⁸⁸ [$\ln(k)$] for the conjugate C_β -addition of piperidine to a series of BMNs. Reproduced with permission from Brinck et al.³⁸⁹

^{xlvi} Determined at the B3LYP/6-31G(d,p) level^{226,227} in Gaussian 09.³²⁹

^{xlvi} The joint knowledge of the initial studies indicates that $E_s(\mathbf{r})$ evaluated at the denser 0.004 a.u. isodensity surface yields better correlations with experimental reactivity data than the at the most commonly used 0.001 a.u. isosurface. This may be understood in terms of the relatively strong and short-ranged interactions considered in these studies.

From **Figure 30** we also find that the $E_s(\mathbf{r})$ profile of the BMNs display $E_{s,\min}$ over the ring carbons, most prominently over the ortho and para positions with respect to the conjugated substituent. These positions are the reactive sites in the NAS (nucleophilic aromatic substitutions) class of reactions that will be addressed in the following. Three distinct cases of NAS reactions were discussed in section 2.1.4; i) addition to sites substituted by F leading to the formation of a σ^F -adduct intermediate and a two-step S_NAr mechanism, ii) addition to sites substituted by heavier halogens ($X=Cl, Br, I$) resulting in a concerted S_NAr mechanism (given a moderately activated reactant) with a σ^X -adduct TS, and iii) reaction at H-substituted sites yielding a concerted VNS mechanism with a σ^H -adduct intermediate.

Concerted S_NAr reactions

Figure 31 shows a series of S_NAr active 1-bromo-4-R-2-nitrobenzenes. They react via a concerted mechanism at a Br-substituted C ring site in ortho position with respect to the activating nitro group ($-NO_2$). In para position to the reactive site an R substituent is attached. R varies from activating (e.g. Cl) to deactivating (e.g. NH_2) over the studied series. The R-group is, furthermore, distant from the site of reaction, thus minimizing its steric effect on the reactions and facilitating evaluation of the $E_s(\mathbf{r})$ descriptor. We have compared the predictions by the $E_s(\mathbf{r})$ descriptor to experimental reaction rates from a study by Berliner et al.³⁹⁰ where piperidine was used as both nucleophile and solvent.

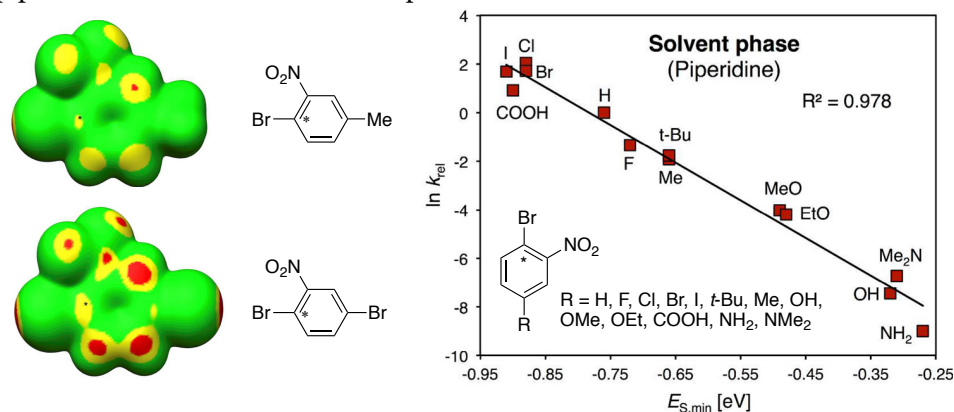


Figure 31. Displaying $E_s(\mathbf{r})$ maps evaluated at the 0.004 a.u. isodensity surface the 1-bromo-4-methyl-2-nitrobenzene (upper left) and 1,4-bromo-2-nitrobenzene (lower left). Coloring in eV: red < -1.4 < yellow < -0.9 < green. The right figure displays the linear correlation plot between $E_{s,\min}$ obtained in piperidine solvent at the site of reaction (*) and the logarithm of the experimental relative rate constants³⁹⁰ [$\ln(k_{rel})$] for the S_NAr reaction with the piperidine nucleophile for a series of 1-bromo-4-R-2-nitrobenzenes. Reproduced with permission from Stenlid et al.³⁹¹ Copyright 2017 American Chemical Society.

The analysis starts by overviewing the $E_s(\mathbf{r})$ maps of **Figure 31**. A number of interesting features can be found; first of all we can note that the reactive S_NAr site is far from the site with the lowest $E_{S,min}$. Prominent $E_{S,min}$ are e.g. found at the NO_2 O atoms, at C-H ring sites active in VNS reactions, and at the extension of the C-Br bond, a site known to participate in halogen bonding. This shows that care must be taken when using $E_s(\mathbf{r})$ and that an appropriate knowledge of the possible reactions is necessary; for the particular molecules under study, only addition of piperidine to the C-Br site will lead to a reaction at the given reaction conditions. The experimental reactivity trends in **Figure 31** can be reproduced with excellent accuracy ($R^2=0.978$) from $E_{S,min}$ at the site of reaction. Care must, however, be taken to account for the solvation effects.^{xlix} If $E_{S,min}$ is obtained by gas phase calculations the corresponding linear correlation is $R^2=0.827$. By including implicit solvation effects (IEF-PCM, see section 3.1.7) the correlation is increased to $R^2=0.869$. However, in order to fully capture the solvation effects of piperidine, explicit H-bonding solvent molecules should be included in the calculations. The need for explicit solvent molecules can be attributed to an amplified solvation ability upon H-bonding of the piperidine solvent compared to its average dielectric response reflected by the dielectric constant. In addition to the above, we note that $E_s(\mathbf{r})$ performs overall better than the $V_s(\mathbf{r})$ descriptor that is not able to identify reactive sites on the arenes. $E_s(\mathbf{r})$ also performs better than LUMO and in-fact gives better correlations than TS calculations.

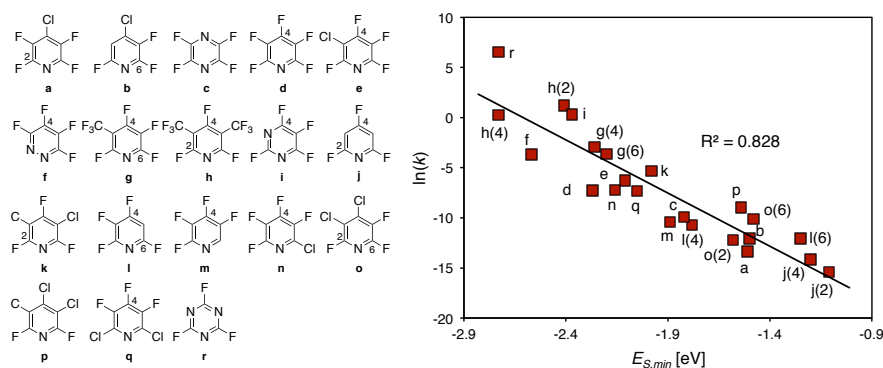


Figure 32. The studied series of fluorinated heteroarenes is shown to the left. The right figure displays the linear correlation plot between $E_{S,min}$ at the sites of reaction and the logarithm of the experimental relative rate constants^{392–395} [$\ln(k)$] for the S_NAr reaction with the NH_3 nucleophile in 40:60 vol% water:dioxin solution. Reproduced with permission from Stenlid et al.³⁹¹ Copyright 2017 American Chemical Society.

^{xlix} Determined at the B3LYP/6-31G(d,p) level^{226,227} in Gaussian 09³²⁹ accounting for solvation effects by IEF-PCM and by including one explicit H-bond accepting piperidine solvent molecule to the H-bonding R substituents NH_2 , OH and COOH.

Step-wise S_NAr reactions and regioselectivity

Regioselectivities can also be obtained from $E_S(\mathbf{r})$. This was e.g. shown by the study of a series of fluorinated heteroarenes displayed in **Figure 32**. These structures have multiple sites active in the S_NAr reaction with known experimental isomer distributions upon reaction with e.g. NH_3 in 40:60 vol% water:dioxin solution.^{392–395} The HF/F⁻ leaving group results in a late TS that is typically more difficult to capture by a ground state descriptor than an early TS (the 1-bromo-4-R-2-nitrobenzenes above e.g. have early TSs). Consequently a weaker correlation between experimental data and $E_{S,min}$ at the sites of reaction is expected.¹ The R^2 for this series is 0.826, which is not increased by accounting for solvation effects. Irrespectively, the sites of the various compounds are correctly ranked with only one exception (the **o** compound of **Figure 32**) highlighting that $E_S(\mathbf{r})$ can well be used for estimations of regioisomeric distributions.

VNS reactions

The S_NAr sites rarely corresponds to the arene ring position of the lowest $E_{S,min}$. This is instead often found at a ring C-H site. Nucleophilic substitution reactions at these sites are possible given a suitable nucleophile, e.g. the chloromethyl phenyl sulfone carbanion leading to the VNS type of reactions. **Figure 33** shows a series of VNS active heteroarenes of varying ring size and multiple possible sites of reaction. Also for this series of rather dissimilar compounds, $E_{S,min}$ at the site of reaction can reproduce trends in the experimental reaction rates where a linear correlation gives an R^2 of 0.941.¹ Further discussions are included in **Paper VIII**.

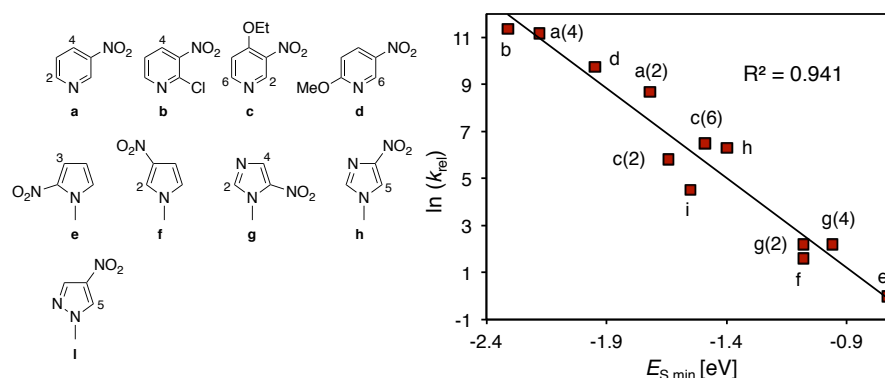


Figure 33. To the left are the studied series of VNS active heteroarenes shown. The right figure displays the linear correlation plot between $E_{S,min}$ at the sites of reaction and the logarithm of the experimental³⁹⁶ relative rate constants [$\ln(k_{rel})$] for the VNS. Reproduced with permission from Stenlid et al.³⁹¹ Copyright 2017 American Chemical Society.

¹ $E(\mathbf{r})$ based on KS wave function at the B3LYP/6-31G(d,p) level^{226,227} in Gaussian 09.³²⁹

4.2.3. Halogen bonding

Halogen bonds are relatively weak intermolecular interactions comparable in strength and characteristics to hydrogen bonds (see section 2.1.4). Shown in **Figure 34** is a series of halobenzenes comprising $C_6H_{(5-y)}F_yX$ [$X=Cl, Br, I$; $y=0, 2, 5$] molecules that form halogen bonds with e.g. the carbonyl oxygen of acetone. This is a challenging test for $E_S(\mathbf{r})$ since the LUMO orbital shifts from an aromatic π^* orbital to a halogen σ^* orbital over the series. As is seen in the $E_S(\mathbf{r})^1$ map of 1-bromo-3,5-difluorobenzene in the insert of **Figure 34**, an $E_{S,min}$ is formed in at the Br-extension of the Br-C bond. Such $E_{S,min}$ are also found at the tip of the X atom for all of the other considered halobenzenes. The $E_{S,min}$ coincide with the position of σ -holes ($V_{S,max}$) of the compounds. Riley et al. computed halogen bond interaction energies (ΔE_{int}) at the MP2/aug-cc-pVDZ(-PP) level for the considered series and found a close correlation between the magnitude of ΔE_{int} and $V_{S,max}$ ($R^2=0.975$).²⁹⁸ Similarly we obtain excellent correlations between ΔE_{int} and $E_{S,min}$ ($R^2=0.979$). The LUMO energy (ϵ_{LUMO}) gives a corresponding correlation of $R^2=0.816$. Interestingly, $E_{S,min}$ and $V_{S,max}$ show a relatively weak mutual correlation of $R^2=0.936$ suggesting that $E_{S,min}$ and $V_{S,max}$ may provide complementary information. Forming a multi-linear relationship between the two descriptors, the correlation between the computed and the predicted ΔE_{int} increases to R^2 of 0.993 (right plot of **Figure 34**), thus suggesting that the studied halogen bonds comprise a mixture of electrostatics and charge-transfer interactions.

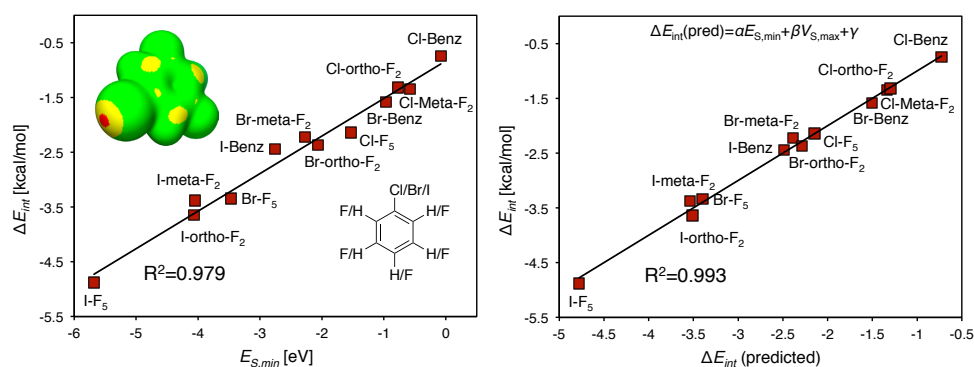


Figure 34. To the left are computed [MP2/aug-cc-pVDZ(-PP)]²⁹⁸ halogen bond interaction energies (ΔE_{int}) compared to the $E_{S,min}$ value at the tip of the Cl, Br or I atom. The right figure shows the computed versus the predicted ΔE_{int} , $\Delta E_{int}(\text{predicted}) = 0.367E_{S,min} - 1.503V_{S,max} - 0.352$ [eV]. The insert in the left figure displays $E_S(\mathbf{r})$ evaluated at the 0.004 a.u. isodensity surface of the 1-bromo-3,5-difluorobenzene molecule. Coloring in eV: red < -2.0 < yellow < -0.8 < green. Reproduced with permission from Brinck et al.³⁸⁹

4.2.4. Lewis acidity and basicity of metal and oxide nanoparticles

This part of the thesis will investigate chemical interactions at transition metal and oxide nanoparticles aided by the $V(\mathbf{r})$, $\bar{I}(\mathbf{r})$ and $E(\mathbf{r})$ ground state properties. Transition metal and oxide nanoparticles are versatile materials used in numerous existing and emerging applications. Their interaction behavior with the surrounding media is central to their performance; however, their interactions are often of complex nature, wherefore both experimental efforts and modeling are necessary to gain a comprehensive understanding thereof. Although smaller than their macroscopic parent material, NPs are still large entities from a computational point of view where the complete sampling of interaction space is usually unattainable. For this reason it is of interest to use computationally efficient ground state properties in rationalizing NPs' interaction behavior. This could for instance be used for the identification of new materials for medical therapy, drug release or heterogeneous catalysis, but could also be useful tools in e.g. the evaluation of nanotoxicity. Another motivation for the study of NP is as benchmarks in the development of descriptors for extended surfaces as discussed in section 4.2.5.

In **Paper IX** we extended the σ -hole concept²⁹⁰ from molecular theory to metal NP. We showed that σ -holes can be used in the rationalization of interaction propensities and catalytic size-effects of gold and platinum NP. The origin of the σ -hole and its connection to the $E(\mathbf{r})$ property were further analyzed in **Paper X**. **Paper XI** investigated the Lewis acidic and basic characteristics of noble metal NP, whereas **Paper XII** showed that $V(\mathbf{r})$ and $E(\mathbf{r})$ are useful descriptors for the characterization of TiO_2 NP interaction properties. This is a significant result since the interactions of TM oxides are difficult to rationalize using ground state descriptors.^{305,315,328}

The $V_s(\mathbf{r})$ of Au NP and its implications for heterogeneous catalysis

In **Paper IX** it was shown that the surface electrostatic potential can be used to understand the interaction behavior and catalytic activity of gold (and platinum) NP.^{li} We found that regions of positive electrostatic potential (i.e. σ -holes) are

^{li} The $V_s(\mathbf{r})$ were obtained by calculation at the RI-PBE/def2-SV(P) level of theory^{221,353} in Turbomole.³³⁵ The def2-SV(P) implies the use of effective core potentials, and the calculations are in agreement with all-electron relativistic calculations (see **Paper IX**). $V_s(\mathbf{r})$ for the larger Au_{309} and Au_{561} NPs were obtained by PBE²²¹ plane-wave (cut off=300 eV with PAW potentials^{209,210}) calculations in VASP,^{338–342} while absolute $V_s(\mathbf{r})$ were not determined. H_2O and CO interaction energies were determined in Orca³³⁰ at the PBE0-D3(BJ)/Def2-TVZPP//Def2-TVZP level of theory.^{225,233,353,354}

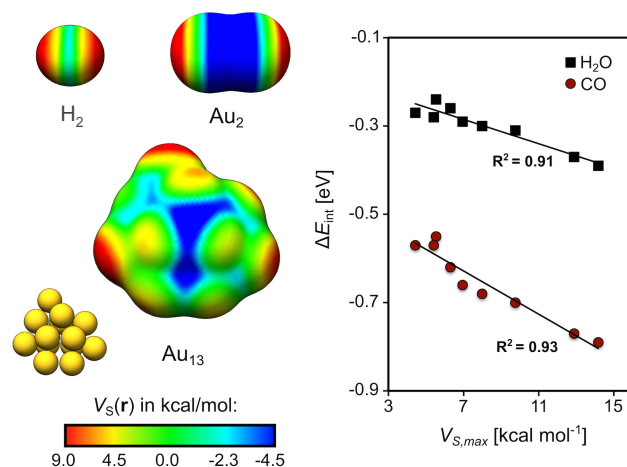


Figure 35. $V_S(r)$ profiles at the 0.001 a.u. isodensity contours of H_2 , Au_2 and the low-energy Au_{13} nanocluster are shown to the left. The rightmost figure shows linear correlation plots between CO and H_2O interaction energies at the unique adsorption sites of Au_{13} . Reproduced with permission from Stenlid et al.³⁹⁷ Copyright 2017 American Chemical Society.

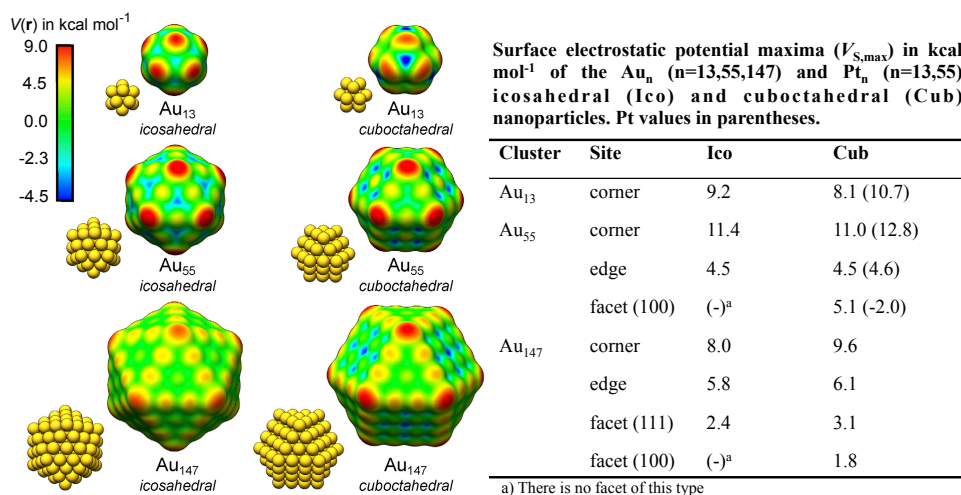


Figure 36. Surface electrostatic potential on the 0.001 a.u. isodensity surface of icosahedral and cuboctahedral Au_{13} , Au_{55} and Au_{147} NPs are shown to the left. $V_{S,max}$ at different atomic positions are given in the table including values for cuboctahedral Pt_{13-55} NPs. Reproduced with permission from Stenlid et al.³⁹⁷ Copyright 2017 American Chemical Society.

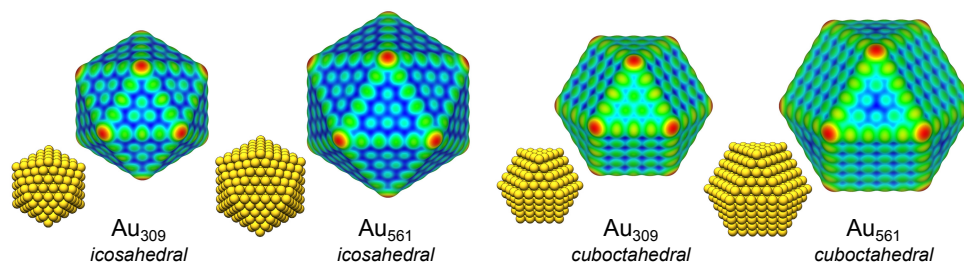


Figure 37. Surface electrostatic potential on the 0.001 a.u. isodensity surface of icosahedral and cuboctahedral Au_{309} and Au_{561} NPs determined by periodic calculations. Note that the $V_s(\mathbf{r})$ are not depicted on the same scale for the different clusters (see section 4.2). Reproduced with permission from Stenlid et al.³⁹⁷ Copyright 2017 American Chemical Society.

displayed on top of the gold atoms, whereas the bridging and hollow regions in between atoms are associated with negative electrostatic potential (hereafter referred to as σ -lumps as introduced in **Paper XI**). The σ -holes, furthermore, coincide with adsorption positions for CO and H_2O molecules. The σ -holes with the largest magnitudes are identified at the most undercoordinated atoms, e.g. corner sites or edges. Surface facet atoms of higher coordination have weaker σ -holes. The electrostatic potential maxima at the σ -hole correlate with adsorption energies as shown in **Figure 35**. From this follows a general rule for σ -hole strengths where corners > edges > facets (see also **Figure 36**), consistent with previous findings.^{398–400}

The origin of the σ -holes can be traced to the electronic valence configuration of Au: $[\text{Xe}]4f^{14}5d^{10}6s^1$. The variations in the surface electrostatic potential can be explained by the partially occupied s -orbitals (neglecting minor $6p$ and $4d$ contributions). Analogously to the simple case of the H_2 molecule, the $6s$ -overlap between two Au atoms gives rise to an occupied and bonding σ -orbital, as well as an unoccupied and antibonding σ^* -orbital. Therefore both H_2 and Au_2 accumulate electron density in the bonding region, whereas the outer regions at the extension of the bonds are deprived of electrons. This leads to the formation of a ring shaped $V_{s,\text{min}}$ (σ -lump) in the bonding region, and $V_{s,\text{max}}$ (σ -holes) at the bond extension (**Figure 35**). The same concepts apply also to more complex Au structures, e.g. the low energy Au_{13} cluster of **Figure 35**, or the symmetric icosahedral and cuboctahedral Au_{13} - Au_{561} clusters of **Figure 36** and **Figure 37**.

Despite the inert nature of metallic gold, it has long been known that nanosized gold has high catalytic activity^{401–403} and that the activity decreases with size.^{398,399} The $V_s(\mathbf{r})$ profile of the Au NP particles in **Figure 36** and **Figure 37** offers a physicochemical rationale to the catalytic size-dependency as explained below. Heterogeneous catalysis is, even in the simplest case, a multi-step process

comprising at the very minimum adsorption, a reaction step and desorption. Effective catalysis resides on the balance of these processes where a substrate with large adsorption affinity may activate the reactant but hamper desorption leading to surface poisoning. The ideal catalyst usually has an intermediate adsorption affinity,³¹⁴ where gold is typically biased towards too weak affinities. In contrast, Au NPs are associated with strong adsorption at the corner and edge atoms where $V_s(\mathbf{r})$ is large, thus yielding an enhanced catalytic activity. As the size of the Au NP grows, the number of corner and edge sites becomes diluted. Hence, although the magnitude of the σ -holes of the undercoordinated sites are essentially constant regardless of the NP size, the low number of active sites on the larger NPs reduces the high catalytic activity.

On the origin of σ -holes on TM nanocompounds

The origin of σ -holes on Au NP was discussed breathily in the preceding section. In **Paper X** this was further investigated^{lii} for a larger selection of TM NP. For the purpose of rationalizing the interaction behavior of TM NPs and the occurrence of TM σ -holes, the σ_s -, σ_p - and σ_d -hole categories of σ -holes were introduced. The designation of the σ -hole depends on whether it can be traced to an electron deficiency in the valence s , p or d orbitals. Mixtures of the above σ -holes exist.

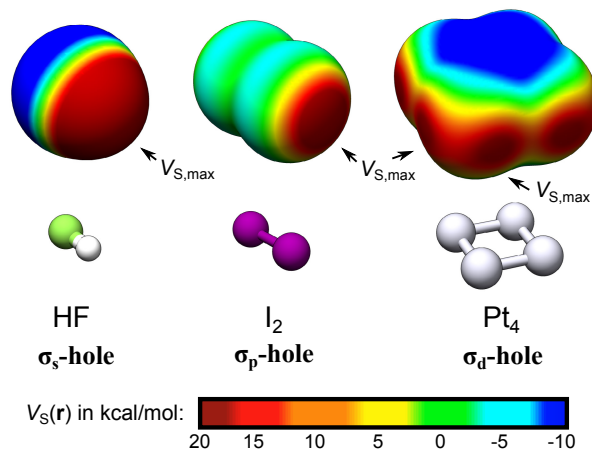


Figure 38. Shows the $V_s(\mathbf{r})$ profiles of HF, I_2 and square planar Pt_4 compounds at the 0.001 a.u. isodensity surfaces. Reprint from Stenlid et al.⁴⁰⁴

^{lii} $V_s(\mathbf{r})$ and $E_s(\mathbf{r})$ were evaluated from KS-orbitals obtained at the PBE0/def2-TZVP(-fg) level of theory for the TM_{13} compounds, whereas the remaining $V_s(\mathbf{r})$ profiles were determined at the PBE0/def2-TZVPP level. Geometries and H_2O interaction energies were obtained in Orca³³⁰ at the PBE0-D3(BJ)/def2-TZVPP//def2-TZVP level.^{225,233,353,354}

In order to describe the new σ -hole categories, a few representative examples will be used. **Figure 38** shows $V_S(\mathbf{r})$ profiles for the HF, I_2 and Pt_4 compounds. The bonding in HF comes from the mixing of a $1s$ orbital of H and an sp^3 hybridized orbital of F to form the bonding and antibonding σ - and σ^* -orbitals. Only the σ -orbital is occupied resulting in electron deficiencies on H since the covalent bond is polarized towards F. The result is a typical σ_s -hole on H. Since the σ -hole originates in the spherically symmetric $1s$ orbital, the formed σ_s -hole is diffuse and non-directional, characteristic of σ_s -holes. In the case of the I_2 molecule, the σ -bonding comes largely from the overlap between two $5p_z$. The bonding again results in the depletion of electrons at the extension of the σ -bond and formation of σ -holes at the two ends of I_2 . These are σ_p -holes. Because of the directional character of the p_z orbitals, the σ_p -holes are directed and localized along the extension of the σ -bond. The difference between the σ_s and σ_d types of σ -holes is best demonstrated by the well known tendency of hydrogen bonds to form interaction angles (e.g. O-H...O) considerable smaller than 180° whereas halogen-bonds typically form interaction angles close to 180° .⁴⁰⁵

The square planar Pt_4 complex serves as example of the σ_d -hole. Pt has a valence occupation of $5d^96s^1$. The partially occupied d -orbitals and the symmetric structure results in $V_{S,max}$ along the extensions of each Pt-Pt bond. In this structure the Pt atoms bind by (s-mixed) $5d_{z^2}$ and $5d_{x^2-y^2}$ orbitals (i.e. the e_g orbitals) that overlap and form σ_d -bonds with occupied σ_d and unoccupied σ_d^* -orbitals. Thus the observed $V_{S,max}$ along the extensions of each Pt-Pt bond are best described as σ_d -holes. The σ_p - and σ_d -holes share the local and directional character.

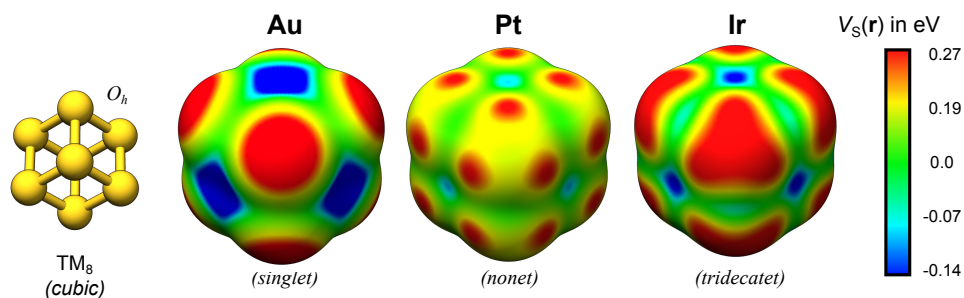


Figure 39. $V_S(\mathbf{r})$ profiles of the cubic O_h TM_8 nanoclusters of Au, Pt and Ir shown at the 0.001 a.u. isodensity surfaces. Readopted from Stenlid et al.⁴⁰⁴

Similar σ_d -holes are also found on the cubic Pt_8 nanoclusters (NBO valence occupation: $5d^{9.04}6s^{0.75}6p^{0.21}$)^{liii} of **Figure 39**. Again it is the $5d_{z^2}$ and $5d_{x^2-y^2}$ orbital overlaps that give rise to the σ_d -hole pattern of the $V_S(\mathbf{r})$ profile. In contrast, the cubic Au_8 ($5d^{9.92}6s^{0.86}6p^{0.22}$) only yields σ_s -holes positioned at the corners of the Au_8 cube. This agrees well with the $6s$ -dominated bonding pattern of Au. The Ir_8 cube ($5d^{7.97}6s^{0.75}6p^{0.29}$) has a different $V_S(\mathbf{r})$ with a triangular shaped $V_{S,\max}$ comprising, what appears to be, a combined σ_s/d -hole. Compared to Pt_8 , Ir_8 has a lower d -occupation and d -orbitals of all angular momenta are partially occupied.^{liii} Thus the σ -hole is best described as an overlap of σ_d -holes of different origins.

The analysis of the Pt_4 and TM_8 nanoclusters above is greatly facilitated by their symmetric structures. An analysis of similar detail is difficult to pursue for other, more complex structures. Irrespectively, we can extract a few general rules that have to be fulfilled in order for σ_d -holes to occur:

- Partially occupied d -orbitals
- Locally symmetric bonding geometry (e.g. cubic)
- Favorable electron configuration (e.g. low spd -hybridization)

Paper X further investigates a series of low-energy TM_{13} nanoclusters (TM=Au, Cu, Pt, Pd, Co, Rh, Ir, Ru including Pt_7Cu_6). Out of these, the Au, Pt and Ir clusters are shown in **Figure 40** and will be discussed below. Au_{13} is the same as in **Paper IX**. For information regarding the remaining clusters the reader is referred to the original paper. The Ir_{13} ($S=1\frac{1}{2}$) and Pt_{13} ($S=1$) clusters have open structures, whereas Au_{13} ($S=1\frac{1}{2}$) has a more compact structure that closer resembles a close-packed arrangement. In agreement with the picture obtained above, Au_{13} displays σ_s -holes at corner sites, whereas Pt_{13} and also Ir_{13} shows $V_S(\mathbf{r})$ profiles dominated by σ_d -holes. Pt_{13} has one σ_s -hole at its weakest adsorption site, and the capping atom of Ir_{13} can be described as a σ_s -hole or mixed σ_d -hole. The remaining σ -holes (14 for Pt and 16 for Ir) are σ_d -holes. Moreover, it is further found that the $V_S(\mathbf{r})$ and $E_S(\mathbf{r})$ profiles agree well, with $V_{S,\max}$ and $E_{S,\min}$ identified at almost identical positions. This is the case for Au, Pt and Ir, whereas some deviations are found for the other TM_{13} clusters as discussed in **Paper X**.

We found that H_2O adsorbs O-down to all identified σ -holes, and the strongest interaction corresponds to the σ -hole of largest magnitude (true for both $V_{S,\max}$ and $E_{S,\min}$), see **Figure 40**. For the Pt_{13} and Ir_{13} the average deviation between the σ -hole position and the H_2O adsorption site is small (~ 0.45 Å)

^{liii} Pt_8 d -occupation: $5d_{xy}^{1.97}5d_{xz}^{1.97}5d_{yz}^{1.97}5d_{x^2-y^2}^{1.56}5d_{z^2}^{1.56}$; Ir_8 d -occupation: $5d_{xy}^{1.65}5d_{xz}^{1.65}5d_{yz}^{1.65}5d_{x^2-y^2}^{1.51}5d_{z^2}^{1.51}$.

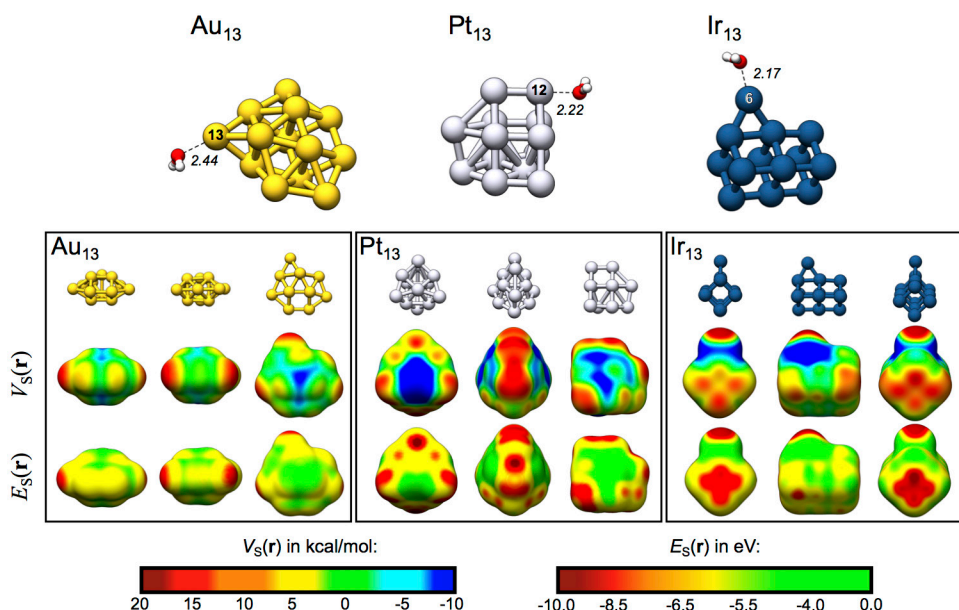


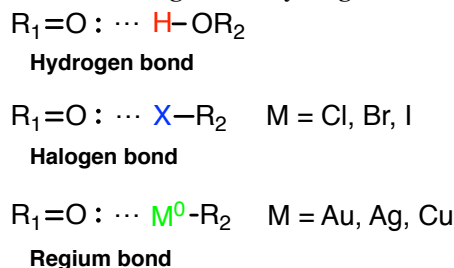
Figure 40. The top figures show the favored H₂O adsorption position onto the Au₁₃, Pt₁₃ and Ir₁₃ nanoclusters. In the bottom figure are the $V_S(\mathbf{r})$ and $E_S(\mathbf{r})$ profiles of the same clusters shown at the 0.001 a.u. isodensity surfaces. Readopted from Stenlid et al.⁴⁰⁴

whereas the deviation is larger (0.83 Å) for Au₁₃. This is an indication of the stronger directionality of the σ_d -holes of Pt₁₃ and Ir₁₃ compared to σ_s -holes of Au₁₃. Low $V_S(\mathbf{r})$ σ -lump regions are located in-between atoms. H₂O was found to adsorb H-down to these regions except for the case of Ir₁₃. The computed interaction energy correlations with $V_{S,\max}$ and $E_{S,\min}$ are good for many of the TM₁₃ clusters, especially for the d^{9-10} TM and the strongest adsorption sites of Ir₁₃. The deviations of the other clusters are discussed further in the original paper.

Regium bonds, σ -holes and σ -lumps of Cu, Ag and Au nanoclusters

The interaction behaviors of Cu, Ag and Au nanoclusters were studied in detail in **Paper XI**. Because of their full d -shell ($d^{10}s^1$), nanomaterial of the noble metals belonging to the Cu-group (group 11) form relatively weak adducts with Lewis bases and acids. This facilitates the close examination of their interaction behavior by the $V(\mathbf{r})$, $\bar{I}(\mathbf{r})$ and $E(\mathbf{r})$ descriptors as described below. The preceding parts of the thesis discuss the creation of σ -holes on Au compounds. We have found that similar σ -holes exist also on Ag and Cu.

Paper XI, furthermore, introduces a new class of bonds – *regium bonds*.^{liv} These interactions take place between an electron deficient region of an Au, Ag or Cu atom and an electron donor (Lewis base). As shown in **Scheme 3**, regium bonds show close resemblance to halogen and hydrogen bonding.



Scheme 3. Comparison between hydrogen, halogen and regium bonding.

In **Paper XI**, interactions (regium bonding) of the H₂O, H₂S, NH₃ and CO Lewis bases onto nanoclusters comprising Au₉, Ag₉ and Cu₉ as well as the larger Ag₁₁, Ag₁₇, and Ag₁₈ were considered, as were the interactions of the Lewis acidic BF₃, BH₃, Na⁺ and HCl (H-down) compounds.^{lv} These eight probe compounds serve as a test set of the local Lewis acidity and basicity of the abovementioned Au, Ag and Cu nanoclusters. The interaction behavior and local interaction energies of the probes are compared to the Lewis acidic and basic characteristics of the noble metal clusters as determined by the $V(\mathbf{r})$, $\bar{I}(\mathbf{r})$ and $E(\mathbf{r})$ properties.

The $V(\mathbf{r})$, $\bar{I}(\mathbf{r})$ and $E(\mathbf{r})$ properties evaluated at their 0.001 isodensity surfaces are shown in **Figure 41** for the Au₉, Ag₉ and Cu₉ compounds (S=1/2 spin state). The figure also shows the LUMO/SOMO (spatially the orbitals are approximately the same; SOMO=singly occupied molecular orbital), as well as the favored adsorption positions for the probe compounds. It is found that Lewis acidic areas ($E_{\text{S,min}}$ and $V_{\text{S,max}} = \sigma$ -holes) are located on top of the metal atoms, whereas Lewis basic sites ($\bar{I}_{\text{S,min}}$ and $V_{\text{S,min}} = \sigma$ -lumps) in general are identified in hollow and bridge sites in between atoms. We note that the LUMO/SOMO of the Au, Ag and Cu clusters is not able to predict the favored adsorption sites, neither is

^{liv} The name reflects the royalty of the considered metals.

^{lv} Computational details: CO interaction energies (ΔE_{int}) are taken from Duanmu et al.,⁴⁰⁶ the other ΔE_{int} were determined at the PBE0-D3(BJ)/def2-TVZPP//def2-TVZP level^{225,233,353,354} in Gaussian 09.³²⁹ $V(\mathbf{r})$ and $E(\mathbf{r})$ were evaluated from KS wave functions obtained at the PBE0/LACV3P*//LANL2-DZ level of theory^{225,233,351,352,354} with the HF xc-admixture reduced to 10%. It was found that a reduced HF admixture results in $E(\mathbf{r})$ of slightly increased quality. The $V(\mathbf{r})$ is insensitive to the level of HF admixture. It was also found that the 0.001 a.u. isosurface gives best overall results for $E_{\text{S}}(\mathbf{r})$ and that $E_{\text{S}}(\mathbf{r})$ is not very sensitive to the use of a smaller basis set such as LACV3P* compared to def2-TVZPP.

the LUMO/HOMO of the closed shell Ag_{18} particle. Hence the use of frontier orbitals fails in this case. That does, however, not rule out orbital analysis *per se*. For these clusters there are e.g. 22-40 virtual orbitals of $\epsilon_i < 0$ that contribute to $E(\mathbf{r})$. For $\bar{I}(\mathbf{r})$, all occupied orbitals contribute. The joint contribution of these orbitals gives a better picture of the interaction tendencies of the particles than merely the frontier orbitals. We shall see that $E(\mathbf{r})$, $\bar{I}(\mathbf{r})$, and $V(\mathbf{r})$ are efficient descriptors for Lewis acid and Lewis basic interactions of group 11 NPs.

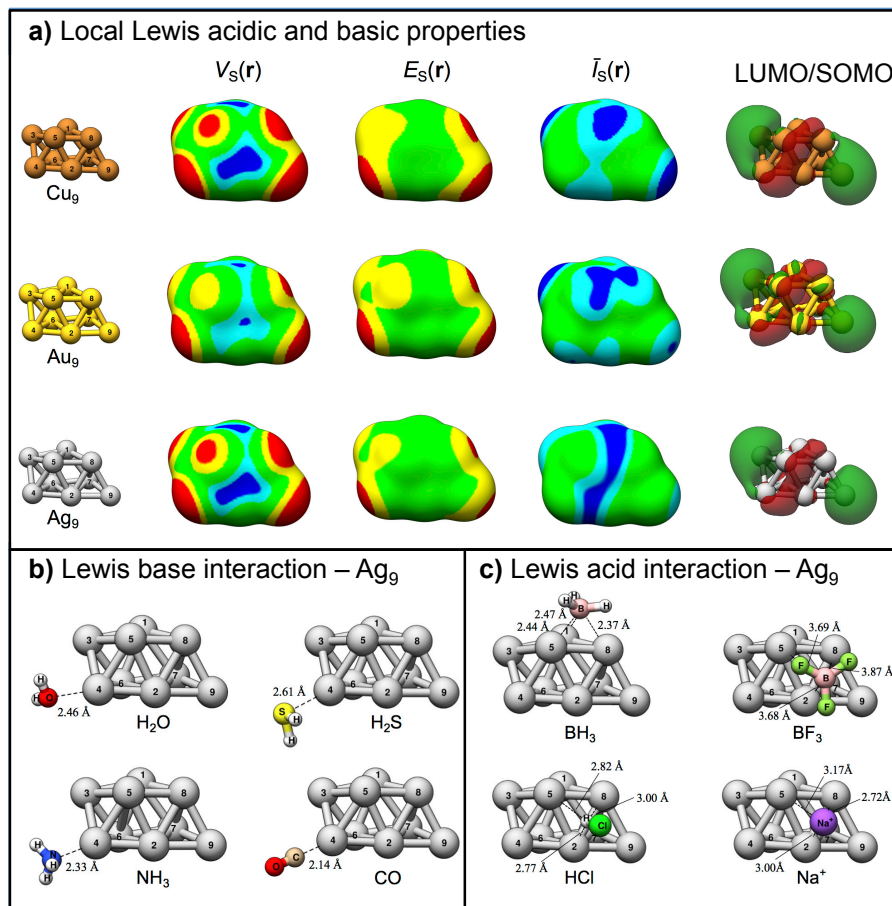


Figure 41. The top figure shows the Au_9 , Ag_9 and Cu_9 nanoclusters with corresponding $V_s(\mathbf{r})$, $E_s(\mathbf{r})$ and $\bar{I}_s(\mathbf{r})$ maps on the 0.001 a.u. isosurface, as well as the LUMO/SOMO orbitals. Color code for $V_s(\mathbf{r})$ in meV: red > 325 ; $150 < \text{yellow} < 325$; $-150 < \text{green} < 150$; $-325 < \text{cyan} < -150$; blue < -325 . $E_s(\mathbf{r})$ in eV: red < -8.0 $< \text{yellow} < -6.0$ $< \text{green}$. $\bar{I}_s(\mathbf{r})$ have different color codes for the different metals, in eV: Cu: blue < 5.8 $< \text{cyan} < 5.9$ $< \text{green}$; Ag: blue < 6.1 $< \text{cyan} < 6.3$ $< \text{green}$; Au: blue < 7.2 $< \text{cyan} < 7.5$ $< \text{green}$. The bottom figures show, to the left, the favored absorption structures for the Lewis base interactions with Ag_9 , and to the right the favored structures upon interaction with Lewis acids.

Table 3. R^2 coefficients for the linear relationships between site-resolved Lewis base interaction energies and the local $E_{S,\min}$ and $V_{S,\max}$ for the Au_9 , Ag_9 and Cu_9 nanoclusters.

	Cu_9		Ag_9		Au_9	
	$E_{S,\min}$	$V_{S,\max}$	$E_{S,\min}$	$V_{S,\max}$	$E_{S,\min}$	$V_{S,\max}$
H_2O	0.988	0.946	0.989	0.971	0.985	0.949
H_2S	0.963	0.941	0.968	0.971	0.916	0.856
NH_3	(-) ^a	(-) ^a	0.987	0.961	(-) ^a	(-) ^a
CO	(-) ^a	(-) ^a	0.911	0.918	(-) ^a	(-) ^a

^{a)} Not determined.

The positions for the adsorption of the Lewis acids are in good agreement with the characterization of the particles by the $V(\mathbf{r})$ and $\bar{I}(\mathbf{r})$ properties. Adsorption trends are fairly well reproduced by $V_{S,\min}$ and $\bar{I}_{S,\min}$, but not as strong as for the Lewis base adsorption (*vide infra*). This is due to the increased complexity upon interaction with the Lewis acids, as discussed further in the **Paper XI**, including molecular deformation and interaction via multiple sites (e.g. via both H and B for BH_3). The simplest adsorbent Na^+ has a strong correlation ($R^2=0.95$) versus $V_{S,\min}$ showing the potential of $V(\mathbf{r})$ for studies of interactions with electron accepting compounds.

For the adsorption of Lewis bases, the analysis is facilitated by a clean interaction between the electron lone pair region of the adsorbate and the atomic sites of the clusters without e.g. the steric interaction of the side groups. The interaction trends are all well reproduced by $E_{S,\min}$ and $V_{S,\max}$ as seen in **Table 3** and **Figure 42**. The deviations from this is e.g. CO adsorption that has a more complex interaction behavior than the other adsorbents due to CO 's ambivalent adsorption character with both donation and back-donation interactions. The CO trends are, however, much better than trends reported by Duanmu et al.⁴⁰⁶ obtained by comparison to partial atomic charge of the CM5M^{281} type. H_2S adsorption to Au_9 is also an outlier; H_2S adsorption is accompanied by a strong tendency for the cluster to reconstruct, why the correlations are reduced.

The Lewis base interactions cannot all be considered purely electrostatic in nature. This is indicated by the fact that the $V_{S,\min}$ at the Lewis bases does not capture the trends in their average adsorption energies. Further information can be obtained by comparison of the interaction behavior particle to particle. Looking for instance at the *total* correlation of H_2O , i.e. including H_2O adsorption to all the sites of Au_9 , Ag_9 and Cu_9 , the total linear correlation coefficients of $R^2=0.790$ and 0.823 are obtained for $V_{S,\max}$ and $E_{S,\min}$. By a multi-linear relationship between $V_{S,\max}$ and $E_{S,\min}$ a larger part of the interaction trends can be retrieved yielding $R^2=0.850$. Performing the same procedure for H_2S adsorption gives a more

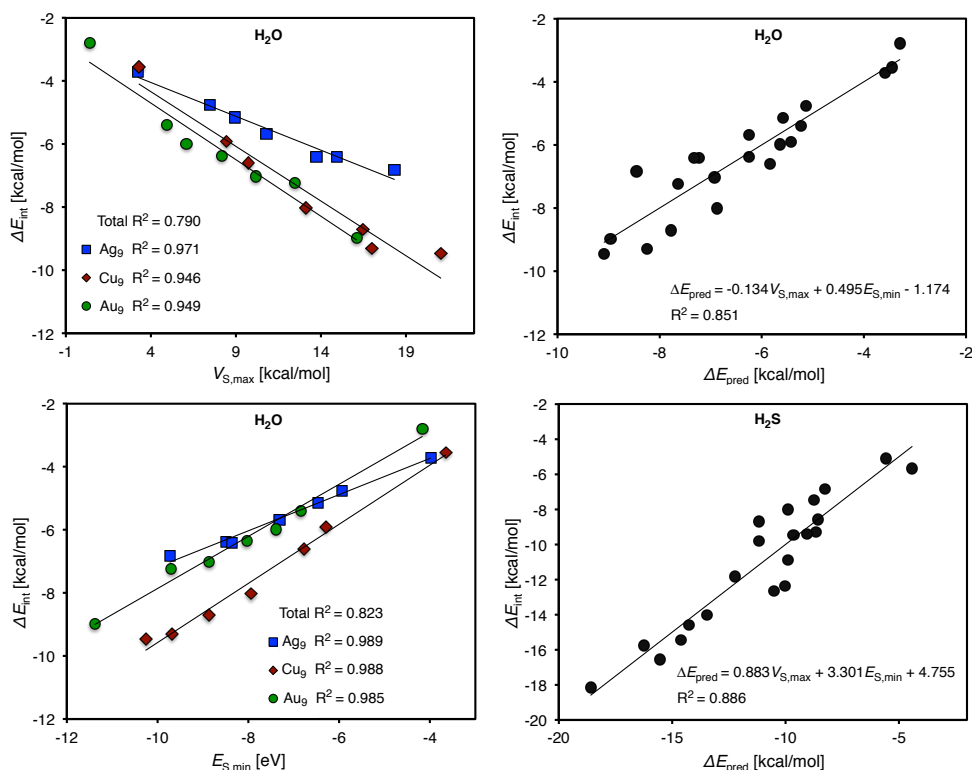


Figure 42. Particle resolved linear correlation plots between H_2O interaction energies (ΔE_{int}) and $V_{\text{S,max}}$ (top left) as well as $E_{\text{S,min}}$ (bottom left). Adsorption to all Au_9 , Ag_9 and Cu_9 sites compared to multi-linear correlations between $V_{\text{S,max}}$ and $E_{\text{S,min}}$ for H_2O (top right) and H_2S (bottom right); $V_{\text{S,max}}$ ($E_{\text{S,min}}$) in kcal mol⁻¹ (eV) in the multi-linear equations.

pronounced effect going from the individual R^2 of 0.11 and 0.50 for $V_{\text{S,max}}$ and $E_{\text{S,min}}$, respectively, to $R^2=0.886$ for the multi-linear relation (see **Figure 42**). From this analysis one can conclude that H_2S interactions involve a larger portion of charge-transfer whereas the H_2O interactions are mainly electrostatic in nature.

CO adsorption onto the larger Ag nanoclusters was compared to atomic CM5M charges by Duanmu et al., who found clear linear trends.⁴⁰⁶ However, $V_{\text{S,max}}$ and $E_{\text{S,min}}$ compare more favorably with the CO interaction energies than CM5M charges ($V_{\text{S,max}}$ and $E_{\text{S,min}}$ **Figure 43**). The same is true when comparing to other atomic charges such as NBO, Mulliken or Bader charges (see **Paper XI**). The total correlations over all sites and particles are fairly good suggesting that this could be used as a calibration curve for the estimation of interaction trends for other Ag NPs not included in **Paper XI**. All that is needed is the assignment of local $V_{\text{S,max}}$ and/or $E_{\text{S,min}}$ for the new NPs.

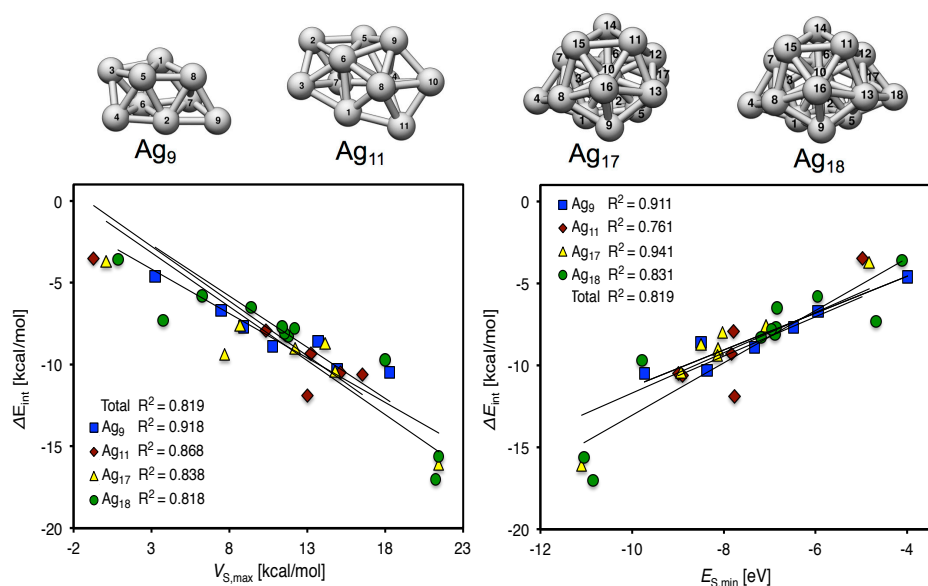


Figure 43. Linear correlation plots between CO interaction energies (ΔE_{int}) and $V_{S,\text{max}}$ (left) as well as $E_{S,\text{min}}$ (right).

Lewis acidity of TiO₂ nanoparticles

The study of transition metal oxides is challenging in general terms. One has in particular been found it difficult to rationalize interaction properties of oxides based on simple ground state descriptors.^{305,315,328} The novelty of **Paper XII** is that it shows the first examples of the ability of the $E(\mathbf{r})$ and $V(\mathbf{r})$ descriptors for the estimation of local Lewis acidity of oxide compounds.^{lvi} In **Paper XII** emphasis was directed on the H₂O, H₂S, NH₃ and CO Lewis bases interactions with TiO₂ nanoparticles. TiO₂ is a common material in many applications including dye-sensitized solar cells,^{409,410} gas sensors,⁴¹¹ photocatalysts,^{412–414} gas and water purification,^{413,415–419} sunscreens and pigments. In addition, certain phases of Ti_xO_{2x-1} NPs are toxic,⁴²⁰ why understanding of the interactions of titanium oxides are of further importance.

Figure 44 shows a series of low energy (TiO₂)_n, n=7-10, nanoparticles identified by Berardo et al.⁴²¹ It also includes favored adsorption positions for the H₂O, H₂S, NH₃ and CO Lewis bases onto (TiO₂)₇, as well as the LUMO and the

^{lvi} Interaction energies (ΔE_{int}) are determined at the PBEo-D3(BJ)//PBEo level in Gaussian 09 with LANL2TZ(+f) basis set^{351,407,408} on Ti, and a 6-31+G(d,p) for the main elements during optimization and a 6-311+G(2df,2p) basis set for the final energy evaluations. $V(\mathbf{r})$ and $E(\mathbf{r})$ were evaluated from KS wave functions obtained at the PBEo/LANL2TZ [Ti]-6-311+G(2d,2p) level of theory.^{225,351,407,408}

$V_S(\mathbf{r})$ and $E_S(\mathbf{r})$ profiles of $(\text{TiO}_2)_7$. TiO_2 is a largely ionic compound consisting of Ti^{4+} and O^{2-} ions. Thus it is not surprising that the magnitudes of both the $V_{S,\text{max}}$ and $E_{S,\text{min}}$ are much larger than those found on e.g. the TM metal nanoclusters in the preceding parts of this thesis. It was found that the positions of the $V_{S,\text{max}}$ and $E_{S,\text{min}}$ coincide well with the identified adsorption sites, i.e. the Ti^{4+} ions. It was also found that all four adsorbates interact by very similar modes in the sense that all interactions are largely electrostatically driven.

As seen in **Figure 45**, the interaction trends are well reproduced for all adsorbates by both $V_{S,\text{max}}$ and $E_{S,\text{min}}$. The linear trends are strong within each individual adsorbate-particle series, but also for all particles in total. As was also suggested for the case of Ag NP of **Paper XI**, the obtained linear correlations can be used as calibration curves to estimate site-resolved interaction energies of other TiO_2 NPs as long as their local $V_{S,\text{max}}$ and $E_{S,\text{min}}$ are determined. This was tested in **Paper XII** by the formation of calibration curves from the $n=7$ and 8 NPs for estimations of the $n=9$ and 10 NPs' interaction energies. For H_2O this gives a small root mean square deviation (RMSD) of 0.07 eV, and thus encouraging results for using this approach on a larger scale. We also found that it is possible to predict the interaction energies of all adsorbates simultaneously by the formation of multi-linear descriptor including $V_{S,\text{max}}$ at the TiO_2 adsorption sites as well as the

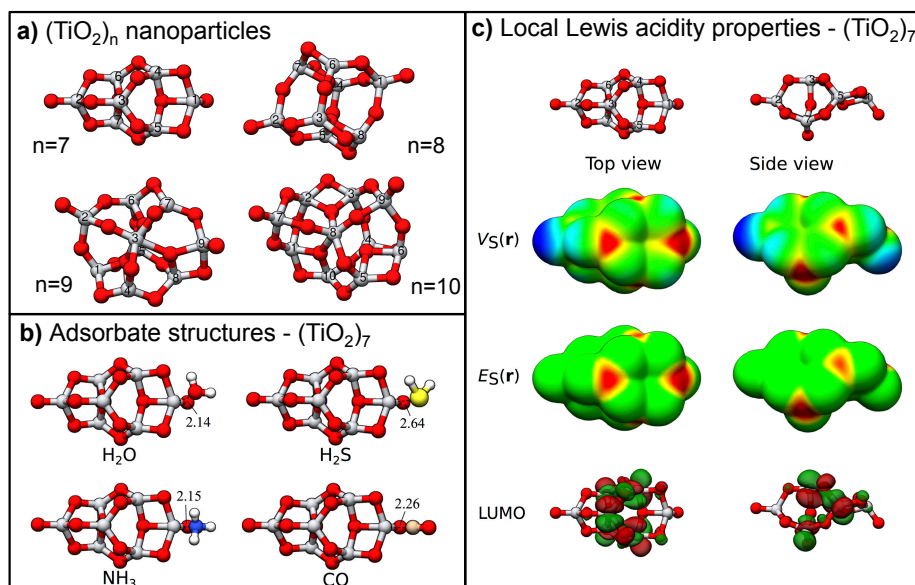


Figure 44. In a) are the structures of the $(\text{TiO}_2)_n$, $n=7-10$, NP shown, b) shows the favored adsorption sites for the considered Lewis bases onto $(\text{TiO}_2)_7$, and c) shows the $V_S(\mathbf{r})$, $E_S(\mathbf{r})$ at the 0.001 a.u. isodensity surface, and LUMO of the $(\text{TiO}_2)_7$ particle. Color code (colors are centered on), $V_S(\mathbf{r})$ in kcal mol^{-1} : blue = -40, cyan = -20, green = 0, yellow = 50, red > 95; $E_S(\mathbf{r})$ in eV: green = -5.0, yellow = -10.0, red = -30.0.

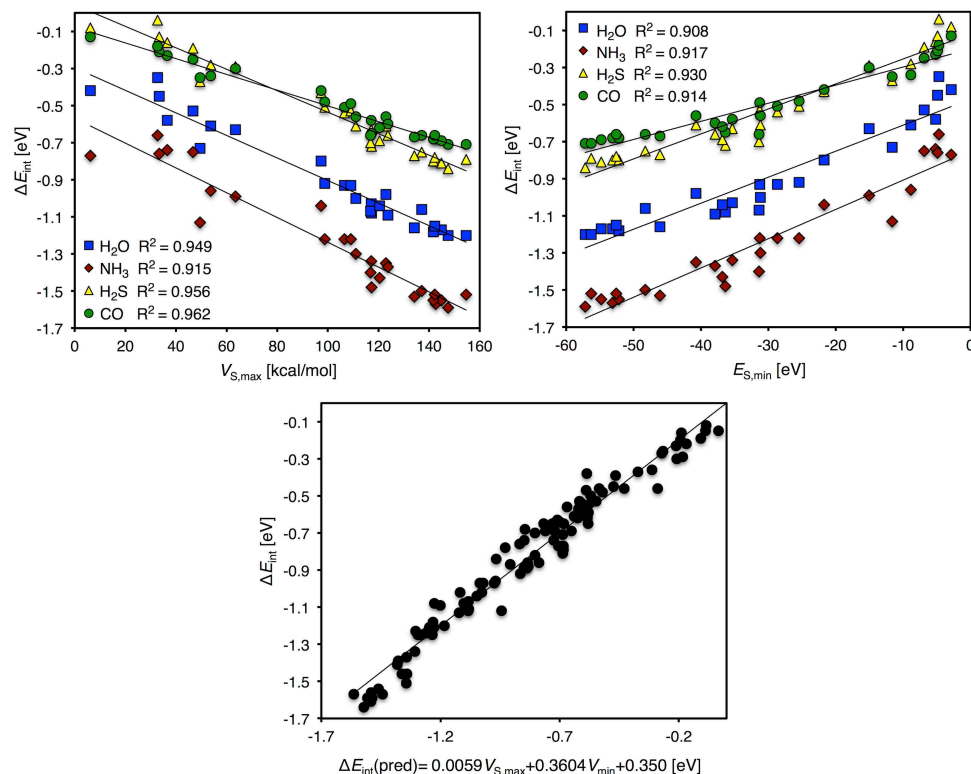


Figure 45. Linear correlation plots between calculated interaction energies (ΔE_{int}) and $V_{S,\text{max}}$ (top left) and $E_{S,\text{min}}$ (top right) at the site of interactions for the $(\text{TiO}_2)_n$, $n=7-10$, NPs. The bottom figure show the correlation between ΔE_{int} and predicted ΔE_{int} from the multi-linear combination of $V_{S,\text{max}}$ of the TiO_2 NP and V_{min} of the Lewis base ($R^2=0.963$).

spatial minima in $V(\mathbf{r})$ [V_{min}] at the interaction site of the Lewis bases. The multi-linear correlation between yields a universal trend with an R^2 of 0.963 (**Figure 45**). All taken together, the results of **Paper XII** are promising for future applications in rationalization and prediction of oxide interactions.

4.2.5. Molecular adsorption on extended metal and oxide surfaces

The $E_S(\mathbf{r})$ and $V_S(\mathbf{r})$ properties are well suited also for the study of extended transition metal and oxide surfaces as discussed in **Paper XIII**. However, the computational evaluation of both these properties has to be adapted and generalized in order to fit a solid-state framework as outlined in **Paper XIII** and in section 4.2.1 of this thesis. $E(\mathbf{r})$ is calculated by eq. 4.17 (or 4.18 for spin-polarized calculations) of section 4.2.1, whereas $V(\mathbf{r})$ is evaluated using the modified form below:

$$V(\mathbf{r}) = \sum_A \frac{Z_A}{|\mathbf{R}_A - \mathbf{r}|} - \int \frac{\rho(\mathbf{r}')d\mathbf{r}'}{|\mathbf{r}' - \mathbf{r}|} - V^{\text{vac}} \quad (4.20)$$

The $V(\mathbf{r})$ is thereby shifted back from the system-dependent relative scale of a periodic calculation to an (approximately) absolute scale by the comparison to the electrostatic potential at the mid-point of the vacuum region (V^{vac}), facilitating intercompound comparison.

Figure 46 shows $E_S(\mathbf{r})$ and $V_S(\mathbf{r})$ evaluated^{lvii} on a selection of surfaces; the stoichiometric (1×1)-Cu₂O(111), TiO₂(110)^{lviii} and Pt(111). For Cu₂O(111) the most prominent $E_{S,\text{min}}$ and $V_{S,\text{max}}$ are located at the Cu_{CUS} atom identifying this as the primary electrophilic site on this surface. As described in sections 4.1.3 and 4.1.4 this is well in line with the previously described interactions of the H₂O, H₂S and methanol nucleophiles onto this surface. Furthermore, the $V_{S,\text{min}}$ of largest magnitude is located at the O_{CUS} correctly marking this as the most Lewis basic surface site. Concerning the TiO₂(110) surface it is known from both experiments and computations that the five-fold coordinated Ti_{5f} is the surface site most susceptible to interactions with nucleophiles, in agreement with the $E_S(\mathbf{r})$ and $V_S(\mathbf{r})$ profiles of the surface.^{424–427} On the Pt(111) surface H₂O and CO favor the Pt *on top* site over the bridge or hollow sites.^{167,272,428–430} The *on top* sites coincide with the positions of the $E_{S,\text{min}}$ and $V_{S,\text{max}}$ on the surface. In summary, $E_S(\mathbf{r})$ and $V_S(\mathbf{r})$ provide useful information on the adsorption properties of the surfaces. They can be used to identify sites of interaction and rationalize experimental and computational results.

Regarding adsorption trends, both $E_{S,\text{min}}$ and $V_{S,\text{max}}$ show promising results also for surfaces. A selection of examples is included in **Paper XIII**. Firstly it was found that $E_{S,\text{min}}$ and $V_{S,\text{max}}$ rank the electrophilicity of the low-index Cu *fcc* surfaces as (110)>(100)>(111) in agreement with the results of Wang and Nakamura.¹⁶³ Adsorption trends as a function of metal are also captured. High quality experimental data for CO adsorption energies onto transition metal *fcc* (111) surfaces has been summarized by Wellendorff et al.⁴²³ In **Figure 47.a** adsorption energies for Cu, Pt, Ni, Rh and Ir are compared with $E_{S,\text{min}}$ at the metal *on top* site yielding a correlation coefficient (R^2) of 0.886. This is a fairly good correlation, much better than the 0.260 of $V_{S,\text{max}}$. Thus it seems the difference in

^{lvii} The calculations were carried out at the PBE level of theory for the *fcc* metals and at the PBE-D3(BJ)+U level^{221,233,236,354} for the oxides using periodic slab models in the VASP^{338–342} software package

^{lviii} TiO₂(110) is the most common low-index TiO₂ surface.⁴²²

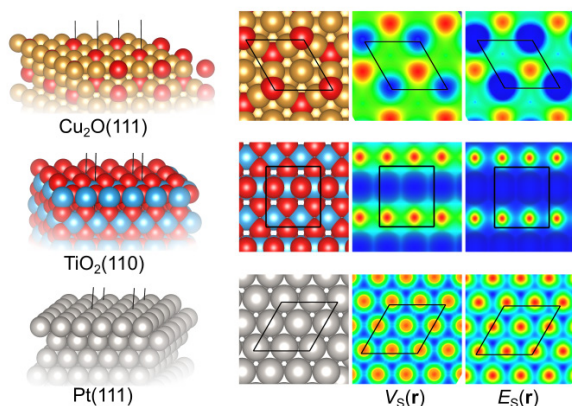


Figure 46. Structures and corresponding $V_S(\mathbf{r})$ and $E_S(\mathbf{r})$ profiles at the 0.001 a.u. isodensity contour for a selection of surfaces. The (1×1) surface unit cells are marked for the oxides, the (2×2) for Pt.

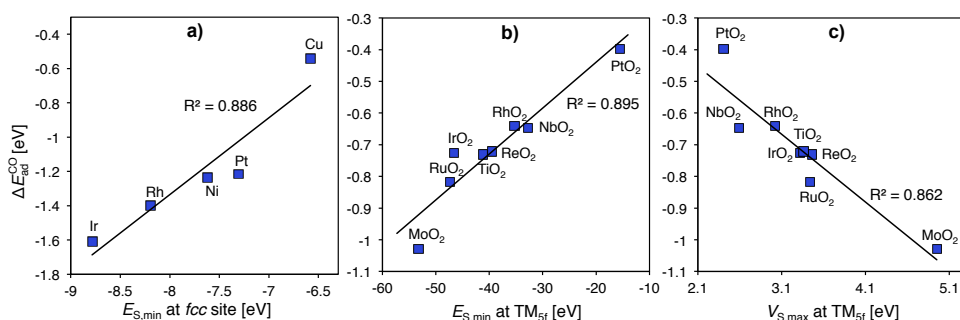


Figure 47. Showing correlation for CO adsorption energies ($\Delta E_{\text{ad}}^{\text{CO}}$) compared to local descriptor values at the adsorption site. In a): experimental⁴²³ $\Delta E_{\text{ad}}^{\text{CO}}$ versus $E_{S,\text{min}}$ for fcc TM(111) surfaces. In b) and c): computed $\Delta E_{\text{ad}}^{\text{CO}}$ versus $E_{S,\text{min}}$ and $V_{S,\text{max}}$ for TMO₂ oxides of the rutile family.

adsorption tendencies over the series of metals is reflected by the charge-transfer capabilities of the surfaces rather than variations in the Coulombic interaction. This is in agreement with the success of the d -band model that captures orbital-mixing effects but downplays electrostatics (section 3.4.5).

Figure 47.b-c shows adsorption trends for CO versus $E_{S,\text{min}}$ and $V_{S,\text{max}}$ on a series of TMO₂ oxides of the rutile family, TM=Mo, Ru, Ir, Re, Ti, Rh, Nb, Pt. Oxides are considerably more complex to study experimentally than metals, why accurate experimental data for large series of congeneric surfaces are difficult to

find. Thus the herein reported adsorption energies (ΔE_{ad}) were calculated by DFT^{lix} (details in **Paper XIII**). CO adsorbs at the $\text{Ti}_{5\text{f}}$ site and the corresponding ΔE_{ad} shows good correlations with the local $E_{\text{S,min}}$ and $V_{\text{S,max}}$ ($R^2=0.895$ and 0.862). The correlation can be increased to $R^2=0.962$ by the formation of a multi-linear relationship between $E_{\text{S,min}}$ and $V_{\text{S,max}}$ ($\Delta E_{\text{pred}}=0.0086E_{\text{S,min}}-0.1064V_{\text{S,max}}-0.0240$ [eV]). This suggests a mixed charge-transfer and electrostatically controlled interaction.

In summary, the applicability of $E_{\text{S}}(\mathbf{r})$ and $V_{\text{S}}(\mathbf{r})$ has been shown for both transition metal and oxide surfaces. The descriptors provide information on regioselectivity and reproduce interaction trends with nucleophiles. The results for oxides are remarkable since these compounds are known to be notoriously difficult to describe by simple ground state descriptors.^{305,315,328} As in the cases of molecules and nanoparticles, the potential applications of the descriptors are broad (see chapter 5).

^{lix} The calculations were carried out at the PBE-D3(BJ)+U level of theory^{221,233,236,354} using periodic slab models in the VASP^{338–342} software package. Lattice parameters and +U values were taken from Xu et al.⁴³¹

5. Outlook and concluding remarks

As a conclusion to this thesis, a few words of perspective will be given. Within this thesis two seemingly different but *de facto* largely overlapping fields of chemistry have been considered. These encompass corrosion of copper-based materials and fundamental studies of chemical interactions of molecules, particles and surfaces.

Regarding copper-based materials, this thesis has contributed with answers concerning the behavior of copper materials under the expected conditions of a future repository for SNF in Sweden – in particular with respect to the corrosion of nanostructured copper materials and copper oxide surfaces in aqueous solution. The results are in support of the established copper-water thermodynamics for the copper-water system and in agreement with parallel experimental work by other groups. In summary, the prevailing scientific questions with regards to the SNF repository, following the presented work, are related to the mechanism and kinetics of the sulphidation of cuprite (and of other initially formed Cu corrosion products), and the mechanism of long-term sulphide induced copper corrosion.

The investigations of the copper materials have many links to the general studies of chemical interactions – partly as a source of inspiration in the evolution of our analysis methods from a molecular perspective towards a focus on solid materials, and partly as a test case for the newly developed methods. As demonstrated in the presented work, the joint toolbox of the $E(\mathbf{r})$, $V(\mathbf{r})$ and $\tilde{I}(\mathbf{r})$ properties provides a useful arsenal for the study of chemical interactions of molecules, nanoparticles and extended surfaces. Notably, this also includes compounds based on transition metal oxides that are notoriously difficult to rationalize based on simple descriptors. An excellent application for the descriptors is as initial *reactivity maps* or *interaction affinity maps* for the fundamental understanding and visualization of chemical reactivity, potentially providing a new chapter to the basic physical chemistry textbooks. Other uses are envisaged in retrosynthetic analysis and for identification of drug candidates. The descriptors are, moreover, particularly well adapted for use in large-scale screenings of new materials, possibly in conjugation with artificial intelligence and machine learning. Potential areas of application are e.g. heterogeneous catalysis, CO₂ capturing or H₂ storage, and docking in enzymatic active sites. An inherited deficiency of $\tilde{I}(\mathbf{r})$ and $E(\mathbf{r})$ is, however, that they are only defined for one-determinantal methods (e.g. KS-DFT or HF) in their original forms. This restricts their potential to systems that are well described within this framework and prevents benchmarking with high-level methods. Ryabinkin et al.⁴³² have, however, recently suggested an extension of the $\tilde{I}(\mathbf{r})$ property to correlated wave functions. Future directions for the descriptors could follow this path. All things considered, one of the largest advantages of the studied descriptor is their high accuracy to computational cost ratio, which will grant their future applicability.

List of abbreviations

A	Helmholtz free energy
a.u.	atomic units
AES	Auger Electron Spectroscopy
B3LYP	A DFT hybrid xc-functional
BL	Bilayer
BMN	Benzylidenemalononitriles
CLS	Core-Level Shift
CS	Coordinatively Saturated site
CUS	Coordinatively Unsaturated site
D3(BJ)	D3 dispersion correction with Becke-Johnson damping
DFA	Density Functional Approximation
DFT	Density Functional Theory
DOS	Density Of States
$E(\mathbf{r})$	Local electron attachment energy
EA	Electron affinity
ECP	Effective Core Potential
EDA	Energy Decomposition Analysis
E_F	Fermi level, Fermi energy
EFP	Effective Fragment Potential
Eh	Redox potential
$E_{S,max}$	Isosurface maximum in $E(\mathbf{r})$
fcc	face-centered cubic
G	Gibbs free energy
GGA	Generalized Gradient Approximation
GKS	Generalized Kohn-Sham
GTO	Gaussian-Type Orbital
H	Enthalpy
\hat{H}	The Hamilton operator
HF	Hartree-Fock
HOMO	Highest Occupied Molecular Orbital
I	Ionization energy
$\bar{I}(\mathbf{r})$	Local average ionization potential

$\bar{I}_{S,\min}$	Isosurface minimum in $\bar{I}(\mathbf{r})$
LCAO	Linear Combination of Atomic Orbitals
LUMO	Lowest Unoccupied Molecular Orbital
MD	Molecular Dynamics
ML	Monolayer
MM	Molecular Mechanics
NAS	Nucleophilic Aromatic Substitution
NP	NanoParticle
PAW	Projector-Augmented Wave
PBE	A DFT GGA xc-functional
PBEo	A DFT hybrid xc-functional
PCM	Polarizable Continuum Model (e.g. IEF-PCM and COSMO)
PES	Potential Energy Surface
QM	Quantum Mechanics
R^2	Coefficient of determination, or correlation coefficient
RDF	Radial Distribution Function
S	Entropy
SA	Simulated Annealing
S_NAr	Nucleophilic Aromatic Substitution
SNF	Spent Nuclear Fuel
STM	Scanning Tunneling Microscopy
TM	Transition Metal
TS	Transition-State
$V(\mathbf{r})$	Electrostatic Potential
V_{\min}	Spatial minimum in $V(\mathbf{r})$
VNS	Vicarious Nucleophilic Substitution
$V_{S,\max}$	Isosurface maximum in $V(\mathbf{r})$
$V_{S,\min}$	Isosurface minimum in $V(\mathbf{r})$
WFT	Wave-Function Theory
xc	exchange-correlation
XPS	X-ray Photoemission Spectroscopy
$\rho(\mathbf{r})$	Electron density, $ \Psi(\mathbf{r}) ^2$
Ψ	Wave-function

Acknowledgements

My dear friends, colleagues and family members – this thesis could not have been accomplished without your help. My sincerest thanks to all of you!

To my supervisor **Tore Brinck**. It has been a true pleasure working with you. Thanks for educating me in quantum chemistry and for trusting me with these projects. Thanks also for always being available for discussions, for finding and correcting even the smallest little error and for keeping an eye on me during my various scientific excursions.

My co-supervisors **Johannes Johansson** and **Christofer Leygraf**, I cannot thank you enough. Johannes – your unlimited curiosity and sharp analysis have been a wonderful resource. Thanks for your guidance, encouragement and friendship. Christofer – your expertise, scientific split-vision and experimental perspective have been inspiring and truly valuable to our projects. I am grateful for all your help and advice.

I would also like to express my deepest gratitude to my collaborators and co-authors **Jonas Weissenrieder**, **Markus Soldemo**, **Mats Götelid**, **Zahra Besharat**, **Anneli Önsten**, **Milad Yazdi**, **Kess Marks**, **Magnus Johnson**, **Henrik Öström**, **Peter Carlqvist**, and **Lars Kloo**. This thesis would not have been possible without your contributions.

Special thanks are also directed to **Mårten Ahlquist**, **Fredrik Schaufelberger**, **Jan Stenlid**, **Maria Halldin Stenlid**, **Henrik Öberg**, my supervisors **Tore**, **Johannes**, and **Christofer**, my co-authors and colleagues **Mats**, **Jonas**, **Camilla**, and **Björn Dahlgren** for invaluable comments on the thesis and meticulous proofreading.

In addition I would like to acknowledge **Christina Lilja** of the Swedish Nuclear fuel and Waste Management Company for her continuous support and feedback. Special thanks are also directed to **Pavel Korzhavi**, **Claudio Lousada**, and **Jan Rosdahl** for computational assistance.

Always with insightful scientific advice, a profound generosity of your technical expertise and a big heart, **Björn Dahlgren** I am fortunate to be your friend and colleague. Please bike safely!

Camilla Gustafsson, I am lucky to have shared this journey with you. Thanks for your inspiration and for all the good memories!

To all other past and current members of the Brinck group – **Max, Mats, Henrik, Mika, Björn E, Dhebbajaj, Anirudh, Martin, Lucas, Polina** and **Erik** (our honorary member) – you have made these years truly enjoyable. Thank you very much!

My sincerest appreciations are also directed to all my friends and colleagues at applied physical chemistry over the years. We've had so much fun together – cheers!

Ricardo, 'Ricardinho', it has been an honor getting to know you. Thank you for embracing me in your Portuguese culture and for not crashing the Clio. See you 7.30 at the gym /the PP-crew. Muito Obrigado!

Lena, Ulla and **Vera**, all your advice and support have been much appreciated!

Thanks also to my extended family, to my friends and all my "gangs" – the lunch gang, the football and innebandy gangs – you know who you are! **Rasmus Karlsson**, thanks for your dedication organizing the QM journal club and chairing the 2014/15 graduate students board and council. Thanks also to all members of the board and to the organizing committee of the 2015 PhD day.

Financial support from the Swedish Nuclear fuel and Waste Management Company (SKB), and the KTH CHE excellence award is gratefully acknowledged. I am also thankful for the generous computational resources provided by the Swedish National Infrastructure for Computing (SNIC), the National Supercomputer Centre (NSC) at Linköping University and the PDC Centre for High Performance Computing (PDC-HPC).

Stina, ditt stöd betyder så oerhört mycket. Tack för din kärlek och för att du bubblar av glädje, påhittighet och energi. Tillsammans med dig är inget omöjligt. Älskar dig!

Till min fantastiska familj – **Mamma, Pappa** och **Rasmus**: Tack för allt ni har gjort för mig genom åren, för att ni alltid engagerar er och alltid tar er tid. Ni är helt enkelt bäst!

Bibliography

1. SKB, Spent nuclear fuel for disposal in the KBS-3 repository, TR-10-13, Swedish Nuclear Fuel and Waste Management Co, **2010**.
2. SKB, Long-term safety for the final repository for spent nuclear fuel at Forsmark: Main report of the SR-Site project, TR-11-01, Swedish Nuclear Fuel and Waste Management Co, **2011**.
3. www.world-nuclear.org, World Nuclear Association, accessed 11th of August 2017.
4. POSIVA, SKB, Safety functions, performance targets and technical design requirements for a KBS-3V repository: Conclusions and recommendations from a joint SKB and Posiva working group, Posiva SKB Report 01, Posiva Oy and Swedish Nuclear Fuel and Waste Management Co, **2017**.
5. J. Noronha, Deep Geological Repository Conceptual Design Report Crystalline / Sedimentary Rock Environment, NWMO report APM-REP-00440-0015 R001, Nuclear Waste Management Organization, Canada, **2016**.
6. SKB, Design, production and initial state of the canister, TR-10-14, Swedish Nuclear Fuel and Waste Management Co, **2010**.
7. F. King, *Corrosion*, **2013**, 69, 986.
8. SKB, Design premises for a KBS-3V repository based on results from the safety assessment SR-Can and some subsequent analyses, TR-09-22, Swedish Nuclear Fuel and Waste Management Co, **2009**.
9. SSM, Granskningsrapport Systemövergripande frågor, SSM2011-1135-16, Swedish Radiation Safety Authority, **2016**.
10. J. W. Erning, M. Sailer, C. Pescatore, F. Boissier, J. Kessler, J. Kotra, S. Löw, J. C. Mayor, S. Stroes-Gascoyne, T. Tokunaga, and K. Compton, The post-closure radiological safety case for a spent fuel repository in Sweden, Nuclear Energy Agency Report NEA/RWM/PEER(2012)2, **2012**.
11. H. Eyring, *J. Chem. Phys.*, **1935**, 3, 107.
12. M. J. S. Phipps, T. Fox, C. S. Tautermann, and C.-K. Skylaris, *Chem. Soc. Rev.*, **2015**, 44, 3177.
13. M. von Hopffgarten and G. Frenking, *Wiley Interdiscip. Rev. Comput. Mol. Sci.*, **2012**, 2, 43.
14. F. M. Bickelhaupt and E. J. Baerends, "Reviews in Computational Chemistry", ed. Kenny B. Lipkowitz and Donald B. Boyd, **2000**, John Wiley & Sons, Inc., pp. 1.
15. P. Politzer, J. S. Murray, and T. Clark, *J. Mol. Model.*, **2015**, 21, 52.
16. S. F. Boys and F. Bernardi, *Mol. Phys.*, **2002**, 100, 65.
17. K. Morokuma, *J. Chem. Phys.*, **1971**, 55, 1236.
18. K. Kitaura and K. Morokuma, *Int. J. Quantum Chem.*, **1976**, 10, 325.
19. K. Morokuma, *Acc. Chem. Res.*, **1977**, 10, 294.
20. R. Z. Khaliullin, E. A. Cobar, R. C. Lochan, A. T. Bell, and M. Head-Gordon, *J. Phys. Chem. A*, **2007**, 111, 8753.
21. D. G. Fedorov and K. Kitaura, *J. Comput. Chem.*, **2007**, 28, 222.
22. T. Ziegler and A. Rauk, *Theoret. Chim. Acta*, **1977**, 46, 1.
23. T. Ziegler and A. Rauk, *Inorg. Chem.*, **1979**, 18, 1755.
24. T. Ziegler and A. Rauk, *Inorg. Chem.*, **1979**, 18, 1558.
25. J. P. Foster and F. Weinhold, *J. Am. Chem. Soc.*, **1980**, 102, 7211.
26. A. E. Reed, R. B. Weinstock, and F. Weinhold, *J. Chem. Phys.*, **1985**, 83, 735.
27. E. D. Glendening, *J. Phys. Chem. A*, **2005**, 109, 11936.

28. E. D. Glendening and A. Streitwieser, *J. Chem. Phys.*, **1994**, *100*, 2900.
29. B. Jeziorski, R. Moszynski, A. Ratkiewicz, S. Rybak, K. Szalewicz, and H. L. Williams, "Methods and techniques in computational chemistry: METECC-94", ed. E. Clementi, **1993**, Vol. B, STEF, Cagliari.
30. B. Jeziorski, R. Moszynski, and K. Szalewicz, *Chem. Rev.*, **1994**, *94*, 1887.
31. H. L. Williams and C. F. Chabalowski, *J. Phys. Chem. A*, **2001**, *105*, 646.
32. R. G. Pearson, "Chemical Hardness", **1997**, Wiley-VCH Verlag GmbH & Co. KGaA.
33. J. S. Murray, T. Brinck, P. Lane, K. Paulsen, and P. Politzer, *THEOCHEM*, **1994**, *307*, 55.
34. T. Brinck, *J. Phys. Chem. A*, **1997**, *101*, 3408.
35. J. S. Murray, T. Brinck, and P. Politzer, *Chem. Phys.*, **1996**, *204*, 289.
36. P. Politzer and J. S. Murray, *Mod. Aspect. Electroc.*, **2006**, *39*, 1.
37. P. Sjöberg, J. S. Murray, T. Brinck, and P. Politzer, *Can. J. Chem.*, **1990**, *68*, 1440.
38. T. Brinck, "Theoretical Organic Chemistry", ed. C. Párkányi, 1st Edn ed., **1998**, Vol. 5, Elsevier Science B.V., Amsterdam.
39. M. Schlosser and R. Ruzziconi, *Synthesis*, **2010**, *13*, 2111.
40. J. Miller, "Aromatic Nucleophilic Substitution", **1968**, Elsevier, Amsterdam.
41. J. March and M. B. Smith, "March's Advanced Organic Chemistry, Reactions, Mechanism and Structure", 6th ed. **2007**, John Wiley & Sons, New York.
42. M. Małkosza, *Chem. Soc. Rev.*, **2010**, *39*, 2855.
43. F. Terrier, "Modern Nucleophilic Aromatic Substitution", **2013**, Wiley-VCH, Weinheim, Germany.
44. M. N. Glukhovtsev, R. D. Bach, and S. Laiter, *J. Org. Chem.*, **1997**, *62*, 4036.
45. I. Fernández, G. Frenking, and E. Uggerud, *J. Org. Chem.*, **2010**, *75*, 2971.
46. M. Liljenberg, T. Brinck, B. Herschend, T. Rein, S. Tomasi, and M. Svensson, *J. Org. Chem.*, **2012**, *77*, 3262.
47. A. H. M. Renfrew, J. A. Taylor, J. M. J. Whitmore, and A. Williams, *J. Chem. Soc., Perkin Trans. 2*, **1993**, 1703.
48. J. Goliński and M. Małkosza, *Tetrahedron Lett.*, **1978**, *19*, 3495.
49. M. Małkosza and J. Winiarski, *Acc. Chem. Res.*, **1987**, *20*, 282.
50. M. Małkosza and K. Wojciechowski, *Chem. Rev.*, **2004**, *104*, 2631.
51. M. Małkosza, *Synthesis*, **2011**, *2011*, 2341.
52. M. Małkosza, *Chem. Eur. J.*, **2014**, *20*, 5536.
53. T. Brinck, J. S. Murray, and P. Politzer, *Int. J. Quantum Chem.*, **1992**, *44*, 57.
54. P. Politzer, P. Lane, M. C. Concha, Y. Ma, and J. S. Murray, *J. Mol. Model.*, **2007**, *13*, 305.
55. E. Roduner, *Chem. Soc. Rev.*, **2006**, *35*, 583.
56. J. Kleis, J. Greeley, N. A. Romero, V. A. Morozov, H. Falsig, A. H. Larsen, J. Lu, J. Mortensen, M. Dułak, K. S. Thygesen, J. K. Nørskov, and K. W. Jacobsen, *Catal. Lett.*, **2011**, *141*, 1067.
57. S. Royer and D. Duprez, *ChemCatChem*, **2011**, *3*, 24.
58. R. Ferrando, J. Jellinek, and R. L. Johnston, *Chem. Rev.*, **2008**, *108*, 845.
59. P. Di Pietro, G. Strano, L. Zuccarello, and C. Satriano, *Curr. Top. Med. Chem.*, **2016**, *16*, 3069.
60. D. Kwatra, A. Venugopal, and S. Anant, *Transl. Cancer Res.*, **2013**, *2*, 330.
61. M. Kopp, S. Kollenda, and M. Epple, *Acc. Chem. Res.*, **2017**, *50*, 1383.
62. P. C. Stair, *J. Am. Chem. Soc.*, **1982**, *104*, 4044.
63. A. Zecchina, C. Lamberti, and S. Bordiga, *Catal. Today*, **1998**, *41*, 169.

64. M. W. Abee, Doctoral thesis, Virginia Polytechnic Institute and State University, **2001**.
65. W. K. Hall, B. E. Spiewak, R. D. Cortright, J. A. Dumesic, H. Knözinger, H. Pfeifer, V. B. Kazansky, and G. C. Bond, “*Handbook of Heterogeneous Catalysis*”, ed. G. Ertl, H. Knözinger, and J. Weitkamp, **1997**, Wiley-VCH Verlag GmbH, pp. 689.
66. A. Nilsson and L. G. M. Pettersson, “*Chemical Bonding at Surfaces and Interfaces*”, ed. A. Nilsson, L. G. M. Pettersson, and J. K. Nørskov, **2008**, Elsevier, Amsterdam, pp. 57.
67. USGS, U.S. Geological Survey, Mineral Commodity Summaries, January 2017 (<https://minerals.usgs.gov/>), Retrieved August 11, 2017.
68. N. N. Greenwood and A. Earnshaw, “*Chemistry of the Elements (Second Edition)*”, 2:nd ed., **1997**, Butterworth-Heinemann, Oxford, 1173.
69. A. Lossin, “*Copper. Ullmann’s Encyclopedia of Industrial Chemistry*”, **2001**, Wiley-VCH Verlag GmbH & Co. KGaA.
70. M. W. Covington, N. L. Church, W. H. Dresher, and B. R. Cooper, “*Digital Encyclopedia of Applied Physics*”, **2003**, WILEY-VCH Verlag GmbH & Co KGaA.
71. C. Leygraf, I. Odnevall Wallinder, J. Tidblad, and T. E. Graedel, “*Atmospheric Corrosion*”, **2016**, 2nd ed., John Wiley & Sons, Hoboken, NJ.
72. P. A. Korzhavyi and B. Johansson, Literature review on the properties of cuprous oxide Cu₂O and the process of copper oxidation, TR-11-08, Swedish Nuclear Fuel and Waste Management Co, **2011**.
73. J. Zhang and H. W. Richardson, “*Copper Compounds. Ullmann’s Encyclopedia of Industrial Chemistry*”, **2016**, Wiley-VCH Verlag GmbH & Co. KGaA.
74. K. C. Waugh, *Catal. Today*, **1992**, *15*, 51.
75. A. Paracchino, V. Laporte, K. Sivula, M. Grätzel, and E. Thimsen, *Nat. Mater.*, **2011**, *10*, 456.
76. A. A. Gokhale, J. A. Dumesic, and M. Mavrikakis, *J. Am. Chem. Soc.*, **2008**, *130*, 1402.
77. T. Minami, Y. Nishi, T. Miyata, and J. Nomoto, *Appl. Phys. Express*, **2011**, *4*, 62301.
78. H. M. Wei, H. B. Gong, L. Chen, M. Zi, and B. Q. Cao, *J. Phys. Chem. C*, **2012**, *116*, 10510.
79. B. P. Rai, *Solar Cells*, **1988**, *25*, 265.
80. E. I. Solomon, U. M. Sundaram, and T. E. Machonkin, *Chem. Rev.*, **1996**, *96*, 2563.
81. B. K. Meyer, A. Polity, D. Reppin, M. Becker, P. Hering, P. J. Klar, T. Sander, C. Reindl, J. Benz, M. Eickhoff, C. Heiliger, M. Heinemann, J. Bläsing, A. Krost, S. Shokovets, C. Müller, and C. Ronning, *Phys. Status Solidi B*, **2012**, *249*, 1487.
82. P. A. Korzhavyi, I. Soroka, M. Boman, and B. Johansson, *Solid State Phenom.*, **2011**, *172–174*, 973.
83. A. Werner and H. D. Hochheimer, *Phys. Rev. B*, **1982**, *25*, 5929.
84. S. S. Hafner and S. Nagel, *Phys. Chem. Minerals*, **1983**, *9*, 19.
85. Y. Li and P. A. Korzhavyi, *Dalton Trans.*, **2017**, *46*, 529.
86. J. M. Zuo, M. Kim, M. O’Keeffe, and J. C. H. Spence, *Nature*, **1999**, *401*, 49.
87. I. L. Soroka, A. Shchukarev, M. Jonsson, N. V. Tarakina, and P. A. Korzhavyi, *Dalton Trans.*, **2013**, *42*, 9585.
88. P. A. Korzhavyi, I. L. Soroka, E. I. Isaev, C. Lilja, and B. Johansson, *Proc. Natl. Acad. Sci. U.S.A.*, **2012**, *109*, 686.
89. D. Miller, *J. Phys. Chem.*, **1908**, *13*, 256.

90. F. Fischer, *Zeitschrift für Elektrochemie*, **1903**, 9, 507.
91. H. W. Gillett, *J. Phys. Chem.*, **1908**, 13, 332.
92. Q. Xu, B. Huang, Y. Zhao, Y. Yan, R. Noufi, and S.-H. Wei, *Appl. Phys. Lett.*, **2012**, 100, 61906.
93. J. C. W. Folmer, F. Jellinek, and G. H. M. Calis, *J. Solid State Chem.*, **1988**, 72, 137.
94. J. C. W. Folmer and F. Jellinek, *J. Less-Common MET.*, **1980**, 76, 153.
95. F. King, C. Lilja, and M. Vähänen, *J. Nucl. Mater.*, **2013**, 438, 228.
96. C. Sena, J. Salas, and D. Arcos, Aspects of geochemical evolution of the SKB near field in the frame of SR-Site, TR-10-59, Swedish Nuclear Fuel and Waste Management Co, **2010**.
97. M. Laaksoharju, M. Gimeno, L. Auqué, J. Gómez, J. Smellie, E.-L. Tullborg, and I. Gurban, Hydrogeochemical evaluation of the Forsmark site, model version 1.1, R-04-05, Swedish Nuclear Fuel and Waste Management Co, **2004**.
98. L. F. Auqué, M. J. Gimeno, I. Puigdomenech, J. Smellie, and E.-L. Tullborg, Groundwater chemistry around a repository for spent nuclear fuel over a glacial cycle. Evaluation for SR-Can, TR-06-31, Swedish Nuclear Fuel and Waste Management Co, **2006**.
99. F. King, C. Lilja, K. Pedersen, P. Pitkänen, and M. Vähänen, An update of the state-of-the-art report on the corrosion of copper under expected conditions in a deep geologic repository, SKB, **2010**.
100. E.-L. Tullborg, J. Smellie, A.-C. Nilsson, M. J. Gimeno, L. F. Auqué, V. Brüchert, and J. Molinero, SR-Site - sulphide content in the groundwater at Forsmark, TR-10-39, Swedish Nuclear Fuel and Waste Management Co, **2010**.
101. SKB, Site description of Forsmark at completion of the site investigation phase. SDM-Site Forsmark, TR-08-05, Swedish Nuclear Fuel and Waste Management Co, **2008**.
102. SKB, Data report for the safety assessment SR-Site, TR-10-52, Swedish Nuclear Fuel and Waste Management Co, **2010**.
103. J. Salas, M. J. Gimeno, L. Auqué, J. Molinero, J. Gómez, and I. Juárez, SR-Site - hydrogeochemical evolution of the Forsmark site, TR-10-58, Swedish Nuclear Fuel and Waste Management Co, **2010**.
104. SKB, Design, production and initial state of the buffer, TR-10-15, Swedish Nuclear Fuel and Waste Management Co, **2010**.
105. SKB, Corrosion calculations report for the safety assessment SR-Site, TR-10-66, Swedish Nuclear Fuel and Waste Management Co, **2010**.
106. F. Grandia, C. Domènech, D. Arcos, and L. Duro, Assessment of the oxygen consumption in the backfill. Geochemical modelling in a saturated backfill, R-06-106, Swedish Nuclear Fuel and Waste Management Co, **2006**.
107. K. Lundgren, Final disposal of fuel - electron radiation outside copper canister, TR-04-06, Swedish Nuclear Fuel and Waste Management Co, **2004**.
108. K. Pedersen, The Microbe project: Achievements of a 10-year research programme, R-13-49, Swedish Nuclear Fuel and Waste Management Co, **2013**.
109. Å. Björkbacka, S. Hosseinpour, C. Leygraf, and M. Jonsson, *Electrochem. Solid-State Lett.*, **2012**, 15, C5.
110. Å. Björkbacka, S. Hosseinpour, M. Johnson, C. Leygraf, and M. Jonsson, *Radiat. Phys. Chem.*, **2013**, 92, 80.
111. Å. Björkbacka, M. Yang, C. Gasparrini, C. Leygraf, and M. Jonsson, *Dalton Trans.*, **2015**, 44, 16045.

112. C. M. Lousada, I. L. Soroka, Y. Yagodzinskyy, N. V. Tarakina, O. Todoshchenko, H. Hänninen, P. A. Korzhavyi, and M. Jonsson, *Sci. Rep.*, **2016**, 6, 24234.
113. Å. Björkbacka, C. M. Johnson, C. Leygraf, and M. Jonsson, *J. Electrochem. Soc.*, **2017**, 164, C201.
114. Å. Björkbacka, C. M. Johnson, C. Leygraf, and M. Jonsson, *J. Phys. Chem. C*, **2016**, 120, 11450.
115. I. Neretnieks and A. J. Johansson, Corrosion of the copper canister inside due to radiolysis of remaining water in the insert, SKBdoc 1419961, Swedish Nuclear Fuel and Waste Management Company, **2014**.
116. B. Beverskog and I. Puigdomenech, *J. Electrochem. Soc.*, **1997**, 144, 3476.
117. G. Hultquist, *Corros. Sci.*, **1986**, 26, 173.
118. G. Hultquist, M. J. Graham, O. Kodra, S. Moisa, R. Liu, U. Bexell, and J. L. Smialek, *Corros. Sci.*, **2015**, 95, 162.
119. G. Hultquist, P. Szakálos, M. J. Graham, A. B. Belonoshko, G. I. Sproule, L. Gråsjö, P. Dorogokupets, B. Danilov, T. AAstrup, G. Wikmark, G.-K. Chuah, J.-C. Eriksson, and A. Rosengren, *Catal. Lett.*, **2009**, 132, 311.
120. G. Hultquist, M. J. Graham, P. Szakalos, G. I. Sproule, A. Rosengren, and L. Gråsjö, *Corros. Sci.*, **2011**, 53, 310.
121. P. Szakálos, G. Hultquist, and G. Wikmark, *Electrochem. Solid-State Lett.*, **2007**, 10, C63.
122. C. Cleveland, S. Moghaddam, and M. E. Orazem, *J. Electrochem. Soc.*, **2014**, 161, C107.
123. M. Pourbaix, “*Atlas of electrochemical equilibria in aqueous solutions*”, **1966**, Pergamon Press, Oxford.
124. E. Mattsson, *Brit. Corros. J.*, **1980**, 15, 6.
125. I. Puigdomenech and C. Taxén, Thermodynamic data for copper: Implications for the corrosion of copper under repository conditions, TR-00-13, Swedish Nuclear Fuel and Waste Management Co, **2000**.
126. D. Landolt, “*Corrosion and Surface Chemistry of Metals*”, **2007**, EPFL Press, Lausanne.
127. A. Hedin, A. J. Johansson, and L. Werme, *Corros. Sci.*, **2016**, 106, 303.
128. G. Hultquist, M. J. Graham, J. L. Smialek, and O. Kodra, *Corros. Sci.*, **2016**, 106, 306.
129. A. Hedin, A. J. Johansson, and L. Werme, *Corros. Sci.*, **2016**, 108, 215.
130. F. King, Critical review of the literature on the corrosion of copper by water, TR-10-69, Swedish Nuclear Fuel and Waste Management Co, **2010**.
131. F. King and C. Lilja, *Corros. Eng. Sci. Techn.*, **2011**, 46, 153.
132. T. Åkermarck, *Corros. Eng. Sci. Techn.*, **2013**, 48, 475.
133. F. King, A. J. Johansson, and C. Lilja, *Corros. Eng. Sci. Techn.*, **2013**, 48, 477.
134. A. Hedin, C. Lilja, A. J. Johansson, and I. Puigdomenech, Samlad Redovisning om kopparkorrosion i syrgasfritt vatten, SKBdoc 1473304, Swedish Nuclear Fuel and Waste Management Company, **2015**.
135. D. D. Macdonald and S. Sharifi-Asl, Is copper immune to corrosion when in contact with water and aqueous solutions?, SSM Report 2011:09, Swedish Radiation Safety Authority, **2011**.
136. T. W. Hicks, Quality Assurance in SKB's Copper Corrosion Experiments, SSM Report 2015:29, Swedish Radiation Safety Authority, **2015**.
137. P. Szakálos and S. Seetharaman, Corrosion of copper canister, SSM Report 2012:13, Swedish Radiation Safety Authority, **2012**.

138. NIST Chemistry Webbook (<http://webbook.nist.gov/chemistry/>), Retrieved August 11, 2017.
139. CRC Handbook of Chemistry and Physics, 97th Edition, <https://www.crcpress.com/CRC-Handbook-of-Chemistry-and-Physics-97th-Edition/Haynes/p/book/9781498754286>.
140. C. M. Lousada, R. M. F. Fernandes, N. V. Tarakina, and I. L. Soroka, *Dalton Trans.*, **2017**, 46, 6533.
141. P. A. Korzhavyi and B. Johansson, Thermodynamic properties of copper compounds with oxygen and hydrogen from first principles, TR-10-30, Swedish Nuclear Fuel and Waste Management Co, **2010**.
142. P. C. Novelli, P. M. Lang, K. A. Masarie, D. F. Hurst, R. Myers, and J. W. Elkins, *J. Geophys. Res., Atmos.*, **1999**, 104, 30427.
143. A. J. Johansson and T. Brinck, Mechanisms and energetics of surface reactions at the copper-water interface: A critical literature review with implications for the debate on corrosion of copper in anoxic water, TR-12-07, Swedish Nuclear Fuel and Waste Management Co, **2012**.
144. A. J. Johansson, C. Lilja, and T. Brinck, *J. Chem. Phys.*, **2011**, 135, 84709.
145. L. Lapeire, E. Martinez Lombardia, K. Verbeken, I. De Graeve, L. A. I. Kestens, and H. Terryn, *Corros. Sci.*, **2013**, 67, 179.
146. E. Martinez-Lombardia, Y. Gonzalez-Garcia, L. Lapeire, I. De Graeve, K. Verbeken, L. Kestens, J. M. C. Mol, and H. Terryn, *Electrochim. Acta*, **2014**, 116, 89.
147. L. Lapeire, E. M. Lombardia, I. D. Graeve, H. Terryn, and K. Verbeken, *J. Mater. Sci.*, **2017**, 52, 1501.
148. G. Hultquist, M. J. Graham, O. Kodra, S. Moisa, R. Liu, U. Bexell, and J. L. Smialek, Corrosion of copper in distilled water without molecular oxygen and the detection of produced hydrogen, SSM Report 2013:07, Swedish Radiation Safety Authority, **2013**.
149. G. Valette, *J. Electroanal. Chem. Interfac.*, **1982**, 139, 285.
150. J. H. Stenlid, A. J. Johansson, and T. Brinck, *Phys. Chem. Chem. Phys.*, **2014**, 16, 2452.
151. J. H. Stenlid, A. J. Johansson, L. Kloo, and T. Brinck, *J. Phys. Chem. C*, **2016**, 120, 1977.
152. J. H. Stenlid, M. Soldemo, A. J. Johansson, C. Leygraf, M. Göthelid, J. Weissenrieder, and T. Brinck, *Phys. Chem. Chem. Phys.*, **2016**, 18, 30570.
153. J. H. Stenlid, A. J. Johansson, C. Leygraf, and T. Brinck, *Corros. Eng. Sci. Techn.*, **2017**, 52, 50.
154. C. M. Lousada, A. J. Johansson, and P. A. Korzhavyi, *J. Phys. Chem. C*, **2015**, 119, 14102.
155. C. M. Lousada, A. J. Johansson, and P. A. Korzhavyi, *Surf. Sci.*, **2017**, 658, 1.
156. C. M. Lousada, A. J. Johansson, and P. A. Korzhavyi, *Phys. Chem. Chem. Phys.*, **2017**, 19, 8111.
157. C. Riplinger and E. A. Carter, *J. Phys. Chem. C*, **2015**, 119, 9311.
158. C. X. Kronawitter, C. Riplinger, X. He, P. Zahl, E. A. Carter, P. Sutter, and B. E. Koel, *J. Am. Chem. Soc.*, **2014**, 136, 13283.
159. R. Zhang, J. Li, B. Wang, and L. Ling, *Appl. Surf. Sci.*, **2013**, 279, 260.
160. X. Yu, X. Zhang, S. Wang, and G. Feng, *Appl. Surf. Sci.*, **2015**, 343, 33.
161. M. Boman, R. Berger, Y. Andersson, M. Hahlin, F. Björefors, T. Gustafsson, and M. Ottosson, *Corros. Eng. Sci. Techn.*, **2014**, 49, 431.

162. M. Ottosson, M. Boman, P. Berastegui, Y. Andersson, M. Hahlin, M. Korvela, and R. Berger, *Corros. Sci.*, **2017**, *122*, 53.
163. G.-C. Wang and J. Nakamura, *J. Phys. Chem. Lett.*, **2010**, *1*, 3053.
164. S. Yamamoto, K. Andersson, H. Bluhm, G. Ketteler, D. E. Starr, T. Schiros, H. Ogasawara, L. G. M. Pettersson, M. Salmeron, and A. Nilsson, *J. Phys. Chem. C*, **2007**, *111*, 7848.
165. J. Ren and S. Meng, *J. Am. Chem. Soc.*, **2006**, *128*, 9282.
166. J. Ren and S. Meng, *Phys. Rev. B*, **2008**, *77*, 54110.
167. T. Schiros, H. Ogasawara, L.-Å. Näslund, K. J. Andersson, J. Ren, S. Meng, G. S. Karlberg, M. Odelius, A. Nilsson, and L. G. M. Pettersson, *J. Phys. Chem. C*, **2010**, *114*, 10240.
168. K. Andersson, A. Gómez, C. Glover, D. Nordlund, H. Öström, T. Schiros, O. Takahashi, H. Ogasawara, L. G. M. Pettersson, and A. Nilsson, *Surf. Sci.*, **2005**, *585*, L183.
169. K. Andersson, G. Ketteler, H. Bluhm, S. Yamamoto, H. Ogasawara, L. G. M. Pettersson, M. Salmeron, and A. Nilsson, *J. Am. Chem. Soc.*, **2008**, *130*, 2793.
170. M. Soldemo, J. H. Stenlid, Z. Besharat, N. Johansson, A. Önsten, J. Knudsen, J. Schnadt, M. Göthelid, T. Brinck, and J. Weissenrieder, *submitted to J. Phys. Chem. C*, **2017**.
171. M. Ottosson, M. Boman, P. Berastegui, Y. Andersson, M. Hahlin, M. Korvela, and R. Berger, "Copper in ultra pure water", **2016**, Swedish Nuclear Fuel and Waste Management Company Technical Report TR-16-01, SKB Report TR-16-01, Swedish Nuclear Fuel and Waste Management Company.
172. M. Boman, M. Ottosson, R. Berger, Y. Andersson, M. Hahlin, F. Björefors, and T. Gustafsson, Corrosion of copper in ultrapure water, R-14-07, Swedish Nuclear Fuel and Waste Management Co, SKB, **2014**.
173. A. Bengtsson, A. Chukharina, L. Eriksson, B. Hallbeck, L. Hallbeck, J. Jonasson, and L. Johansson, Development of a method for the study of H₂ gas emission in sealed compartments containing canister copper immersed in O₂-free water, TR-13-13, Swedish Nuclear Fuel and Waste Management Co, SKB, **2013**.
174. J. P. Simpson and R. Schenk, *Corros. Sci.*, **1987**, *27*, 1365.
175. T. E. Eriksen, P. Ndalamba, and I. Grenthe, On the corrosion of copper in pure water, TR-88-17, Swedish Nuclear Fuel and Waste Management Co, **1988**.
176. T. E. Eriksen, P. Ndalamba, and I. Grenthe, *Corros. Sci.*, **1989**, *29*, 1241.
177. K. Möller, Kopparkorrosion i rent syrefritt vatten, SKI Rapport 95:72, Swedish Nuclear Power Inspectorate, **1995**.
178. R. Becker and H.-P. Hermansson, Evolution of hydrogen by copper in ultrapure water without dissolved oxygen, SSM Report 2011:34, Swedish Radiation Safety Authority, **2011**.
179. A. B. Belonoshko and A. Rosengren, *Philos. Mag. B*, **2012**, *92*, 4618.
180. A. B. Belonoshko and A. Rosengren, *Langmuir*, **2010**, *26*, 16267.
181. J. Johansson, A. Blom, A. Chukharkina, and K. Pedersen, Study of H₂ gas emission in sealed compartments containing copper immersed in O₂-free water, TR-15-03, Swedish Nuclear Fuel and Waste Management Co, **2015**.
182. C. Cleveland, M. E. Orazem, and S. Moghaddam, *J. Electrochem. Soc.*, **2016**, *163*, Y5.
183. K. Spahiu and I. Puigdomenech, *J. Electrochem. Soc.*, **2016**, *163*, Y3.
184. F. King, M. Kolar, M. Vähänen, and C. Lilja, *Corros. Eng. Sci. Techn.*, **2011**, *46*, 217.

185. Xi. Lian, P. Xiao, S.-C. Yang, R. Liu, and G. Henkelman, *J. Chem. Phys.*, **2016**, *145*, 44711.
186. Z.-J. Zuo, J. Li, P.-D. Han, and W. Huang, *J. Phys. Chem. C*, **2014**, *118*, 20332.
187. X. Lian, P. Xiao, R. Liu, and G. Henkelman, *J. Chem. Phys.*, **2017**, *146*, 111101.
188. N. Smart, B. Reddy, D. Nixon, A. Rance, and A. J. Johansson, Miniature Canister (MiniCan) Corrosion experiment Progress report 5 for 2008–2013, P-14-19, Swedish Nuclear Fuel and Waste Management Co, **2014**.
189. A. J. Johansson, C. Lilja, L. Sjögren, A. Gordon, L. Hallbeck, and L. Johnsson, *Corros. Eng. Sci. Techn.*, **2017**, *52*, 54.
190. A. Gordon, L. Sjögren, C. Taxén, and A. J. Johansson, Retrieval and post-test examination of packages 4 and 5 of the MiniCan field experiment, TR-16-12, Swedish Nuclear Fuel and Waste Management Co, **2017**.
191. F. King and C. Lilja, Localised corrosion of copper canisters in bentonite pore water, TR-13-27, Swedish Nuclear Fuel and Waste Management Co, SKB, **2013**.
192. F. King and C. Lilja, *Corros. Eng. Sci. Techn.*, **2014**, *49*, 420.
193. J. M. Smith, J. C. Wren, M. Odziemkowski, and D. W. Shoesmith, *J. Electrochem. Soc.*, **2007**, *154*, C431.
194. H. M. Hollmark, P. G. Keech, J. R. Vegelius, L. Werme, and L.-C. Duda, *Corros. Sci.*, **2012**, *54*, 85.
195. J. Chen, Z. Qin, and D. W. Shoesmith, *Electrochim. Acta*, **2011**, *56*, 7854.
196. J. Smith, Z. Qin, F. King, L. Werme, and D. W. Shoesmith, *Corrosion*, **2007**, *63*, 135.
197. J. Chen, Z. Qin, and D. W. Shoesmith, *J. Electrochem. Soc.*, **2010**, *157*, C338.
198. T. Martino, R. Partovi-Nia, J. Chen, Z. Qin, and D. W. Shoesmith, *Electrochim. Acta*, **2014**, *127*, 439.
199. D. D. Macdonald, F. Mao, C. Dong, and S. Sharifi-Asl, Measurement of Parameter Values for Predicting Corrosion Phenomena on Copper in Swedish HLNW Repositories - Phase IV: Impact of Chloride Ion on the Passivity and Pitting of Copper, SSM Report 2016:30, Swedish Radiation Safety Authority, **2016**.
200. A. Szabo and N. S. Ostlund, “*Modern Quantum Chemistry*”, **1995**, Dover.
201. F. Jensen, “*Introduction to Computational Chemistry*”, **2013**, John Wiley & Sons.
202. A. R. Leach, “*Molecular Modeling: Principles and Applications*”, **2001**, 2nd ed. , Pearson Education, Ltd., Harlow, England.
203. R. M. Martin, “*Electronic Structure: Basic Theory and Practical Methods*”, **2004**, Cambridge University Press.
204. E. van Lenthe, E. J. Baerends, and J. G. Snijders, *J. Chem. Phys.*, **1993**, *99*, 4597.
205. C. van Wüllen, *J. Chem. Phys.*, **1998**, *109*, 392.
206. M. Douglas and N. M. Kroll, *Ann. Phys.*, **1974**, *82*, 89.
207. B. A. Hess, *Phys. Rev. A*, **1986**, *33*, 3742.
208. M. Reiher, *Theor. Chem. Acc.*, **2006**, *116*, 241.
209. P. E. Blöchl, *Phys. Rev. B*, **1994**, *50*, 17953.
210. G. Kresse and D. Joubert, *Phys. Rev. B*, **1999**, *59*, 1758.
211. T. Koopmans, *Physica*, **1934**, *1*, 104.
212. J. F. Janak, *Phys. Rev. B*, **1978**, *18*, 7165.
213. T. Helgaker, P. Jorgensen, and J. Olsen, “*Molecular Electronic-Structure Theory*”, **2014**, John Wiley & Sons.
214. C. Riplinger and F. Neese, *J. Chem. Phys.*, **2013**, *138*, 34106.
215. P. Hohenberg and W. Kohn, *Phys. Rev.*, **1964**, *136*, B864.
216. M. Levy, *Proc. Natl. Acad. Sci. U.S.A.*, **1979**, *76*, 6062.

217. M. Levy, *Phys. Rev. A*, **1982**, 26, 1200.
218. W. Kohn and L. J. Sham, *Phys. Rev.*, **1965**, 140, A1133.
219. J. P. Perdew and K. Schmidt, *AIP Conf. Proc.*, **2001**, 577, 1.
220. S. H. Vosko, L. Wilk, and M. Nusair, *Can. J. Phys.*, **1980**, 58, 1200.
221. J. P. Perdew, K. Burke, and M. Ernzerhof, *Phys. Rev. Lett.*, **1996**, 77, 3865.
222. J. Tao, J. P. Perdew, V. N. Staroverov, and G. E. Scuseria, *Phys. Rev. Lett.*, **2003**, 91, 146401.
223. D. C. Langreth and J. P. Perdew, *Phys. Rev. B*, **1977**, 15, 2884.
224. D. C. Langreth and J. P. Perdew, *Phys. Rev. B*, **1980**, 21, 5469.
225. C. Adamo and V. Barone, *J. Chem. Phys.*, **1999**, 110, 6158.
226. A. D. Becke, *J. Chem. Phys.*, **1993**, 98, 5648.
227. P. J. Stephens, F. J. Devlin, C. F. Chabalowski, and M. J. Frisch, *J. Phys. Chem.*, **1994**, 98, 11623.
228. Y. Zhao and D. Truhlar, *Theor. Chem. Acc.*, **2008**, 120, 215.
229. S. Grimme, *J. Chem. Phys.*, **2006**, 124, 34108.
230. J. Heyd, G. E. Scuseria, and M. Ernzerhof, *J. Chem. Phys.*, **2003**, 118, 8207.
231. J. Heyd, G. E. Scuseria, and M. Ernzerhof, *J. Chem. Phys.*, **2006**, 124, 219906.
232. T. Yanai, D. P. Tew, and N. C. Handy, *Chem. Phys. Lett.*, **2004**, 393, 51.
233. S. Grimme, J. Antony, S. Ehrlich, and H. Krieg, *J. Chem. Phys.*, **2010**, 132, 154104.
234. M. Dion, H. Rydberg, E. Schröder, D. C. Langreth, and B. I. Lundqvist, *Phys. Rev. Lett.*, **2004**, 92, 246401.
235. J. Wellendorff, K. T. Lundgaard, A. Møgelhøj, V. Petzold, D. D. Landis, J. K. Nørskov, T. Bligaard, and K. W. Jacobsen, *Phys. Rev. B*, **2012**, 85, 235149.
236. S. L. Dudarev, G. A. Botton, S. Y. Savrasov, C. J. Humphreys, and A. P. Sutton, *Phys. Rev. B*, **1998**, 57, 1505.
237. C. Kittel, "Introduction to Solid State Physics", 8th ed., John Wiley & Sons, New York.
238. R. Hoffmann, *Angew. Chem. Int. Ed. Engl.*, **1987**, 26, 846.
239. H. J. Monkhorst and J. D. Pack, *Phys. Rev. B*, **1976**, 13, 5188.
240. D. Porezag, T. Frauenheim, T. Köhler, G. Seifert, and R. Kaschner, *Phys. Rev. B*, **1995**, 51, 12947.
241. J. J. P. Stewart, *J. Comput. Chem.*, **1989**, 10, 209.
242. M. J. S. Dewar and D. M. Storch, *J. Am. Chem. Soc.*, **1985**, 107, 3898.
243. F. Jensen, "Introduction to Computational Chemistry", Second ed., **2006**, Wiley, 22.
244. P. N. Day, J. H. Jensen, M. S. Gordon, S. P. Webb, W. J. Stevens, M. Krauss, D. Garmer, H. Basch, and D. Cohen, *J. Chem. Phys.*, **1996**, 105, 1968.
245. A. C. T. van Duin, S. Dasgupta, F. Lorant, and W. A. Goddard, *J. Phys. Chem. A*, **2001**, 105, 9396.
246. J. Tomasi, B. Mennucci, and R. Cammi, *Chem. Rev.*, **2005**, 105, 2999.
247. E. Cancès, B. Mennucci, and J. Tomasi, *J. Chem. Phys.*, **1997**, 107, 3032.
248. E. Cancès and B. Mennucci, *J. Math. Chem.*, **1998**, 23, 309.
249. A. Klamt and G. Schüürmann, *J. Chem. Soc., Perkin Trans. 2*, **1993**, 799.
250. A. Klamt and V. Jonas, *J. Chem. Phys.*, **1996**, 105, 9972.
251. K. Mathew, R. Sundararaman, K. Letchworth-Weaver, T. A. Arias, and R. G. Hennig, *J. Chem. Phys.*, **2014**, 140, 84106.
252. L. Verlet, *Phys. Rev.*, **1967**, 159, 98.

253. H. J. C. Berendsen, J. P. M. Postma, W. F. van Gunsteren, A. DiNola, and J. R. Haak, *J. Chem. Phys.*, **1984**, *81*, 3684.
254. S. Nosé, *Mol. Phys.*, **1984**, *52*, 255.
255. W. G. Hoover, *Phys. Rev. A*, **1985**, *31*, 1695.
256. G. King and A. Warshel, *J. Chem. Phys.*, **1989**, *91*, 3647.
257. J. W. Essex and W. L. Jorgensen, *J. Comput. Chem.*, **1995**, *16*, 951.
258. G. Henkelman, B. P. Uberuaga, and H. Jónsson, *J. Chem. Phys.*, **2000**, *113*, 9901.
259. J. W. Ochterski, Thermochemistry in Gaussian. www.gaussian.com (accessed Dec 08, 2015).
260. W.-X. Li, C. Stampfl, and M. Scheffler, *Phys. Rev. B*, **2003**, *68*, 165412.
261. D. A. McQuarrie, “*Statistical Mechanics*”, **2004**, University Science Books, Sausalito.
262. G. Makov and M. C. Payne, *Phys. Rev. B*, **1995**, *51*, 4014.
263. J. Neugebauer and M. Scheffler, *Phys. Rev. B*, **1992**, *46*, 16067.
264. K. Hermann, “*Crystallography and Surface Structure: An Introduction for Surface Scientists and Nanoscientists*”, **2016**, Wiley-VCH Verlag GmbH & Co. KGaA.
265. A. Nilsson, *J. Electron. Spectrosc. Relat. Phenom.*, **2002**, *126*, 3.
266. N. Mårtensson and A. Nilsson, *J. Electron. Spectrosc. Relat. Phenom.*, **1995**, *75*, 209.
267. O. Takahashi and L. G. M. Pettersson, *J. Chem. Phys.*, **2004**, *121*, 10339.
268. V. Nilsson, M. Van den Bossche, A. Hellman, and H. Grönbeck, *Surf. Sci.*, **2015**, *640*, 59.
269. M. V. den Bossche, N. M. Martin, J. Gustafson, C. Hakanoglu, J. F. Weaver, E. Lundgren, and H. Grönbeck, *J. Chem. Phys.*, **2014**, *141*, 34706.
270. L. Köhler and G. Kresse, *Phys. Rev. B*, **2004**, *70*, 165405.
271. M. Birgersson, C.-O. Almbladh, M. Borg, and J. N. Andersen, *Phys. Rev. B*, **2003**, *67*, 45402.
272. J. Carrasco, A. Hodgson, and A. Michaelides, *Nat. Mater.*, **2012**, *11*, 667.
273. J. Tersoff and D. R. Hamann, *Phys. Rev. B*, **1985**, *31*, 805.
274. K. Fukui, T. Yonezawa, and H. Shingu, *J. Chem. Phys.*, **1952**, *20*, 722.
275. F. Jensen, “*Introduction to Computational Chemistry*”, 2nd ed., **2006**, Wiley, pp. 488.
276. A. Devaquet, *Mol. Phys.*, **1970**, *18*, 233.
277. R. G. Parr and W. Yang, *J. Am. Chem. Soc.*, **1984**, *106*, 4049.
278. R. S. Mulliken, *J. Chem. Phys.*, **1955**, *23*, 1833.
279. P. Löwdin, *J. Chem. Phys.*, **1950**, *18*, 365.
280. F. L. Hirshfeld, *Theo. Chem. Acc.*, **1977**, *44*, 129.
281. A. V. Marenich, S. V. Jerome, C. J. Cramer, and D. G. Truhlar, *J. Chem. Theory Comput.*, **2012**, *8*, 527.
282. R. F. W. W. Bader, “*Atoms in Molecules - A Quantum Theory*”, **1990**, Oxford University Press.
283. U. C. Singh and P. A. Kollman, *J. Comput. Chem.*, **1984**, *5*, 129.
284. B. H. Besler, K. M. Merz, and P. A. Kollman, *J. Comput. Chem.*, **1990**, *11*, 431.
285. P. Politzer and D. G. Truhlar, “*Chemical Applications of Atomic and Molecular Electrostatic Potentials*”, **1981**, Plenum Press.
286. P. Politzer and J. S. Murray, *Theor. Chem. Acc.*, **2002**, *108*, 134.
287. J. S. Murray and P. Politzer, *Wiley. Interdiscip. Rev. Comput. Mol. Sci.*, **2011**, *1*, 153.

288. P. Sjöberg and P. Politzer, *J. Phys. Chem.*, **1990**, *94*, 3959.
289. P. Sjöberg, J. S. Murray, T. Brinck, P. Evans, and P. Politzer, *J. Mol. Graph.*, **1990**, *8*, 81.
290. T. Clark, M. Hennemann, J. Murray, and P. Politzer, *J. Mol. Model.*, **2007**, *13*, 291.
291. J. Murray, P. Lane, T. Clark, K. Riley, and P. Politzer, *J. Mol. Model.*, **2012**, *18*, 541.
292. M. M. Francl, *J. Phys. Chem.*, **1985**, *89*, 428.
293. P. Jin, J. S. Murray, and P. Politzer, *Int. J. Quantum Chem.*, **2004**, *96*, 394.
294. T. Brinck, J. S. Murray, and P. Politzer, *Int. J. Quantum Chem.*, **1993**, *48*, 73.
295. H. Hagelin, J. S. Murray, P. Politzer, T. Brinck, and M. Berthelot, *Can. J. Chem.*, **1995**, *73*, 483.
296. E. D. Stevens, *Mol. Phys.*, **1979**, *37*, 27.
297. S. J. Harris, S. E. Novick, J. S. Winn, and W. Klemperer, *J. Chem. Phys.*, **1974**, *61*, 3866.
298. K. Riley, J. Murray, J. Fanfrlík, J. Řezáč, R. Solá, M. Concha, F. Ramos, and P. Politzer, *J. Mol. Model.*, **2011**, *17*, 3309.
299. T. Brinck, J. S. Murray, P. Politzer, and R. E. Carter, *J. Org. Chem.*, **1991**, *56*, 2934.
300. T. Brinck, J. S. Murray, and P. Politzer, *J. Org. Chem.*, **1991**, *56*, 5012.
301. M. Liljenberg, T. Brinck, B. Herschend, T. Rein, G. Rockwell, and M. Svensson, *J. Org. Chem.*, **2010**, *75*, 4696.
302. P. Politzer, J. S. Murray, and F. A. Bulat, *J. Mol. Model.*, **2010**, *16*, 1731.
303. F. A. Bulat, M. Levy, and P. Politzer, *J. Phys. Chem. A*, **2009**, *113*, 1384.
304. H. Zhuang, A. J. Tkalych, and E. A. Carter, *J. Phys. Chem. C*, **2016**, *120*, 23698.
305. F. Calle-Vallejo, N. G. Inoglu, H.-Y. Su, J. I. Martínez, I. C. Man, M. T. M. Koper, J. R. Kitchin, and J. Rossmeisl, *Chem. Sci.*, **2013**, *4*, 1245.
306. F. Calle-Vallejo, J. I. Martínez, J. M. García-Lastra, P. Sautet, and D. Loffreda, *Angew. Chem. Int. Ed.*, **2014**, *53*, 8316.
307. F. Calle-Vallejo, J. Tymoczko, V. Colic, Q. H. Vu, M. D. Pohl, K. Morgenstern, D. Loffreda, P. Sautet, W. Schuhmann, and A. S. Bandarenka, *Science*, **2015**, *350*, 185.
308. F. Calle-Vallejo, D. Loffreda, M. T. M. Koper, and P. Sautet, *Nat. Chem.*, **2015**, *7*, 403.
309. P. K. Chattaraj, U. Sarkar, and D. R. Roy, *Chem. Rev.*, **2006**, *106*, 2065.
310. A. T. Maynard, M. Huang, W. G. Rice, and D. G. Covell, *Proc. Natl. Acad. Sci. U.S.A.*, **1998**, *95*, 11578.
311. R. G. Parr, L. v. Szentpály, and S. Liu, *J. Am. Chem. Soc.*, **1999**, *121*, 1922.
312. L. R. Domingo, P. Perez, and R. Contreras, *Tetrahedron*, **2004**, *60*, 6585.
313. B. Hammer and J. K. Nørskov, *Nature*, **1995**, *376*, 238.
314. T. Bligaard and J. K. Nørskov, "Chemical Bonding at Surfaces and Interfaces", ed. A. Nilsson, L. G. M. Pettersson, and J. K. Nørskov, **2008**, Elsevier, Amsterdam, pp. 255.
315. J. K. Nørskov, F. Abild-Pedersen, F. Studt, and T. Bligaard, *Proc. Natl. Acad. Sci. U.S.A.*, **2011**, *108*, 937.
316. J. K. Nørskov, F. Studt, F. Abild-Pedersen, and T. Bligaard, "Energy Trends in Catalysis, in *Fundamental Concepts in Heterogeneous Catalysis*", **2014**, John Wiley & Sons, Hoboken, pp. 85.

317. J. K. Nørskov, T. Bligaard, J. Rossmeisl, and C. H. Christensen, *Nat. Chem.*, **2009**, *1*, 37.
318. B. Hammer and J. K. Nørskov, *Advances in Catalysis*, **2000**, *45*, 71.
319. J. N. Brønsted, *Chem. Rev.*, **1928**, *5*, 231.
320. M. G. Evans and M. Polanyi, *Trans. Faraday Soc.*, **1938**, *34*, 11.
321. P. Liu and J. K. Nørskov, *Phys. Chem. Chem. Phys.*, **2001**, *3*, 3814.
322. D. M. Newns, *Phys. Rev.*, **1969**, *178*, 1123.
323. P. W. Anderson, *Phys. Rev.*, **1961**, *124*, 41.
324. S. Schnur and A. Groß, *Phys. Rev. B*, **2010**, *81*, 33402.
325. T. Hofmann, T. H. Yu, M. Folse, L. Weinhardt, M. Bär, Y. Zhang, B. V. Merinov, D. J. Myers, W. A. Goddard, and C. Heske, *J. Phys. Chem. C*, **2012**, *116*, 24016.
326. T. H. Yu, T. Hofmann, Y. Sha, B. V. Merinov, D. J. Myers, C. Heske, and W. A. Goddard, *J. Phys. Chem. C*, **2013**, *117*, 26598.
327. H. Xin, A. Vojvodic, J. Voss, J. K. Nørskov, and F. Abild-Pedersen, *Phys. Rev. B*, **2014**, *89*, 115114.
328. H. B. Tao, L. Fang, J. Chen, H. B. Yang, J. Gao, J. Miao, S. Chen, and B. Liu, *J. Am. Chem. Soc.*, **2016**, *138*, 9978.
329. Gaussian 09, Revision D.01, M. J. Frisch, et al., Gaussian, Inc., Wallingford CT, **2009**.
330. F. Neese, *Wiley Interdiscip. Rev. Comput. Mol. Sci.*, **2012**, *2*, 73.
331. Jaguar, version 7.9, Schrödinger, LLC, New York, NY, 2012.
332. ADF2012, SCM, Theoretical Chemistry. Vrije Universiteit, Amsterdam.
333. M. W. Schmidt, K. K. Baldridge, J. A. Boatz, S. T. Elbert, M. S. Gordon, J. H. Jensen, S. Koseki, N. Matsunaga, K. A. Nguyen, S. Su, T. L. Windus, M. Dupuis, and J. A. Montgomery, *J. Comput. Chem.*, **1993**, *14*, 1347.
334. M. S. Gordon and M. W. Schmidt, "Theory and Applications of Computational Chemistry", ed. Clifford E. Dykstra, G. Frenking, Kwang S. Kim, and Gustavo E. Scuseria, **2005**, Elsevier, Amsterdam, 1167.
335. TURBOMOLE V6.4 **2012**, a development of University of Karlsruhe and Forschungszentrum Karlsruhe GmbH, 1989-2007, TURBOMOLE GmbH, since 2007; available from <http://www.turbomole.com>.
336. I. S. Ufimtsev and T. J. Martinez, *J. Chem. Theory Comput.*, **2009**, *5*, 2619.
337. J. Kästner, J. M. Carr, T. W. Keal, W. Thiel, A. Wander, and P. Sherwood, *J. Phys. Chem. A*, **2009**, *113*, 11856.
338. G. Kresse and J. Hafner, *Phys. Rev. B*, **1993**, *47*, 558.
339. G. Kresse and J. Hafner, *Phys. Rev. B*, **1993**, *48*, 13115.
340. G. Kresse and J. Hafner, *Phys. Rev. B*, **1994**, *49*, 14251.
341. G. Kresse and J. Furthmüller, *Phys. Rev. B*, **1996**, *54*, 11169.
342. G. Kresse and J. Furthmüller, *Comp. Mater. Sci.*, **1996**, *6*, 15.
343. J. A. Howard and B. Mile, "Electron Spin Resonance: Specialists Periodic Reports", **1988**, Vol. 11B, London.
344. J. A. Howard, R. Sutcliffe, J. S. Tse, and B. Mile, *Chem. Phys. Lett.*, **1983**, *94*, 561.
345. R. J. Van Zee and W. Weltner, *J. Chem. Phys.*, **1990**, *92*, 6976.
346. M. B. Gawande, A. Goswami, F.-X. Felpin, T. Asefa, X. Huang, R. Silva, X. Zou, R. Zboril, and R. S. Varma, *Chem. Rev.*, **2016**, *116*, 3722.
347. I. Persson, *Pure Appl. Chem.*, **2010**, *82*, 1901.
348. M. Zobel, *Acta. Cryst.*, **2016**, *72*, 621.
349. V. S. Bryantsev, M. S. Diallo, and W. A. Goddard III, *J. Phys. Chem. B*, **2008**, *112*, 9709.

350. A. Schäfer, H. Horn, and R. Ahlrichs, *J. Chem. Phys.*, **1992**, 97, 2571.
351. P. J. Hay and W. R. Wadt, *J. Chem. Phys.*, **1985**, 82, 299.
352. “Jaguar, version 7.9, User Manual”, Schrödinger LLC: New York **2014**.
353. F. Weigend and R. Ahlrichs, *Phys. Chem. Chem. Phys.*, **2005**, 7, 3297.
354. S. Grimme, S. Ehrlich, and L. Goerigk, *J. Comput. Chem.*, **2011**, 32, 1456.
355. J. Nakamura, J. M. Campbell, and C. T. Campbell, *J. Chem. Soc., Faraday Trans.*, **1990**, 86, 2725.
356. C. T. Campbell and K. A. Daube, *J. Catal.*, **1987**, 104, 109.
357. E. D. Glendening, A. E. Reed, J. E. Carpenter, and F. Weinhold, “The NBO 3.0 Program Manual”, **1990**.
358. A. Soon, M. Todorova, B. Delley, and C. Stampfl, *Phys. Rev. B*, **2007**, 75, 125420.
359. L. I. Bendavid and E. A. Carter, *J. Phys. Chem. B*, **2013**, 117, 15750.
360. A. Önsten, M. Göthelid, and U. O. Karlsson, *Surf. Sci.*, **2009**, 603, 257.
361. A. Önsten, J. Weissenrieder, D. Stoltz, S. Yu, M. Göthelid, and U. O. Karlsson, *J. Phys. Chem. C*, **2013**, 117, 19357.
362. J. Heyd and G. E. Scuseria, *J. Chem. Phys.*, **2004**, 121, 1187.
363. J. Heyd and G. E. Scuseria, *J. Chem. Phys.*, **2004**, 120, 7274.
364. N. Nilius, H. Fedderwitz, B. Gross, C. Noguera, and J. Goniakowski, *Phys. Chem. Chem. Phys.*, **2016**, 18, 6729.
365. K. H. Schulz and D. F. Cox, *Phys. Rev. B*, **1991**, 43, 1610.
366. M. Soldemo, J. H. Stenlid, Z. Besharat, M. G. Yazdi, A. Önsten, C. Leygraf, M. Göthelid, T. Brinck, and J. Weissenrieder, *J. Phys. Chem. C*, **2016**, 120, 4373.
367. D. F. Cox and K. H. Schulz, *Surf. Sci.*, **1991**, 256, 67.
368. Z. Besharat, J. H. Stenlid, M. Soldemo, K. Marks, A. Önsten, M. Johnson, H. Öström, J. Weissenrieder, T. Brinck, and M. Göthelid, *J. Chem. Phys.*, **2017**, 146, 244702.
369. P. T. Kristiansen, F. Massel, L. Werme, C. Lilja, and L.-C. Duda, *J. Electrochem. Soc.*, **2015**, 162, C785.
370. P. Marcus, “Corrosion Mechanisms in Theory and Practice”, 3rd ed., **2011**, CRC Press, pp. 395.
371. A. Galtayries and J.-P. Bonnelle, *Surf. Interface Anal.*, **1995**, 23, 171.
372. J. Lin, J. A. May, S. V. Didziulis, and E. I. Solomon, *J. Am. Chem. Soc.*, **1992**, 114, 4718.
373. A. J. Cohen, P. Mori-Sánchez, and W. Yang, *Phys. Rev. B*, **2008**, 77, 115123.
374. P. Mori-Sánchez, A. J. Cohen, and W. Yang, *J. Chem. Phys.*, **2006**, 125, 201102.
375. M. J. G. Peach, A. M. Teale, T. Helgaker, and D. J. Tozer, *J. Chem. Theory Comput.*, **2015**, 11, 5262.
376. Y. Zhao and D. G. Truhlar, *J. Phys. Chem. A*, **2005**, 109, 5656.
377. V. Vlček, H. R. Eisenberg, G. Steinle-Neumann, L. Kronik, and R. Baer, *J. Chem. Phys.*, **2015**, 142, 34107.
378. J. P. Perdew, W. Yang, K. Burke, Z. Yang, E. K. U. Gross, M. Scheffler, G. E. Scuseria, T. M. Henderson, I. Y. Zhang, A. Ruzsinszky, H. Peng, J. Sun, E. Trushin, and A. Görling, *Proc. Natl. Acad. Sci. U.S.A.*, **2017**, 114, 2801.
379. B. Ehresmann, B. Martin, A. H. C. Horn, and T. Clark, *J. Mol. Model.*, **2003**, 9, 342.
380. T. Clark, *J. Mol. Model.*, **2010**, 16, 1231.
381. T. Bauer, C. M. Jäger, M. J. T. Jordan, and T. Clark, *J. Chem. Phys.*, **2015**, 143, 44114.
382. C. Kramer, B. Beck, and T. Clark, *J. Chem. Inf. Model.*, **2010**, 50, 429.

383. L. Kleinman, *Phys. Rev. B*, **1981**, 24, 7412.
384. C. Campañá, B. Mussard, and T. K. Woo, *J. Chem. Theory Comput.*, **2009**, 5, 2866.
385. R. M. Feenstra and M. Widom, *Ultramicroscopy*, **2013**, 130, 101.
386. R. M. Feenstra, N. Srivastava, Q. Gao, M. Widom, B. Diaconescu, T. Ohta, G. L. Kellogg, J. T. Robinson, and I. V. Vlassiouk, *Phys. Rev. B*, **2013**, 87, 41406.
387. R. Ramprasad, P. von Allmen, and L. R. C. Fonseca, *Phys. Rev. B*, **1999**, 60, 6023.
388. C. F. Bernasconi and R. B. Killion, *J. Org. Chem.*, **1989**, 54, 2878.
389. T. Brinck, P. Carlqvist, and J. H. Stenlid, *J. Phys. Chem. A*, **2016**, 120, 10023.
390. E. Berliner and L. C. Monack, *J. Am. Chem. Soc.*, **1952**, 74, 1574.
391. J. H. Stenlid and T. Brinck, *J. Org. Chem.*, **2017**, 82, 3072.
392. R. D. Chambers, D. Close, W. K. R. Musgrave, J. S. Waterhouse, and D. L. H. Williams, *J. Chem. Soc., Perkin Trans. 2*, **1977**, 1774.
393. R. D. Chambers, P. A. Martin, J. S. Waterhouse, D. L. H. Williams, and B. Anderson, *J. Fluorine Chem.*, **1982**, 20, 507.
394. R. D. Chambers, P. A. Martin, G. Sandford, and D. L. H. Williams, *J. Fluorine Chem.*, **2008**, 129, 998.
395. R. Bolton and J. P. B. Sandall, *J. Chem. Soc., Perkin Trans. 2*, **1976**, 1541.
396. F. Seeliger, S. Błażej, S. Bernhardt, M. Małosza, and H. Mayr, *Chem. Eur. J.*, **2008**, 14, 6108.
397. J. H. Stenlid and T. Brinck, *J. Am. Chem. Soc.*, **2017**, 139, 11012.
398. B. Hvolbæk, T. V. W. Janssens, B. S. Clausen, H. Falsig, C. H. Christensen, and J. K. Nørskov, *Nano Today*, **2007**, 2, 14.
399. T. V. W. Janssens, B. S. Clausen, B. Hvolbæk, H. Falsig, C. H. Christensen, T. Bligaard, and J. K. Nørskov, *Top. Catal.*, **2007**, 44, 15.
400. H. Li, L. Li, A. Pedersen, Y. Gao, N. Khetrapal, H. Jónsson, and X. C. Zeng, *Nano Lett.*, **2015**, 15, 682.
401. M. Haruta, T. Kobayashi, H. Sano, and N. Yamada, *Chem. Lett.*, **1987**, 16, 405.
402. G. C. Bond and D. T. Thompson, *Cat. Rev. - Sci. Eng.*, **1999**, 41, 319.
403. M. Stratakis and H. Garcia, *Chem. Rev.*, **2012**, 112, 4469.
404. J. H. Stenlid, A. J. Johansson, and T. Brinck, *Crystals*, **2017**, 7, 222.
405. Z. P. Shields, J. S. Murray, and P. Politzer, *Int. J. Quantum Chem.*, **2010**, 110, 2823.
406. K. Duanmu and D. G. Truhlar, *J. Phys. Chem. C*, **2014**, 118, 28069.
407. W. R. Wadt and P. J. Hay, *J. Chem. Phys.*, **1985**, 82, 284.
408. P. J. Hay and W. R. Wadt, *J. Chem. Phys.*, **1985**, 82, 270.
409. A. Hagfeldt, G. Boschloo, L. Sun, L. Kloo, and H. Pettersson, *Chem. Rev.*, **2010**, 110, 6595.
410. M. Grätzel, *Nature*, **2001**, 414, 338.
411. G. N. Chaudhari, D. R. Bambole, A. B. Bodade, and P. R. Padole, *J. Mater. Sci.*, **2006**, 41, 4860.
412. S. U. M. Khan, M. Al-Shahry, and W. B. Ingler, *Science*, **2002**, 297, 2243.
413. A. Fujishima, T. N. Rao, and D. A. Tryk, *J. Photochem. Photobiol. C*, **2000**, 1, 1.
414. A. Fujishima, X. Zhang, and D. A. Tryk, *Surf. Sci. Rep.*, **2008**, 63, 515.
415. A. Junkaew, P. Maitarad, R. Arróyave, N. Kungwan, D. Zhang, L. Shi, and S. Namuangruk, *Catal. Sci. Tech.*, **2017**, 7, 356.
416. C. Sun, *Chem. Phys. Lett.*, **2013**, 557, 106.
417. O. Diwald, T. L. Thompson, T. Zubkov, S. D. Walck, and J. T. Yates, *J. Phys. Chem. B*, **2004**, 108, 6004.

418. S. Yamazoe, T. Okumura, Y. Hitomi, T. Shishido, and T. Tanaka, *J. Phys. Chem. C*, **2007**, *111*, 11077.
419. J.-M. Herrmann, *Catal. Today*, **1999**, *53*, 115.
420. Y. Yang, B. Chen, J. Hower, M. Schindler, C. Winkler, J. Brandt, R. Giulio, J. Ge, M. Liu, Y. Fu, L. Zhang, Y. Chen, S. Priya, and M. F. Hochella, *Nat. Commun.*, **2017**, *8*, 194.
421. E. Berardo, H.-S. Hu, H. J. J. van Dam, S. A. Shevlin, S. M. Woodley, K. Kowalski, and M. A. Zwijnenburg, *J. Chem. Theory Comput.*, **2014**, *10*, 5538.
422. H. Perron, C. Domain, J. Roques, R. Drot, E. Simoni, and H. Catalette, *Theor. Chem. Acc.*, **2007**, *117*, 565.
423. J. Wellendorff, T. L. Silbaugh, D. Garcia-Pintos, J. K. Nørskov, T. Bligaard, F. Studt, and C. T. Campbell, *Surf. Sci.*, **2015**, *640*, 36.
424. C. T. Campbell and J. R. V. Sellers, *Chem. Rev.*, **2013**, *113*, 4106.
425. Y. Zhao, Z. Wang, X. Cui, T. Huang, B. Wang, Y. Luo, J. Yang, and J. Hou, *J. Am. Chem. Soc.*, **2009**, *131*, 7958.
426. B. Hammer, S. Wendt, and F. Besenbacher, *Top Catal.*, **2010**, *53*, 423.
427. K. Onda, B. Li, J. Zhao, K. D. Jordan, J. Yang, and H. Petek, *Science*, **2005**, *308*, 1154.
428. J. A. Strosio and D. M. Eigler, *Science*, **1991**, *254*, 1319.
429. G. S. Blackman, M.-L. Xu, D. F. Ogletree, M. A. Van Hove, and G. A. Somorjai, *Phys. Rev. Lett.*, **1988**, *61*, 2352.
430. H. Steininger, S. Lehwald, and H. Ibach, *Surf. Sci.*, **1982**, *123*, 264.
431. Z. Xu, J. Rossmeisl, and J. R. Kitchin, *J. Phys. Chem. C*, **2015**, *119*, 4827.
432. I. G. Ryabinkin and V. N. Staroverov, *J. Chem. Phys.*, **2014**, *141*, 84107.